University of Southampton

Faculty of Medicine

Clinical and experimental sciences

Characterisation of 3D tissue microstructures and cell distributions in human lung tissue using correlative micro-CT and immunofluorescence

by

Matthew John Lawson

ORCID ID: 0000-0003-0115-1698

Thesis for the degree of Doctor of Philosophy in Infection, Inflammation and Immunity

December 2020

University of Southampton

Abstract

Faculty of Medicine
School of Clinical and Experimental Sciences
Thesis for the degree of Doctor of Philosophy in Infection, Inflammation and Immunity

Characterisation of 3D tissue microstructures and cell distributions in human lung tissue using correlative micro-CT and immunofluorescence

By Matthew John Lawson

Micro-CT (µCT) is a non-destructive three-dimensional (3D) imaging technique used for imaging microscopic structures. The human lungs contain a highly specialised and complex series of 3D networks and structures used for the transport of air and blood that drives gas exchange. The lungs also contain an extensive cellular population of structural and immune cells critical to normal lung function which are widely studied using destructive two-dimensional (2D) histological imaging techniques.

In order to study lung microstructure the 3D imaging provided by µCT was combined with the specific localisation of cell antigens provided by immunofluorescence (IF) to develop a correlative imaging workflow. Automated co-registration of 2D IF images to µCT volumes was possible by the novel use of tissue autofluorescence to automatically identify matching structural features between the µCT and fluorescence images. This was used to inform image transformation tools which overcame sectioning artefacts to enable the direct localisation of specific cell types within the µCT tissue volume, which was only possible by correlating the images. Previous localisation of cell types and features in µCT has mostly relied on time consuming methods of manual segmentation. The interconnected 3D network of pulmonary microvasculature, down to a 25 µm thickness, was segmented semi-automatically from co-registered µCT datasets. The developed workflow automated previous bottlenecks of image registration and segmentation to significantly decrease the total time taken to generate correlative imaging data.

The correlative µCT and IF imaging workflow was used to investigate chronic obstructive pulmonary disease (COPD) as an exemplar respiratory disease with known effects on lung tissue microstructures and cell populations. A progressive decline in lung function occurs in COPD which has been well-studied using clinical 3D imaging techniques, but the 3D microstructure has been less studied. Eleven surgically resected human lung tissue biopsies, fixed in formalin and embedded in paraffin (FFPE), were split into two age-matched clinical groups (6 non-COPD and 5 mild-moderate COPD) based on lung function scores. The blood vessel network in each of the tissue samples was semi-automatically segmented for comparative assessments. The volume and size of the blood vessels did not differ significantly between the two groups. The networks were also assessed by generating a skeletonised blood vessel network which, despite no significant differences being recorded, indicated a potential reduction in the average number of blood vessel branches from 5.3 per mm^3 in non-COPD tissue to 1.4 per mm^3 in mild-moderate COPD tissue.

IF staining of cytokeratin-18 (Ck18) was used to identify airway epithelium within the same grouped lung tissue volumes as the blood vessels. Airway epithelium damage and loss is reported in COPD however the number of tissues containing airways (n=8) was not sufficient to determine

any biologically significant changes between the groups. IF staining was also used to localise mast cells and macrophages identified using AA1 and CD68 respectively. As exemplar infiltrating cells with a known role in many respiratory diseases, these were used to demonstrate the versatility of the correlative imaging workflow to identify individual cell types which were not visible at the resolution of the μCT. Automated cell counts of whole tissue sections, utilising DAPI nuclei staining, ranged between 100 and 1,000 cells per mm^2 of tissue cross-sections. The segmented individual cells were used to provide a novel distribution of mast cells in relation to the 3D networks in the grouped tissue volumes. This showed that the vast majority of mast cells were located within 2 mm of the nearest blood vessel with a peak number of mast cells located around 0.5 mm from the nearest blood vessel. Preliminary work on macrophages showed a higher number of cells per section and a higher degree of cell clustering.

Overall the development and application of the correlative μCT and IF imaging workflow to FFPE lung tissue samples demonstrated the capabilities of this work for investigating 3D tissue microstructure and cell types. These were used on a pilot study for investigating microstructural networks and infiltrating cells in mild-moderate COPD, which can be used as the basis for larger studies in the future. The total time to generate the data is significantly faster (<2 weeks) compared to existing manual techniques (several months) and it is applicable to the huge range of FFPE tissues held in biobanks and archives for future studies.

Table of Contents

Table of Tables

Table of Figures

Table of Figures

Table of Figures

Research Thesis: Declaration of Authorship

Print name: Matthew John Lawson

Title of thesis: Characterisation of 3D tissue microstructures and cell distributions in human lung tissue using correlative micro-CT and immunofluorescence

I declare that this thesis and the work presented in it are my own and has been generated by me as the result of my own original research.

I confirm that:

1. This work was done wholly or mainly while in candidature for a research degree at this University;
2. Where any part of this thesis has previously been submitted for a degree or any other qualification at this University or any other institution, this has been clearly stated;
3. Where I have consulted the published work of others, this is always clearly attributed;
4. Where I have quoted from the work of others, the source is always given. With the exception of such quotations, this thesis is entirely my own work;
5. I have acknowledged all main sources of help;
6. Where the thesis is based on work done by myself jointly with others, I have made clear exactly what was done by others and what I have contributed myself;
7. Parts of this work have been published as:

Lawson, M.J., Katsamenis, O., Olding, M., Larkin, O., Haig, I., Schneider, P., Lackie, P., Warner, J. 2020. 3D mapping of blood vessel networks and cells in COPD and non-COPD lung tissue samples using micro-computed tomography and immunofluorescence. *ERJ Open Research*, 6(21), DOI: 10.1183/23120541.lsc-2020.21

Lawson, M.J., Katsamenis, O., Chatelet, D., Alzetani, A., Larkin, O., Haig, I., Schneider, P., Lackie, P., Warner, J. Immunofluorescence-guided segmentation of three-dimensional features in micro-computed tomography datasets of human lung tissue. *Pending submission in Royal Society Open Science*.

Signature: ..... Date: 08/12/20

Acknowledgements

I would like to thank my supervisors Jane Warner, Peter Lackie and Philipp Schneider for their constant help and support throughout this project. Their guidance and help on anything no matter how small was crucial to me being able to complete this PhD.

Thank you to Orestis Katsamenis and David Chatelet for all of their help in µCT imaging, image processing, scripting and analysis. The workflow developed in this report would not have been possible without their vital inputs. Also to fellow PhD students Stephanie Robinson, Elaine Ho and Harry Rossides as the other correlative µCT students for their helpful insight and collaboration on this project.

All the staff and students at the Biomedical Imaging Unit reed a big thanks for housing me over the past four years and making feel like part of the group has been great. Also for the discussions and general support over cake in the tea room and how to get the word dollop in here have really helped keep me going over the duration of the project. Also the staff and student of the Histochemistry Research Unit, µVis X-ray imaging unit and the PCD team need thanking for all of their practical help and allowing the use of their facilities. Finally the clinical and research staff/students involved in the human lung tissue projects require a special mention as without them I would have had no samples to use in my project.

The project students Oliver Hope and Georgia May need thanking for their work which has contributed to parts of this thesis and helped me see new areas of data processing and analysis.

My industrial partners at Nikon X-Tek Systems Ltd. require thanks for providing funding and the hardware required for this project, most notably Ian Haig and Oliver Larkin who acted as industrial supervisors who let me get on with the project in the direction I wanted to go.

Lastly I would like to thank all my family and friends for their constant support throughout these turbulent times which I have been working on this PhD. Laura and the guinea pigs require special mention for their emotional support throughout my time here, and especially to Bertie whom this work is dedicated to.

List of Abbreviations

2D	Two-Dimensional
3D	Three-Dimensional
*α*SMA	Alpha-Smooth Muscle Actin
AA1	Anti-Mast Cell Tryptase
APES	3-Aminopropyltriethoxysilane
CD(x)	Cluster of Differentiation (number)
Ck18	Cytokeratin-18
CLEM	Correlative Light and Electron Microscopy
CO_2	Carbon Dioxide
COPD	Chronic Obstructive Pulmonary Disease
CPU	Computer Processing Unit
CT	Computed Tomography
DAB	3,3'-Diaminobenzidine
DAPI	4',6-Diamidino-2-phenylindole
EV	EVITA
FEV_1	Forced Expiratory Volume in 1 second
FFPE	Formalin-Fixed Paraffin-Embedded
FOV	Field of View
FVC	Forced Vital Capacity
GOLD	Global Initiative for Obstructive Lung Disease
GPU	Graphics Processing Unit
H&E	Haematoxylin and Eosin
HL	Human Lung
HRCT	High Resolution Computed Tomography
IF	Immunofluorescence
IFF	Immunofluorescence Buffer
IgE	Immunoglobulin E
IHC	Immunohistochemistry
IPF	Idiopathic Pulmonary Fibrosis
µCT	Micro(focus)-Computed Tomography
MRI	Magnetic Resonance Imaging
NA	Numerical Aperture
O_2	Oxygen
PBS	Phosphate-Buffered Saline
RAM	Random Access Memory
ROI	Region of Interest
SIFT	Scale Invariant Feature Transform
TL	Target Lung

Chapter 1 Introduction

1.1 The Lung

The lungs form the major part of the respiratory systems responsible for the transport of oxygen from the air into the blood stream and the removal of carbon dioxide (CO_2) from the body. On a basic level the pair of lungs are comprised of a three-dimensional (3D) network of tubes which end in millions of microscopic sacs called alveoli. These alveoli make up the majority of lung tissue and provide the largest surface area exposed to the external environment in the body, an estimated 100 m^2 is in contact with 10,000 L of air each day, which is required for efficient gas exchange (Wang *et al.*, 2008).

1.1.1 Anatomy of the lung

The human lungs comprise of five lobes (two in the left and three in the right lung) containing an extensive 3D network of airways and blood vessels, a model representing these networks is shown in Figure 1.1. Each lobe is made up of secondary lobules that are surrounded by connective tissue septa known as the interlobular septa. The lungs are surrounded by the pleural surface acting as the 'skin of the lungs' which contains the lung parenchyma. The pleural membranes secrete fluid to lubricate the lungs allowing the free movement over the thoracic wall required during breathing (Aung *et al.*, 2019). The lower respiratory system, connecting to and found within the lungs, starting from the trachea (10-25 mm diameter) consists of two functional zones. The conducting zone begins at the trachea and extends all the way to the terminal bronchiole (see Figure 1.2). As the airways progress through this zone they branch into the two main bronchi (one for each lung, 11-18 mm diameter) which in turn branch into the secondary bronchi (one for each of the five lobes, ~8 mm diameter) and dividing again into the tertiary bronchi (~5.5 mm diameter) which supply the segments of each lobe (Aung *et al.*, 2019). The branching of the airways continues to form the bronchioles (starting at ~4.5 mm diameter) which continue to branch until the end of the conducting zone at the terminal bronchiole (ending at ~0.6 mm diameter). Here the airways transition into the respiratory zone, where gas exchange takes place, which is comprised of the respiratory bronchioles (~0.5 mm diameter), alveolar ducts and ending with the alveolar sacs (~0.2-0.4 mm diameter) that contain the alveoli (Biga *et al.*, 2020). As the airways decrease in size the cross sectional area dramatically increases from ~25 mm^2 in the trachea to ~1800 mm^2 in the terminal bronchioles, this also acts to help reduce airflow resistance in the smallest areas of the respiratory tract (Martin *et al.*, 2013). The lung parenchyma comprises the majority of the lung tissue volume (~84%) which includes airways, blood vessels and alveolar

structures which are less than 20-25 µm in diameter (Townsley, 2011).

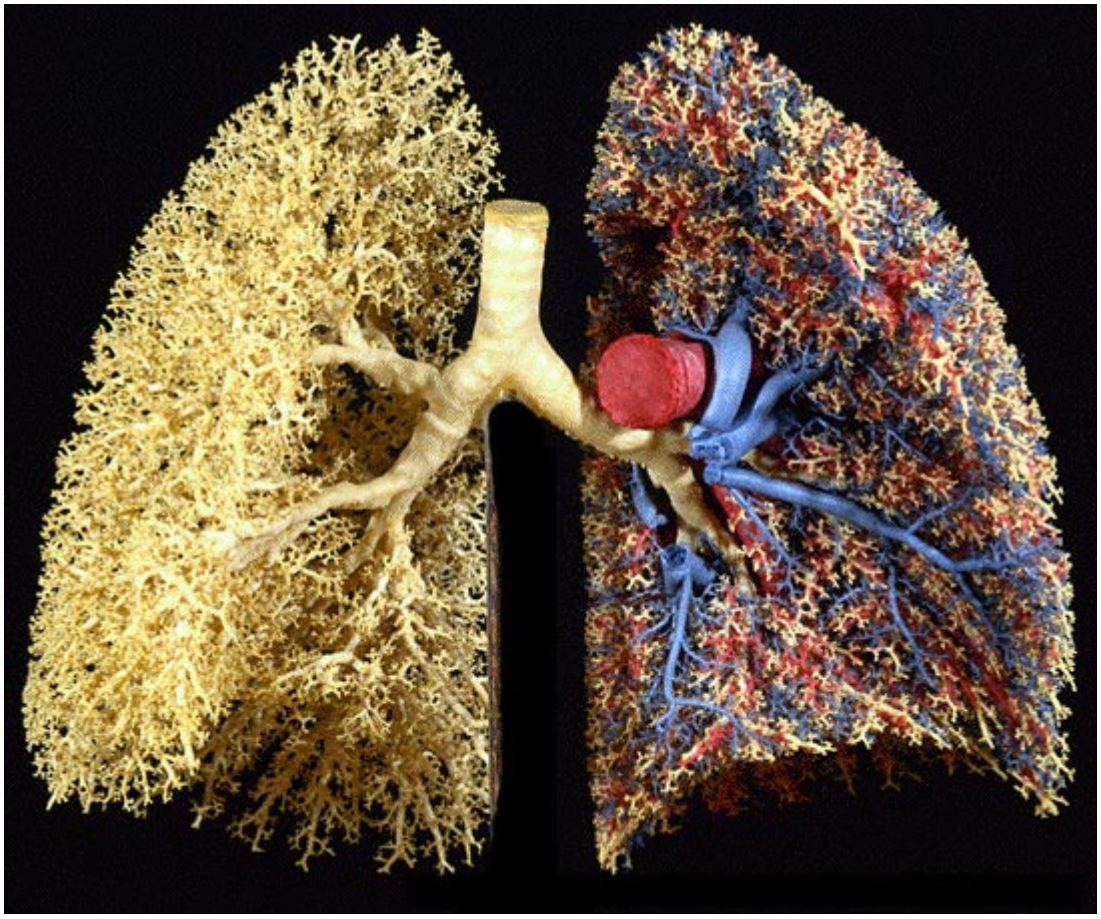

Figure 1.1: **Latex cast used to represent the human lung anatomy containing the airways (white), arterial tree (red), and venous tree (blue).** The three trees form complex interwoven structures that mirror each other all of the way out to the terminal branches. Beyond the terminal branches lie the alveoli and capillaries not visible at the scale of this image. Image reproduced under the terms of the Creative Commons licence attribution - NonCommercial - NoDerivatives 4.0 International from (Weibel, 2009).

As the airways decrease in size through the respiratory tree there is a progressive change in their structure and physiological function. The supporting hyaline cartilage, visible as C-shaped rings connected by smooth muscle in the trachea, decreases down the respiratory tree to the point where there is no supporting cartilage beyond the tertiary bronchi (Biga *et al.*, 2020). However, the smooth muscle layer which is responsible for changing the diameter of the airways to control airflow in the respiratory tree increases as the airways get smaller (Hsia *et al.*, 2016). In the respiratory zone the respiratory bronchioles and alveolar ducts are surrounded by connective tissue (the intralobular interstitium) whereas the alveolar sacs are surrounded by the interalveolar septa (Aung *et al.*, 2019).

1.1.2 Airway epithelium

The epithelium lines the inner surface of the airways, which acts to moisten the airways and also functions as a barrier protecting the lungs from airborne pathogens and foreign particulates (Stanke, 2015). The structure of the epithelium changes through the conducting and respiratory zones of the airways, particularly at branching points, as seen in Figure 1.2. In the upper respiratory tract down to the tertiary bronchi the epithelium consists of pseudostratified ciliated columnar cells (bronchial epithelium) which transition to ciliated simple columnar epithelium in the larger bronchioles (bronchiolar epithelium). In the terminal and respiratory bronchioles the epithelium transitions to ciliated simple cuboidal epithelium. The respiratory zone transitions into the alveoli which are lined with alveolar type I and II cells that constitute the alveolar epithelium.

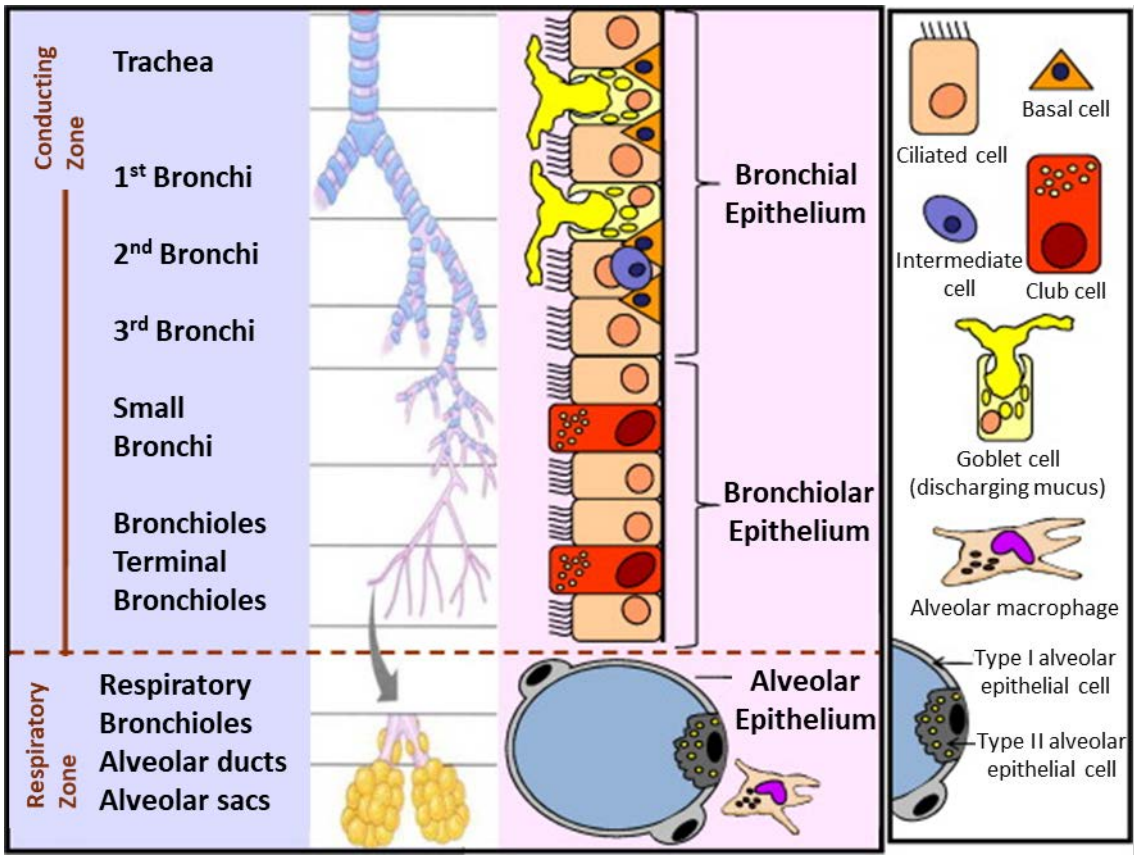

Figure 1.2: **Summary of the lower respiratory tract and the cell types present in the airway epithelium.** The conducting zone consists of the trachea and bronchi, the level of cartilage (blue rings) decreases down towards the bronchioles. The bronchial epithelium contains many goblet cells and a high number of ciliary cells to facilitate mucociliary clearance. As the airways decrease in size in the epithelium becomes more bronchiolar with the presence of club cells. The respiratory zone contains the alveoli where gas exchange takes place. The alveoli are lined with two distinct types of alveolar epithelial cells. Image adapted with permission (license number 5004150464954) from (BéruBé *et al.*, 2010).

1.1.3 Proximal airway structure

The large airways (>2 mm diameter) in the conducting zone make up the proximal airways. As mentioned previously, these airways consist of mostly ciliated columnar epithelial cells with neighbouring goblet cells and each make up approximately 30% of the total cell populations present in this part of the epithelium. These cells are exposed to the airway lumen and extend down to the basal lamina. Mucus produced from goblet cells trap foreign particles and debris from the air, which is cleared by the cilia (of the ciliated cells) that beat in one direction, moving the mucus towards the throat via mucociliary clearance (Vareille *et al.*, 2011; Miller and Spence, 2017). The basal cells, which represent another 30% of the cellular population do not come in contact with the airway lumen instead they sit upon the top layer of the basement membrane comprised of structural glycoproteins (basal lamina) (Miller and Spence, 2017). Basal cells are nearly cuboidal cells which have some ability to function as a stem cell population to differentiate into the other cells types and act to repair any damage to the epithelium (Hogan *et al.*, 2014). More widely distributed through the proximal airway epithelium are neuroendocrine cells, forming approximately 8% of the cell population, which act to regulate smooth muscle tone via the secretion of serotonin and calcitonin. Club cells are secretory cells located after the transition to bronchiolar epithelium and function to protect this portion of the airways. Club cells secrete glycosaminoglycan a component of lung surfactant, lysozymes and cytochrome P450 enzymes which can detoxify foreign particles as well as having the ability to differentiate to replace damaged cells (Hogan *et al.*, 2014). The lamina propria, which lies beneath the epithelium, is a thin layer of fibro-elastic tissue. Within the lamina propria and the submucosa there are smooth muscle layers and seromucous glands, responsible for secreting lysozyme and glycoprotein directly into the airway lumen (Hogan *et al.*, 2014). Surrounding the outermost layer of the distal airways, either the smooth muscle or the cartilage rings, is the adventitia which connects the airways to the surrounding lung parenchyma via fibro-elastic tissue (Aung *et al.*, 2019).

1.1.4 Distal lung tissue features

The distal lung tissue contains the respiratory zone which consists of the terminal bronchioles, respiratory bronchioles, alveolar ducts, alveoli and the surrounding lung parenchyma as seen in Figure 1.3. These form the respiratory subunits of the lung known as the acini or the secondary pulmonary lobules. As the airways progress through the respiratory zone towards the alveoli they become thinner and the cells more specialised for respiration (Hsia *et al.*, 2016). The respiratory bronchioles consist of ciliated cuboidal epithelium with greater numbers of club cells further down towards the alveolar ducts. Beneath the epithelium is a layer of smooth muscle and collagenous elastic tissue. The bronchioles divide into the alveolar ducts terminating at the

alveolar sac, which contains numerous individual alveoli as detailed in Figure 1.3. The alveolar ducts and openings of the alveolar sacs contain small amounts of smooth muscle which provide regulation of alveolar air movements (Biga *et al.*, 2020). The alveolar walls are very thin (0.2-2.5 µm) and consist of a single layer of simple squamous epithelial cells which neighbour the capillary beds, supplied by the pulmonary artery; this is where gas exchange takes place (Hsia *et al.*, 2016). The pulmonary vein carries the oxygenated blood back from the capillary bed to supply oxygen to the rest of the body whereas the CO_2 from the blood is transported back up the respiratory tree and exhaled. Fluids critical to the immune system are transferred between the capillary beds of the pulmonary veins and the lymph vessels (lymphatics) (Weber *et al.*, 2018). A 3D meshwork of collagen and elastic fibres surround these structures allowing them to expand and contract during inhalation and exhalation.

The alveoli consist of type I and type II epithelial cells. Up to 97% of the alveoli is covered by a very large (surface area 5,100 μm^2) and thin, ~0.2-2.5 µm thick) (Weibel, 2015) squamous epithelial lining of type I epithelial cells; which are fused to capillary endothelial cells to facilitate gas exchange (BéruBé *et al.*, 2010; Biga *et al.*, 2020). These 2D measurements of alveolar thickness were approximated from electron microscopy imaging of processed 2D ultra-thin sections, which resulted in the range reported due to tissue distortions changing the tissue from the *in vivo* state. Type II alveolar epithelial cells are small round/cuboidal cells which represent 60% of the total cells in the surface epithelium and cover the remaining 3-5% of the surface area. These cells predominantly release surfactant, a lipoprotein complex which reduces surface tension and prevents alveoli from fully collapsing when exhaling (Miller and Spence, 2017). Unlike type I cells, the type II cells can divide and differentiate into type I cells to repair and replace the alveolar lining (Hogan *et al.*, 2014).

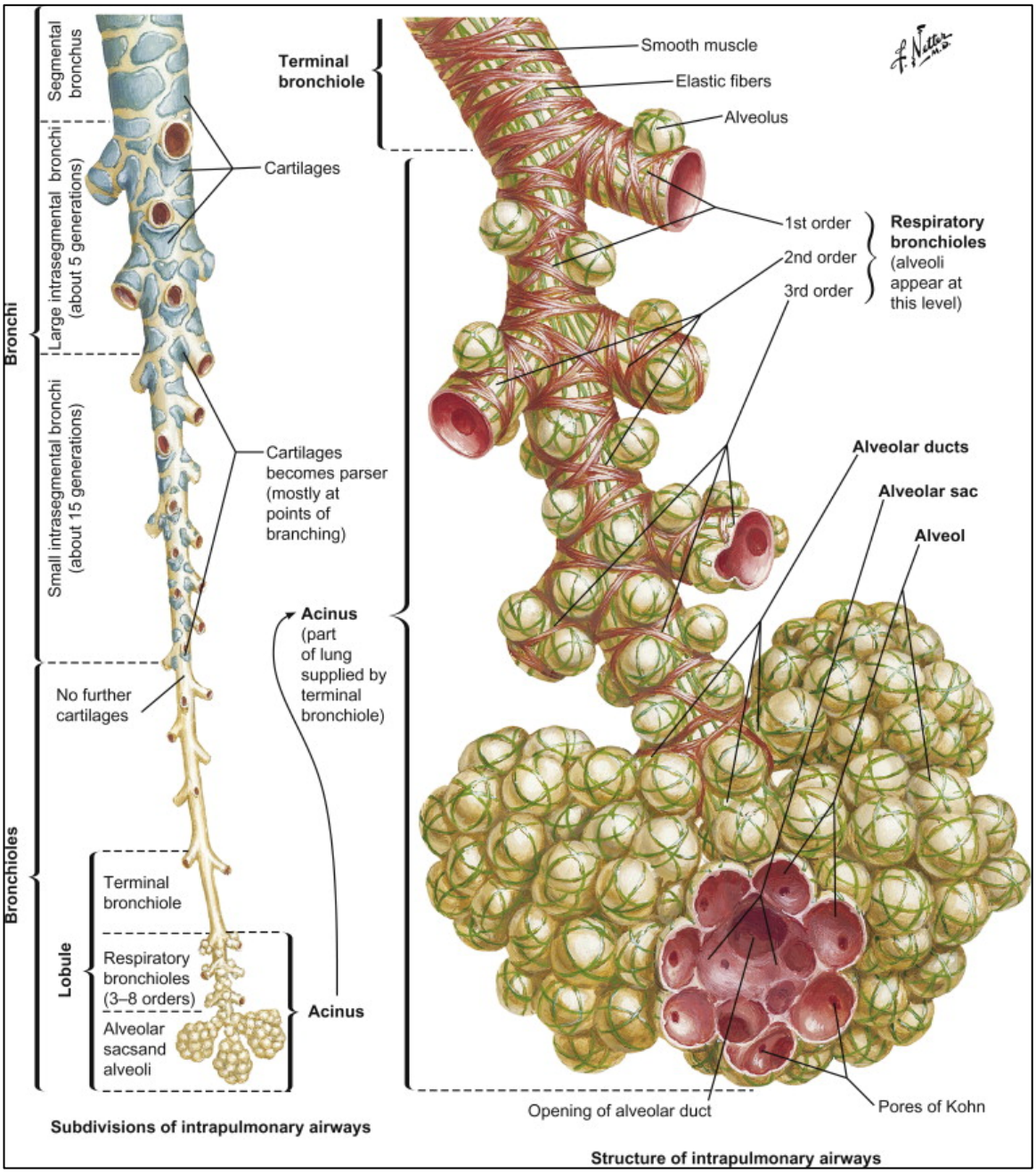

Figure 1.3: **Comprehensive diagram of the structures present in the distal respiratory tract.** The left side of the figure shows the conducting zone leading to the respiratory zone (acinus) magnified on the right side of the figure. The alveoli receive air from the respiratory bronchiole via the alveolar ducts, this is where gas exchange takes plane. Figure reproduced with permission (license number: 5004150053077) from (Suarez *et al.*, 2012).

1.1.4.1 Cytokeratin in the airway epithelium

Cytokeratins are structural proteins that form intermediate filaments in the epithelium which are responsible for maintaining tissue integrity. The expression of different cytokeratins is dependent

on the type of epithelial cell it is present in and what stage of differentiation the cells are undergoing (Zhang *et al.*, 2016). Cytokeratin-18 (Ck18) is an intermediate filament protein present in some epithelial cells and expressed in some cancer cells, however Ck18 is not present in stratified squamous epithelium or alveolar epithelium (Lauerová *et al.*, 1988). Cytokeratins are obligate heterodimers and Ck18 is commonly co-expressed alongside Cytokeratin-8 and together form important structural roles in the epithelium. Ck18 is a common marker used to identify epithelial cells in numerous tissues including the lungs. However, Ck18 is also highly expressed in, and used as a marker for, numerous cancers; most notably breast cancer (Woelfle *et al.*, 2004).

1.1.5 Lung Physiology

The blood vessels form an extensive 3D network within the lungs and are an essential component in gas exchange, taking oxygen from the air and delivering throughout the body and also transporting CO_2 to the lungs for expulsion from the circulation. However, compared to the airways, they are under-represented in respiratory research especially in chronic conditions defined by airway loss (Hueper *et al.*, 2015). The blood vessels are split into two networks of pulmonary arteries (one for each lung) and four networks of pulmonary veins (two for each lung). Unlike the rest of the body the arteries transport the de-oxygenated blood from the heart to the lungs whereas the veins transport oxygenated blood to the heart for distribution throughout the body (Hsia *et al.*, 2016). Therefore the pulmonary arteries have thinner walls and contain less elastic tissue than systemic arteries transporting oxygenated blood in the rest of the body (Townsley, 2011). The pulmonary veins vary in size up the respiratory tree up to a 10 mm diameter towards the heart and contain longitudinal bundles of smooth muscle. The blood vessels connect to and from the lung parenchyma, containing the capillaries surrounding the interalveolar septa, occupying about 20% of the total parenchyma volume (Hsia *et al.*, 2016). The blood vessels joined to the capillaries start from approximately 25 µm diameter and increase in size the further from the capillaries the vessels are. The structure and arrangement of the pulmonary blood vessels mirrors the arrangement of the airways, maintaining similar sizes and branch numbers as the airways down the respiratory tree (Glenny, 2011; Schiller *et al.*, 2019), as was seen in the model in Figure 1.1. Unlike the airways the blood vessels contain high levels of collagen and smooth muscle throughout the respiratory tract until the point the vessels branch into capillaries in the distal respiratory tract. The blood vessels inner surface is lined with endothelium which forms a barrier which oxygen, small molecules and, of particular importance in the lung, immune cells can cross into the surrounding tissue (Jambusaria *et al.*, 2020). Surrounding the endothelium is the blood vessel wall which contains smooth muscle cells, fibroblasts and pericytes as well as non-cellular structural elements including collagens and elastin (Townsley, 2011). Within the

pulmonary artery walls cells expressing alpha-smooth muscle actin (*α*SMA) are found, as well as to a lesser extent surrounding the bronchial airways. *α*SMA is important in the development of branching vessels and budding airways (Moiseenko *et al.*, 2017). In normal lung function *α*SMA is partly responsible for maintaining blood vessel homeostasis and levels of elasticity of smooth muscle in the vessel walls (Zhang *et al.*, 2018).

Within the lobes of the lung each secondary lobule is supplied with air from one centrally located bronchiole and blood is supplied from a pulmonary artery branch. These two closely associated parts of a 3D network are termed the bronchovascular bundle, which are formed in each of the secondary lobules. Following gas exchange in the alveoli the newly oxygenated blood leaves the capillaries into the pulmonary artery for use elsewhere in the body. This relationship between the airways and blood vessels in the bronchovascular bundle is essential for normal lung function. If any part of the bundle is disrupted or damaged, as a result of disease, then gas exchange will be impaired resulting in the possible loss or remodelling of the remaining airways and blood vessels in the bronchovasuclar bundle (Rahaghi *et al.*, 2019). The amount of O_2 in the alveoli will have a direct effect on the level of O_2 in the blood. If airflow is reduced or blocked due to disease then the levels of O_2 will decrease and the levels of CO_2 will increase, which can lead to an increase in the acidity of the blood (Johnson Jr *et al.*, 2010).

Pulmonary arteries and airways are normally as straight as possible for maximum efficiency in the delivery of blood and air to and from the lungs. The shape of the blood vessels and airways can be described using tortuosity, this is an assessment of the 'twistiness' of 3D networks. Tortuosity of vessels and airways will change as the lungs expand and contract during normal breathing. The vessel will straighten more upon inhalation of air and expansion of the lung whereas it will become slightly more tortuous upon exhalation and lung contraction. A more tortuous path can also be caused by abnormal development or as a response to disease (Alilou *et al.*, 2018) resulting in vessels which curve, twist, loop or kink down the respiratory tract. The higher the tortuosity of the networks the less efficient the delivery of blood and air will be, which actively hinders gas exchange down in the distal respiratory tract.

1.1.6 Infiltrating immune cells

The lungs contain an extensive surface area of epithelium which is constantly exposed to the potentially harmful outside environment caused by the inhalation of particles, allergens and pathogens. To protect the lung environment from these potential harms the immune system has developed protection against these insults without causing excess damage to the lung tissue (Yamasaki and Eeden, 2018). Innate immunity is the generic response to foreign entities and in

the lung is driven by the epithelium which can automatically sense the presence of pathogens via an array of receptors (Hartl *et al.*, 2018). The main innate responses by the airway epithelium include increased mucus secretion, regulation of barrier tightness and secretion of antimicrobial proteins. Resident and infiltrating immune cells recruited from various mediators in response to pathogens form part of the acquired immune response. These form a more specified response to pathogens that present antigens which form the immunological memory which can destroy the pathogen by inhibiting its growth, most notably by the action of T and B lymphocytes (McDade *et al.*, 2016). In this study two immune cells types were used as exemplars which are involved in the lungs' immune response to foreign entities, these being mast cells and macrophages.

1.1.6.1 Mast Cells

Mast cells play a key role in the immune response following exposure to allergens or toxic particles, driving inflammation and repair processes. Mast cells are approximately 8-20 µm in diameter (Schulman *et al.*, 1983) and their structure is defined by dense, membrane-bound granules. These granules contain an acidic proteoglycan matrix which mediators such as histamine and tryptase are attached to (Virk *et al.*, 2016). These are stored within the mast cell until activation in response to pathogens where the mediators are released via exocytosis. They are widely distributed throughout the body, most notably found in areas exposed to the external environment such as the skin and beneath the epithelial surfaces of the respiratory tract (Virk *et al.*, 2016). Mast cells contribute to the innate and active immune response to respiratory pathogens, however they are also directly involved in respiratory diseases characterised by pathologic inflammation or remodelling of the tissue. This could be caused by increased mast cell activity above healthy levels, chronic insult or the inability for the mast cell activation to deal with the pathogen. The serine protease tryptase is often used as a marker to identify and localise mast cell activity by using the antibody AA1 (anti-mast cell tryptase) in immuno-histological studies (see section 1.5) (Malik *et al.*, 2018).

1.1.6.2 Macrophages

Phagocytic cells line the respiratory tract to engulf and clear foreign substances entering the lung, the majority of these phagocytic cells are macrophages (~90%), which are found within lung tissues and throughout the respiratory tract down to the alveoli. Macrophages provide an immune response following phagocytosis of a pathogen via pathogen recognition receptors (innate immunity) and antigen presentation (active immunity) (Dewhurst *et al.*, 2017). They also contribute to mucociliary clearance after phagocytosis of a pathogen the ciliated cells of the epithelium beat to up to remove the macrophage from the respiratory tract. Visualised using a light microscope the appearance of macrophages can change depending on exposure to different

pathogens or particulates, a common example visualised in smokers lung are carbon macrophages where the macrophages have phagocytosed carbon present in the inhaled smoke from a cigarette (Stämpfli and Anderson, 2009).

In the lung at least two different populations of macrophages exist. The main two populations being alveolar macrophages which are found in the airway spaces of the respiratory tract and interstitial macrophages which are found in the lung parenchyma (Byrne *et al.*, 2016). Macrophages are found in a range of sizes (5-25 µm diameter) and alveolar macrophages are typically larger than the interstitial macrophages (Dewhurst *et al.*, 2017). Resident macrophages are present within the lungs and self-replicate via a mechanism that is dependent on signalling from stimulating factors (Yamasaki and Eeden, 2018). Macrophages not native to the lung can also be recruited to the lungs in response to foreign entities entering the lung. CD68 (cluster of differentiation 68) is a highly expressed protein present in macrophages, it is a transmembrane glycoprotein which binds to tissue specific lectins or selectins, allowing macrophages to locate and move onto particular targets. CD68 has been used as a common marker in immuno-staining of many different tissue types and is one of the few cluster of differentiation expressed in both types of pulmonary macrophages (Byrne *et al.*, 2016).

1.2 Lung pathology

As highlighted in the previous sections the lung is a highly specialised organ essential for life and proper functioning is required for a good quality of life. Inflammatory diseases of the lung can be life threatening and impact quality of life. Chronic conditions such as chronic obstructive pulmonary disease (COPD), asthma and pulmonary fibrosis are all complex and result in a reduction or loss of airflow in the lungs. The thickness and the continuity of the epithelium can be compromised in varying diseases leading to severe respiratory problems including increased risk of infection and inflammation. If the damage is substantial then it can lead to loss of epithelial integrity resulting in inflammatory cell infiltration and collagen deposition, leading toward airway obstruction and failure (O'Koren *et al.*, 2013). COPD was chosen as an exemplar because of its well-studied effects on lung tissue microstructure and due to the high availability of lung tissue samples from COPD patients.

1.2.1 COPD lung pathology

COPD is one of the most common forms of morbidity and mortality in the adult population. At the end of 2020, COPD ranked 3rd worldwide in mortality and disease burden behind cardiovascular disease and stroke (Barnes, 2020). COPD describes multiple progressive lung

diseases characterised by airflow limitation and/or airway obstruction due to damage to the small airways or the lung parenchyma due to inflammatory processes, which are not fully reversible. The main cause of the inflammatory response is inhalation of noxious particles, most prominently from cigarette smoking but can also be caused by environmental air pollution (Vogelmeier *et al.*, 2017). Chronic exposure to the noxious particles leads to increased mucus production, damage to the structure of the airways and finally remodelling and loss of the airways are caused by the inflammatory responses (Martin *et al.*, 2013). COPD's symptoms are characterised by increasing breathlessness (dyspnea), chronic cough and increased sputum production. Airway remodelling is known to be a direct consequence of the chronic inflammation which affects the overall airway morphology prior to airway loss. These include bronchial diameter, airway wall thickness, changing tortuosity and the number of branches in the airway network (Bodduluri *et al.*, 2018). Blood vessels are also affected by cigarette smoke, like the airway epithelium in COPD, which causes vascular endothelial damage, remodelling of the vessel walls and microvasculature loss occurs in several organs as well as lungs including the heart, brain and kidney (Blanco *et al.*, 2016; Vaes *et al.*, 2020).

The pathology of COPD comprises a variable combination of small airway disease (obstructive bronchiolitis) and destruction of the lung parenchyma (emphysema) (Vestbo *et al.*, 2013). The processes characterising COPD is an increase in chronic pulmonary inflammation, which will continue even if the patient ceases smoking (Ballarin *et al.*, 2012). Innate and adaptive immune cells (macrophages, mast cells, neutrophils, B-cells, $CD4^+$/$CD8^+$ T-cells) all contribute to part of the inflammatory response in COPD (Bracke and Brusselle, 2015). Excess proteinase released from neutrophilic inflammation, oxidative stress leading to apoptosis and an imbalance between cell replenishment and cell death all contribute towards loss of alveolar septa and the development of emphysema (Kirkham and Barnes, 2013; Crisford *et al.*, 2018). In later stages of COPD, particularly in aging patients still smoking, cell senescence (cessation of cell division) and the development of auto-immunity can occur as the disease progresses. Chronic bronchitis is another pathology associated with COPD, which is characterised by inflammation of the bronchial airways causing damage to the cilia, impairing mucociliary clearance and reducing airflow. This is caused by hyperplasia and hypertrophy of mucus producing glands resulting in increased mucous production. Bronchiectasis is a process resulting from chronic infection associated with older patients with COPD, and also younger patients with cystic fibrosis or primary ciliary dyskinesia (Robinson and Morgan, 2018), in which there is permanent dilation of the bronchi indicated by chronic cough and increased mucus production (Barker, 2002). All of these different processes develop and interact together over the course of COPD progression, culminating in the impaired ability to forcibly exhale air which is a crucial part of COPD diagnosis (Kahnert *et al.*, 2018).

1.2.1.1 Emphysema

Emphysema, as mentioned previously, is a common lung condition associated with COPD characterised by alveoli damage causing air trapping which impairs gas exchange. This is caused by a loss of elastin-containing tissues in the distal airways which can effect just the respiratory bronchiole (centrilobular emphysema) or the whole acinus (panacinar emphysema) (Smith *et al.*, 2014). Chronic inflammation results in excess neutrophil recruitment, which in turn produces elastase to break down elastin, and also down regulates enzyme a_1-antitrypsin which would normally prevent the breakdown of elastin (Cosio *et al.*, 2016). Mean linear intercept is a measurement used to assess the severity of emphysema by calculating, on 2D histological serial sections, the mean free distance between different gas exchange surfaces over the lung volume (Crowley *et al.*, 2019). The greater the distance between gas exchange surfaces indicates more severe emphysema as a result of alveoli destruction. This loss of alveoli structure and trapping of air in the lungs can lead to an increase in CO_2 levels in the lungs and in the blood circulation.

1.2.1.2 Diagnosis and treatment of COPD

Primary diagnosis of COPD is made by spirometry, which scores lung function. Calculated by the ratio between the air forcible exhaled in one second (FEV_1) and the total amount of air which can be exhaled (FVC). The resulting ratio indicates the level of airway obstruction and if the value remains below 0.7, after administration of a bronchodilator, the patient is diagnosed with COPD; assuming the patient has the appropriate symptoms and predisposing risk factors (Vogelmeier *et al.*, 2017). FEV_1 is chosen as a metric for diagnosis because it is directly affected by airway resistance and reduced elastic recoil seen in emphysema (Bhatt *et al.*, 2016). Diagnosis of COPD is sub-divided into four main classifications defined by the Global Initiative for Obstructive Lung Disease (GOLD) (Vestbo *et al.*, 2013), which are summarised in Table 1.1.

Table 1.1: **Summary of the GOLD classification used in the diagnosis of COPD.**

Gold Stage	Descriptor	FEV_1 (% predicted)
GOLD 1	Mild	≥ 80%
GOLD 2	Moderate	50-79%
GOLD 3	Severe	30-49%
GOLD 4	Very Severe	<30%

More recently the GOLD classification have been subdivided again according to co-morbidities and disease exacerbations in the A-D classifications (Kahnert *et al.*, 2018). This is now a separate measurement which informs on the disease burden and future risks of disease exacerbation. These revised guidelines taking into account FEV_1 and patient history of disease exacerbations are designed to provide a more accurate and reliable diagnosis of COPD (Vogelmeier *et al.*, 2017).

Following diagnosis of COPD via spirometry several treatments are proposed for the management and prevention of further disease progression, the main one being the cessation of cigarette smoking. The most common medications given to patients with COPD are: bronchodilators to increase FEV_1, anti-inflammatories to reduce disease exacerbations and antibiotics to prevent secondary infections. Many pharmacological treatments are used to reduce symptoms and the severity/frequency of exacerbations however, no existing medication prevents the long-term decrease in lung function as COPD progresses (Vogelmeier *et al.*, 2017). Lung volume reduction surgery is used in some cases of COPD and is mainly effective (over pharmacological treatments) in patients with upper lobe emphysema and low exercise capacity (Group, 2003).

1.2.2 Fibrosis

Pulmonary fibrosis is a common feature of many respiratory diseases including COPD, this presents as a scarring of the lung tissue impairing lung function. Excessive numbers of active fibroblasts and collagen accumulation in the lung parenchyma cause structural defects that impair gas exchange (Ryu *et al.*, 2014). There are numerous known causes for fibrosis including allergens, chemicals and toxic environmental particles, as well as numerous pathologies with unknown causes, particularly in idiopathic pulmonary fibrosis (IPF) (Wilson and Wynn, 2009). In the case of COPD chronic inflammation of lung tissue the repair response to injury is impaired resulting in a fibrotic response.

1.2.3 Asthma

Asthma is another example of a chronic lung disease, and is one of the most common, affecting approximately 300 million people worldwide (Dharmage *et al.*, 2019). Asthma is sub-divided into two different types, allergic (extrinsic) and non-allergic (intrinsic). Allergic asthma, more typical in early life, is caused by high levels of immunoglobulin E (IgE) and diagnosed by positive skin prick tests to common allergens (Sharma *et al.*, 2018; Komi and Bjermer, 2019). Non-allergic asthma patients, more typical in later life, do not have circulating IgE (Pakkasela *et al.*, 2020). The pathology for both types of asthma is similar, consisting of chronic inflammation of the airways and unlike COPD, causes airway obstruction due to contraction of smooth muscle and bronchial

hyper-responsiveness (Barnes, 2017). Mast cells play an important role in asthma in response to chronic inflammation as mast cells become embedded in the epithelium resulting in hypertrophy, hyperplasia and smooth muscle dysfunction (Komi and Bjermer, 2019).

1.2.4 Lung cancer

Lungs cancer is the unregulated proliferation of cells within the lung tissue leading to the formation of a tumour. In this study the majority of human lung tissue samples came from patients undergoing cancer resection surgery. This is a treatment option for non-small cell lung cancers, the most common type of lung cancer. Excess tissue was collected using a scalpel from surgically resected material from patients who gave informed consent prior to surgery.

1.3 Clinical imaging techniques

The development of imaging technologies over the past 150 years has provided greater insight into disease processes, in the case of COPD this is the visualisation of airway and parenchymal abnormalities. The main features of COPD visualised using clinical imaging are the loss of airways and the development of emphysema leading to the destruction of the parenchyma. For macroscopic imaging of the airways and general lung tissue medical computed tomography (CT) and magnetic resonance imaging (MRI) provide 3D imaging in the mm scale. Imaging the microscopic structures generally uses 2D light microscopy of histologically stained tissue biopsy sections, a technique that has been used for over 100 years and is still commonly used in research and clinical diagnosis to this day.

1.3.1 Computed tomography (CT)

Computed tomography (CT) is a well-established, non-destructive imaging technique, which uses X-ray transmission through an object/the body to create images and was first used as a clinical tool in 1971 (Hsieh, 2003). CT can provide a spatial resolution of 2 mm and is used to resolve airways (down to 2.5 mm diameter) and assess levels of emphysema at relatively low radiation doses (van Rikxoort and Ginneken, 2013). The modern hospital high resolution (HR) CT machine is ‘donut shaped’ to house the curved detector which is used to reduce scan times, however it limits the maximum resolution of the image, to increase this a flat panel system is required (Goldman, 2007). HRCT provides a higher dose of radiation to the patient but provides greater spatial resolution of approximately 0.8 mm whilst still using a curved detector for capturing X-rays, however this is still not sufficient to image the terminal bronchioles and the respiratory zone which are the main areas of interest in COPD (Milne and King, 2014; Koo *et al.*, 2018). The main

positive for clinical respiratory imaging is that the lungs are captured *in vivo* following inhalation or exhalation of air by the patient. This can visualise the lungs in an inflated state, something not feasibly possible *ex vivo*. One major limitation affecting image quality is the movement of the patient, which can be minimised but not removed entirely, and can make it difficult to discern features near the resolution limit of clinical CT.

1.3.1.1 Magnetic resonance imaging (MRI)

MRI is another example of commonly used 3D clinical imaging, MRI works using strong magnetic fields and radio waves to generate images of organs and physiological processes in the body. MRI is not typically used to image the lung due to the high levels of air present with multiple air-tissue interfaces which provide poor contrast and signal on the MRI. Functional lung studies have used MRI to study levels of ventilation by using a contrast agent, typically a hyperpolarised noble gas, to visualise airflow in the lungs (Milne and King, 2014).

1.3.2 Histopathology

Histopathology uses human tissue samples, most often biopsies, for diagnosis and research using techniques established over 100 years ago. Soft tissue samples (e.g. lung tissue) are typically fixed in formalin (a mixture of ethanol and formaldehyde) as soon as possible after removal from the patient to preserve the biological structure of the tissue and cells. Fixed tissue can only be stored for up to three days in ethanol before the tissue begins to degrade, for more permanent preservation the tissue is embedded, most commonly in paraffin wax. This whole process is known to cause some structural changes and tissue shrinkage is a well reported and accepted side effect of fixation and embedding (Schneider and Ochs, 2014). For routine histopathology the formalin fixed paraffin embedded (FFPE) tissue is cut into thin sections using a microtome (Fischer *et al.*, 2008). Prior to staining and imaging the tissue the paraffin wax is removed and the tissue rehydrated using graded alcohols.

Haematoxylin and eosin (H&E) is the most commonly used tinctorial stain in histopathology for clinical diagnosis and research studies of multiple respiratory diseases including COPD (Rahaghi *et al.*, 2019). Haematoxylin stains nuclei with a deep blue colour and the eosin stains the remaining tissue features in various shades of pink (soft tissue), red (red blood cells) and orange (Fischer *et al.*, 2008). Figure 1.4 shows an example of H&E stained human lung tissue, many of the structural features are distinct from one another especially the blood vessels due to the presence of red blood cells, the airways due to dense nuclei staining in the epithelium and the alveoli which have a distinct morphology. Traditional histopathology uses a 2D light microscope where an expert manually inspects the tissue for hallmarks of disease (Poobalasingam *et al.*, 2016). Switching

between the objectives seen in Figure 1.4 visualises the structural and cellular details at higher magnifications. H&E stained sections of resected tissue are used as the gold standard for the diagnosis for many lung diseases requiring tissue biopsies (Hsia *et al.*, 2010). Most commonly a handful of tissue sections at different depths of the tissue volume are stained, inspected and used to make a diagnosis. There are thousands of different tinctorial stains used for visualising different tissue and cell types which have been used in research and clinical setting, however H&E remains the most prominent and was the only tinctorial stain used in this project.

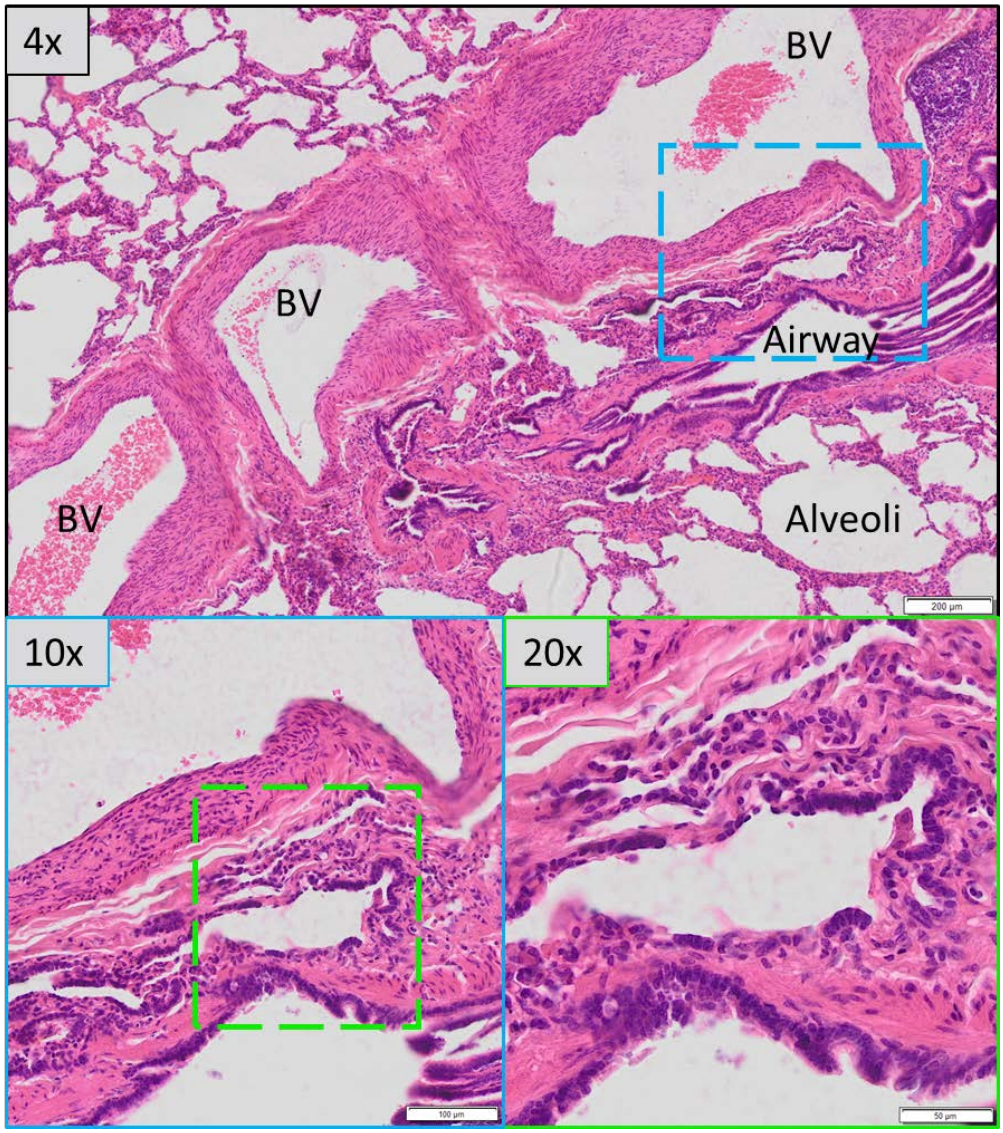

Figure 1.4: **Histopathology lung tissue sample stained with haematoxylin and eosin (H&E) and visualised on a light microscope using three different objectives.**The upper image shows part of an H&E stained tissue section using a 4x objective. Blood vessels (BV), a partially collapsed airway and an exemplar alveoli are labelled on the upper image, the red staining within the blood vessels are red blood cells, and the dense nuclei staining of the airway is the airway epithelium. The lower left image shows the area of tissue in the blue dashed box captured using a 10x objective. The lower right image shows the area in the green dashed box captured using a 20x objective.

1.4 Micro-CT (µCT) imaging techniques

1.4.1 µCT development

The resolution of clinical CT (≥0.8 mm) is insufficient for imaging the small airways (often defined as airways <2mm diameter) and alveoli (<100 µm diameter) of the lungs, where we would expect to see loss and/or damage in COPD (Koo *et al.*, 2018). The development of microfocus CT (µCT) has allowed researchers to image isolated tissue samples at spatial resolutions between 1-10µm (Metscher, 2009). µCT uses a fixed position X-ray source with rotation of the object. A flat-panel detector is used to image the X-ray projections to create high resolution radiographs, generating reconstructed 3D images with a small voxel (3D pixel) size. This provides superior resolution compared to curved panel detectors in clinical CT, which are optimised for fast acquisition times, due to the combination of being in a fixed position and better capturing of X-rays to generate the radiographs. The dramatic increase in resolution is the biggest advantage µCT has over HRCT for imaging much smaller structural defects, which would be missed on a conventional CT. This resolution increase is caused by higher power stationary x-ray sources, in close proximity to the object, which have small spot sizes for X-ray generation from a target metal. This combined with longer exposure times provides higher X-ray flux which improves the contrast and resolution of the images produced. However, the trade-off is that the radiation dose and scan times are significantly greater in µCT whilst the sample sizes are smaller (and inert i.e. not alive) than those used in clinical CT.

1.4.2 The µCT system

Figure 1.5 shows a schematic diagram of the developed µCT system. In the source an electron gun is fired in vacuum at a focussed (hence microfocus) spot a few microns in diameter on a target metal like tungsten or molybdenum, the electrons then generate a high power X-ray beam. The target metal and energy of the X-rays determine the level of flux, a higher flux will deliver better image contrast by providing a higher dynamic range of absorptions and transmissions through an object. The X-ray beam is cone shaped and projects X-rays over a flat panel detector, which acquires 2D projection data of the subject (in the path of the X-rays) at each projection angle (Lee *et al.*, 2003). The 2D projections are captured for each rotation angle of the specimen and sent to the PC producing very large datasets which are reconstructed into a 3D dataset. The source-to-object distance and source-to detector distance determine the geometric magnification, cone-beam angle and field of view (FOV) (Lee *et al.*, 2003). The power, current and voltage of the electron beam can be manipulated to change the properties of the X-rays which in turn changes the attenuation, penetration and focus of the X-ray beam.

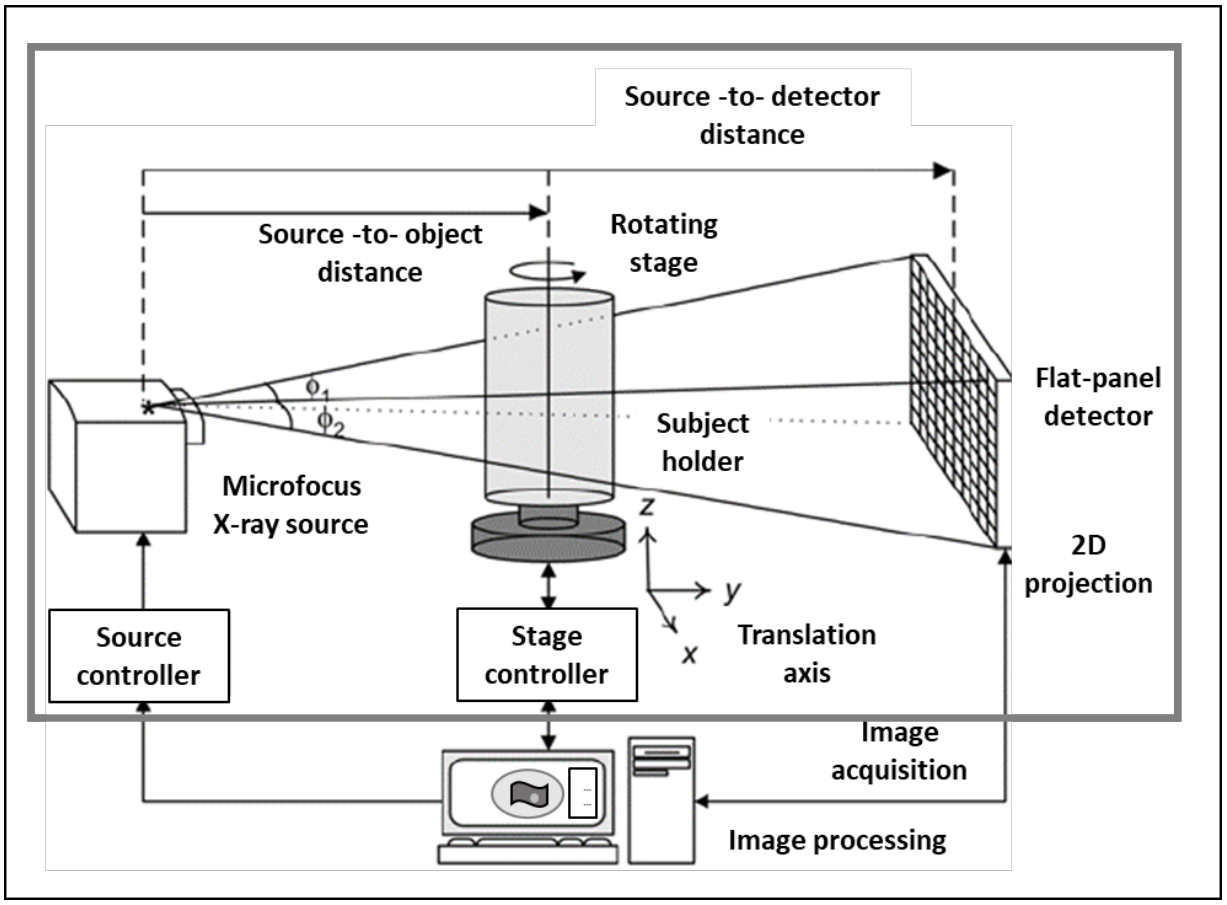

Figure 1.5: **A schematic representation of the inner workings of a standard lab-based µCT scanner.**An electron beam is fired at a focussed point on a target material to generate X-rays from the source. The X-rays are emitted as a cone beam, the angle (φ1 and φ2) of which, as well as the source-to-object distance and source-to detector distance, determine the system geometric parameters such as magnification ratio and filed of view (FOV). The object is rotated in a constant angular velocity whilst being continuously irradiated. The flat-panel detector acquires 2D X-ray projection data at a given integration time, these projection images are used for reconstruction into a 3D dataset. Image adapted under the terms of the creative commons CC-BY licence from (Lee *et al.*, 2003).

1.4.3 Applications of µCT in biological research

The main use of µCT imaging is in the engineering and material sciences investigating heavy metals which are easily visualised using X-rays, however the use of µCT in biological research has been more widely adopted in the last 10 years. Most early biological research used µCT to image hard tissue with high X-ray absorbance, common examples include trabecular and cortical bone morphology (Bouxsein *et al.*, 2010). µCT studies imaging bone have been used to study aging and disease, most notably changes to bone morphology in osteoporosis (Núñez *et al.*, 2018). µCT

imaging of bone has been used in a forensic setting for evaluating cracks and trauma to bone to determine what object was used to cause injury in criminal cases (Norman *et al.*, 2018). For imaging soft tissues, which do not have the same X-ray absorbance as bone, contrast agents such as iodine or heavy metal stains were applied to the tissue prior to scanning to provide them with the contrast required for clear µCT imaging (Metscher, 2009; de Bournonville *et al.*, 2019). Contrast agents have also been used to visualise both mineralised and soft tissue in bone to represent the structural and functional (i.e. bone marrow) features in bone (Kerckhofs *et al.*, 2018). The main issue with the majority of contrast agents is that they prevent further investigation of the sample after µCT scanning is complete. This prevented follow up studies of the same sample using traditional histological imaging.

1.4.3.1 Applications in respiratory research

Contrast agents have been used in soft lung tissue in order to perform analysis of the blood vessels and airspaces in lung tissue, for example measuring a quantitative decrease in lung tissue airspaces in fibrotic tissue (Kampschulte *et al.*, 2013). However, contrast agents typically require the sample to be incubated in a solution (e.g. Lugol's Iodine) for several days prior to imaging and following µCT imaging cannot be used for other imaging techniques like histology. Therefore contrast agents were not suitable for use in this project which aimed to look at correlative imaging techniques with µCT. Fixed and dried lung tissue has also been used to calculate the mean linear intercept on small cores of human lung tissue with COPD (McDonough *et al.*, 2011). Before 2015 it was commonly seen as impossible to get clear images of soft tissue microstructure in FFPE samples, without contrast agents, using µCT due to the low X-ray absorption contrast between the tissue and the paraffin wax. Scott and colleagues (Scott *et al.*, 2015) addressed this by demonstrating the use of µCT on FFPE soft tissue using low energy X-rays and opened up the use of µCT to use in non-contrast enhanced soft tissue imaging. This soft tissue optimised µCT was developed at the University of Southampton, which utilised techniques to produce low energy X-ray imaging with sufficient flux to produce high image contrast between different biological structures with similar attenuation values. This first example used lung as an exemplar due to the distinct heterogeneity of the tissue with different X-ray absorption levels it could be imaged clearly using low energy X-rays, and has led to multiple studies using µCT in respiratory research. More recently µCT has been used in cross-dimensional studies to investigate the damage to small airways in different stages of COPD (Koo *et al.*, 2018). Figure 1.6 shows an example of µCT imaging of human lung tissue visualised in 2D and 3D, without the use of contrast agents, with labelled features which can also be identified in traditional H&E histological imaging.

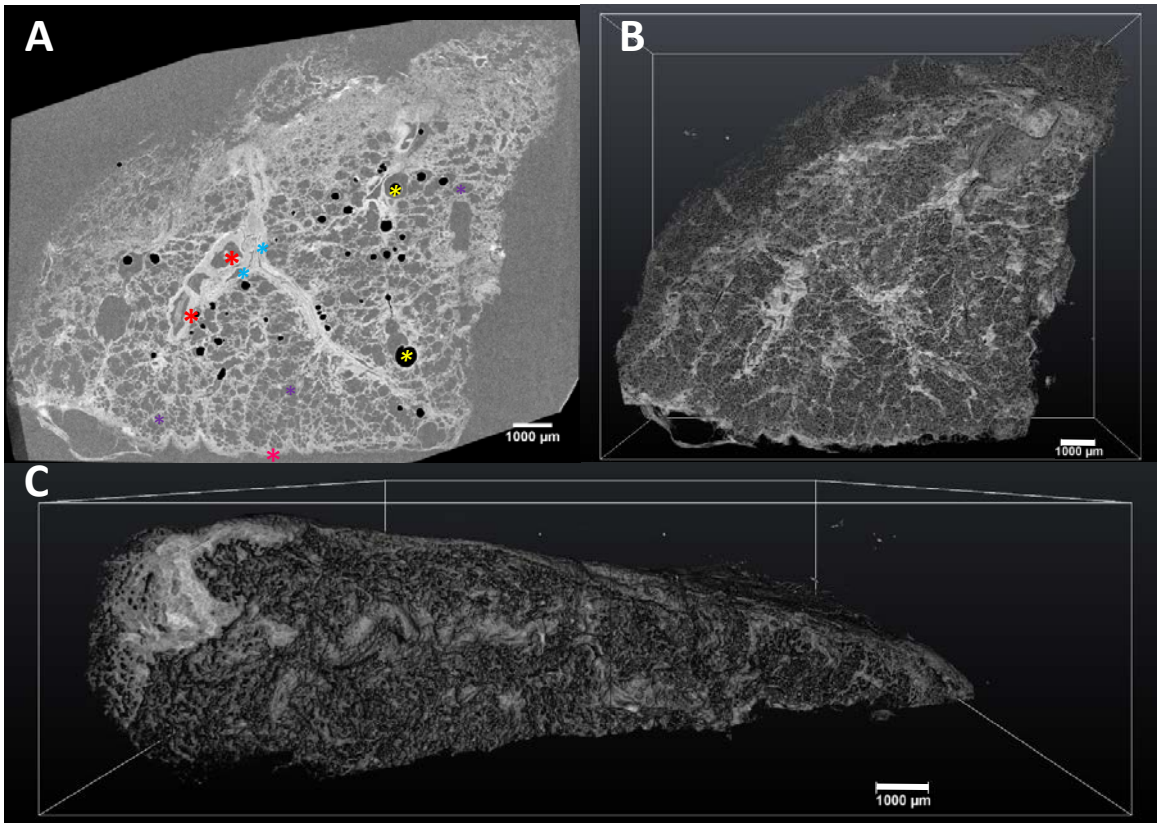

Figure 1.6: **Exemplar reconstructed µCT data in 2D and 3D of FFPE human lung tissue sample.** A: Reconstructed µCT slice in the *xy*-plane of the µCT volume with a voxel size of 8.5 µm. Examples of key features of the lung tissue are labelled: airways (blue *), blood vessels (red *), alveoli (purple *), pleural surface (pink *), masked air bubble artefacts (black voids containing yellow *). B: 3D volume rendering of the lung tissue volume visualised from the front of the tissue block (*xy*-plane). C: 3D volume rendering visualised from the side of the tissue block (*yz*-plane).

Even more recently µCT has been used to investigate the histological structure of soft tissues using just non-destructive µCT imaging, this has been dubbed 3D X-ray histology (Katsamenis *et al.*, 2019). Figure 1.7 shows where 3D X-ray histology is proposed to bridge the gap between previously used imaging techniques, providing 3D imaging of the tissue microstructure not seen with clinical CT or histopathology alone. These recent developments have contributed to the wider use of µCT imaging in respiratory research with numerous studies investigating different respiratory diseases being published in the last five years (Jones *et al.*, 2016; Koo *et al.*, 2016; Morales *et al.*, 2016; Robinson *et al.*, 2019).

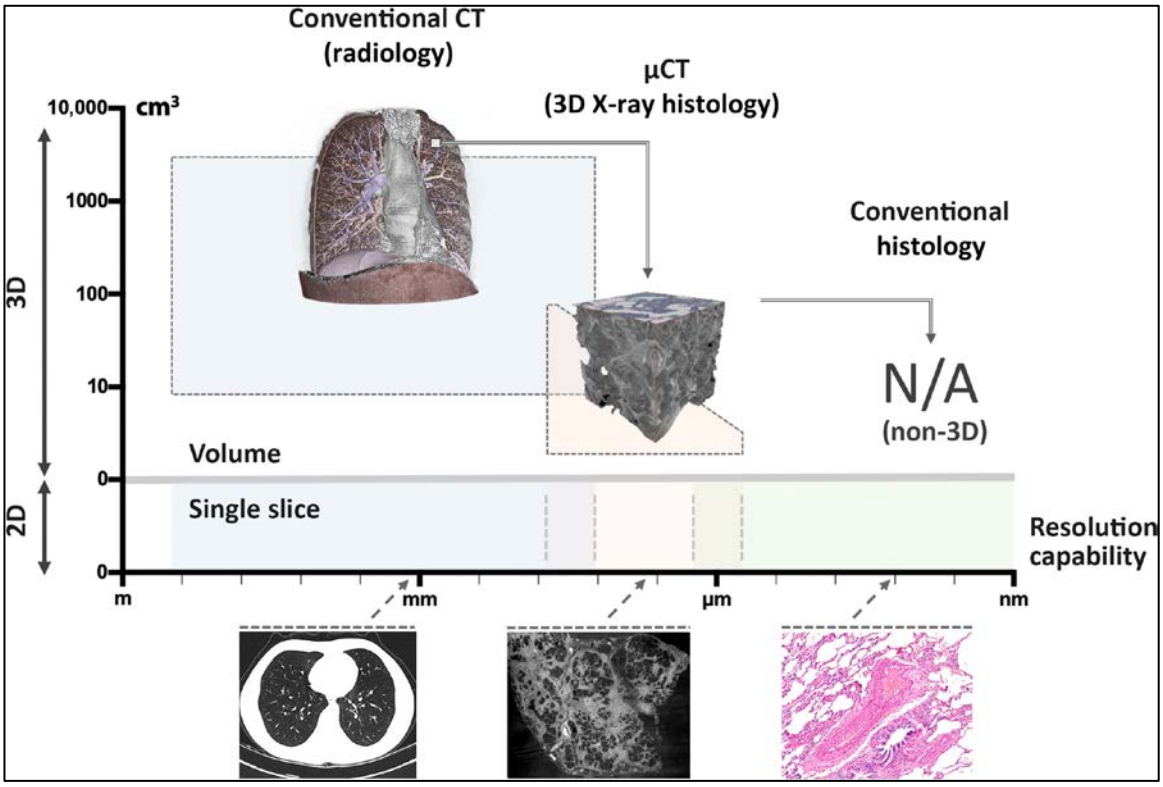

Figure 1.7: **Schematic illustrating where µCT is proposed to fit between 3D clinical CT and 2D histopathology.** Currently in lung pathology, anatomic 3D imaging is performed by HRCT, whereas high resolution 2D cellular analysis is conducted by conventional histology. µCT fits between these traditional imaging modalities, allowing for 3D analysis of biopsy samples at microscopic resolutions. Image reproduced under the terms of the creative commons CC-BY licence from (Katsamenis *et al.*, 2019).

1.5 Immunocytochemistry

Immunocytochemistry builds upon the image staining techniques using tinctorial stains such as H&E (described in section 1.3.2), which used chemical reactions to produce colour changes in the tissue and can be viewed using a 2D light microscope. Immunocytochemistry relies on specific reactions using antibodies which is achieved using antigenicity to specifically bind to a structure or cell in the tissue. The localisation of this binding reaction can be visualised by binding structures containing chromogens or fluorophores, as shown in Figure 1.8.

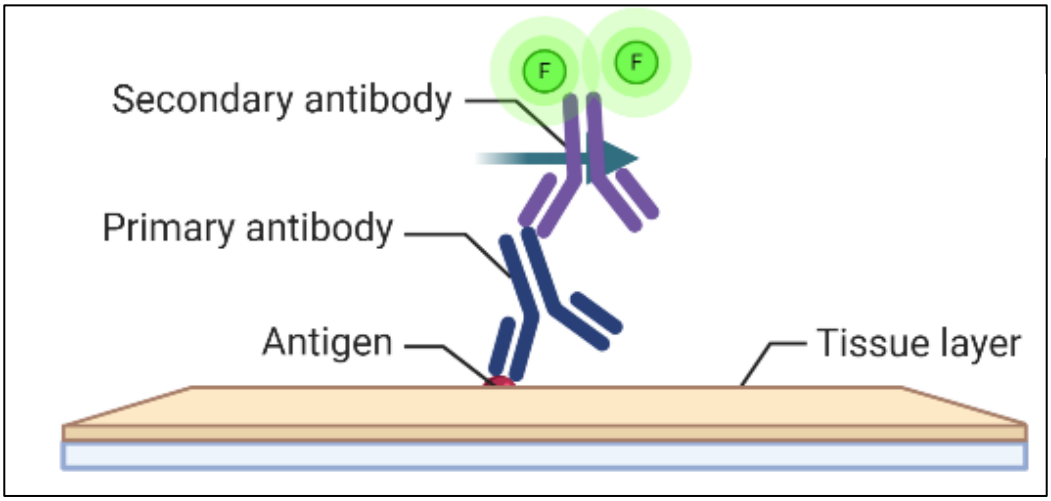

Figure 1.8: **Schematic representation of antibody binding to specific antigens utilised in immunocytochemistry.**The primary antibody is raised to specifically target an antigen which is present in the tissue. This specific binding can be localised by using a secondary antibody which targets and binds to the primary antibody. This secondary will also have a chromogen or fluorophore attached for visualisation down a microscope. Image made with BioRender.com

1.5.1 Bright-field imaging

Immunohistochemistry (IHC) is a technique used to visualise antigen-antibody binding in tissue sections using 2D bright-field microscopy. A primary antibody raised in a different animal to the tissue is designed to target and bind to the antigen of a specific cell type. In IHC the site of antibody binding is illustrated by a coloured histochemical reaction (chromogen) generated by an enzyme label on a secondary antibody, reacting with an additional chemical, which is clearly visible on a light microscope (Ramos-Vara, 2005). DAB (3,3'-Diaminobenzidine) is the most common chromogen generated in IHC, which is used to highlight the antigen-antibody binding which presents as a brown stain. A tinctorial counter-stain is often applied (e.g. haematoxylin) to provide context for the localisation of the specific immuno-staining. An example of an IHC image can be found in section 3.2.1. IHC has been widely used in both clinical histopathology and respiratory research to investigate the localisation of specific tissues, cells, enzymes and signalling molecules in numerous diseases including COPD.

1.5.2 Fluorescence imaging

Fluorescence is a process that occurs when a fluorochrome molecule absorbs light at a specific energy and wavelength and then emits photons at a lower energy with a longer wavelength. The difference in wavelength and energy is known as the Stokes shift (Borst and Visser, 2010). Figure 1.9 shows a Jablonski energy diagram of fluorescence that represents the excitation of a molecule that leads to the emission of fluorescent light (Jablonski, 1933). This phenomenon is utilised in imaging of tissue and cells using fluorescence microscopy. Instead of the full range of visible light used in bright-field microscopy, fluorescence imaging uses specific wavelengths of light which are absorbed by different molecules in tissues/cellular structures and released as fluorescent light at a lower energy and longer wavelength than the original fluorescent light.

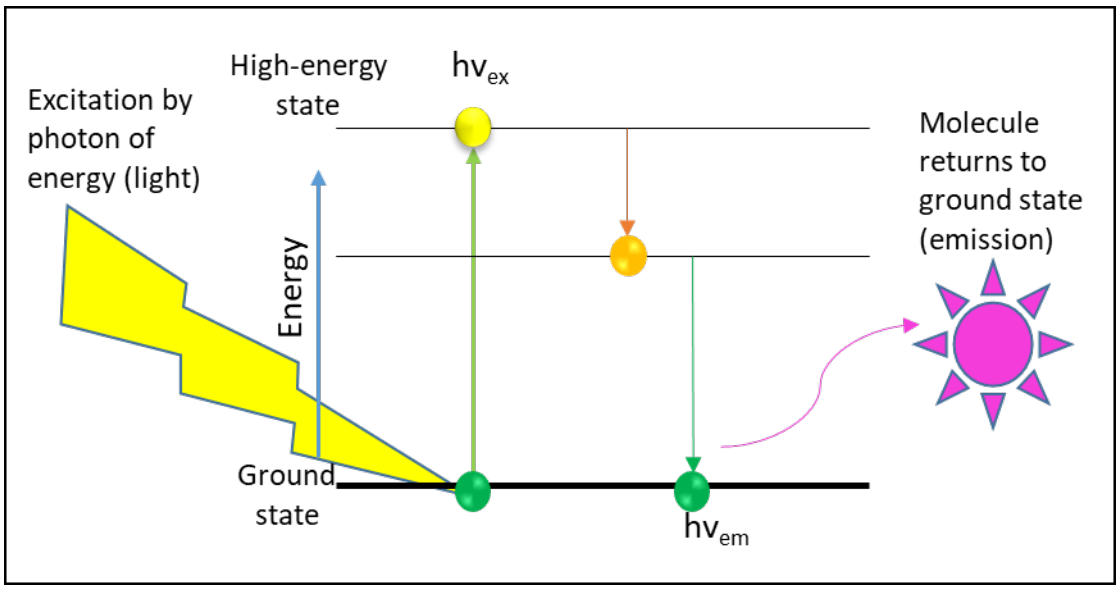

Figure 1.9: **A Jablonski energy diagram of electron excitation and emission resulting in fluorescence.** An electron is excited by a specific wavelength of light and is excited to a higher energy level (hv_{ex}). As the electron returns back to ground state some of the energy is given off as heat and the remainder is emitted as lower energy fluorescent light (hv_{em}) with a longer wavelength than the origin excitation light. Based on original by (Jablonski, 1933).

1.5.3 Immunofluorescence

Immunofluorescence (IF) imaging uses the same basic process for visualising the antigen-antibody binding as IHC. The main difference is that the chromogen, visualised with visible light, is replaced with a fluorophore which is excited and visualised at a specific wavelength of fluorescent light. A secondary antibody (raised in another animal against the primary), with an attached fluorophore, targets the primary antibody, binds to it and is used to highlight the location of the initial binding.

Figure 1.10 shows a representation of how IF works alongside some exemplar images of IF staining of human lung tissue. Using fluorescence microscopes which can excite multiple wavelengths of light via filters and dichroic mirrors (traditional fluorescence microscope) or specific wavelength lasers via tuneable crystals (confocal microscope) it is possible to stain for multiple cell types using IF on the same section. This is limited by the types of antibody used and the number of excitation wavelengths available on the fluorescence microscope and the viability of staining is also determined by autofluorescence which can also be seen in green in Figure 1.11.

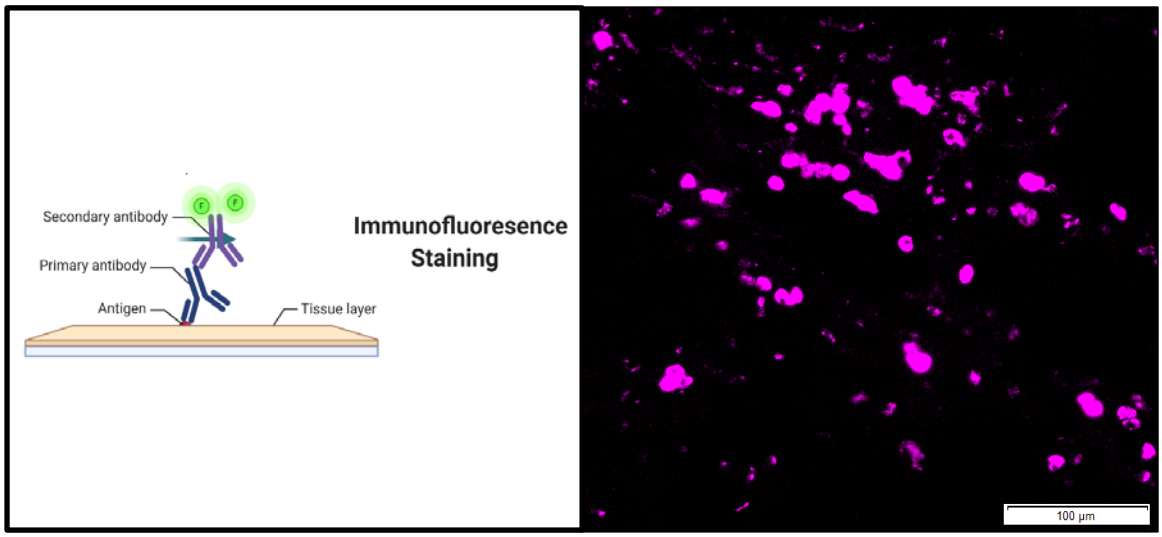

Figure 1.10: **Exemplar image of a human lung tissue section stained for immunofluorescence.** The left image shows a representation of the process of IF staining. In the image example on the right the tissue is lung, the antigen is CD68, the primary antibody is raised against CD68, the secondary is raised against the animal of the primary (mouse) and the attached fluorophore (AlexaFluor®647) is imaged using a fluorescence microscope. This is visualised as the pink cellular staining in the right image captured using a 10x objective.

1.5.4 Autofluorescence

Autofluorescence, or intrinsic fluorescence, is often regarded as background fluorescence signal. It is often present in fixed soft tissues and occurs when tissue is exposed to and excited by the imaging wavelength of fluorescent light, causing emission of a strong fluorescence signal from unstained sections (Pahlevaninezhad *et al.*, 2014). This is often seen as a major problem with fluorescent imaging of fixed tissue as the autofluorescence signal can obscure the signal from the fluorophore used for IF staining. Dense structural proteins have the highest intrinsic autofluorescence. The extracellular matrix generates stronger autofluorescence signal than the cellular component; this is because collagen and elastin have a relatively high quantum yield

relative to most cells which do not contain any fluorescent molecules (Monici, 2005). Fluorescence quenching is a process commonly used when staining tissue for IF to decrease the fluorescence intensity of a sample so that the fluorophores have a stronger signal than the background autofluorescence. This relies on specific molecular interactions to decrease the quantum yield of fluorescence from endogenous fluorophores via multiple different approaches such as energy transfer and molecular rearrangement induced directly by quencher molecules (Maillard *et al.*, 2021). However, quenching was not used in this project due to the novel utilisation of the autofluorescence as described in section 3.4.2.

Changes occurring in the cellular and tissue state during pathological processes, such as malignant cancers, can result in differing excitation intensities of endogenous fluorophores (Khosroshahi and Rahmani, 2012). Quantitative autofluorescence imaging of human lung tissue has reported that the cartilage autofluorescence intensity was four times greater than other structures including epithelium (Pahlevaninezhad *et al.*, 2014). Autofluorescence has been used in previous studies as a label free method for identifying lung cancer in sectioned human lung tissue (Wang *et al.*, 2017). Figure 1.11 shows what tissue autofluorescence can look like down the fluorescence microscope and how the strong signal, highlighting most tissue microstructure, could interfere with IF staining using a fluorophore of overlapping excitation or emission wavelengths of light.

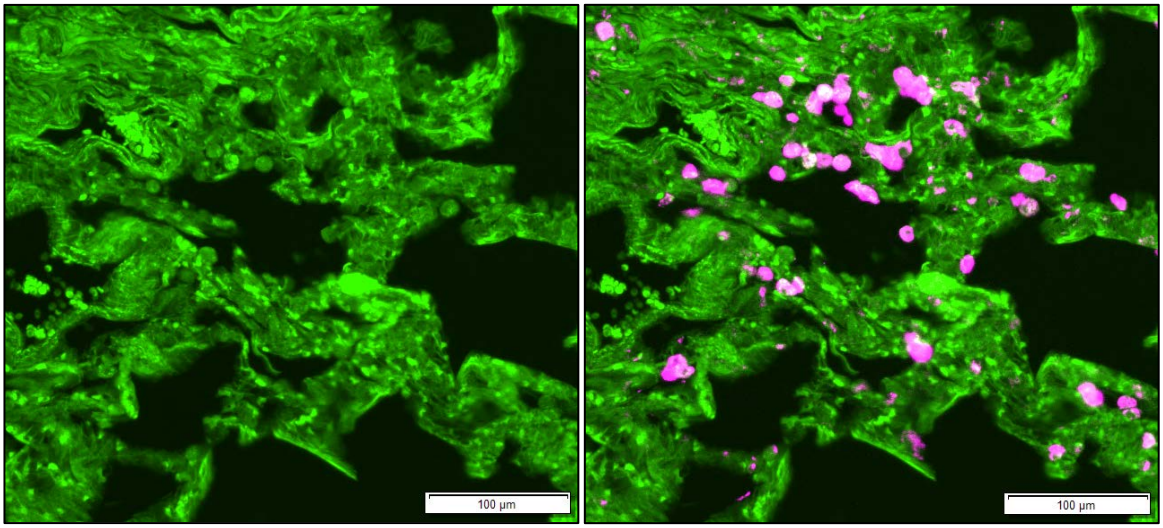

Figure 1.11: **Exemplar tissue autofluorescence captured during fluorescence imaging.** The left image shows tissue autofluorescence of a fixed human lung tissue section captured at 490 nm excitation (FITC channel, 1 s exposure). The right image shows the same area of tissue autofluorescence with the CD68 positive IF staining visualised using an AlexaFluor®647 fluorophore overlaid in pink. Both images captured using a 10x objective.

1.5.4.1 DAPI staining

DAPI (4',6-diamidino-2-phenylindole) is a common nuclear counterstain, similar to haematoxylin in IHC, used in fluorescence imaging. DAPI binds to adenine-thymine areas of DNA (i.e. in the cell nucleus) and produces strong fluorescence signal when excited by light at a wavelength of 372 nm. DAPI has been used to confirm cellular staining in IF by providing a useful reference for cell localisation. Figure 1.12 shows an exemplar image of DAPI staining visualised using a fluorescence microscope, here the nuclei staining produces a strong signal which is easily separated from background autofluorescence at the imaging excitation and emission wavelengths of light used.

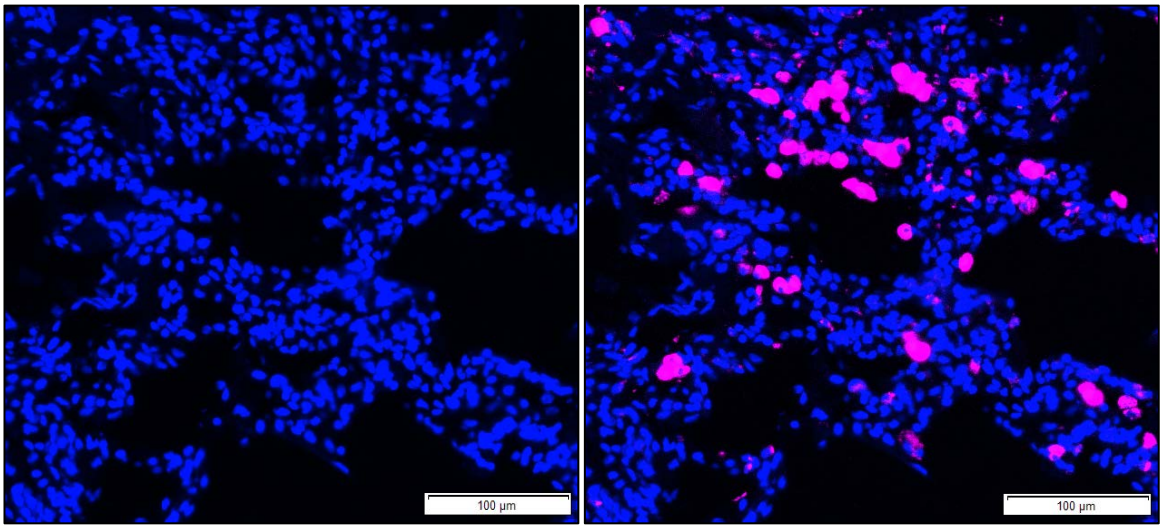

Figure 1.12: **Exemplar image of DAPI staining of cell nuclei captured using fluorescence imaging.** The left image shows positive DAPI staining of cell nuclei on a fixed human lung tissue section captured at 372 nm excitation. The right image shows the same area of DAPI staining with the CD68 positive IF staining overlaid in pink. Both images captured using a 10x objective.

1.5.5 IF use in lung

Due mainly to the high levels of tissue autofluorescence produced from fluorescence imaging of FFPE human lung tissue, IF has not been widely used on this type of tissue compared to IHC (Robertson and Isacke, 2011). IF has been used to identify structural changes in IPF using multiple fluorescent probes and DAPI staining to analyse changes in these features (Seibold *et al.*, 2013). However, the typical method for immunostaining FFPE tissue remains IHC which has lower image contrast than IF (Robertson *et al.*, 2008).

1.6 Correlative imaging

Correlative imaging is the process of combining the information from two or more imaging modalities of the same sample or specimen to further enhance understanding of the structures and/or processes involved. This has been used to supplement the information provided from one imaging modality or provide a wider-field perspective on imaging focussed on a small area of the sample at high resolution. The reverse is also true where lower resolution imaging has been used to scout the location of a sample for high resolution imaging. This provides multi-scale imaging of the same tissue or specimen of interest, which can provide much greater information than a single scale alone. One common use is correlative light and electron microscopy (CLEM) which has combined immuno-histological staining to identify specific cell types with serial blockface scanning electron microscopy to analyse the underlying ultrastructure (Russell *et al.*, 2017). CLEM requires direct alignment of the two different imaging modalities, this is most commonly achieved by using additional fiducial markers as reference points in both images (Kukulski *et al.*, 2012). A common example is the use of fluorescence beads with metallic cores which can be seen in both the fluorescence and electron microscopy images (Kukulski *et al.*, 2012; Schellenberger *et al.*, 2014). More recent technological developments have focussed on a single piece of equipment which can acquire images from multiple modalities. These are still not widely available and many are still under development but they have been utilised for CLEM (Timmermans and Otto, 2015) and also correlative CT and fluorescence imaging of animal models (Dunning and Bazalova-Carter, 2020). Automated serial sectioning of a specimen combined with live fluorescence and electron microscopy imaging has also been used to provide near real-time imaging of cells in 3D at multiple scales (Bushby *et al.*, 2012). This data can be reconstructed to provide functional information about molecules, organelles, cells and tissues which can be quantified in 3D (Blazquez-Llorca *et al.*, 2015). Other correlative imaging techniques combine MRI and fluorescence imaging of tissue slices and live animals at a millimetre resolution, however this is difficult to perform simultaneously as the acquisition methods can be affected by the magnetic field required for MRI (Leblond *et al.*, 2010). The correlative imaging techniques mentioned above plus many other recent developments in correlative imaging in biological research using a multitude of imaging techniques including light, fluorescence and electron microscopy as well as X-ray imaging, spectroscopy and many more are discussed in this recent review (Ando *et al.*, 2018). Correlative imaging has continued to develop with recent studies using more correlative imaging techniques in the same study. One recent example of this has proposed the use of high resolution µCT imaging to bridge the gap between light and electron microscopy for more extensive correlative studies of cellular structures (Bayguinov *et al.*, 2020).

1.6.1 µCT and 2D light microscopy

In the context of this study, correlative imaging using µCT and traditional 2D light microscopy has been employed in numerous studies of lung tissue. Correlation of 3D µCT data with 2D histology images of paraffin wax sections, from the same lung tissue block, has been used in the identification and 3D localisation of specific tissue components and cell types. An example of the side by side comparison and similarities in the visualised structural features of FFPE lung tissue in both µCT and H&E images can be seen in Figure 1.13. In order to identify and analyse lung networks and fibroblasts in IPF, within a 3D lung volume, Jones & colleagues (Jones *et al.*, 2016) identified fibroblastic foci using tinctorial stained tissue sections. These were manually segmented in the µCT volume to reveal that the fibroblast foci were not interconnected in 3D and formed a widely distributed heterogeneous pattern through the lung tissue. The correlative imaging process was developed further in the paper by Robinson & colleagues (Robinson *et al.*, 2019) who used IHC to specifically identify lymphatic vessels in human lung tissue. This highlighted the advantage of using immunostaining to identify specific features within the µCT and used the 3D data from the µCT to manually interpolate the 3D networks of lymphatics. The resulting segmentation was then used to model the fluid flow to and from the lymphatics in 3D. Koo & colleagues (Koo *et al.*, 2018) used µCT for identifying areas containing small airways in their lung tissue and then performed 2D analysis of the terminal bronchioles in COPD by correlating with tinctorial stained tissue sections. This study found destruction of the bronchioles before a loss of lung function is observed in COPD. Correlative µCT with both tinctorial stained tissue and IHC have been used to study the pathology of IPF by showing the localisation of various cell types in the context of microstructural changes seen in IPF (Tanabe *et al.*, 2020).

These studies all highlighted the main advantages of using µCT in respiratory research, most notably the ability to determine histological detail of tissue microstructures in 3D (Katsamenis *et al.*, 2019). µCT is also non-destructive which enabled these correlative studies with traditional 2D histology to provide more information overall compared with 2D imaging alone. Correlating this information provides 3D structural context to the specific functional imaging provided by 2D tinctorial or immunocytochemistry tissue staining. However the main current issue for correlative 2D histology and 3D µCT imaging is the exceedingly time consuming manual techniques for image registration, which is required for generating data from these images. This severely limits the feasibility of this approach in practice and this report addresses some of the key issues to help to

move the field forward.

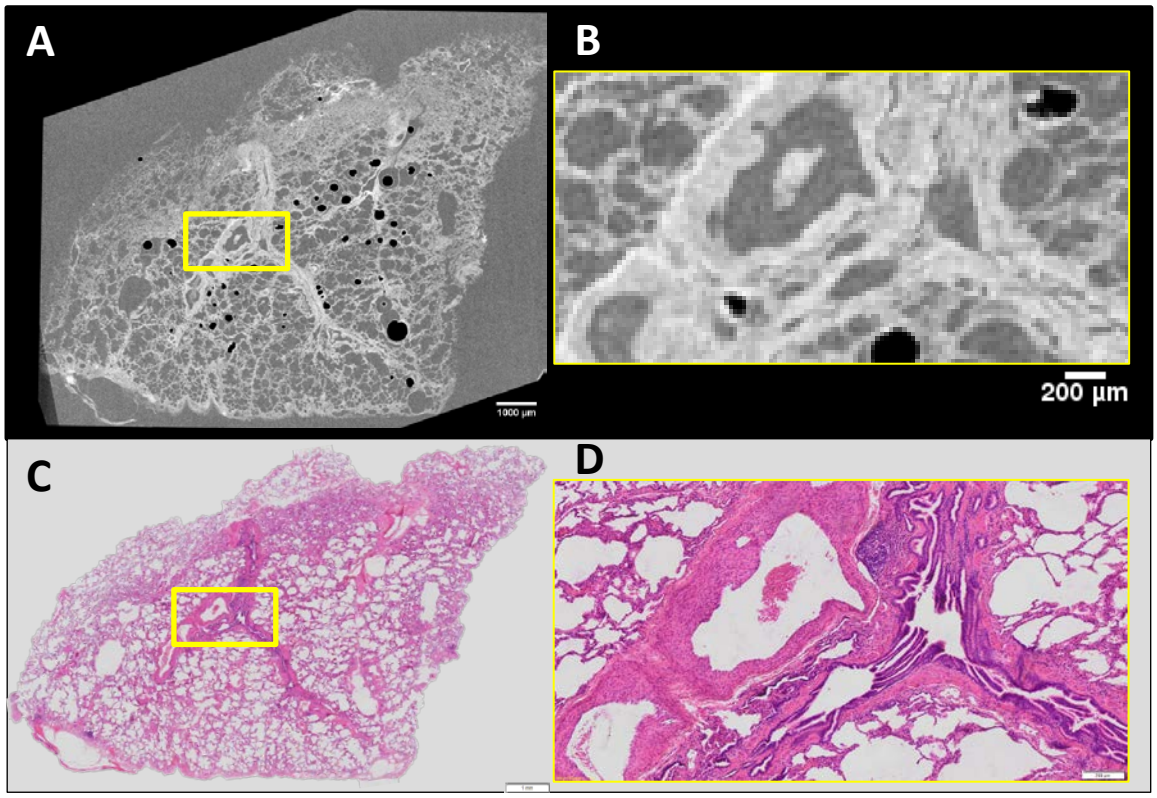

Figure 1.13: **Side by Side comparative imaging of fixed lung tissue using µCT and H&E staining.** The left column represents wide-field images of a single µCT slice of fixed human lung tissue (A) and H&E stained section of the same tissue (C). The right images show magnified areas of the tissue with both imaging modalities highlighted by the yellow box (B & D). These images highlight the structural similarity between both imaging modalities despite the large difference in resolution. The µCT also provides non-destructive 3D imaging beyond the plane shown in this figure, something 2D histology cannot provide.

1.6.2 Plane correspondence for 2D-3D registration

Plane correspondence is particularly important when correlating 2D microscopy and 3D µCT data in order to visualise the same plane of the dataset in both imaging modalities. Visualisation of 3D data is most often seen in a 2D view (plane) on a computer screen or on paper. A definition and visualisation of the 2D planes involved with 3D data is summarised in Figure 1.14. The example shown (and the data used in this project) is of a FFPE lung tissue block which has been scanned using µCT. The *xy*-plane describes the front face of the dataset and is the most commonly used plane for visualising data in 2D. The *z*-plane is the depth of a 3D dataset and is often used to

denote the slice number of a µCT dataset viewed in the *xy*-plane. The top/bottom and sides can be visualised using the *xz* and *yz*-planes respectively.

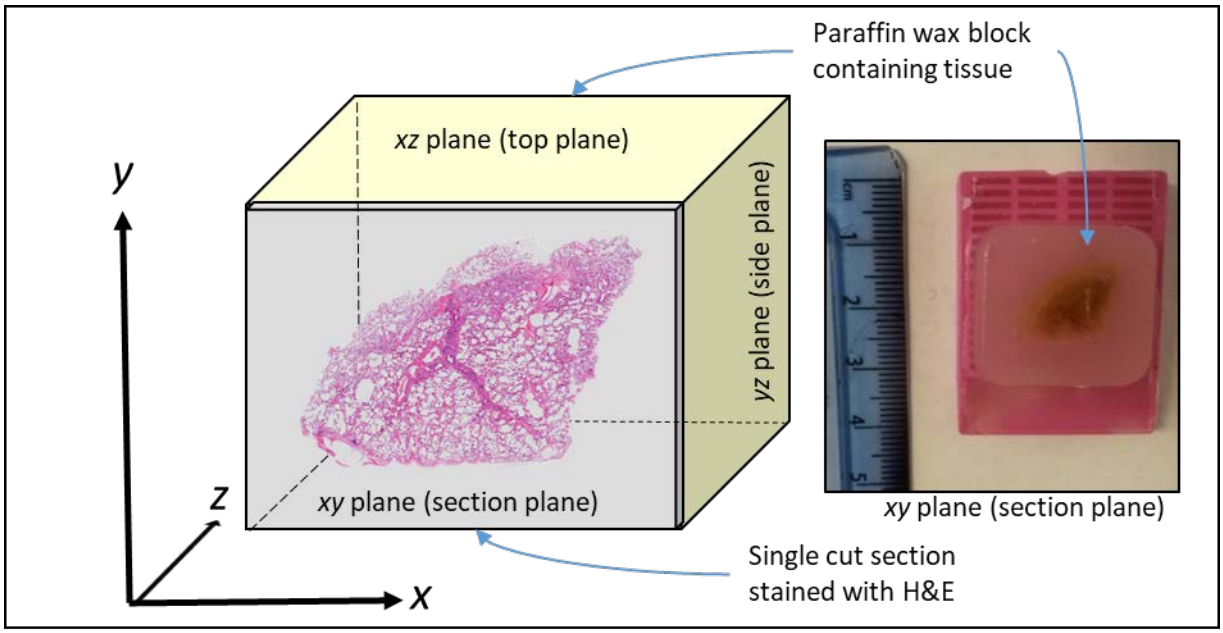

Figure 1.14: **Plane definition of FFPE tissue block for visualising the µCT data in different planes.** The cuboidal cartoon on the left represents the 3D wax block on the right with the planes exaggerated to ease plane identification and a H&E image representing one section of tissue from the block. Scanning the tissue sample upright results in a stack of CT images in the *xz* (top) plane. Digital re-slicing of the µCT data is required to view the FFPE block from the side (*yz* plane) or from the front (*xy* plane).

1.6.3 Registration

Registration is an important process in correlative imaging to ensure that the images captured using multiple imaging modalities show the same area of the specimen and enable direct mapping of features between images. For 2D-3D registration the first step is to complete the plane correspondence described in the previous section. This allows the 3D data to be visualised as 2D slices which match the plane of the physically cut 2D section images. However the process of registration can be very difficult especially if the scale and dimensions of the registered images are different. The majority of existing image registration require manual location and identification of matching features in both imaging modalities, which is very time consuming and subject to user bias.

1.7 Segmentation

Segmentation is the process of identifying and highlighting a specific feature or area of interest from the rest of an image via the generation of a segmentation mask (Wollatz *et al.*, 2017), as seen in Figure 1.15. This can be used to extract information about specific features from an image containing many different features, as is typical in biological images. For example a tissue histology image could be segmented to just identify and label the blood vessels. Segmentation has been used widely in the correlative imaging field to transfer the information provided from one imaging modality (e.g. 2D histology) onto another imaging modality (e.g. 3D µCT). The majority of previous studies have used manual segmentation to highlight specific features of cell types identified in the 2D immuno-histological images on the corresponding µCT planes (Vasilescu *et al.*, 2012; Jones *et al.*, 2016; Robinson *et al.*, 2019). Manual segmentation requires the user to identify and 'paint' the areas of the image by hand using a mouse or tablet on digital images. This is an exceedingly time consuming process with the time required increasing depending on the amount of segmentation required per image and the number of images requiring segmentation. For a µCT sub-volume, of a total size of 1 mm x1 mm x0.5 mm at a resolution of 5-10 µm, it takes on average 40 constant hours of work to segment a network on lung µCT images by an expert user (Robinson, 2020). Automated methods for image segmentation exist which are either basic (using binary thresholding in high contrast images) or exceedingly complex (using machine learning and neural networks). These methods for automating segmentation continue to be developed but currently there is no known method for directly transferring information from 2D histology into the 3D µCT without extensive manual intervention.

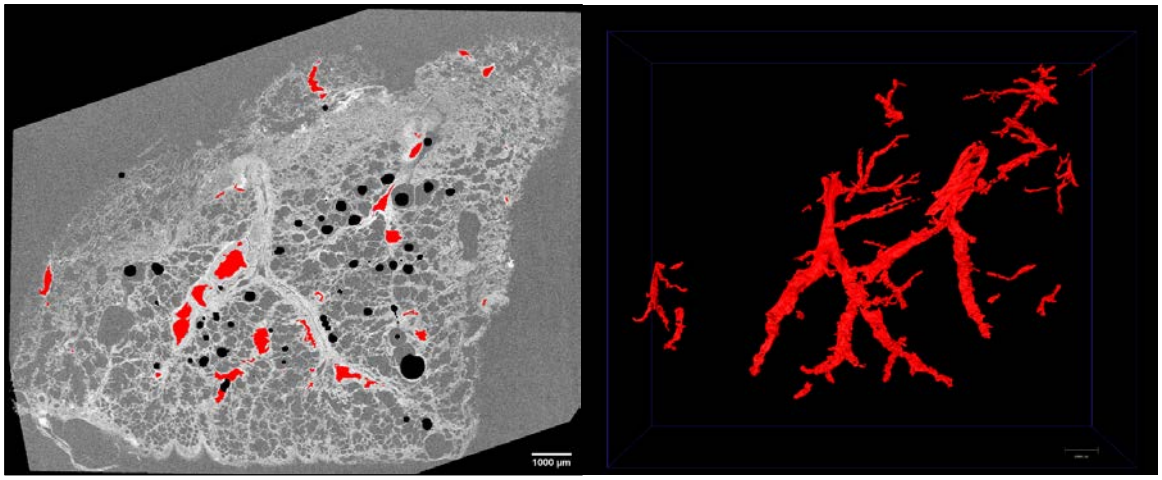

Figure 1.15: **Exemplar segmentation of µCT dataset highlighting blood vessels (red) on a 2D plane and displayed as a 3D surface.** The left image shows a 2D µCT slice which has been segmented to highlight the location of each blood vessel lumen in the image. This process was repeated over hundreds of images to build a network of 3D segmentation and is visualised as a 3D surface render in the right image.

1.8 Image processing

Image processing is commonly used to ease the visualisation, compatibility and analysis of captured digital images. Many processing techniques can be applied to both µCT and immuno-histological images, especially to assist with correlative imaging. Rudimentary image processing techniques most commonly used for the imaging techniques used in this project involve image cropping, resizing (scaling), rotation and file type conversion. Other physical changes to the image such as background subtraction are used on fluorescence images to ensure the background pixel intensities are minimised to ensure the best image contrast. This is often combined with brightness/contrast corrections to ensure the imaged features have visible pixel/voxel values. Brightness/contrast setting (histograms) are also adjusted in images with high intensity or noisy backgrounds like µCT images. Image filtration can be applied to noisy images by changing the pixel values to highlight structures or refine edges to make them clearer in the image (Chandel and Gupta, 2013). Thresholding uses the histogram of pixel/voxel values in the image to create a binary version of the image where all pixel/voxels are assigned a pixel value of one or zero (essentially black and white). This is often used to highlight a single feature with a high pixel/voxel intensity from the remainder of the image and is commonly used to generate segmentation masks (Arifin and Asano, 2006). However, this can only effectively be used in high contrast imaging techniques otherwise non-desired features can be highlighted by thresholding too. Binarised images generated from thresholding can be subject to more image processing steps for in depth analysis. Image processing often involves several steps which are fine-tuned to the type of image the user is working with. Although some processing steps can be automated the majority still require manual input, often by image analysis experts, which can be time consuming and subject to user bias.

1.9 Limitations with current correlative imaging techniques

Soft tissue imaging with µCT is still a relatively new technique and can result in image artefacts which disrupt visualisation and analysis of the resulting µCT dataset. During µCT imaging the rotation of the sample causes the creation of ring artefacts (bright bands) on the reconstructed images originating at the centre of rotation; which remains unchanged as the subject rotates on a fixed axis (Jan and Andrei, 2004). Also the sample rotation can result in the sample moving if it is not fixed properly which will completely disrupt the reconstruction algorithms and fail to produce usable images. The presence of heavy metals or particularly dense tissue structure can result in bright image artefacts which obscure the surrounding tissue in the radiograph. Edge artefacts appear where the specimen is at the limit of the field of view which causes diagonal areas in the

corners of the image to appear 'darker' than the rest of the image. Most of these can be addressed using post-processing and filtration to minimise the presence of artefacts on the final reconstructed image. In addition to this, the large size of the data (approx. 50 GB per scan) requires computers handling the data to have sufficient memory (RAM) to open and process the data. This also leads to data storage issues which can prove to be expensive, unreliable and difficult to share with others.

The resolution of the μCT is not as high as traditional histology, until recently resolutions of scans were typically greater than 10 μm for biological samples. This makes direct comparison between histology and μCT difficult due to the difference in resolution, more recently the resolution has been increased in μCT scans but this is still not to the same scale as traditional histology. This means that μCT can distinguish microstructural information but not cellular or sub-cellular detail provided by histology. The contrast of soft tissue μCT images is also not as high as 2D histology with similar intensities between the tissue and background (i.e. the paraffin wax) found using the majority of μCT scanners.

A further issue currently preventing μCT from being used in large clinical studies is the acquisition and processing time for the very large datasets produced during a single scan. Obtaining high resolution (<10 μm) scans of tissue would take around 15-17 hours in 2015, this has been reduced to around 7-9 hours currently. This however, is still too long for potential studies using a higher-throughput of samples in the future. After the long data acquisition time there is an even longer data processing and data analysis time which, with mostly manual methods, can take several weeks to months to complete. This is even longer if the samples are used in correlative studies which require the tissue to be sectioned, stained and imaged prior to registration. As previously stated the majority of registration techniques are manual and are exceedingly time consuming. With a single lung μCT dataset taking several months to image, process and analyse, seriously limiting the feasibility for larger studies.

1.10 Hypothesis

Developing/utilising image processing tools to increase automation will decrease the time taken to correlate datasets from µCT and immuno-histological imaging for analysis compared to existing manual techniques.

The 3D network of blood vessels, imaged by µCT, can be localised and provide data to quantify the 3D characteristics of the blood vessel network within the lung microstructure.

Identifying cellular localisation data from 2D immuno-histological data can be quantified in 3D and correlated with the 3D microstructures.

1.11 Aims

1. Develop a correlative µCT and immuno-histological imaging workflow which facilitates a higher-throughput of FFPE soft tissue samples via automation of the co-registration and segmentation of tissue microstructures and cell types.
2. Use the developed workflow to image and investigate clinical tissue samples as an exemplar study of FFPE lung tissue
3. Identify, localise and perform 3D analysis of the blood vessel networks in 'normal' (non-COPD) lung tissue
4. Use immuno-based localisation of cell types to analyse the airway epithelium in 'normal' (non-COPD) lung tissue as an example of an identified structural feature
5. Use the immuno-based localisation to identify individual exemplar immune cells present in the lung which are relevant to respiratory diseases
6. Demonstrate the applicability of workflow and quantitative parameters to compare pilot samples from COPD and non-COPD groups

Chapter 2 Material and methods

This chapter will contain all the materials (tissue samples, equipment and software) and the standard methods which were established before this project began. For novel methodology developments see chapter 3.

2.1 Samples used in project

Human lung tissue was obtained from patients undergoing resection surgery at Southampton University Hospital Trust. Patients gave signed informed consent prior to surgery; Southampton and South West Ethics committee A (LREC number: 08/H0502/32) provided ethical approval for the project. Each patient sample was linked to an ID number, for this project samples from the Human Lung (HL), Target Lung (TL) and EVITA (EV) cohorts of patients were used. Table 2.1 provides a summary of the samples used for method development and results chapters. For full patient clinical information, including the tissue which was scanned but not selected for study, see appendix A.1.

Table 2.1: **Summary of the tissue identifiers and key information of FFPE lung tissue used in this project**.

Tissue ID	Grouped ID	Chapter used in	Indication and Procedure	Age	FEV_1 %predicted	FEV_1/FVC	GOLD status	Smoking history	µCT scan resolution	No. sections cut
HL093	Lung1	3	Bronchiectasis lobectomy	31	77	0.79	0	none	8.5	100
HL098	Lung2	3	Pneumothorax bullectomy	21	n/a	n/a	n/a	none	6.0	200
HL079	Lung3	3	Pneumothorax bullectomy	21	n/a	n/a	n/a	none	6.0	200
HL094	Non-COPD-1	4, 5	Cancer lobectomy	67	100	0.77	0	Current	6.0	200
HL382	Non-COPD-2	4, 5	Cancer lobectomy	66	97	0.75	0	Ex-smoker	9.0	50
EV027	Non-COPD-3	4, 5	Cancer lobectomy	69	63	0.81	0	Ex-smoker	6.0	200
EV020	Non-COPD-4	4, 5	Cancer lobectomy	70	126	0.75	0	Ex-smoker	5.0	180
EV104	Non-COPD-5	4, 5	Cancer lobectomy	66	85	0.79	0	Current	6.0	181
HL119	Non-COPD-6	4, 5	Cancer lobectomy	66	85	0.75	0	Current	6.0	200
HL066B	COPD-1	4, 5	Cancer lobectomy	71	74	0.56	2	Current	8.5	200
HL086	COPD-2	4, 5	Cancer lobectomy	76	69	0.62	2	Current	6.0	200
EV118i	COPD-3	4, 5	Cancer lobectomy	64	68	0.64	2	Current	6.0	200
HL384	COPD-4	3, 4, 5	Cancer lobectomy	70	83	0.66	1	Ex-smoker	9.0	50
TL1127	COPD-5	4, 5	Cancer lobectomy	65	65	0.59	2	Ex-smoker	10.0	200

Tissue for method development (chapter 3) was selected from archived FFPE lung samples from patients who were young (<40) and did not have COPD. This was to enable the development of registration techniques on tissue not containing substantial fibrosis, emphysema or any other significant structural defects caused by disease. Tissue for chapters 4 & 5 were selected from archived (HL and EV samples) and recently collected (TL samples) lung tissue samples. Two age matched groups were created from different lung function scores (FEV_1/FVC) from spirometry measures. These were the non-COPD (FEV_1/FVC average of 0.8) and mild-moderate COPD (FEV_1/FVC average of 0.6) tissue groups.

2.1.1 Data archiving and organisation

The sample ID number, which is linked to databased patient information mentioned above, was used as an identifier of all images and data generated from each sample. Photos of the tissue blocks before scanning were used for archiving the samples and tracking the tissue through the entire scanning process. All images and data files (both raw and processed) were saved in the research folder of the Biomedical Imaging Unit's (Faculty of Medicine, University of Southampton) file store system and is backed up every day. The CT data is also backed up on the μ-vis X-ray imaging centre (Faculty of Engineering and Physical Sciences, University of Southampton) data store on physical external hard drives. Details of supplementary videos can be found in Appendix A.7 with the files available from the following DOI: http://doi.org/10.5281/zenodo.4309950

2.1.2 Sample preparation

The majority of surgical human lung samples were processed and archived prior to the beginning of this project, by staff at the Southampton General Hospital, using standard techniques which were also used for the more recently collected TL samples. All human lung samples used in this project taken from surgery (approx. 1-2cm in diameter) were fixed in neutral buffered formalin for 48 hours and embedded in paraffin wax using a Thermo Scientific HistoStar paraffin wax embedder (ThermoFisher, UK). FFPE lung tissue was mounted onto a plastic cassette following standard histopathological protocols (Hsia *et al.*, 2010) by staff in the Histochemistry Research Unit, University of Southampton. This is represented by the first two steps of the histopathological workflow in Figure 2.1 which would traditionally continue to destructive tissue sectioning followed by staining and imaging via a standard light microscope.

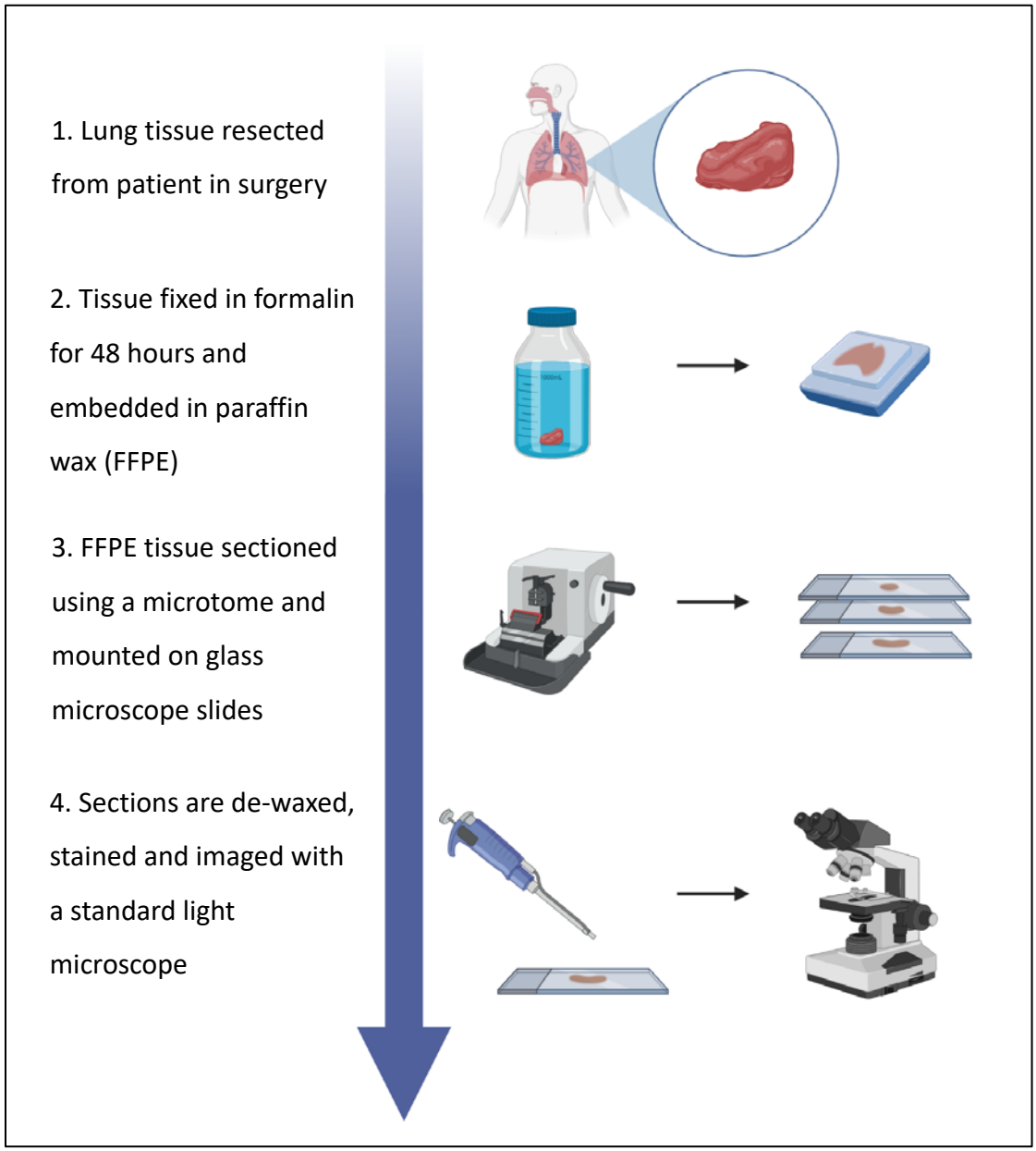

Figure 2.1: **Summary of the standard FFPE processing protocol for surgical biopsy tissue.** This workflow shows the key stages of tissue extraction, fixation and embedding. Traditionally after embedding in paraffin wax the tissue is destructively sectioned using a microtome prior to tissue staining and imaging. Figure adapted from Elaine Ho, created with Biorender.com

2.2 Equipment and software

A full summary of all the laboratory equipment used for this project is shown in appendix A.2, for all the different software used see appendix A.3.

2.3 Use of IRIDIS HPC computing

Due to the computationally intensive processing (very high memory demands) of the image processing and segmentation of large datasets, the IRIDIS 5 visualisation cluster (10 core CPU, 192 GB RAM, 8 GB Nvidia M60 Tesla GPU) was used. Utilising this resource significantly decreased processing time of µCT and immunofluorescence images. IRIDIS was used specifically for work requiring Avizo (including high resolution visualisations), segmentation and interpolation using ITK-SNAP (detailed in sections 3.5.2 and 3.6) and for handling large µCT datasets using Fiji as well as decreasing processing time of bubble segmentations which implemented rudimentary machine learning detailed in the section 3.3.1.

2.4 Micro-CT imaging

All samples were scanned using a novel prototype µCT system optimised for unstained soft tissues (Med-X; Nikon X-Tek Systems Ltd., Tring, UK) (Katsamenis *et al.*, 2019). This scanner contains a multi-material target X-ray source which can be operated at 130kVp. For all the imaging in this project the molybdenum target was used to generate low energy X-rays, optimised for providing sufficient image contrast between wax and tissue in FFPE samples. The Med-X uses a 2000 x 2000 pixel flat panel detector with a high dynamic range for capturing the radiographs, scan parameters and manipulator were controlled from the attached workstation. For this project no other µCT systems or sources were used for volumetric imaging of the FFPE samples.

2.4.1 Sample preparation for CT

Standard FFPE lung tissue mounted on cassettes were initially placed in a specially designed holder for scanning on the cassette, this was then modified to scan the tissue after removal from the cassette using Styrofoam as shown in Figure 2.2. The reasons for removing the plastic cassette and how it affected µCT scan quality are detailed in section 3.2.

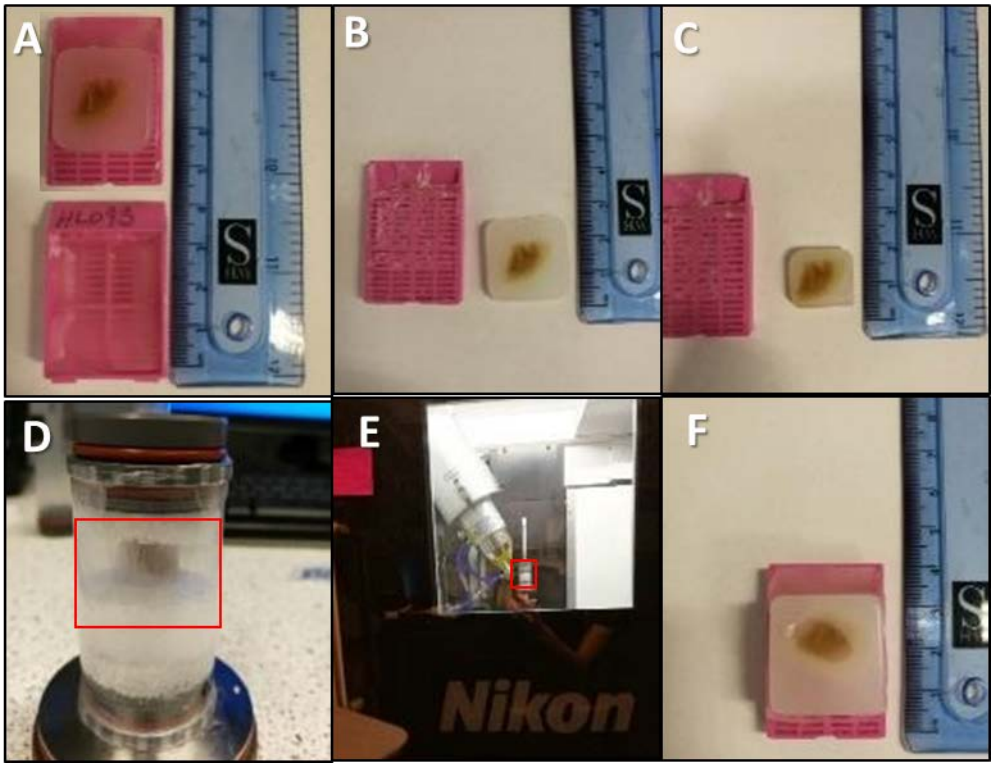

Figure 2.2: **Initial FFPE tissue processing and µCT scanning setup using a custom made holder.** A: The FFPE lung tissue as it arrives on the plastic cassette, the identification label for the tissue is on the rear in this case HL093. B: The paraffin wax containing the lung tissue is removed from the cassette using a scalpel. C: The excess paraffin wax surrounding the tissue is trimmed down to approximately 1-2 cm using a scalpel and the edges are smoothed. D: The FFPE block (highlighted) is fixed between two layers of foam, to prevent movement of the sample, inside the custom made container. E: The container holding the FFPE block is placed on the stage inside the Nikon Med-X µCT scanner (Nikon X-Tek Systems Ltd.). F: Following the µCT scan, the trimmed down wax is re-embedded in wax and mounted back onto the cassette; so that it can be sectioned with a microtome in the future.

2.4.2 Scanning parameters

Technical details of the scanning protocol were based on those of Scott (Scott *et al.*, 2015) but have been further developed and optimised for soft tissue imaging by Katsamenis and colleagues (Katsamenis *et al.*, 2019). Scan times were approximately 8-9 hours and lung volumes were imaged at isotropic voxel sizes between 5-10 µm; ensuring that the entire tissue was in the field of view. The spatial resolution (voxel size) was altered by changing the geometric magnification (i.e. proximity of the sample to the X-ray source) depending on the size of the tissue in the sample. So long as the X-ray settings were consistent the voxel size at specific source to object distances was

consistent across all scans. Therefore, smaller tissue could be scanned at a higher resolution because it could be placed closer to the X-ray source permitting full 360° rotation with the whole tissue staying in the field of view.

Technical details for image acquisition were as follows: the µCT scanner was operated at an X-ray tube potential (peak) of 55 kVp, the filament current was set to 125 µA at a power of 6.9 W using a static reflection molybdenum X-ray target. Exposure time of each image was set to 1.25 s using 4001 projections captured at different sample rotation angles, 4 frames per projection which were reconstructed using proprietary CT reconstruction software (CTPro version V5.1.6054.18526; Nikon X-Tek Systems Ltd). The parameters for reconstruction were set at the time of scanning for automated reconstruction using dual centre of rotation calculations at high quality using a 95% mask radius and minimal beam hardening correction (pre-set 1 or 2). The whole volume was reconstructed and output at a size up to 2000x2000x2000 voxels, as a 32-bit floating point volume image using conventional filtered back projection.

2.4.3 Sample selection using rapid µCT scans

Rapid scans on multiple lung samples were used to inform the choice of samples for the tissue used in chapter 4 and 5. These used different scanning parameters that prioritised scan time over image quality, these scans were acquired and reconstructed in approximately 20 minutes. This allowed multiple samples to be scanned and their viability for use in the project were assessed in a single day (details for this can be found in section 4.3). Technical details for these scans were as follows: the µCT scanner was operated at an X-ray tube potential (peak) of 80 kVp, the filament current was set to 120 µA at a power of 9.6 W using a static reflection molybdenum X-ray target. Exposure time of each image was set to 1 s using 2001 projections, 1 frames per projection and 2x binning was applied to the images. These were reconstructed as 32-bit floating-point volumes at a 15 µm voxel size using proprietary CT reconstruction software (CTPro version V5.1.6054.18526), due to binning the maximum size was limited to 1000x1000x1000 voxels.

2.4.4 Image processing

Following reconstruction the raw floating point (32-bit) volume was imported into Fiji (Schindelin *et al.*, 2012) and converted to 16-bit. The µCT data was resampled such that the *xy* plane was oriented to match the front face of the wax tissue block which the tissue will be sectioned from (Figure 2.3). The 'Rotate_Reslice_Blockface' script (see appendix A.4) was written to speed up the reorientation of the 3D dataset to match the front plane of the tissue volume. The script works by rotating (using bicubic interpolation) and re-slicing (avoiding interpolation) the stack of images

based on lines drawn by the user to calculate the angles of rotation to align to the front plane (histology section plane) of the block.

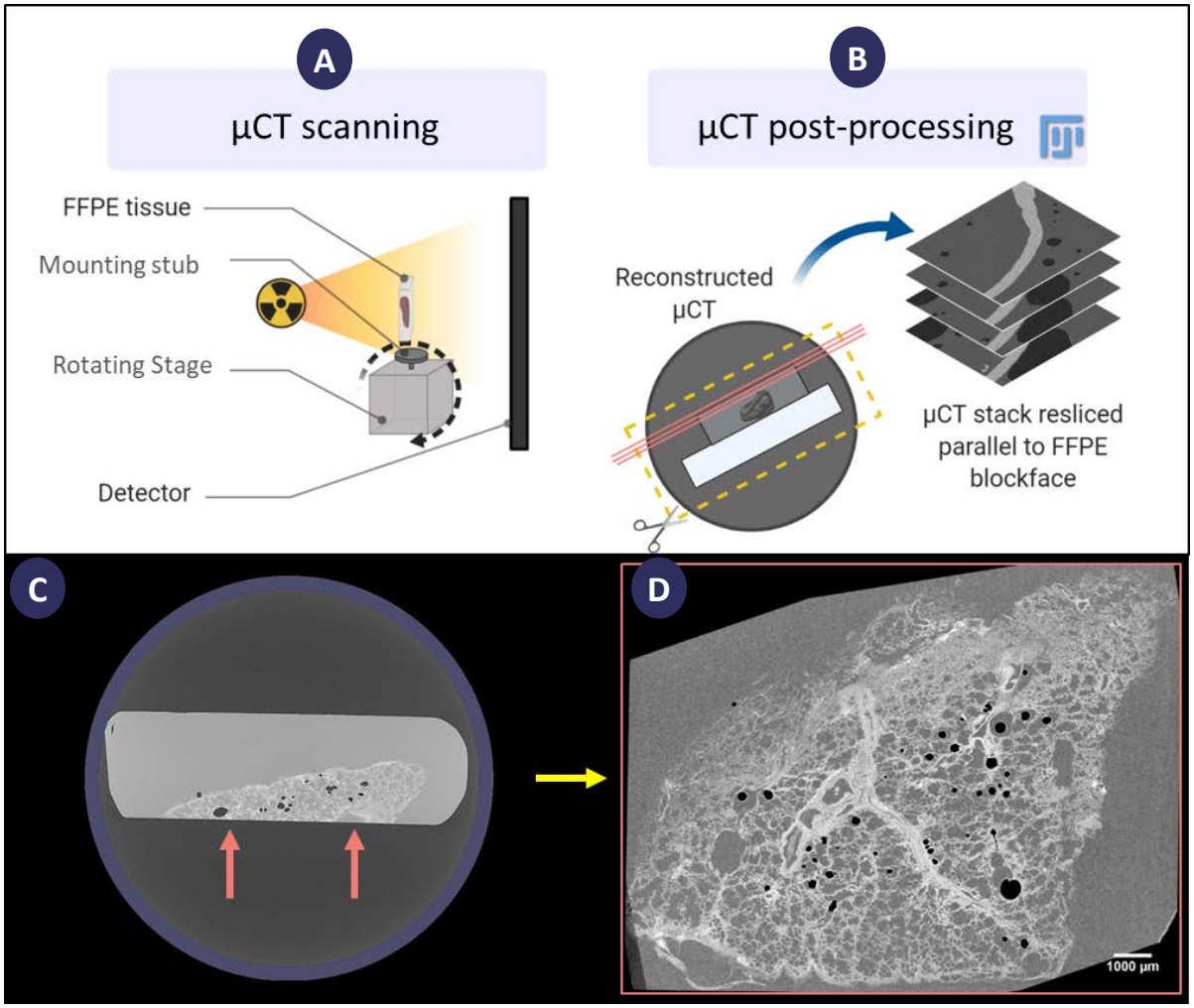

Figure 2.3: **Re-slicing the reconstructed µCT dataset to the front plane of the tissue block.** A: Tissue is µCT scanned upright and reconstructed as a µCT dataset from the top of the block down (*xz* plane). The front face of the block is indicated by the arrows in the lower µCT image. B: The reconstructed µCT volume is cropped and re-sliced using the 'Rotate_Reslice_Blockface' script in Fiji. The resulting stack of images are visible from the front face of the tissue block (*xy* plane, arrows in C), an example slice is seen in D. Upper images adapted from Elaine Ho, created with Biorender.com

2.4.5 Visualisation

The processed 16-bit .tif image stacks were visualised as a series of 2D µCT images in a stack in Fiji and Avizo (version 9.3; Thermo Fisher Scientific), as seen in Figure 2.4. The 3D µCT was visualised using the volume rendering tool in Avizo, here the threshold (colour map) settings were tuned to remove the wax but keep the tissue structure in the 3D visualisation. All segmentation of the µCT

was visualised in Avizo by generating a surface render (smoothness setting: 1.5) with consistent colour maps used on the surface view render.

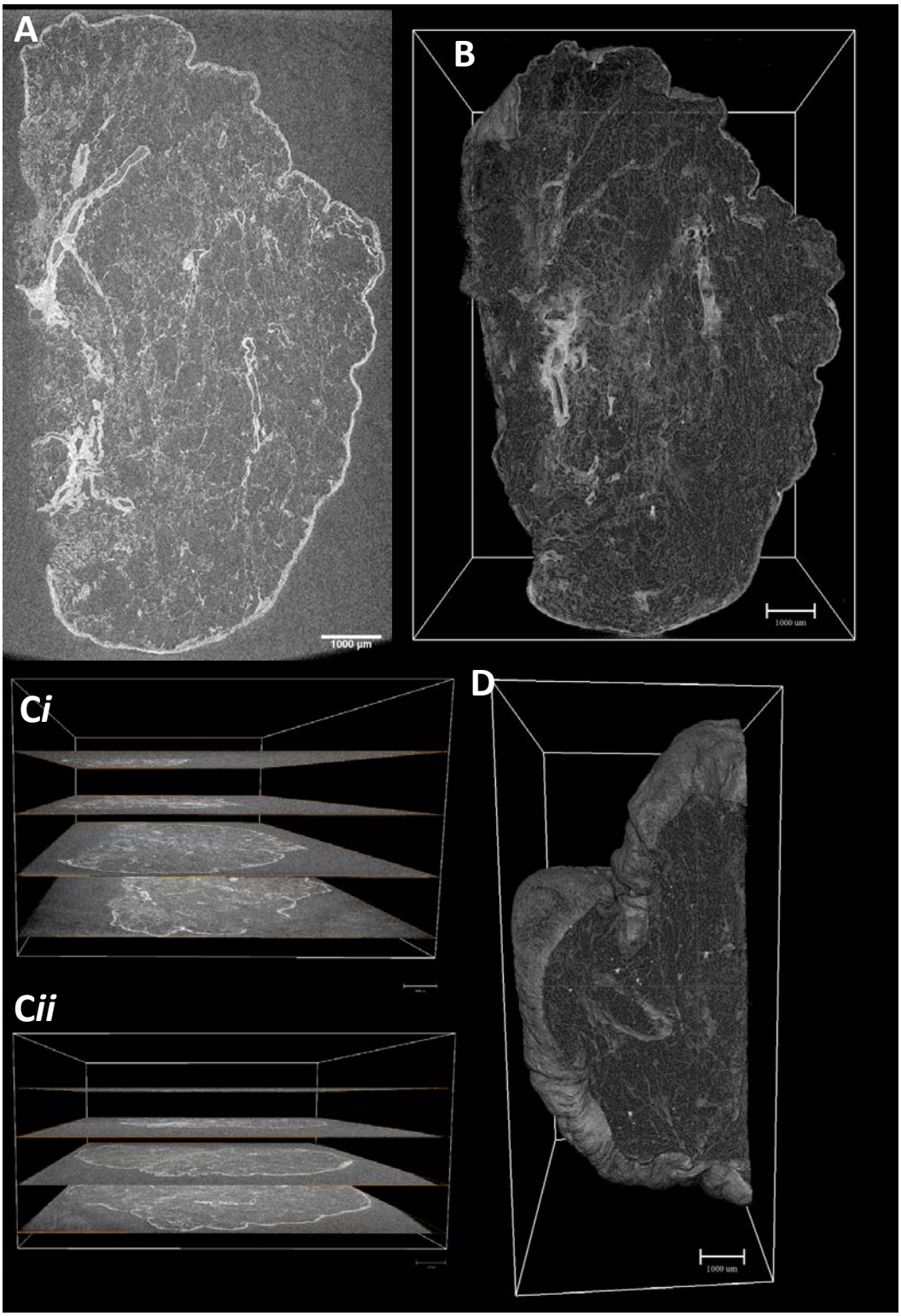

Figure 2.4: **Visualisation of processed µCT data in 2D using Fiji and 3D in Avizo.**The upper panels show the 2D (A) and 3D (B) visualisation of µCT datasets in Fiji and Avizo respectively. The C*i* and C*ii* images, all captured in Avizo, show multiple 2D slices visualised in the 3D space to illustrate that each slice forms the 3D volume. Image D shows the 3D volume rendering from a different perspective to better visualise the 3D nature of the dataset. Scale bars = 1 mm.

2.4.6 Micro-CT imaging workflow

The workflow shown in Figure 2.5 summarises the key parts of the µCT imaging protocols and subsequent image processing detailed in the previous sections for use in this project.

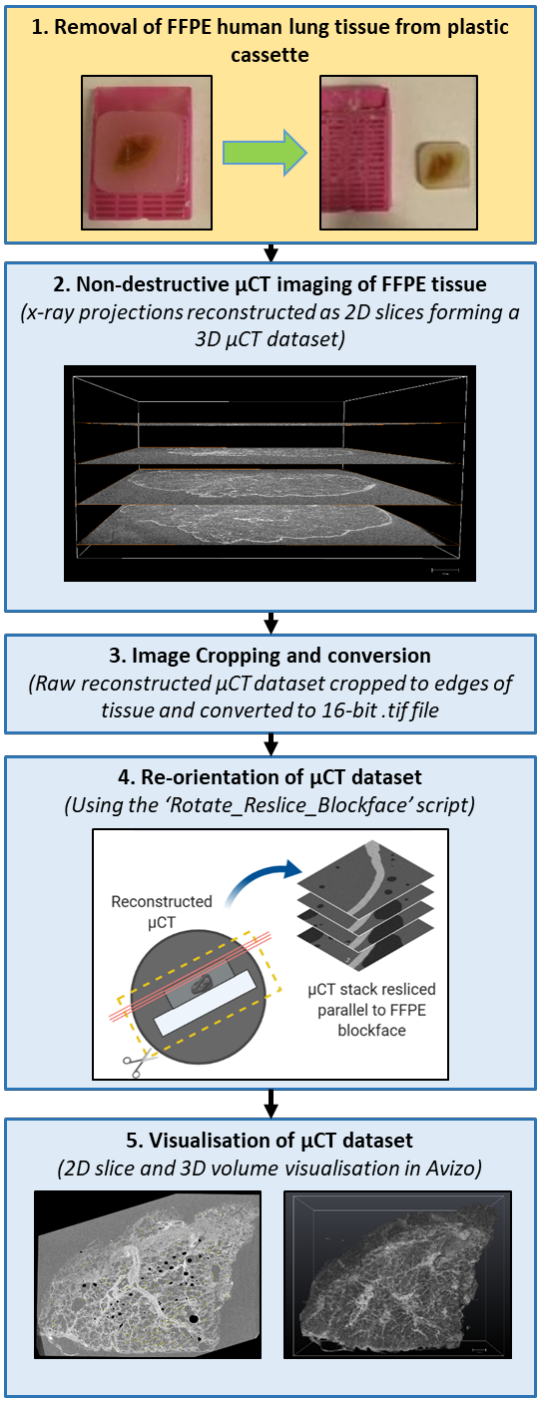

Figure 2.5: **The workflow of µCT imaging and post processing.**1. The FFPE lung tissue is removed from the plastic cassette and excess paraffin wax surrounding the tissue is trimmed down. 2. The tissue block is µCT scanned at a high resolution (<20 µm) and reconstructed into a 3D dataset. 3. The µCT image stack is manually cropped and converted to 16-bit to minimise file sizes. 4. The reconstructed µCT scan is digitally re-sliced to match the front face of the FFPE block. 5. The resulting µCT images are visualised as 2D slices and a 3D volume.

2.5 Bright-field Histology

2.5.1 Sample preparation (post µCT scan)

The FFPE lung tissue blocks, which were removed from the plastic cassette to reduce imaging artefacts (detailed in section 3.2) also had excess paraffin wax trimmed down for µCT scanning to maximise the resolution of the captured images. Following the µCT scan the FFPE tissue needed to be re-mounted onto the cassette to allow tissue sectioning using a standard microtome. This process is summarised in Figure 2.6. The trimmed lung tissue block was placed in the centre of a wax mould and re-embedded in molten wax using a Thermo Scientific HistoStar paraffin wax embedder (ThermoFisher), and the plastic cassette was fixed on the rear of the block as normal. Serial sections (50-200) of the re-embedded lung tissue were cut at a thickness of 4 µm using a Leica RM2135 wax microtome (Leica Biosystems, Nussloch, Germany). These sections were floated on a hot water bath before being mounted onto APES (3-aminopropyltriethoxysilane) coated microscope slides and dried in an incubator for at least 24 hours. Prior to histological staining tissue sections were dewaxed with clearene (Leica Biosystems) and rehydrated through graded alcohols (starting from absolute alcohol).

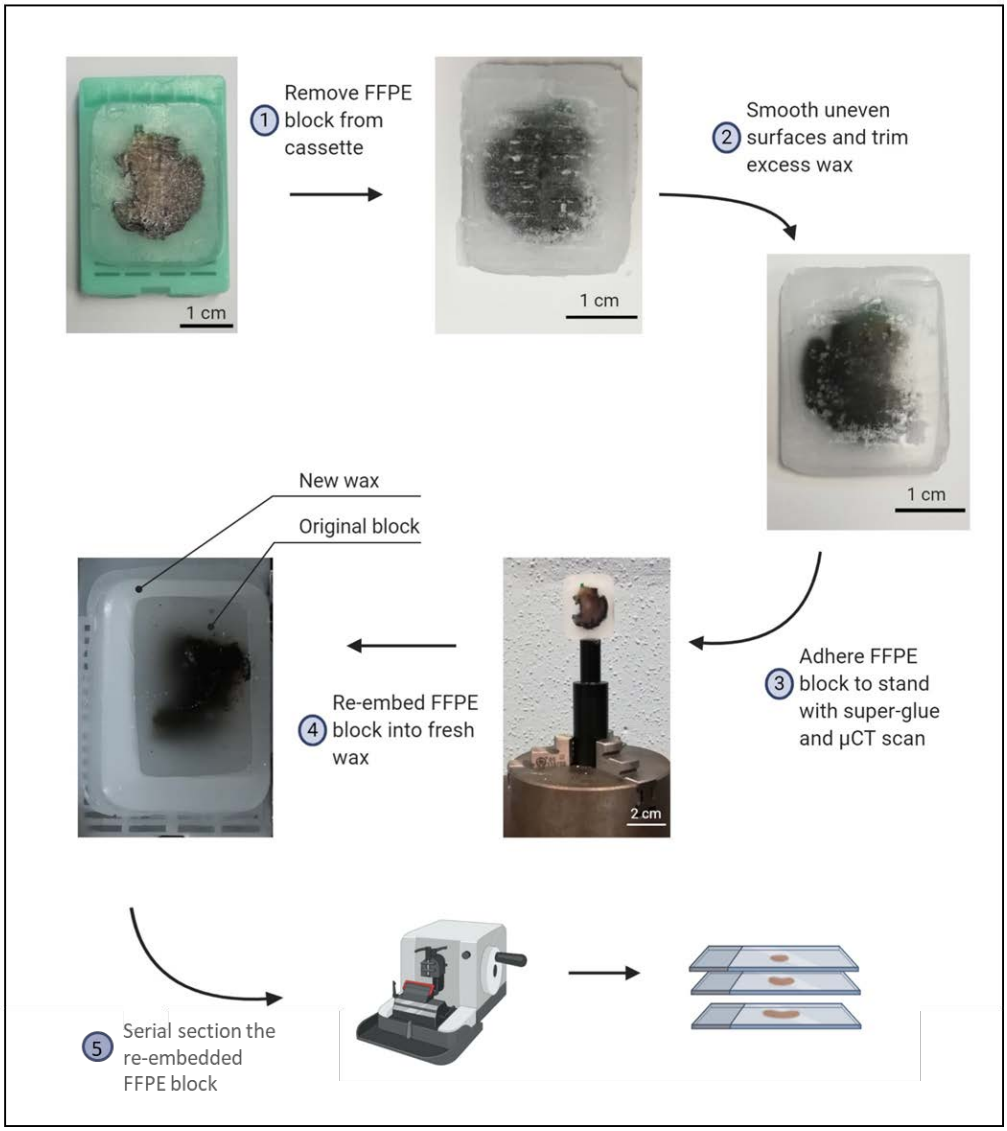

Figure 2.6: **The five main steps of the workflow for FFPE processing from tissue embedding to sectioning.**The resulting tissue sections mounted on glass slides are stored for future use in histological staining. Critically as sectioning is destructive to the tissue the µCT scan needs to be complete before re-embedding and sectioning. Figure adapted from Elaine Ho, created with Biorender.com

2.5.2 H&E staining

H&E staining used stock solutions of Mayer's haematoxylin and eosin made and prepared by the Histochemical Research Unit (HRU, Clinical and Experimental Sciences, Faculty of Medicine, University of Southampton). Staining with H&E followed standard histological protocols (Fischer *et al.*, 2008), sections on slides were cover slipped using Pertex® mounting medium prior to imaging. Sections of tissue from each tissue block (2-3) were stained using H&E for initial visualisation of tissue microstructure and used as reference images for resampling the µCT into the cut histology plane (see section 3.3.2).

2.5.3 Image acquisition

H&E stained slides were imaged using bright field microscopes, in order to quickly assess that the staining was successful slides were initially viewed with a standard light microscope using a 20x magnification objective. Every microscope used for imaging in this project had a 10x objective within the eyepiece. The presence of strong blue staining of the nuclei (haematoxylin) and pink staining of the cytoplasm (eosin) was assessed by eye. After initial visualisation the whole tissue section was imaged using an Olympus dotSlide system (Olympus, JP) using a 10x magnification objective with a Numerical aperture (NA) of 0.4 and digitised as a .vsi file.

2.6 Immunofluorescence

The method of immunostaining FFPE tissue is modified from (Robertson and Isacke, 2011), in this project a single fluorescence probe was used per section. Before applying the antibodies (apart from the *α*SMA) to the tissue, it needed to be pre-treated for antigen retrieval.

2.6.1 Controls

Each staining run contained negative control tissue slides, one section with no antibody staining to determine if any signal is caused by intrinsic autofluorescence and a separate section with only the secondary antibody to ensure no non-specific staining (of the secondary antibody) is occurring. A positive control using a different primary antibody was included in each run, typically a reliable cellular stain like AA1, which was used to check that successful antibody binding was occurring and any staining seen was from a working secondary antibody bound to a primary antibody.

2.6.2 Antigen retrieval

Antigen retrieval is required to ensure that the antibody can reach and bind to its target site in fixed tissue (Shi *et al.*, 2011) and was carried out immediately after dewaxing the tissue. Two pre-treatment methods, pronase pre-treatment and heat mediated (microwave) citrate were compared with a no pre-treatment control for each antibody. Pronase based antigen retrieval was used for all the primary antibodies used in this project which required pre-treatment by providing consistent staining with the strongest signal as evidenced in the results chapters of this thesis. A 0.01% pronase solution in phosphate-buffered saline (PBS) was applied to tissue sections and incubated for 10 minutes before being washed thoroughly with PBS.

2.6.3 Blocking

Following the protocol of Isaack and colleagues a solution of 1% foetal calf serum with 2% bovine serum albumin in 1x PBS dubbed immunofluorescence buffer (IFF) was used for tissue incubation and antibody dilution. The tissue sections were incubated in IFF for 1 hour at room temperature following antigen retrieval. The proteins in the IFF binds to any non-specific binding sites present in the tissue. This is to reduce the primary antibody from binding to these areas of the tissue (endogenous proteins) and causing staining in areas it is not specifically targeted for. As described in later sections (3.4.2) the tissue autofluorescence was used in the methodology and so no quenching step was performed on the tissue sections.

2.6.4 Primary antibodies

After the blocking step, primary antibodies (diluted in IFF) were pipetted onto the slides and incubated overnight in a moist chamber at 4°C. Following the overnight incubation the primary antibody had 3x 5 minutes washes with 1x PBS. Each antibody was titrated to obtain the optimum dilution for staining, so that there was the minimum level of background whilst maintaining the high levels of positive staining. The information about the primary antibodies used in this project are summarised in Table 2.2.

Table 2.2: **Summary table of each of the primary antibodies used in this project.**

Primary antibody [Clone/ID]	Antigen retrieval	Animal raised in	Source (product ref)	Stock concentration	Working dilution	Used to localise	Chapter Results reported
Cytokeratin18 [CY90]	Pronase	Mouse (monoclonal)	Sigma-Aldrich (C8541)	8.4 mg/ml	1:500	Cytokeratin 18 in the airway epithelium	3/5
AA1	Pronase	Mouse (monoclonal)	Abcam (ab2378)	1 mg/ml	1:10000	Mast cell tryptase	5
CD68 [KP1]	Pronase	(Mouse monoclonal)	Abcam (ab955)	n/a	1:100	CD68 protein in macrophage cells	5
aSMA [1A4]	None	Mouse (monoclonal)	Abcam (ab7817)	1 mg/ml	1:10000	Smooth muscle actin	4

2.6.5 Secondary antibodies

Alexa Fluor® 647 labelled secondary antibodies were used for IF imaging, this was always raised against the primary antibody host species, here this was goat anti-mouse (conjugated goat anti-mouse IgG, Fisher Scientific, product ID: A32728). The tissue was incubated in the secondary antibody at a 1:100 dilution in IFF for 1 hour at room temperature. The secondary antibody was thoroughly washed (3x 5 minutes) after the incubation period with 1x PBS.

2.6.5.1 Selecting the right secondary antibody

The choice of secondary antibody fluorochrome, at an imaging wavelength with the least tissue autofluorescence, was based on the results of a lambda scan carried out on a Leica TCS SP8 (Leica) confocal microscope in XY lambda scanning mode. Each laser was used at 30% intensity in turn from 405-633 nm excitation bandwidths and progressively moved in 15 nm steps across the spectrum. Gain was set to ensure reasonable signal strength for autofluorescence as gauged from observation through the eyepiece. In-built confocal software was used to generate curves from the peaks and exported into excel, the results of which are plotted in Figure 2.7. This was used to find available wavelengths of light that produced the least autofluorescence. This showed that the most autofluorescence was at excitation wavelengths in the lower part of the spectrum (<640nm). The optimum secondary antibody that could be used, with the available filters for the fluorescence slide scanner system, was at the far end of the visible light spectrum with a maximum excitation wavelength of 650nm. Therefore the Alexa Fluor® 647 was identified as the best choice for immunofluorescence imaging on fixed lung tissue samples with this microscope.

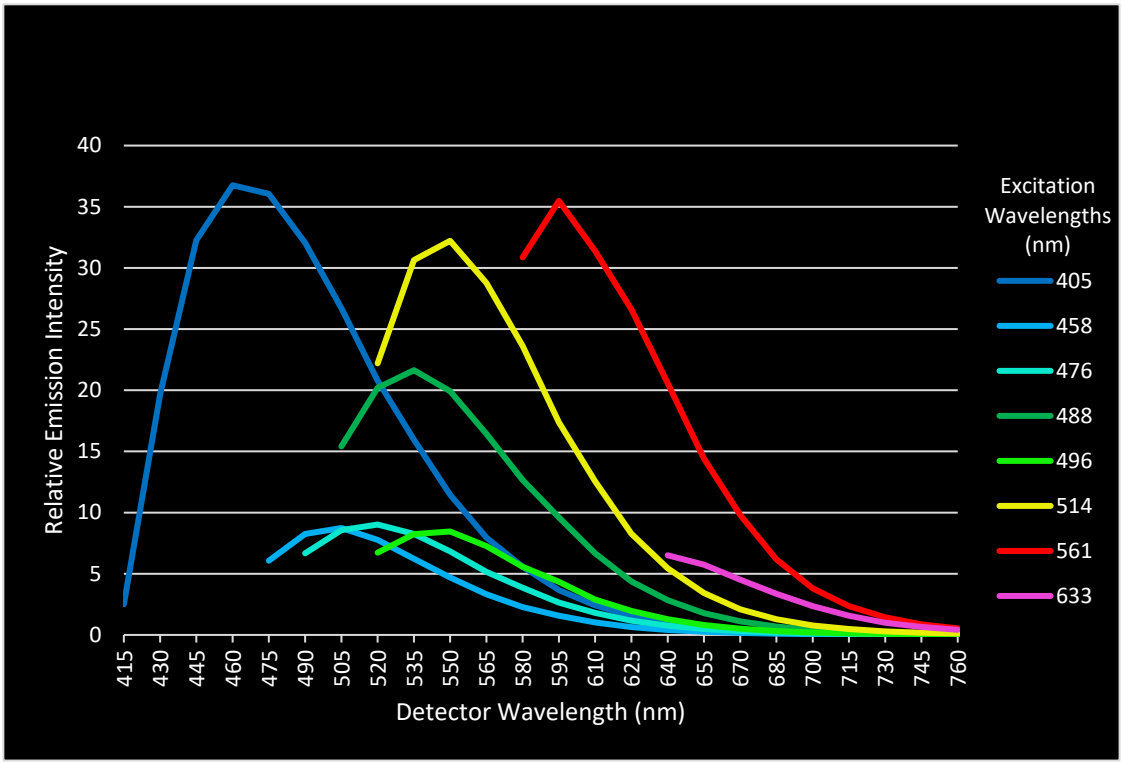

Figure 2.7: **Plot of the results of the lambda scan of autofluorescence in unstained fixed human lung tissue.**The unstained fixed human lung tissue was exposed to several different wavelengths of light using a Leica TCS SP8 confocal microscope and the relative emission intensity for each of these was recorded and plotted as a line graph. Graph produced in Microsoft Excel from data exported directly from the confocal microscope software.

2.6.5.2 Confirming choice of secondary antibody

To assess the results of the lambda scan and confirm the improvement in image contrast produced by the Alexa Fluor® 647 secondary antibody it was compared to preliminary data using an Alexa Fluor® 546 secondary antibody (conjugated goat anti-mouse IgG, Fisher Scientific, product ID: A-11030). Figure 2.8 shows the direct comparison of two FFPE human lung tissue sections stained with the same Ck18 primary antibody using the 546 and 647 secondary antibodies. Staining was successful in both however the signal from the background is much higher in the 546 image (red) compared to the 647 image (pink). The improved contrast between the background tissue and signal enabled threshold based separation of the staining from the background which was not possible using the 546 secondary. Other antibodies were not trialled due to the limited wavelengths of light available on the wide-field fluorescence microscope.

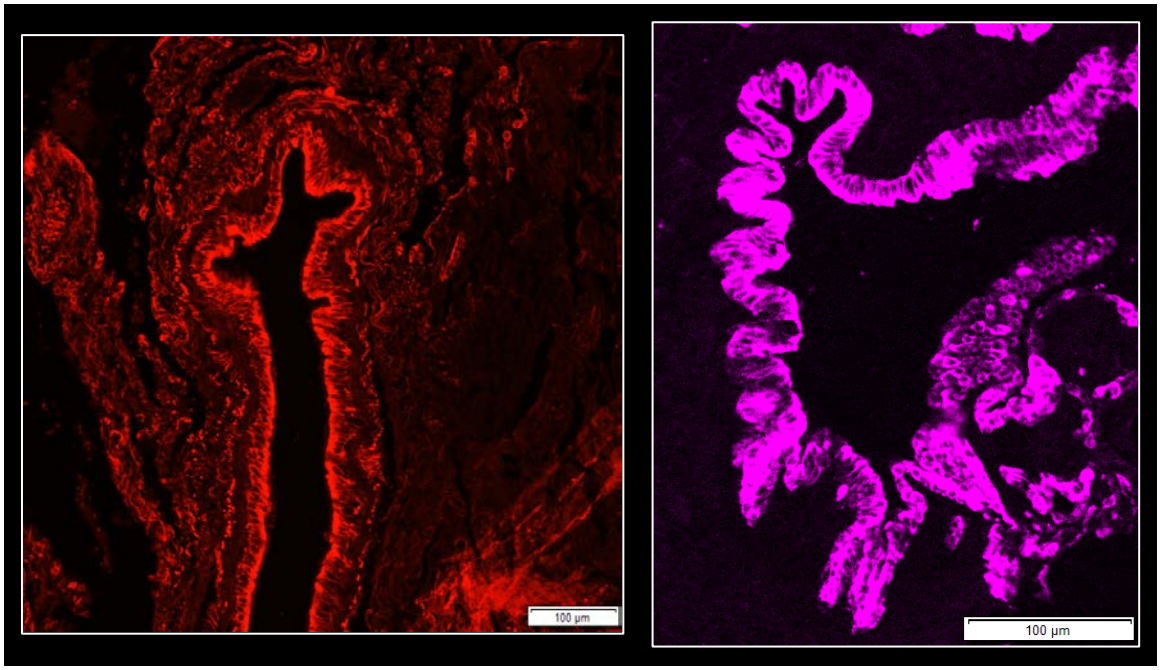

Figure 2.8: **Comparison of Ck18 IF staining of airway epithelium in fixed human lung tissue using two different secondary antibodies.** Both images used the same primary antibody for Ck18. The left hand image used the Alexa Fluor® 546 secondary antibody which was captured using the CY3 channel (552 nm excitation). The right hand image used the Alexa Fluor® 647 secondary antibody which was captured using the CY5 channel (650 nm excitation). The improvement in visualised staining contrast, due to the reduction in background signal, is clearly visible in the staining using the Alexa Fluor® 647 secondary antibody.

2.6.6 DAPI nuclear staining, slide mounting and storage

DAPI was used as a nuclei counterstain following the wash after the secondary antibody, DAPI (Roche, De) was prepared from a powdered stock (provided by the Biomedical Imaging Unit, Faculty of Medicine, University of Southampton) and stored frozen as a stock solution at a dilution of 1mg/ml in dH_2O. The working dilution was 1:500 in PBS, the tissue was incubated in DAPI for 10 minutes at room temperature and washed off thoroughly (3x 5 minutes) in PBS. Finally the slides were mounted in Mowiol aqueous mounting medium (4-88 Harco Chemical Company, Be) and cover-slipped with 0.15 mm thick microscope coverslips. The mounting medium was prepared by adding 30g Mowiol powder to 120 ml of PBS (pH 7.4) and heated (with stirring) for several hours at 60°C until the Mowiol fully dissolved. The solution was then cooled to room temperature. Glycerol (60 ml) and Citifluor 'anti-fade' solution (3.6 ml) (AF3, Agar Scientific, UK) were mixed thoroughly with the Mowiol solution, this was decanted and stored at -20°C.

Slides were stored at 4°C until they were imaged, being kept at this temperature we found that fluorescence labelling remained visible for at least 6 months. However, all stained sections were imaged within a week of the staining to minimise any loss in fluorescence signal.

2.6.7 Wide-field IF image acquisition

The whole area of stained tissue on microscope slides were imaged and digitised using an Olympus VS110 light/fluorescence slide scanner microscope (Olympus, JP). Bright-field images were captured with a 10x objective with an NA of 0.4. Fluorescence images were captured with a 10x objective with an NA of 0.4 using the 4 channel fluorescence slide scanner, with quad band dichroic, fast excitation filter wheel scanning system using a 120W metal halide lamp (Olympus). Images were captured using a selection of the four available channels; for visualising the IF staining with the Alexa Fluor® 647 secondary antibody, the CY5 (629-669 nm excitation/ 646-686 nm emission, exposure time: 250 ms) channel was used. For preliminary IF staining using the Alexa Fluor® 546 secondary antibody (used in section 2.6.5.2), the CY3 (~550 nm excitation/ ~570 nm emission, exposure time: 250 ms) channel was used. The FITC channel (490 nm excitation/ 520 nm emission, exposure time: 1000 ms) was used to capture tissue autofluorescence and the DAPI (372 nm excitation/ 456 nm emission, exposure time: 150 ms) channel for DAPI staining. Focus was calculated automatically using the microscope software. Images were saved as .vsi files that were visualised using the VS Desktop software (Olympus).

2.6.8 Image processing

The histology and fluorescence images produced by the VS110 slide scanner were opened and converted from .vsi files to universal .tif files using VS Desktop, this is because the native .vsi files have poor compatibility with other software. In Fiji the .tif image of each section was manually rotated (using bicubic interpolation) so that it was in a similar orientation to the tissue in the 2D μCT slices in order to enable visual registration between the two images. The background fluorescence, defined as the peak fluorescence signal from the histogram produced in the area of the image not containing any tissue (i.e. area surrounding tissue section), was subtracted from each image channel to enable clearer visualisation of the fluorescence signal.

2.6.9 Visualisation

The raw 2D histology and fluorescence images were visualised in VS Desktop (Olympus, JP) and the downscaled images used for registration were visualised in Fiji. The immunofluorescence images had colour look up tables added to make visualisation easier over the greyscale images. FITC autofluorescence is green, the IF signal (CY5 channel) is pink and DAPI is blue. VS-Desktop provided an overview of the entire slide area with the ability to dynamically pan and zoom around the captured image. The fluorescence channels could be visualised separately or overlaid together as a composite images as shown in Figure 2.9. The fluorescence images saved in a generic read format (.tif) were opened in Fiji as separate images for each channel in the native 16-bit greyscale format. Fiji provided more tools for image processing and visualisation by adjusting the brightness/contrast to highlight the areas with the strongest fluorescence signal (e.g. signal from secondary antibody or DAPI).

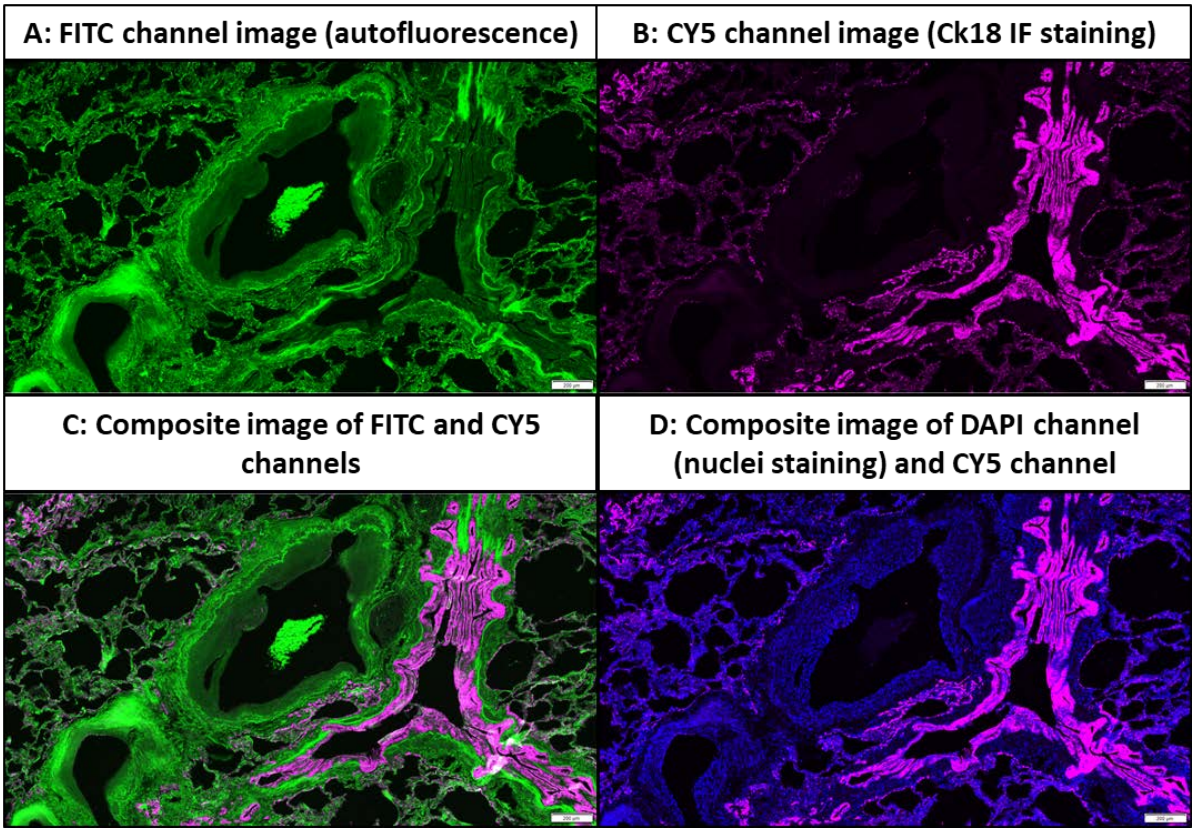

Figure 2.9: **Exemplar visualisation of fluorescence images captured using three different imaging channels.**The upper images (A & B) show exemplar visualisation of individual fluorescent channels using the VS desktop software. The images of the different channels were overlaid to form the composite images shown in the lower images (C & D). The imaging excitation wavelengths were 460 nm (FITC-green), 650 nm (CY5-magenta) and 372 nm (DAPI-blue, contrast changed to visualise tissue at lower intensities). Scale bars = 200 µm.

2.6.10 IF imaging workflow

The workflow presented in Figure 2.10 highlights the key steps undertaken for IF preparation detailed in the previous sections, imaging and processing following the µCT scan workflow (Figure 2.5)

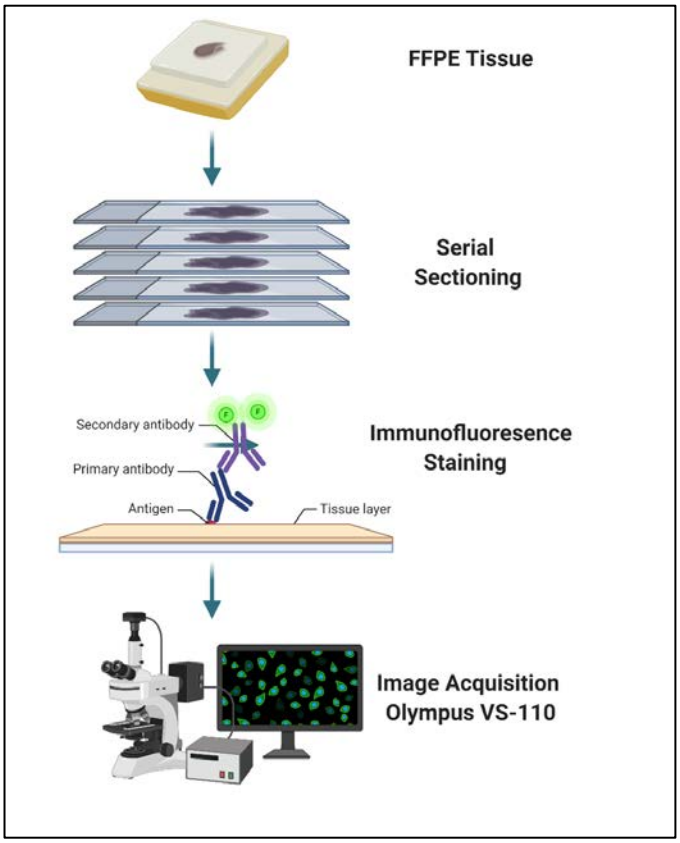

Figure 2.10: **Overall IF imaging workflow following the µCT scan of the tissue.**The re-embedded FFPE tissue is cut into serial sections, mounted onto glass slides and dried for at least 24 hours prior to IF staining. The sections are de-waxed and incubated with a primary antibody overnight before incubation with a secondary antibody with an attached fluorophore. The stained section has a coverslip mounted and the whole tissue section is imaged using a wide-field fluorescence microscope. Image created with Biorender.com

2.7 Statistical analysis

Statistical analysis of the measured metrics comparing non-COPD and COPD tissue in chapters 4 and 5 used unpaired non-parametric analysis. Specifically the Mann-Whitney test to compare ranks was calculated using GraphPad Prism (version 8.4.3). This test was chosen, following a Shapiro-Wilk test for normality which showed that the data was not normally distributed. Categorical data which was not numerical (e.g. smoking history) was analysed using Fisher's exact test. For the blood vessel thickness values (section 4.6) which had a larger number of data points than the other data a two-way ANOVA was performed assuming no sphericity of the data and a Geisser-Greenhouse correction was applied. Area under the curve analysis was also performed on the mean thickness bins with a 95% confidence interval using the Wilson/Brown method. Statistical significance was determined as a P value of <0.05. Additionally all graphs plotting the data reported in chapters 4 and 5 were produced in GraphPad Prism.

Chapter 3 Method development

This chapter will focus on methods developed and applied in order to generate the results seen in chapters 4 and 5. The outline workflow seen in Figure 3.1 highlights the bottlenecks in correlative imaging and segmentation present when this project began. These areas were the focus of method developments to decrease the amount of time and manual intervention required.

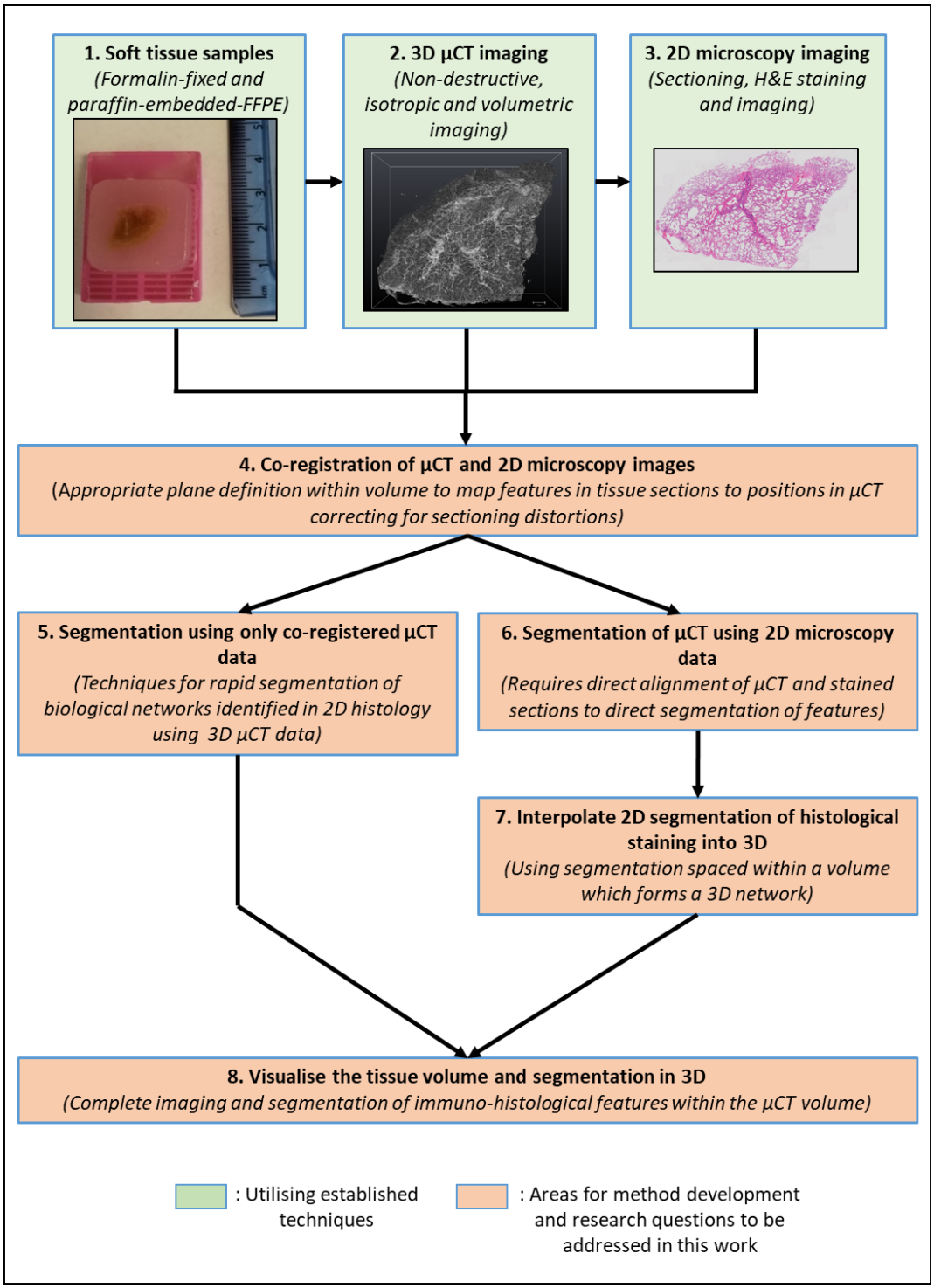

Figure 3.1: **Summary of the proposed correlative imaging workflow highlighting areas for method development addressed in this chapter.**(Previous page). Steps highlighted in green have been previously published. The proposed steps highlighted in orange were identified as areas for development of greater automation. 1: Fresh soft tissue sample preparation via formalin fixation and embedded in paraffin (FFPE) 2: Imaging of lung tissue at a high resolution in 3D using µCT. 3: Section tissue and employ traditional 2D histological imaging techniques to identify specific features not visible in µCT imaging. 4: The first step to address by co-registering the data from steps 2 and 3. 5: Segmentation of 3D networks using the µCT volume whilst avoiding manual segmentation. 6: Localisation of specific features identified by 2D histology within the µCT without manual segmentation. 7: Building non-isotropic segmentation of section staining into 3D isotropic data. 8: Visualise the results of the previous steps together in 3D.

3.1 Aims and objectives

The primary aim of this chapter was to develop a methodology workflow to speed up processing and segmentation of biological features and cell types from imaged µCT data of soft tissue. To facilitate analysis and segmentation on more µCT datasets than was possible using existing manual techniques.

The main objectives for achieving the aim of this chapter were as follows:

1. Confirm best imaging parameters for visualising FFPE lung tissue with µCT
2. Perform successful immunofluorescence staining and imaging of FFPE lung tissue sections
3. Develop registration techniques for matching µCT with 2D histology data
4. Investigate other tools to assist with faster segmentation of features in the µCT lung tissue
5. Produce more automated segmentation of immunocytochemistry staining localisation on the µCT data

3.2 Image acquisition developments

When this project began the µCT scanning parameters were following those used by Scott and Jones (Scott *et al.*, 2015; Jones *et al.*, 2016). These scans also did not use a µCT scanner which had been optimised for soft tissues and so did not produce µCT images with the same level of contrast as seen using the Med-X in this project (full specification in section 2.4). The µCT scans from these projects scanned FFPE human lung tissue on wax blocks attached to a standard plastic cassette which were glued to a carbon fibre tube. This caused image artefacts which negatively affected image quality. The vertical 'streaks' seen in the background of the image (Figure 3.2) are caused by the striations in the back of the plastic cassette absorbing more X-rays in comparison to the paraffin wax. A similar effect can be seen on the air bubbles present in the paraffin wax, these phase fringe artefacts, caused by changes in X-ray absorption between the wax and the air bubble.

In order to remove these artefacts the plastic cassette was removed from the back of the wax tissue block using a scalpel. Another positive of doing this was that without the cassette the excess paraffin wax could be trimmed from around the tissue and the edges rounded to further reduce beam hardening artefacts. The overall size of the block was reduced making it possible to position the sample closer to the X-ray source enabling a higher geometric magnification resulting in a higher resolution (smaller voxel size) scan. The resulting scan from removing the cassette can be seen in Figure 3.2. This successfully removed the 'streak' artefacts from the scan resulting in a much cleaner background without high peaks in X-ray absorption. This did not however, have any effect on the air bubbles artefacts which were still present in the image stack. To address the issues caused by the air bubbles digital post processing of the images was required (see section 3.3.1), rather than physical intervention to the scan setup.

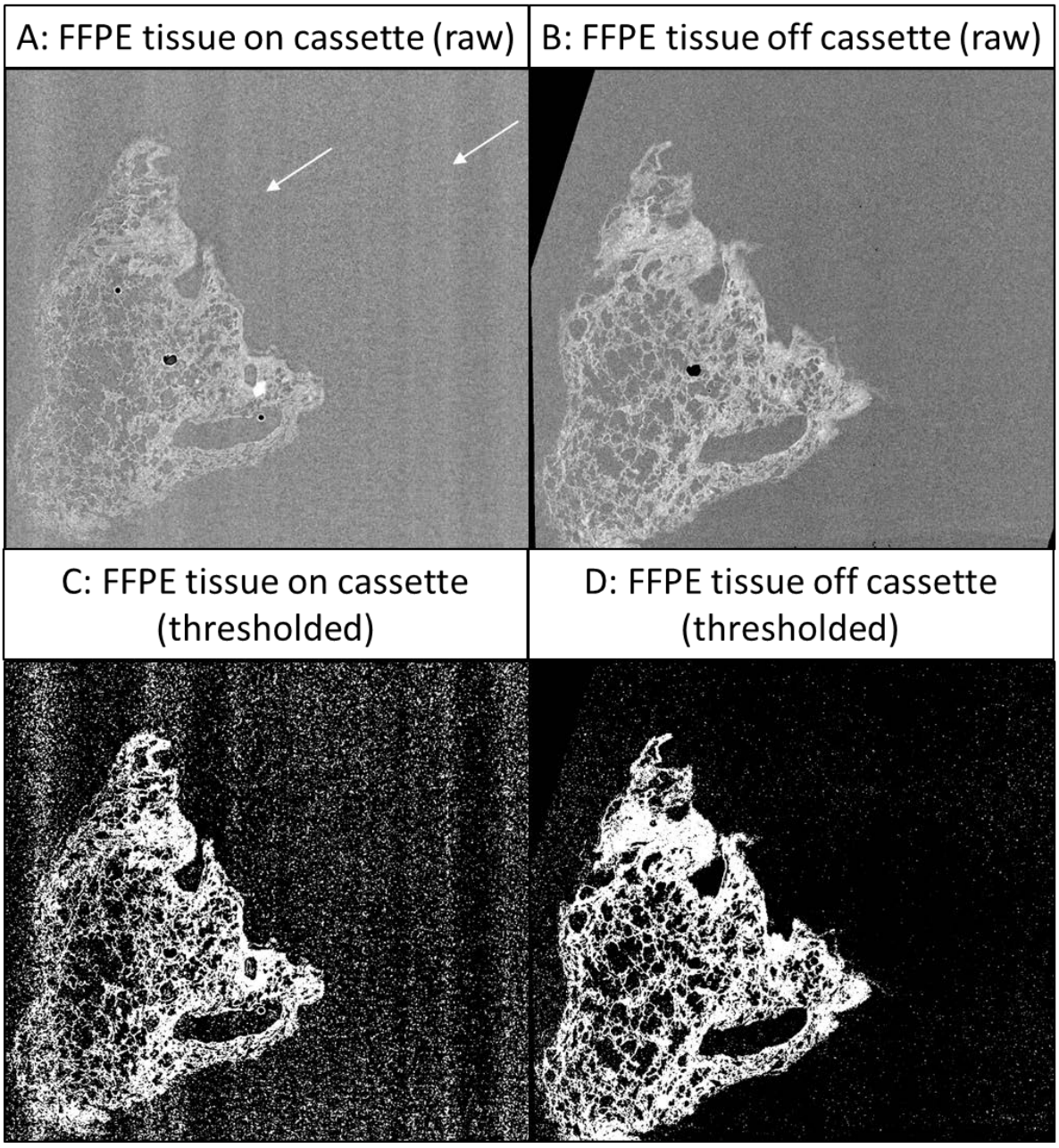

Figure 3.2: **Comparison of µCT images of FFPE tissue before and after removing the plastic cassette.**A & B: Comparable raw reconstructed µCT slices of FFPE lung tissue before and after removing the cassette from the rear of the block. The white arrows in A highlight the 'streak' artefacts caused by the cassette. C & D: Images have been thresholded (to the same range of voxel values) to visualise the artefacts and extra noise caused by the cassette which are almost entirely gone after removing the cassette.

A potential issue with this technique was that the FFPE tissue block could not be sectioned without being attached to the cassette. To address this we experimented with re-attaching the cut down wax block to the cassette. The cut down block was placed in a wax mould that was larger than the block and embedded following the protocol reported in section 2.5.1. The key

difference being that the molten paraffin wax was surrounding existing solid wax rather than tissue, the plastic cassette was re-attached at this step and proved not to hinder sectioning of the tissue once the paraffin wax had set.

3.2.1 Why IF was chosen as secondary imaging modality

Immunofluorescence (IF) was chosen as the primary immunostaining method following direct comparison to immunohistochemistry (IHC). Two consecutive tissue slides were stained with the same primary antibody (CD68) and imaged with IHC and IF. IHC staining was provided by Stephanie Robinson following standard protocols (Crosby *et al.*, 2014). As seen in Figure 3.3, the comparison between IHC and IF reveals similar staining localisation from the same primary antibody but the IF image provided greatly increased contrast between the staining signal and the background.

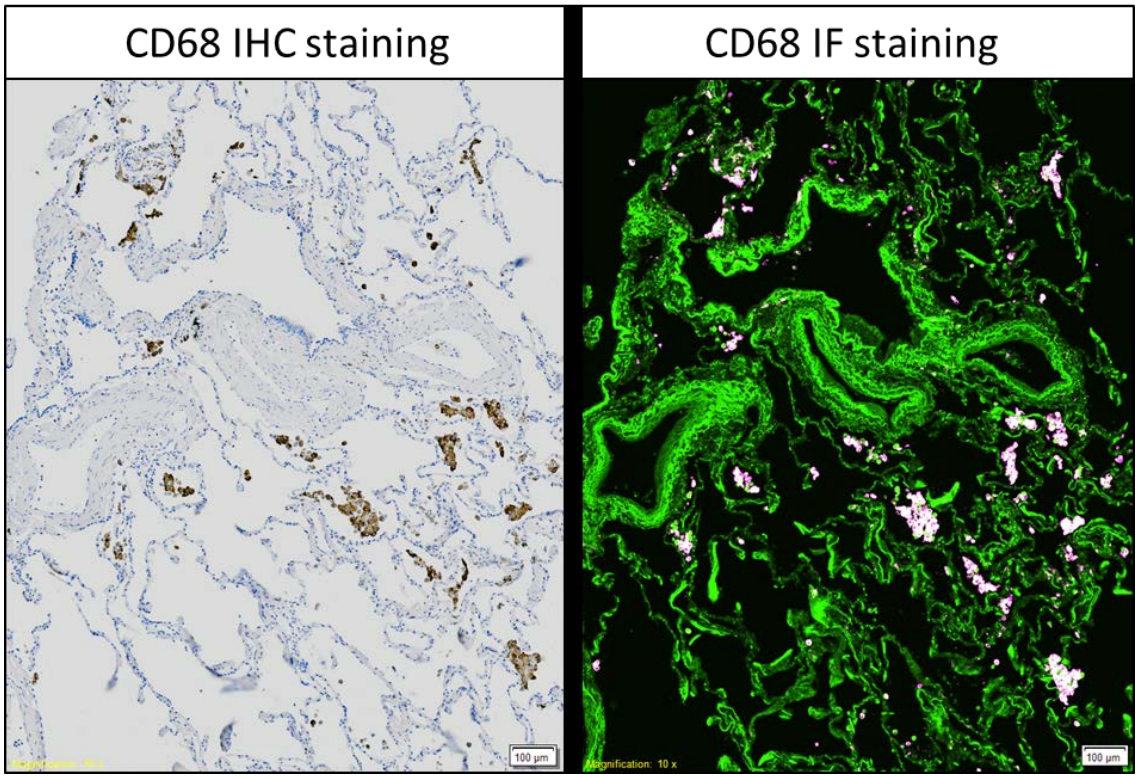

Figure 3.3: **Comparison between IHC and IF staining on consecutive lung tissue sections using the same CD68 primary antibody**.The IHC staining was captured on a light microscope using DAB (brown) staining to localise the CD68 staining with a haematoxylin counterstain (blue). The IF staining was captured using a fluorescence microscope using an Alexa Fluor® 647 secondary antibody (pink/white signal) overlaid on FITC autofluorescence (green). The visually improved contrast and signal strength justified the choice of IF imaging over IHC. Scale bars = 100 µm.

Visual inspection of the two images in Figure 3.3 shows the similarity in the staining across both sections and the immunofluorescence shows consistent staining across both imaging techniques; with no excess background staining in the IF compared to the baseline IHC. The IF more clearly shows the total staining than the IHC allowing easier visualisation of more positive staining. The advantage of using IF staining over IHC was also seen as it has much greater contrast allowing the staining information to be extracted much more easily. The main downsides of using IF are that it is not a permanent stain which will fade over time and it requires specialist fluorescence microscopes to image. However the advantages in image contrast and ease of use for registration (see section 3.4) outweighed these disadvantages.

3.3 Image processing developments

3.3.1 Removing the air bubble artefacts

The µCT scan of the tissue block, after removing the plastic cassette, still contained the phase fringe (bright bands) outlining the air bubbles (black circular voids). However, air bubbles were not present in all tissue blocks and their presence in a block would have been dependent on fixation and embedding of the tissue when it was collected. This project worked on archived tissue and so this was outside our control. Attempts to physically remove the air bubble by melting the wax and re-embedding often gave worse results with a higher number of smaller bubbles which obstructed more of the scan.

Therefore the focus shifted to digital post processing of the scans containing air bubbles to minimise these artefacts. Standard filtration (median, bandpass etc.) and thresholding techniques proved ineffective at identifying the air bubbles individually due to similarities in grey level intensity with other tissue features like red blood cells. Therefore, a trainable segmentation tool was utilised to identify air bubbles in a µCT stack of images. Specifically the Weka trainable segmentation tool (Arganda-Carreras *et al.*, 2017) in Fiji was used. The end result of using Weka was a method for automatically identifying and segmenting the air bubble voids and surrounding ring artefacts as a separate binary dataset. This binary dataset was used to mask the original µCT dataset to remove the ring artefacts from the dataset removing the issues the artefacts caused for visualisation and segmentation. The details of using the trainable segmentation tool are described below; this work was mainly contributed to by 3rd year project student Oliver Hope who completed most of the manual segmentation and training of the classifier.

Within the Weka plugin, µCT images (2D slices) containing air bubbles were loaded for training of the automated segmentation. The air bubble void, including the surrounding ring artefact, was

manually identified (segmented) by the user in Weka and assigned as the areas for segmentation in the classifier. Other areas of the image not containing the artefacts (i.e. tissue and background) were also identified for Weka as areas which were not air bubbles and so not to segment. This was an iterative process with multiple refinement steps of training the classifier to ensure it was only selecting air bubbles and no other areas of the image. This required approximately 50 separate images throughout the µCT volume to complete the training step. The generic workflow of training a classifier for generating segmentation results can be found in Figure 3.4. Weka trainable segmentation works via implementation of a random forest algorithm as described in detail by Polan and colleagues who implemented it for use on CT datasets (Polan *et al.*, 2016). A Fiji script (appendix A.5) which automatically split an image stack up into smaller volumes, applied the classifier to each sub volume and reconstructed them back together again afterwards was used to speed up segmentation.

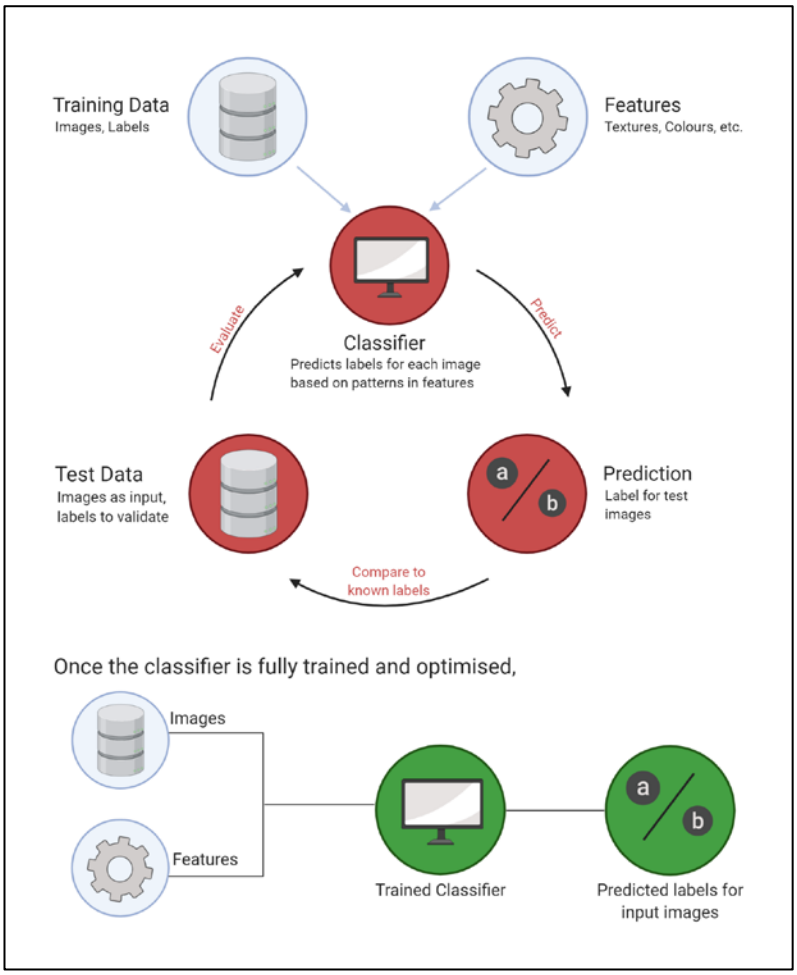

Figure 3.4: **Workflow for using machine learning implemented in Weka to train a classifier for air bubble artefact segmentation.** Training datasets were generated from manual segmentation of the air bubble artefacts from µCT images. This was used to test and train the classifier to the point where Weka could automatically segment the artefacts (features) on µCT images which were not used for training. Figure adapted from Elaine Ho, generated with Biorender.com

The complete segmentation of the air bubbles output from Weka was used as a mask of the original µCT dataset to remove the bubble artefacts seen in Figure 3.5. This bubble segmentation was binarised so that the pixel value of the identified bubbles was set to 0 and the rest of the image set to 1, this image stack was then multiplied by the original µCT stack in Fiji. The majority of the images pixel values were multiplied by 1 and so did not change, the air bubbles were multiplied by 0 and so set their pixel values to 0. After masking the µCT with the bubble segmentation the spheres were still visible in the 3D visualisation of the tissue. In order to remove the artefacts completely the binary bubble segmentation was expanded in each direction (xyz) using the dilate tool in Fiji. The segmented bubbles were dilated by 2 voxels and then used to mask the original dataset, results can be seen in Figure 3.5. In 2D the voids are now completely black, due to the dilation of the mask encompassing the white ring artefacts. In the 3D rendering the bubbles were removed entirely as seen in Figure 3.5 which resulted in the removal of a part of the image that detracted from the interpretation of the tissue structure.

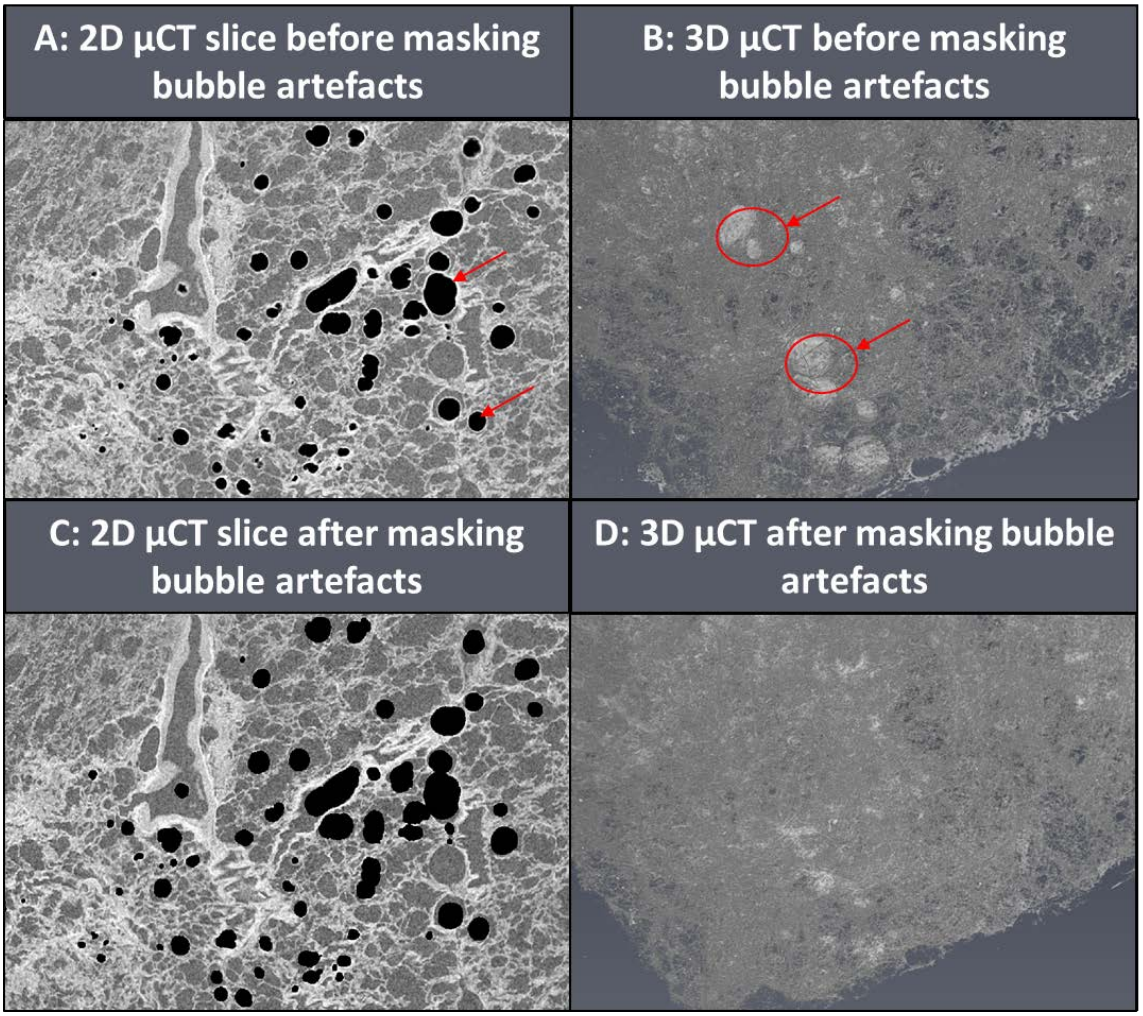

Figure 3.5: **Visual representation of masking the air bubble artefacts on µCT images in 2D and 3D.** A: The raw reconstructed µCT volume in 2D, where the white lines surrounding the air bubbles are visible. B: The raw reconstructed volume visualised in 3D, where spheres in the lung tissue rendering are visible. Both these artefacts are highlighted by red arrows. C & D: The same µCT dataset after the air bubble artefacts were segmented, dilated and used to mask the µCT images. In 2D (C) the white lines are replaced with black void with a voxel value of zero. In 3D (D) these voids are invisible in the rendering and result in a more accurate representation of the lung parenchyma.

3.3.2 Image processing for registration

Precise resampling of the µCT to the cut section plane was required for direct registration between the 2D histology sections and the µCT slice. Using images from 2D H&E stained sections, the 3D µCT volume was rigidly resliced to align with the plane of histology sectioning using the 3-point alignment ('Slice module') in Avizo. A representation of the slice module, shown in Figure 3.6, can change the 3D plane of the µCT slice using 3 reference points placed on the slice. Each

point has an *x,y* corresponding to the position on the 2D slice and a z-value corresponding the slice number in the stack of µCT images. The slice number was changed in the localised area around the *x,y* position of the point, whilst maintaining the slice number in the other areas of the image. This essentially tilted the plane which the µCT slice was being visualised from. Using an H&E stained section as a reference the plane was changed to produce a µCT slice that matched the structural features seen in the H&E image (Figure 3.6). After producing a slice which matched the H&E the 'resample transformed dataset' module was attached to the original µCT dataset and the 'slice module' was selected as a reference image. The µCT was resampled into the plane using lanczos interpolation and output as a new image stack which was used as the primary µCT dataset for registration. This was an iterative process, often requiring repeated plane definition and resampling steps using different positions of the 3 points in the µCT slice. However, this refinement of the plane definition was essential to produce accurately resampled µCT data which matched the sectioned histology plane.

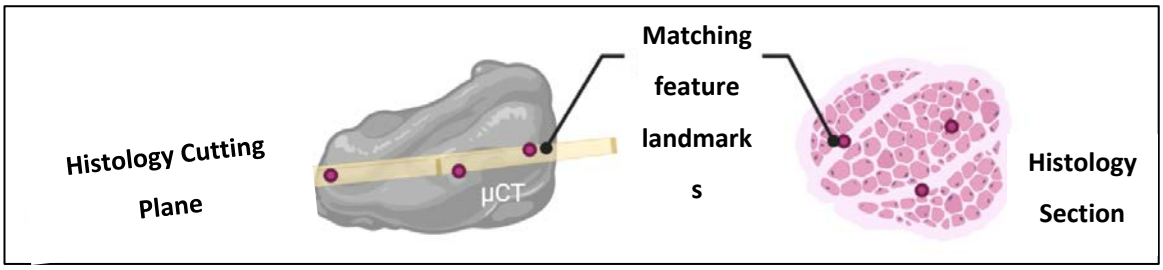

Figure 3.6: **Representation of plane definition of the µCT to match the cut histology plane.** In Avizo three points spread across the image in the 3D space are used to define the plane which the tissue was sectioned for histological imaging. The features are manually matched by eye between the histology reference image and the µCT. Once the matching plane is found the whole µCT volume is resliced and resampled using the defined section plane as the reference. Figure adapted from Elaine Ho, generated with Biorender.com

3.3.3 Image scaling and rotation for registration

The registration techniques described in the next section required images to be the same size and have similar orientation. Therefore each 2D histology/IF image was rotated using bicubic interpolation in Fiji to roughly align the tissue with the orientation of the tissue in the corresponding µCT slice. Once oriented in all three planes the images were, at least for a side by side comparison, registered to each other. However, direct registration of two images required them also to be the same size in the number of pixels in the x and y. To address this difference in

size/resolution one of the images, either the µCT or histology/IF, needed to be scaled to match the other. It was decided that the histology/IF images would be downscaled to the size of the µCT images. This was to prevent the creation of potentially 'false data' by upscaling the µCT to the size of the histology, also this kept file sizes and processing time to a minimum. This was implemented in Fiji using the scale tool, the width and height of the new histology image were the same as the µCT (x and y) using bicubic interpolation and no averaging when downsizing. Overlaying these downscaled images, (as seen in section 3.4.6), revealed the differences between the µCT and the fluorescence images which needed to be overcome for direct registration. Comparing the location of structural features (e.g. blood vessels) there was a visible miss-match between the images of up to 500 µm. These rotated and downscaled images were used as the input images for the registration techniques described in the next section.

3.4 Developing registration of IF to µCT

Prior to this study there were no known or published examples of lab-based correlative µCT and IF imaging with the goal of direct registration between the two imaging modalities. Software which has been developed for other correlative imaging studies such as ecCLEM (Paul-Gilloteaux *et al.*, 2017) were investigated at the start of this project. However, no one software package or plugin existed specifically for automating this type of registration and so many different approaches and techniques were trialled on the µCT and IF images. This started by looking at manual techniques which have worked in studies with similar 2D-3D image registrations.

3.4.1 Manual tools for registration

To address the issue of sectioning artefacts, such as tearing and shrinkage, H&E sections were used to test multiple registration tools in Fiji. Once a working method was found it was tested on the IF images. The Fiji plugins trialled were descriptor based registration (2D/3D), unwarpJ (Sorzano *et al.*, 2005), rigid registration and BigWarp (Bogovic *et al.*, 2016). These were all based on 2D-2D landmark-based registration using a single µCT slice and a histology section as shown in Figure 3.7. The only plugin that produced workable results was the BigWarp plugin in the big data viewer tab in Fiji (Pietzsch *et al.*, 2015). BigWarp produced histology images which had been elastically warped and registered to the corresponding µCT slice. The process for manually using BigWarp is described below.

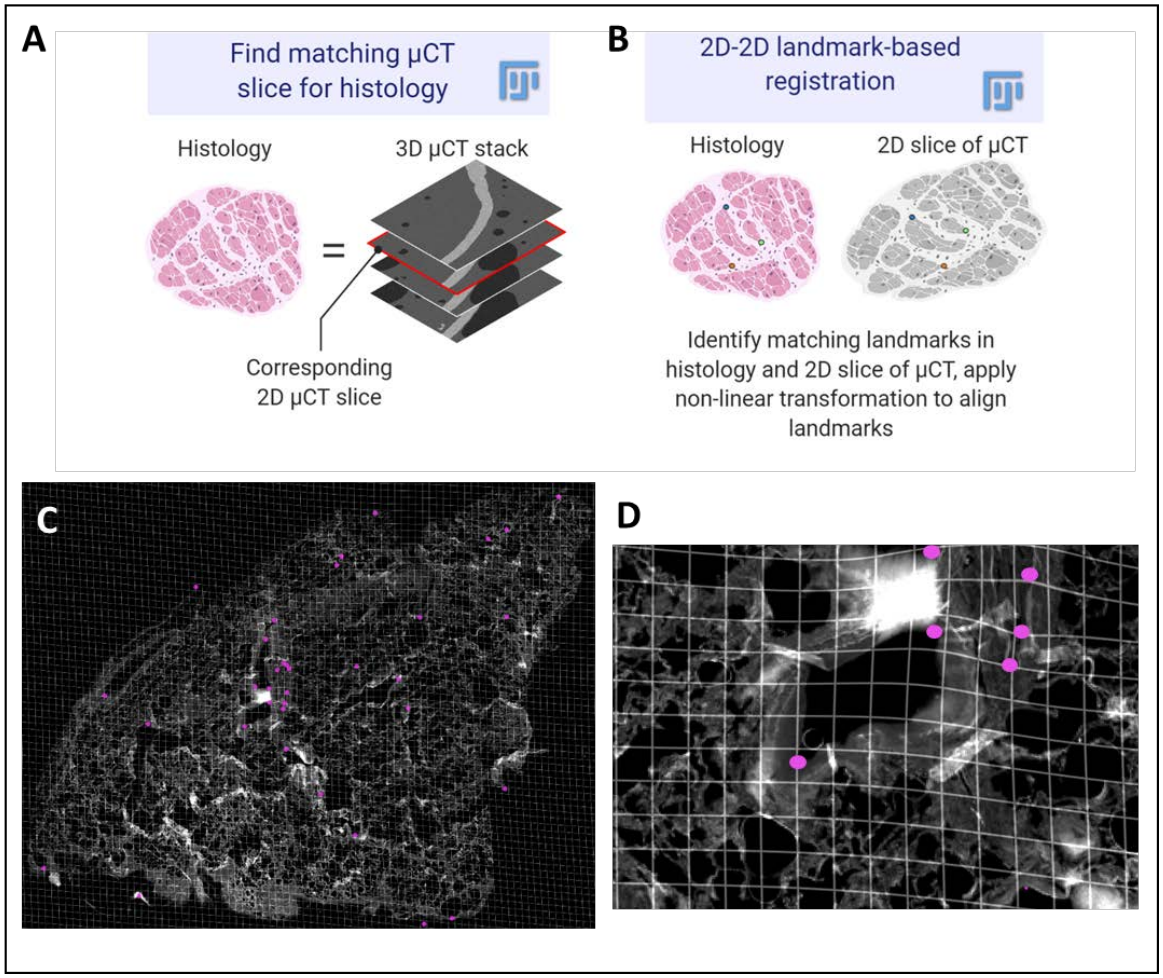

Figure 3.7: **Summary of method for direct 2D-2D image registration between µCT planes and histology sections.**A: The µCT slice which corresponds with the histology section is identified and isolated from the 3D image stack. B: Both 2D images are inputted into BigWarp. Matching features are manually given landmarks in both images which are used to elastically transform the histology image to match the µCT. This is achieved via the generation of a deformation grid (C & D) from the landmark coordinates (pink circles), shown in the lower fluorescent images.

The BigWarp plugin works on a single pair of images which both have to be the same size and greyscale. Because of this the bright-field images were split into the red-green-blue colour channels and the IF images were separated into the separate fluorescence channels. When opening images for use in BigWarp the user decides firstly which image is the 'fixed image'. The µCT slice was chosen because image acquisition was taken before sectioning; this provided a reference structure free of sectioning artefacts (stretching, tearing etc.) Secondly the 'moving image' was a histology or IF image channel, this image had the warp transformation applied to match the µCT (the fixed image). After opening the pair of images in the BigWarp plugin, the user placed manual landmarks on matching structural features manually identified by the user in both

images. This step requires the plane definition step of the µCT to be completed so that matching features appear in the same section and corresponding µCT slice. After placing four pairs of landmarks it is possible to warp the 'moving image', at this point the user can see by overlaying the images where more landmarks are required to make the structural features overlap. This is a time consuming manual process requiring anywhere between 30 and 100 manually placed landmarks on each pair of images. Once the user is satisfied with the level of tissue feature overlap the landmark co-ordinates were exported as a .csv file. The warped image was generated using a Thin Plate Spline method (Rohr *et al.*, 2001) to build a deformation grid (visualised in Figure 3.7) from the point to point landmark matches and applies an elastic transformation to the 'moving image'. The saved landmarks co-ordinates can be used to apply the same transformation on the pair of images again if needed. This was utilised to apply the same transformation to the other colour channels in the H&E image and the other fluorescence channels in the IF image.

3.4.2 Utilising autofluorescence for registration with BigWarp

Fluorescence images are monochromatic (greyscale), unlike bright-field, so did not require colour splitting however a similar notion for registering one channel and applying to the others was used. The tissue autofluorescence imaged in the FITC channel (495 nm excitation) had close resemblance to structures seen in µCT. Therefore the FITC autofluorescence was used as the 'moving image' due to the similarities with the µCT used for registration. After warping the FITC image it was possible to apply the same warping to the other two fluorescence channels by using the same set of landmark co-ordinates. This was essential to the registration process as it proved impossible to manually match the IF staining or DAPI staining to the µCT as they lack visibility of the structural features required for the registration. From one set of landmarks manually placed on the FITC channel and the µCT image all three fluorescence images could be warped to match the µCT slice. The warped fluorescence images were compiled for direct comparison both before and after warping alongside the µCT slice can be seen in section 3.4.6.

3.4.3 Implementing automated feature extraction

BigWarp was a very useful tool for registration of IF images to µCT slices however it was very time consuming, taking a user very familiar with BigWarp and the images on average 30 minutes to register one pair of images. Other users not familiar with either the software or the images took even longer to complete the warping step. Due to the large volume of images requiring warping a more automated tool was required to reduce the time taken and also increase consistency of the registration between individual users.

To automate the warping process the identification of matching features between the images needed to be automatic, fortunately tools already existed in Fiji to automatically pick out and assign matching structural features between different images. One of these tools used is the SIFT (Scale Invariant Feature Transform) correspondence algorithms as described in detail by Lowe (Lowe, 1999; Lowe, 2004). Briefly, SIFT is an algorithm for locating feature points in spatial scale and extracting the position regardless of image size and rotation (Cheung and Hamarneh, 2009). The implementation of SIFT in Fiji is found in the feature extraction plugin and can be used independently of other plugins to assign matching features between images. Within the SIFT plugin the feature detection size filters (default value =4) and affine transformation were selected, this output a series of points on both images which could be exported as .csv files. This .csv file was formatted so that it could be opened as a landmark file in BigWarp and it successfully worked for generating a deformation grid and warping the fluorescence image to the µCT. At this stage it was not as good as the manually defined landmarks but proved a promising option for the possibility of scripting these processes in Fiji to automate the warping process. The manual steps for using SIFT and BigWarp were used to produce a script for the process using the macro recorder in Fiji. To produce the best results this still required some pre-alignment of the tissue to ensure the feature matching works completely. This was used as the basis towards building an automated script for registering and warping the fluorescence images.

3.4.4 Developing the automated warping script

Landmarks generated from SIFT were restricted by the selected filter size often meaning only small or large features were detected. This was addressed by using a macro script which added multiple SIFT feature extraction steps and saving the resulting landmarks from different filter sizes, as regions of interest (ROI) to deliver a novel iterative approach to feature extraction and warping. Running multiple SIFT feature extractions produced many duplicate pairs of landmarks for features detected at different size filters, which was a positive as it showed that the feature extraction was consistent at similar size filters. However, these duplicates broke the BigWarp plugin but could be manually removed from the .csv file in excel but this was time consuming and required manual input. This was automated in the script by introducing a duplicate removal step to the script at the point where the landmarks from the ROI were converted to the BigWarp format for saving. This step would automatically check that a new set of landmarks was not geometrically located within a certain distance to any previously saved set of co-ordinates. These landmark co-ordinates, automatically saved in the BigWarp format, were inputted into the ‘apply BigWarp transform’ plugin to automatically generate the warped images. This step was repeated

for the other two fluorescence channels resulting in all three fluorescence channels being automatically warped to match the corresponding µCT slice.

3.4.5 Workflow of the complete automated warping script

The Automatic feature extraction tools in Fiji were combined with BigWarp to create the 'automated warping script' (appendix A.6), for the whole workflow process. Each step of the script workflow can be seen in Figure 3.8. This script works on files from an input directory which contains the downscaled, rotated fluorescence images separated by fluorescence channels and the matching µCT slices as individual images. Each of these images should have the same identifier for section or slice number at the start of the file name and end with something which identifies the channel or imaging modality. These can then be inputted at the second stage of the workflow in Figure 3.8 after the user selects how many additional image channels needed warping. Multiple SIFT correspondence algorithms with different size filters are run on the pair of images with each set of matching point co-ordinates saved as ROIs. This small loop seen in Figure 3.8 provided the hierarchy of sizes to the matching feature points between the autofluorescence and µCT images. Following the removal of duplicate landmarks the apply BigWarp transform tool is used on the FITC autofluorescence image. The BigWarp transformation is then repeated on the other fluorescence channels of the same tissue section using the same landmarks. The warped fluorescence channels of each section are automatically saved into the output directory alongside the landmark co-ordinates as the ROI and in the BigWarp format with duplicates removed. The script will then repeat on the next set of images until all the images in the input directory have been processed. On average one iteration of the 'automated warping script' will take 2-3 minutes to complete resulting in three warped fluorescence images which are registered to the µCT.

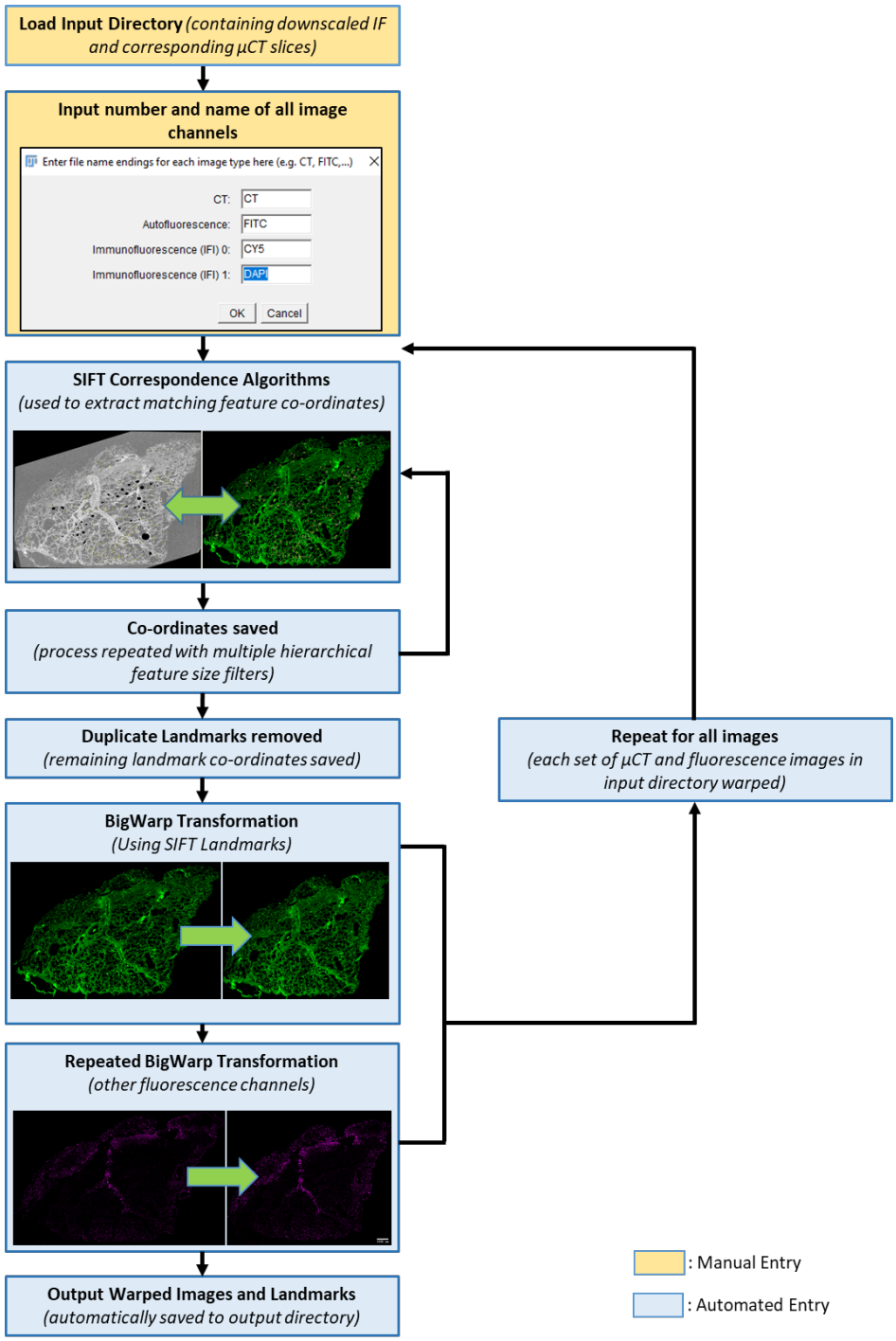

Figure 3.8: **Workflow diagram of working of the 'automated warping script'.**The SIFT (Scale Invariant Feature Transform) correspondence algorithms (Lowe, 1999) were implemented from the feature extraction tools in Fiji and were used to derive the matching points between the images as an ROI. The BigWarp plugin (Bogovic *et al.*, 2016) within the Big Data Viewer was used to apply an affine transformation to the fluorescence channel to warp it to the µCT. The script will warp any additional fluorescence channels providing they were in the input directory with the matching file nomenclature inputted at the start of the script. The output produced and automatically saved warped fluorescent images, the ROIs and the landmark co-ordinates in approximately 2 minutes per pair of images.

3.4.6 Comparing manual to automated

To assess the results of the 'automated warping script' the images were directly compared to the warped images generated by manually defining landmarks in the BigWarp plugin. These co-registered fluorescence images were assessed by the proportion of 'accurate registration'. This was defined as tissue overlapping with tissue or airspaces overlapping airspaces in both the fluorescence and µCT images. 'Inaccurate registration' was defined as areas where airspace overlaps with tissue or *vice versa*. The images were thresholded as an 8-bit mask by selecting the tissue (pixel value 255) and excluding the airspaces (pixel value manually set to 1 after threshold). These images were multiplied together and any pixels with a value of 255 (i.e. tissue value multiplied by airspace value) were designated inaccurate registration with the remainder being designated accurate registration. The amount of registration inaccuracies was visualised by applying a colour map to the resulting image (Figure 3.9-C-E). This was plotted on a bar-chart showing the combined areas of accurate registration (blue and cyan) as one blue column and the inaccurate as the red column (Figure 3.9-F). This process was performed on images which were rigidly registered (rotated with no elastic transformation), manually warped images and images resulting from the 'automated warping script', as seen in Figure 3.9. The proportion of accurately registered pixels corresponding to tissue or air in the autofluorescence and µCT images was increased from ~50% in the best rigidly aligned image planes to ~70% by using BigWarp. The results from manual and automated warping were comparable with near-identical levels of registration; validating the automated warping as a viable technique compared to previous manual methods. As seen on Figure 3.9 the majority of the inaccurate registration came from the tissue periphery, especially along the cut edge of the tissue, where many complex distortions can occur. Central areas of the tissue block resulted in much higher levels of co-registration due to the lack of sectioning artefacts in this area of the tissue.

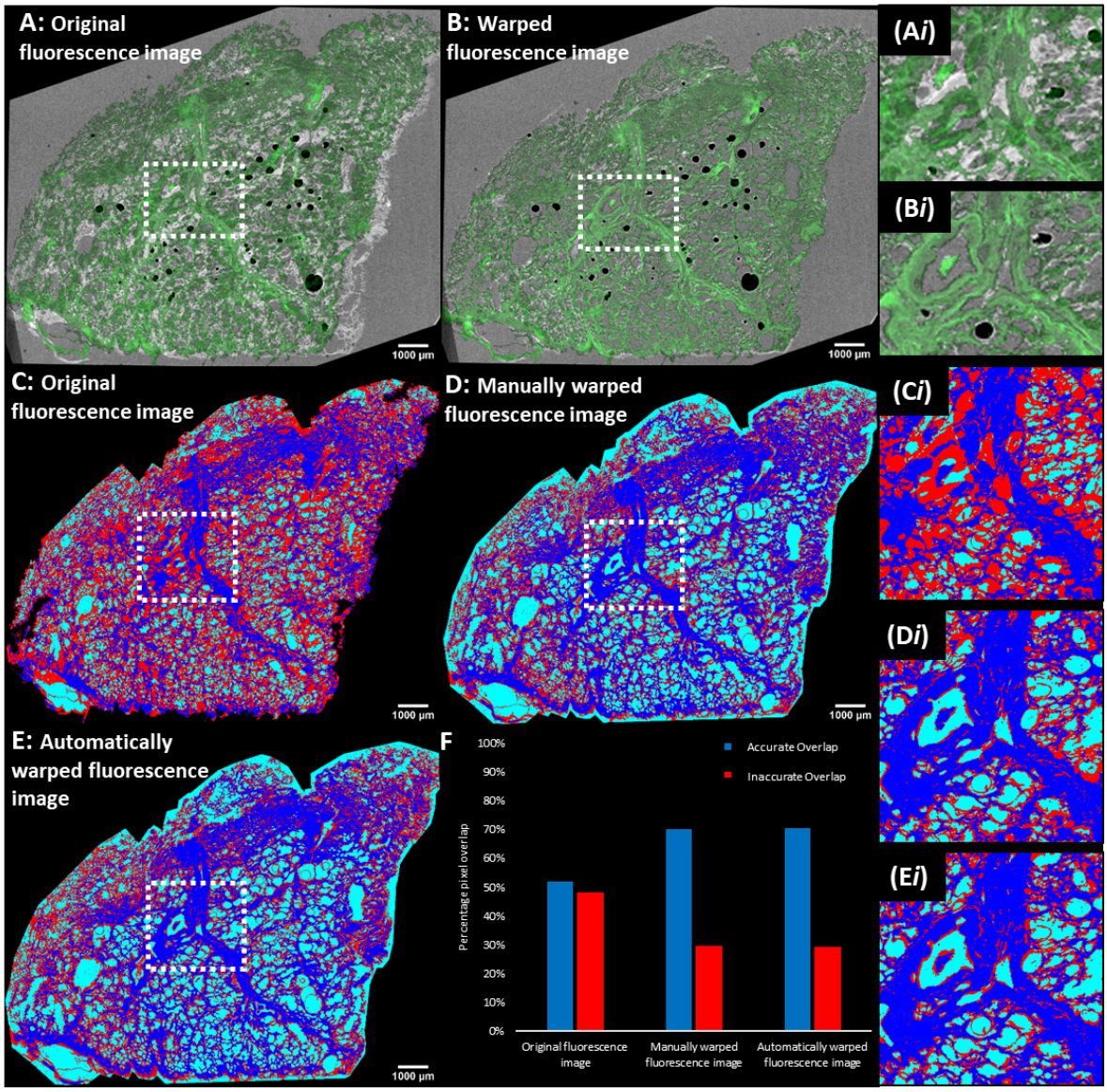

Figure 3.9: **Assessment of fluorescence and µCT image co-registration.**A: Original autofluorescence section (green) overlaid on corresponding µCT plane (grey). B: Warped fluorescence section overlaid on corresponding µCT plane. Inaccurate (tissue-air) overlap shown in red, accurate overlap in cyan (airspace- airspace) or blue (tissue-tissue). C: Original autofluorescence section (as in image A). D: Original autofluorescence section with manually defined warping. E: Original autofluorescence section output from using the 'automated warping script'. A*i*-E*i:* Corresponding magnified images areas in the regions of interests highlighted in panels A*i*-E*i*. F: Bar chart showing the percentage of pixels with accurate (cyan and blue combined) and inaccurate overlap (red) in images C-E.

3.5 Segmentation method development

3.5.1 Manual segmentation

Manual segmentation, a well-established technique, of blood vessel and airway lumens on µCT slices was undertaken in Avizo using H&E and IF section images to assist manual identification of these features. Manual segmentation has the user manually identify and highlight voxels in an image that correspond to the target feature (e.g. blood vessel). The voxels are essentially 'coloured in' using a brush tool directly on the image, this is then repeated for all features in the image and in every image in the 3D dataset. As both the blood vessels and airways form part of a 3D network it was possible to identify them with the assistance of consecutive histology or IF sections to build 3D models of these networks. This can also be achieved from reference stained sections which can be followed from corresponding µCT slices into consecutive µCT slices in the z-direction. Due to the time consuming nature of manual segmentation on large volumes, a cropped sub-volume of interest in the centre of the µCT dataset was manually segmented for comparison to the more automated techniques detailed in the next sections of the report.

3.5.1.1 Airway lumen manual segmentation

The airway lumen was manually segmented and by following the airway in 3D it was possible to segment the network over multiple µCT slices to build a 3D network, as seen in Figure 3.10. However, the lumen was only distinguishable on part of the µCT, in areas where the airway was partially or fully collapsed it was difficult to manually identify and segment the lumen. For example the slice in Figure 3.10-A contains areas of larger airway lumen that are easier to segment and collapsed airway, which is narrower and more difficult to segment. The resolution of the µCT (8.5 µm voxel size) also reduced the ability to segment collapsed lumens which were visible on the higher resolution 2D histology section images but not the µCT images.

The results of the segmentation of all the slices through the cropped volume enabled the creation of a 3D surface in Avizo (Figure 3.10) which allowed for 3D visualisation of the network within the µCT volume (Figure 3.10-B). Here it is clear to see the difficulty involved in manual segmentation of the airway as the collapsed airways mean that the network does not join together as it would be expected to *in vivo*. This can be seen clearly in Figure 3.10 where the airway lumen has collapsed in the lower right hand side of the image compared to the upper right where the lumen remained intact. Figure 3.10-C illustrates the depth of the sample and illustrates why manual segmentation on a slice by slice basis is very time consuming when working with large 3D volumes. Segmentation of the airway lumen using manual segmentation on this small volume

(450x650x200 voxels) took approximately 12 hours to complete, segmenting the full volume manually would have taken more than 2-3x longer to complete.

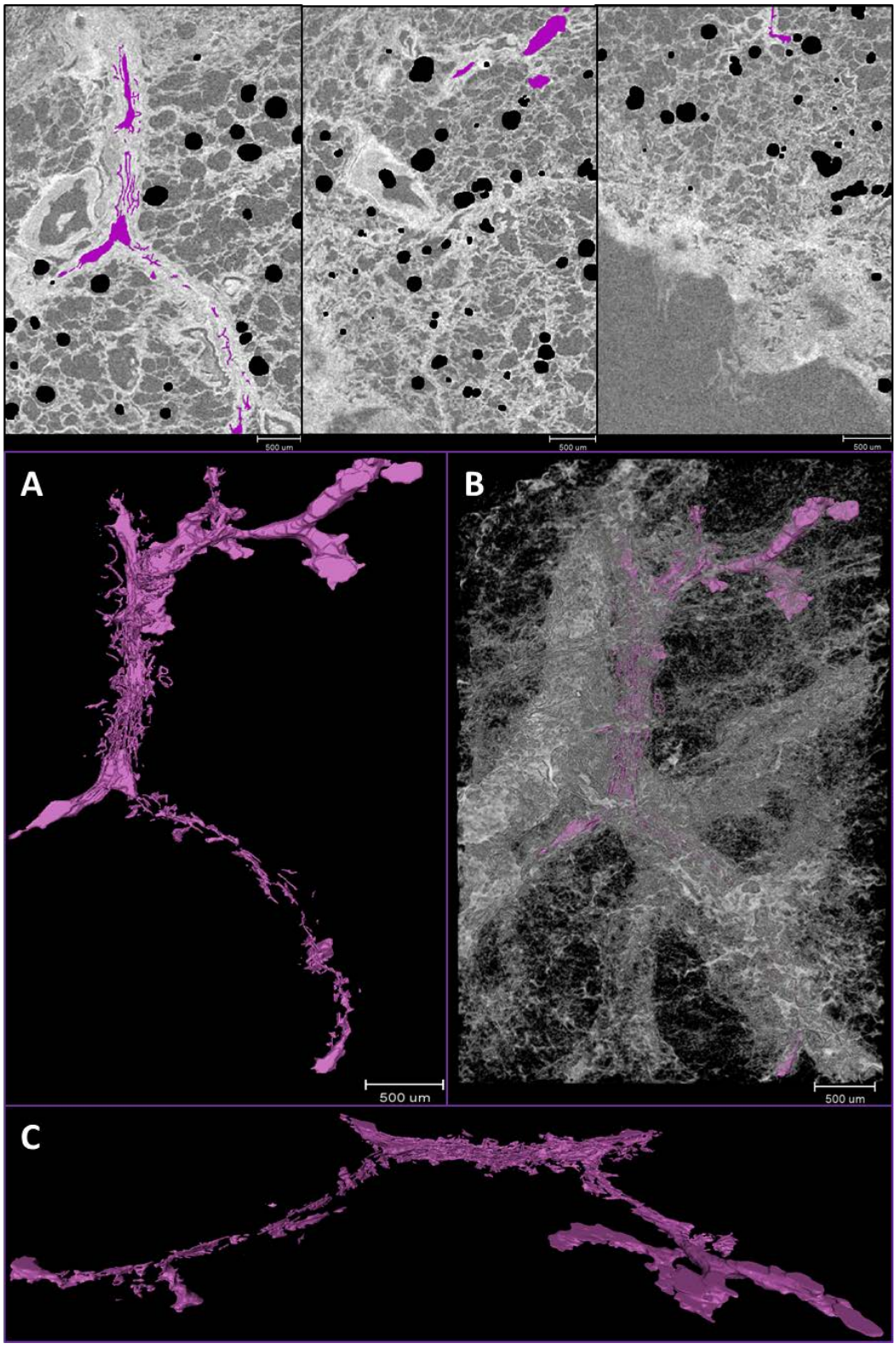

Figure 3.10: **Manual airway lumen segmentation visualised in 2D and 3D.**The upper panels show representative µCT slices through the volume with the airway lumen segmented (purple). The lower panels show the manual lumen segmentation as a 3D surface render. This was visualised independently of the µCT volume (A and C) and also within µCT volume rendering (B).

3.5.1.2 Blood vessel lumen manual segmentation

Blood vessels were more numerous, easier to identify and more evenly distributed in the µCT compared to airways. Due to the thicker walls surrounding the lumen and the presence of red blood cells it was possible to segment the blood vessel lumens with high levels of confidence. However the presence of red blood cells made it difficult to differentiate between blood in the blood vessel lumen and blood vessel walls due to similar levels of X-ray absorbance. The 2D segmentation of the blood vessels can be seen in Figure 3.11, these are the same slices as the airway segmentation in the previous section (Figure 3.10). The blood vessel network visualised as a 3D surface (Figure 3.11) and within the µCT volume (Figure 3.11-B) illustrate the greater volume of blood vessels compared to the airways seen in Figure 3.10. Figure 3.11-C shows the depth and complexity of the blood vessel network in this small cropped region of the µCT lung volume.

The size and complexity of this network meant that it took even longer to segment the blood vessels compared to the airway, this segmentation took approximately 18 hours to complete. Combined with the airway segmentation of the same volume it took approximately 30 hours to segment both networks on this small volume of interest. The largest volumes used in this project were much larger (up to 1600x1800x950 or 2,736,000,000 voxels) and so it would take several days or even weeks to manually segment the networks in each dataset. This highlights the need for a more automated approach to enable more volumes to be segmented in less time.

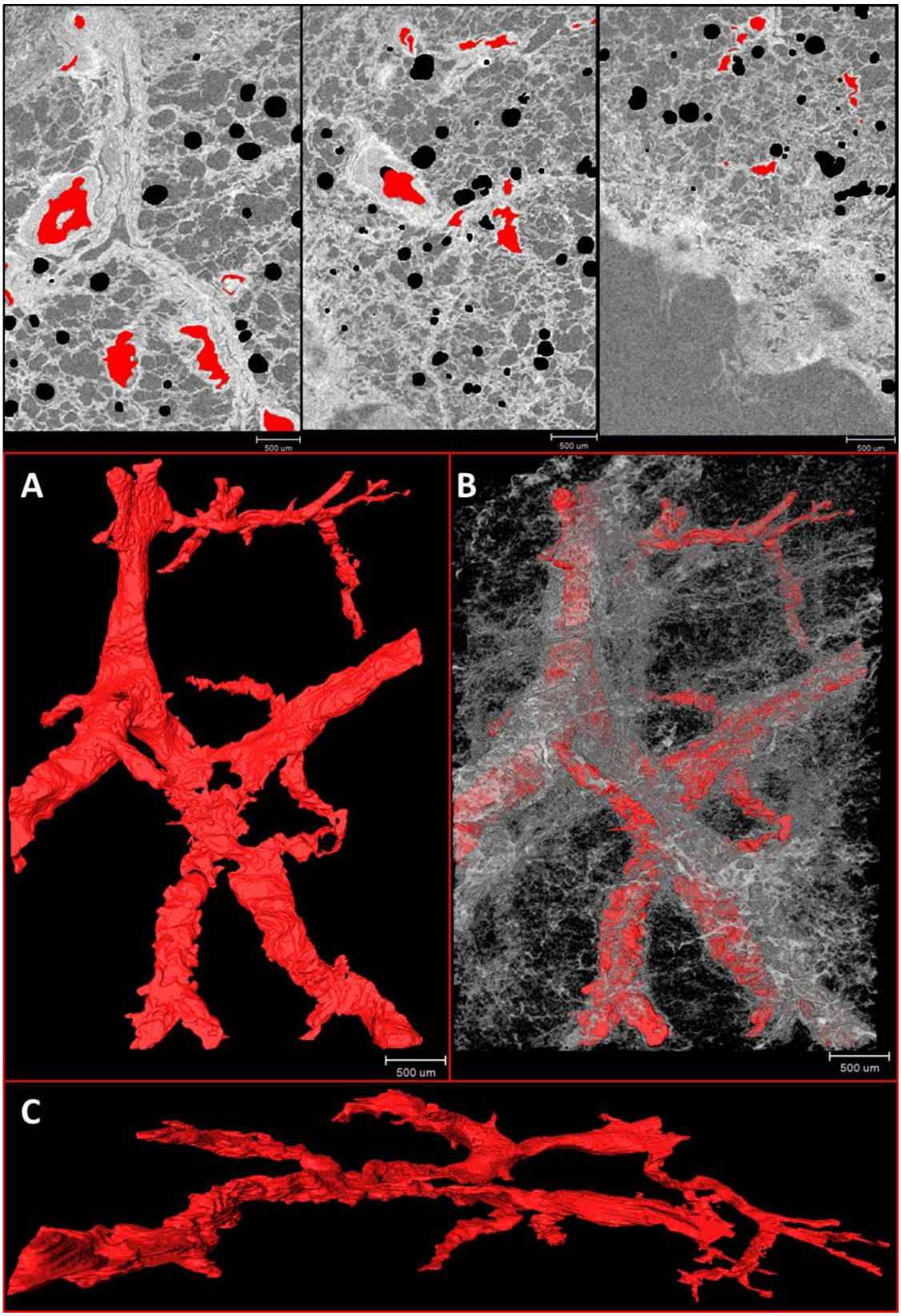

Figure 3.11: **Manual blood vessel lumen segmentation visualised in 2D and 3D.**The upper panels show the same representative µCT slices through the volume as figure 3.10 with the blood vessel lumen segmented (red). The lower panels show the manual lumen segmentation as a 3D surface render. This was visualised independently of the µCT volume (A and C) and also within µCT volume rendering (B).

3.5.2 Semi-automated segmentation

The first area investigated for automation of segmentation was region growing segmentation. A basic implementation used to speed up manual segmentation is commonly known as the 'blow or snake tool' which is present in multiple segmentation software. This starts from a base point selected by the user and as they drag the cursor within the structure of interest the highlight area expands until it meets a boundary. This boundary is determined by a gradient threshold of grey values which can be changed by the user alongside elastic 'pushing' and 'pulling' forces which act as resistance for the boundary. This tool however, was limited to the 2D plane and so each blood vessel lumen on a section still needed to be manually selected and segmented using this tool which was exceedingly time consuming. This was used with limited success on the airways but due to the thinner walls and the nature of the collapsed lumens it had a minor effect on decreasing segmentation times.

This contrast in grey values between the blood vessel lumen and walls facilitated other region growing segmentation methods using thresholding to define the boundaries of the blood vessel lumen. The 'active contour segmentation tool' in the ITK-SNAP software package (V 3.6) (Yushkevich *et al.*, 2006) was used as described below and can be seen working in real time in the Appendix A.7.1 video. Within the software the 16-bit μCT image stack was imported and the 'active contour segmentation tool' was selected. Selected volumes of interest were binarised using an adjustable absolute threshold to define the blood vessel boundaries; so that the lumen was set to zero and the walls of the blood vessels set to one. Reference points for the region growing segmentation to start from (seed points) were manually placed in the centre of the lumen. Running the 'active contour evolution' will cause the segmentation to grow from the seed point and can be observed in real time using the 2D and 3D views. This process can be paused at any point and when finished it can be added back to the original volume and repeated on new volumes of interest. This is an iterative process as each sub volume of segmentation is added with each additional seed point in the volumes of interest. The progress of the segmentation from one seed point is seen in 2D (Figure 3.12-A) and 3D (Figure 3.12-B). The progress of the segmentation after additional seed points were added throughout the volume are shown in 3D (Figure 3.12-B-D, illustrating how the network was 'grown' by adding up to 40 seed points. Blood vessels down to approximately 20 μm diameter were segmented from the whole μCT volumes in 4-5 hours. This time would change depending on the size of the tissue volume and the number of narrower blood vessels present (which take longer to segment correctly).

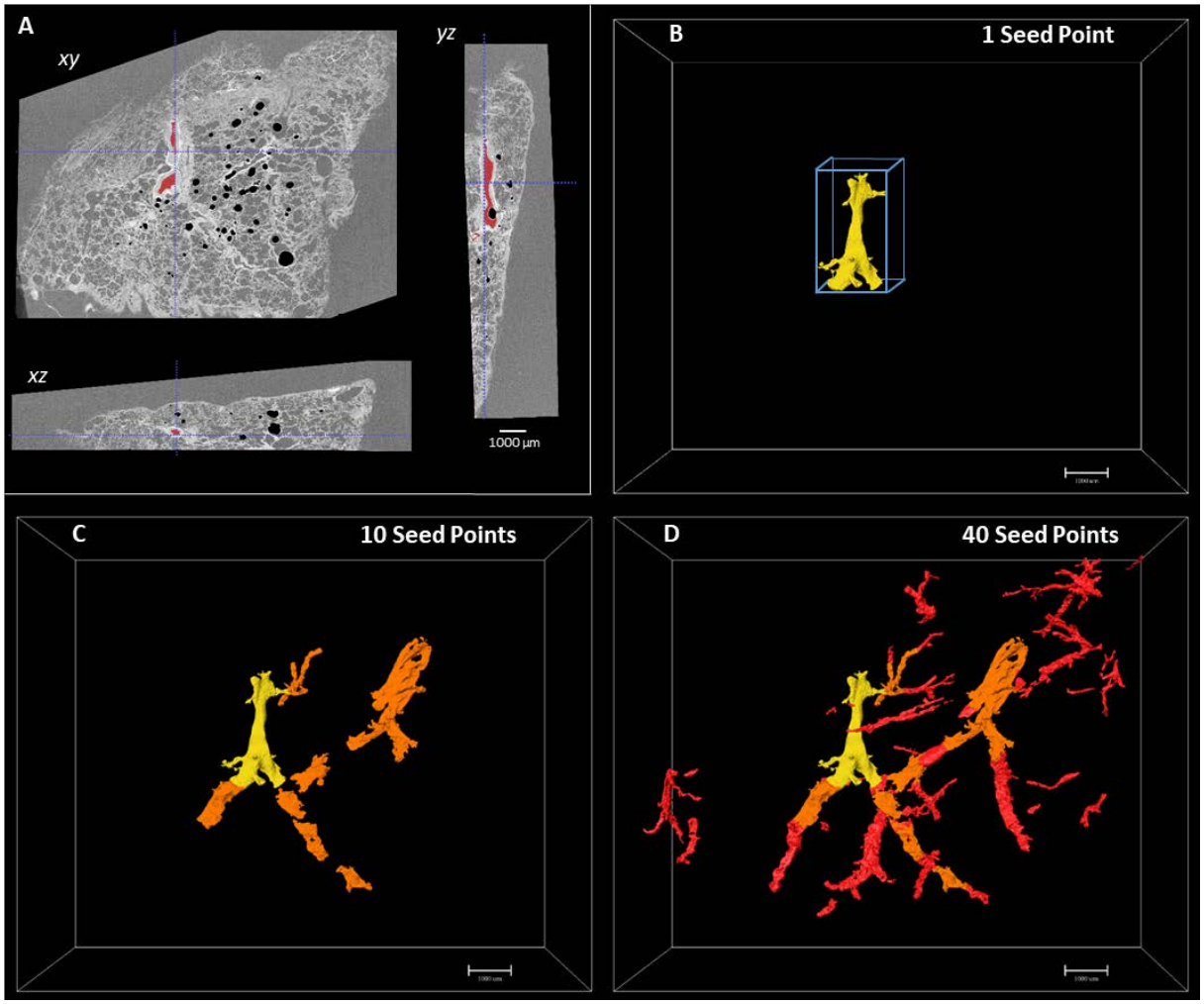

Figure 3.12: **Segmentation of the lung blood vessel network using 'active contour segmentation'.** A: The three orthogonal CT planes as they appear after initiating the 'active contour segmentation' from a single seed point within a sub-volume of interest in ITK-SNAP. B-D: 3D rendering of the blood vessel network as more seed points are added in order to 'grow' the network. Yellow = 1 seed point in 1 sub-volume of interest, orange = 10 seed points in 10 sub-volumes, red = 40 seed points in 40 sub-volumes.

3.5.3 Validation of blood vessel segmentation

Prior to IF staining H&E sections were used as a reference for seed point placement when starting the active contour segmentation of the blood vessels. H&E images were also used to qualitatively assess afterwards whether the blood vessels had all been successfully segmented. Figure 3.13 shows the comparison between a segmented µCT slice and the corresponding H&E section. Here high correspondence between the segmented blood vessels and manually identified blood vessels from the H&E can be observed. However, from a wide-field point of view it can be hard to identify the smaller blood vessels present in the H&E.

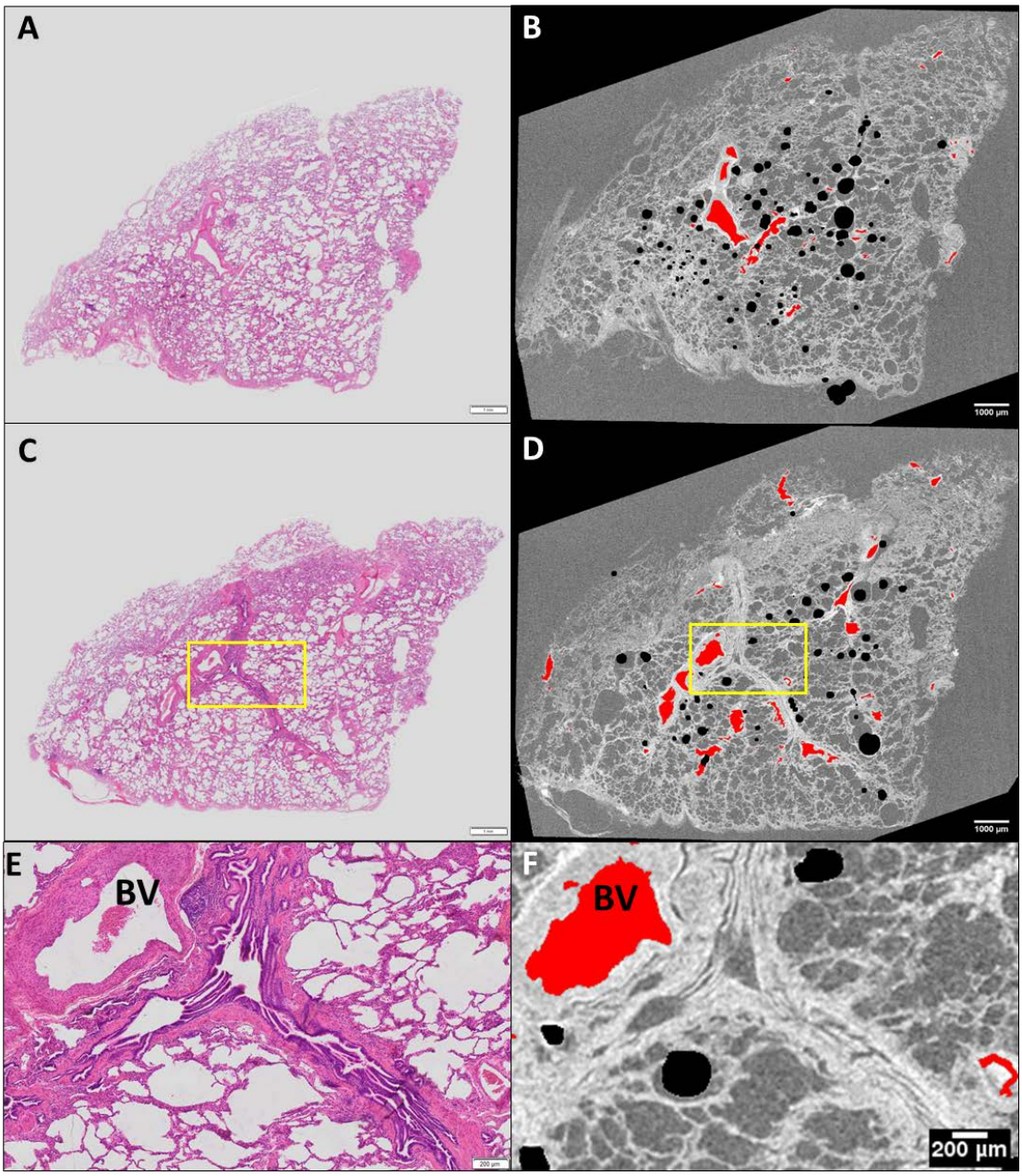

Figure 3.13: **Visual comparison between blood vessels identified in µCT plane and corresponding H&E images.** Upper panels show two wide-field microscopy images of H&E stained lung tissue sections (A&C) alongside matching µCT slices (B & D) containing blood vessel segmentation (red). The lower panels (E & F) show magnified images of an area of tissue containing blood vessels and airways distinguishable on both imaging modalities. Yellow boxes show the area of the wide-field image used in the lower panels.

To assist the confirmation of the segmented blood vessels on wide-field images, IF staining was performed using an alpha-Smooth Muscle Actin (*α*SMA) primary antibody and the results compared between a corresponding IF section and µCT plane. *α*SMA expression present in the blood vessel walls surrounded blood vessel lumen identified by segmentation. Figure 3.14 shows

the results of the IF imaging of *α*SMA staining where these morphological differences can be observed. The overlap between the blood vessel lumen segmentation on the µCT slice and the *α*SMA localisation provided by IF can also be seen in Figure 3.15. *α*SMA expression was also found in the airways however the signal of the airway *α*SMA was weaker than the blood vessels and so could be removed via thresholding the IF image. Morphologically the localisation of the *α*SMA in the airway was found beneath the basal lamina of the airway surrounding the airway epithelium and was not in direct contact with the airway lumen. Whereas in the blood vessels the *α*SMA is found consistently throughout the walls directly neighbouring the lumen.

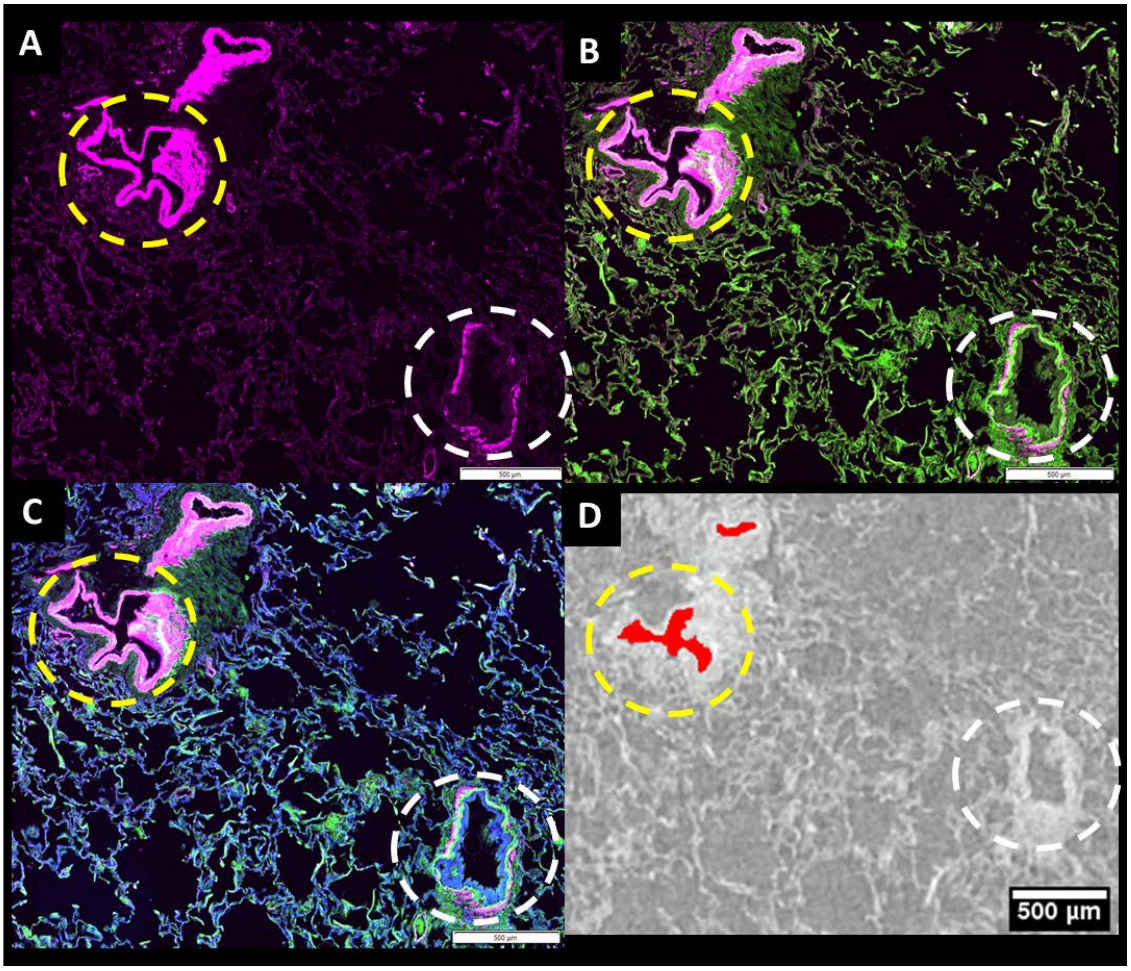

Figure 3.14: **Visual comparison of *α*SMA IF staining and the blood vessel segmentation of the corresponding µCT plane.**The yellow circles highlight an identified blood vessel and the white circles an identified small airway. The differences between *α*SMA localisation surrounding the blood vessel lumen compared to surrounding the basal tissue of the airway is visualised in panels A-C. IF images of human lung tissue highlighting *α*SMA positive staining (pink-panel A), tissue structure provided by FITC autofluorescence (green-panel B) and nuclei staining provided by DAPI staining (blue-panel C). Panel D shows the corresponding area of blood vessel segmentation overlaid on a µCT slice matching the areas of *α*SMA staining for blood vessels and not segmenting the airway lumen.

In order to assess the number of potentially missed blood vessels using 'active contour segmentation' the images were processed as shown in Figure 3.15. It was found that both manual and automated approaches could segment blood vessels down to the same ~25 µm diameter. However, the automated approach was less consistent for segmenting the smaller blood vessels less than 25 µm in diameter. This is understandable as the smallest blood vessels were not easily discernible at the resolution of the µCT scans. Morphologically these missed vessels were either flat/collapsed or filled with red blood cells which were not segmented due to high X-ray absorption of the blood. This justifies the choice of region growing segmentation tools for detecting blood vessels down to ~25 µm equivalent diameter whilst saving considerable time over manual segmentation methods.

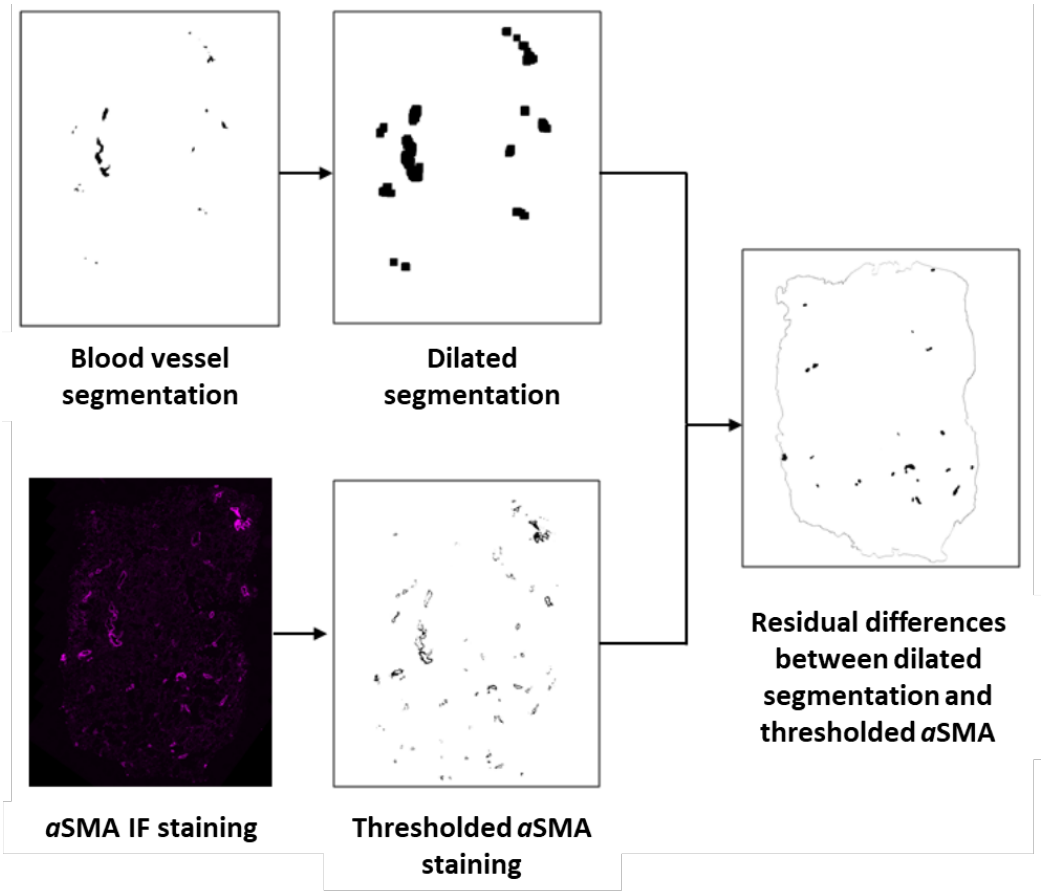

Figure 3.15: **Process of identifying blood vessels detected by *α*SMA immunoreactivity but not by segmentation.**Upper images show the process of dilating the blood vessel segmentation. Lower images show the thresholding of the *α*SMA IF staining. The resulting image shows the difference between the images by subtracting the dilated segmentation from the thresholded *α*SMA image. This preliminary image showed 22 regions of *α*SMA immunoreactivity which did not correspond to blood vessel segmentation. Figure adapted from Georgia May.

To further evaluate the segmentations generated manually and using active contour segmentation, two additional users (project students Georgia May and Maaz Masood) completed more blood vessel segmentations. They were trained with both manual and active contour segmentation and performed segmentation on identical cropped volumes of interest from the same piece of lung tissue. Spatial overlapping indices were used to measure the proportion of overlap between the segmentations (X and Y).

$$Overlap = \frac{x \cap y}{x}$$

This was used to compare manual segmentation generated between users as well as comparing manual and active contour segmentations. Furthermore a Dice similarity coefficient, defined as the ratio of intersection between segmentations, for X and Y to the mean segmentation; calculated using the equation below.

$$Dice\ coefficient = 2\ \frac{x \cap y}{x + y}$$

The results of these comparisons are reported in Table 3.1. The manual segmentation between users showed ≥90% levels of overlap and Dice coefficient, this showed consistency for manual segmentation across multiple users. The very high (98%) overlap and Dice coefficient between the manual and active contour segmentation showed that users were segmenting the same information in significantly less time, this justified the more automated approach over existing manual segmentation.

Table 3.1: **Summary of variability metrics for overlap between users completing manual segmentation and overlap between manual and semi-automated segmentation of blood vessels.**

Metric	Inter-observer variability (manual segmentation with respect to observer A)	Variability between manual and 'active contour segmentation'
Overlap	**92%**	**98%**
Dice similarity coefficient	**90%**	**85%**

Although the manual segmentation was slightly better at identifying the smallest discernible blood vessels it took significantly longer to complete than the active contour segmentation. On the small volume of interest which was segmented it took approximately 3x longer to complete segmentation manually compared to active contour segmentation. This measure was taken from a user who, although trained to use the software, did not have extensive experience with ITK-

SNAP. This decrease in segmentation time will be greater in larger tissue volumes with users that have more experience with the segmentation software.

3.5.4 IF based segmentation

Previously the histology or IF was used as a reference to infer the localisation of specific features or cell types manually within the µCT slices. However, if it was possible to directly register the IF to the µCT then the information could be directly transferred from the IF onto the µCT. Following the development of the 'automated warping script' (section 3.4.5) the output images from this were used as a basis for direct segmentation. The levels of accurate registration illustrated in section 3.4.6 were shown using the autofluorescence image and since the same transformation was applied to the IF channel it would have the same level of registration to the corresponding µCT slice.

IF imaging was chosen due to its superior contrast and specificity over tinctorial stains and IHC. This contrast allowed thresholding to be used to separate the IF staining (for this example Ck18 stained with an AlexaFluor®647 secondary in the CY5 channel- 650 nm excitation) to be isolated from the background as a binary mask. This binary mask could then be directly overlaid as a segmentation mask on the corresponding µCT slice. In order to create a segmentation mask which spanned the section volume, a new stack of images with the same dimensions as the µCT section volume were created. Each 2D IF segmentation mask was inserted in the position (z or slice number) of the corresponding µCT slice within the section volume. This segmentation volume was opened alongside and used to segment the µCT volume in segmentation software, such as Avizo. Within Avizo the segmentation could be visualised and analysed within the software in the same way as manual segmentation created in Avizo could, however this was generated in significantly less time with minimal user inputs. The primary example this was developed for was the segmentation of the airway epithelium using Ck18 IF, images of the segmentation over multiple µCT slices generated using this technique can be seen in Figure 3.16.

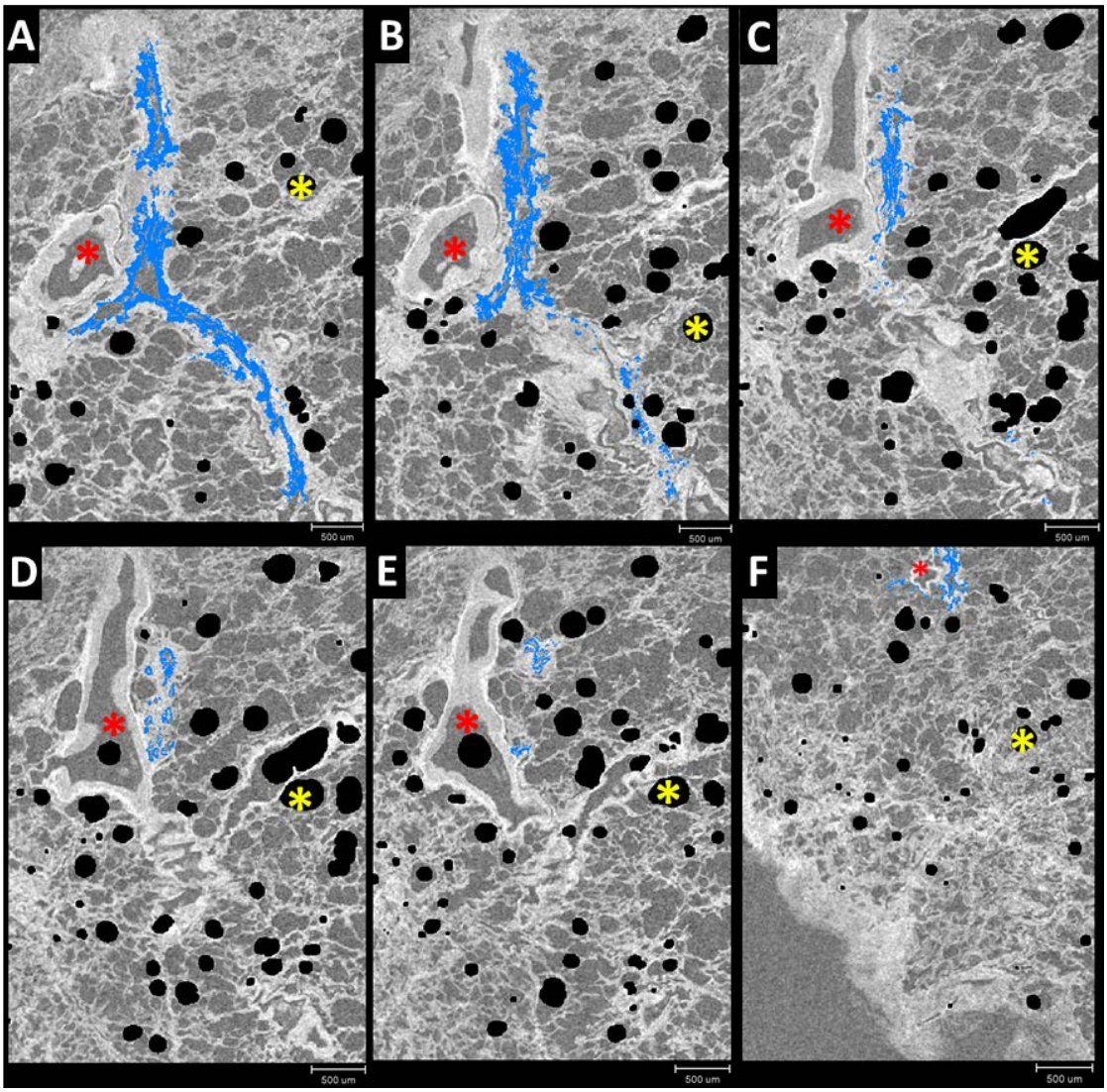

Figure 3.16: **Segmentation of Ck18 positive staining over a series of sections localised in corresponding µCT data.**(A-F): Ck18 positive staining of epithelium (blue) identified on six IF stained tissue sections were co-registered and segmented on the µCT slices down through the lung volume. Ck18 positive areas are not present in the blood vessels (red *). These panels follow the airway over a depth of approximately 400 µm (each image ~65 µm apart). Air bubbles artefacts (yellow *), scale bars = 500 µm.

3.5.5 Comparison to H&E

Similar to the blood vessels, a qualitative comparison to H&E stained sections was used to confirm that the Ck18 staining was localised in the airway epithelium. Two neighbouring sections (approximately 4 µm apart) were stained with H&E and CK18 before being imaged with bright-field microscopy and IF microscopy respectively. Visual inspection of these images in Figure 3.17 revealed that the CK18 staining was present in the same areas of dense haematoxylin staining whilst unstained areas of tissue were consistent with both techniques.

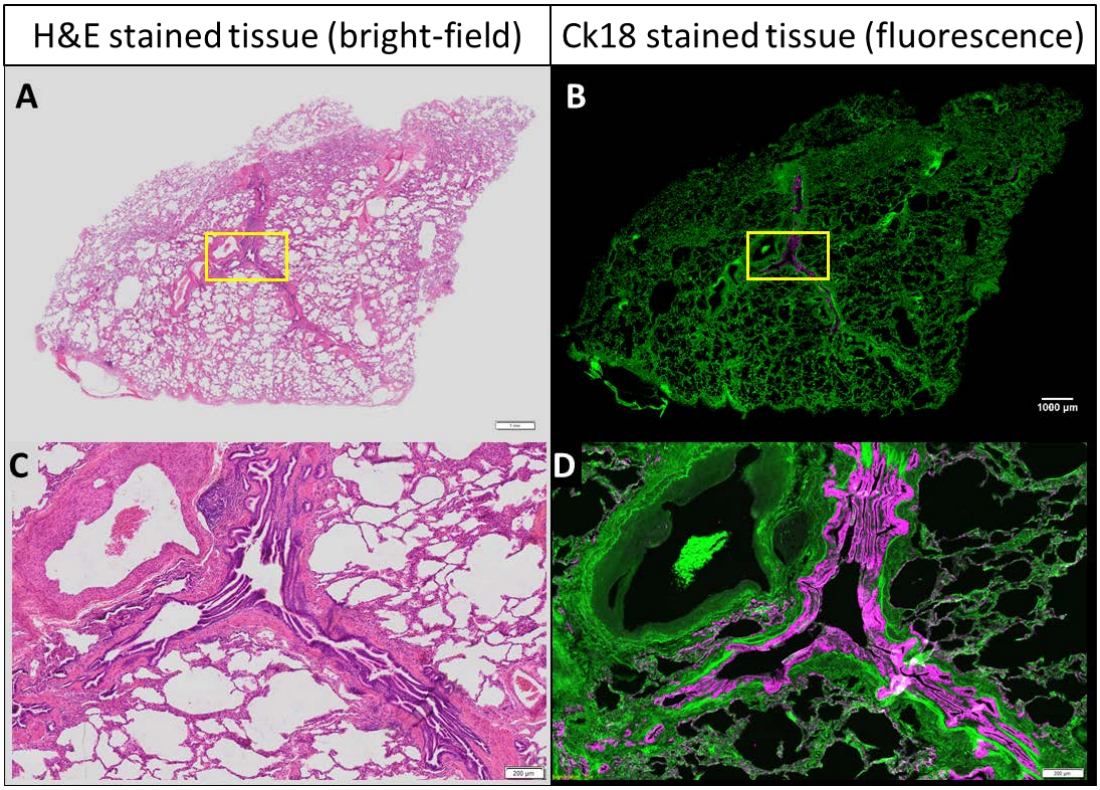

Figure 3.17: **Comparison of H&E bright-field imaging and Ck18 stained IF imaging on neighbouring lung tissue sections.** H&E images (A & C) were captured using standard bright-field imaging. Fluorescence images (B & D) were captured using two channels for autofluorescence using FITC (green) and Ck18 IF using the CY5 channel (pink). Yellow boxes show the area of the wide-field image used in the lower panels. The dense haematoxylin staining (purple) on the H&E image and the pink Ck18 IF staining were seen in the same areas of the airways as evidenced in the lower panels.

3.6 Interpolation of networks

Interpolation is a process used to fill 'gaps' present in 3D objects. Manual interpolation has been successfully used in similar studies for segmenting complex networks in µCT volumes (Robinson *et al.*, 2019). However manual interpolation is a very time consuming process which is subject to user bias and the resolution of the µCT scan. Digital interpolation tools are present in most segmentation software and can be used to automatically fill in the gaps between segmentation masks in 3D. Many different software were critically assessed for viability as an accurate interpolation tool using the IF based Ck18 segmentation. The software chosen was ITK-SNAP because of its implementation of advanced 'ND morphological contour interpolation which works over a greater distance in the volume compared to other software without losing the original data (Zukic *et al.*, 2016).

The IF segmentation data in the 3D volume spanned over 50-200 serial sections from each block, from those every 5th or 10th section was stained and imaged for IF (~20-40 µm apart). The gaps in the segmentation masks were joined in the z-direction using digital interpolation to create a fully 3D network of inferred Ck18 localisation within the section volume, as seen in Figure 3.18. Although identified as the best available technique for interpolation it still generated some interpolation errors, particularly in the collapsed airways as described below.

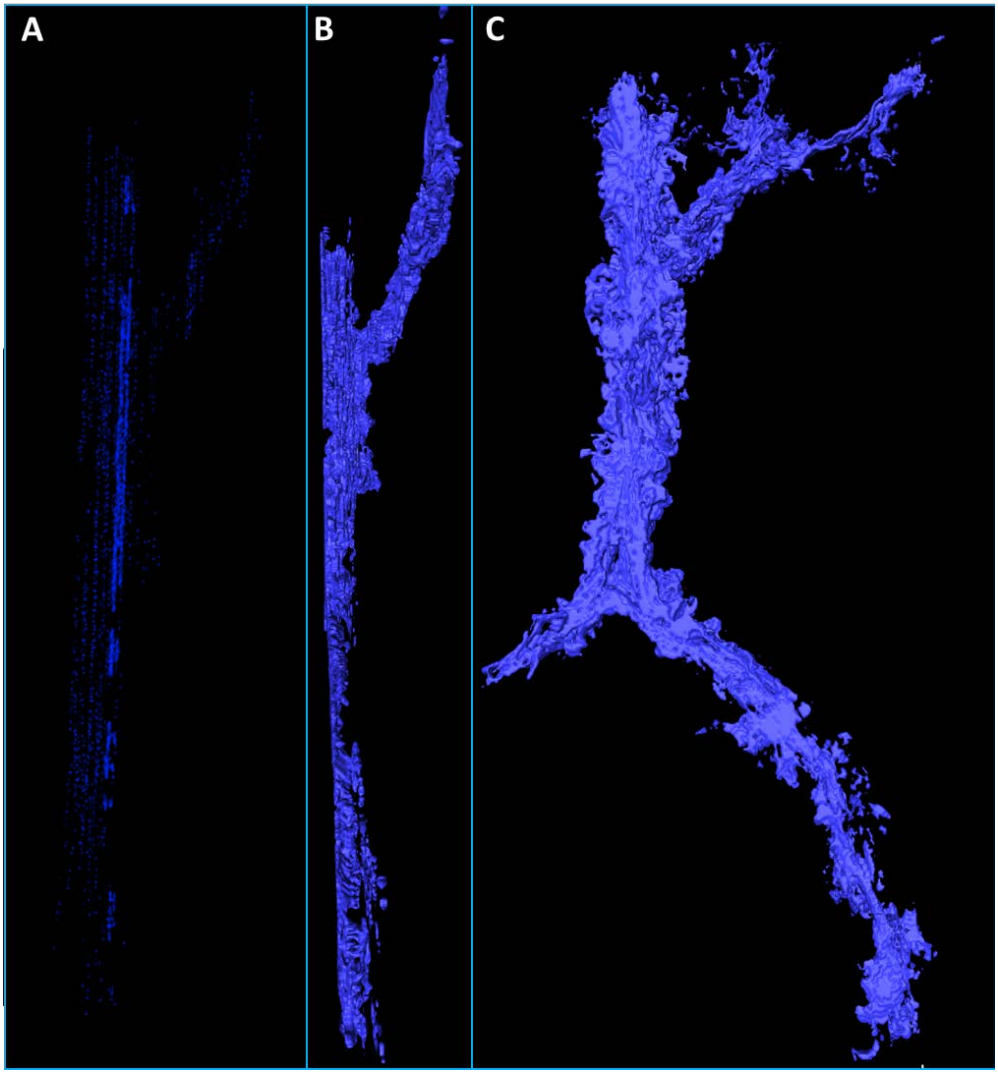

Figure 3.18: **Results of digital interpolation of Ck18 localisation visualised as a 3D surface.** The segmented Ck18 staining was complete over several tissue sections spaced throughout the section volume (A). Interpolation was successfully used the 2D segmentation to 'fill the gaps' in the volume to generate a 3D volume of inferred CK18 localisation (B&C).

3.6.1 Interpolation errors

Interpolation errors were identified as segmentation leaking into airspaces or alveoli, as seen in red in Figure 3.19. This occurred because the interpolation software packages don't take directly into account the network information provided by the µCT. To rectify this an additional step was added using a binarised µCT image. This was generated by applying an absolute threshold to the µCT volume; separating the tissue and paraffin wax (airspaces) in the µCT dataset. The interpolated segmentation mask was multiplied by this binary µCT image which removed any segmented voxels in the airspaces or lumen. The masked interpolation was exported to Avizo as a segmentation mask for the original µCT dataset.

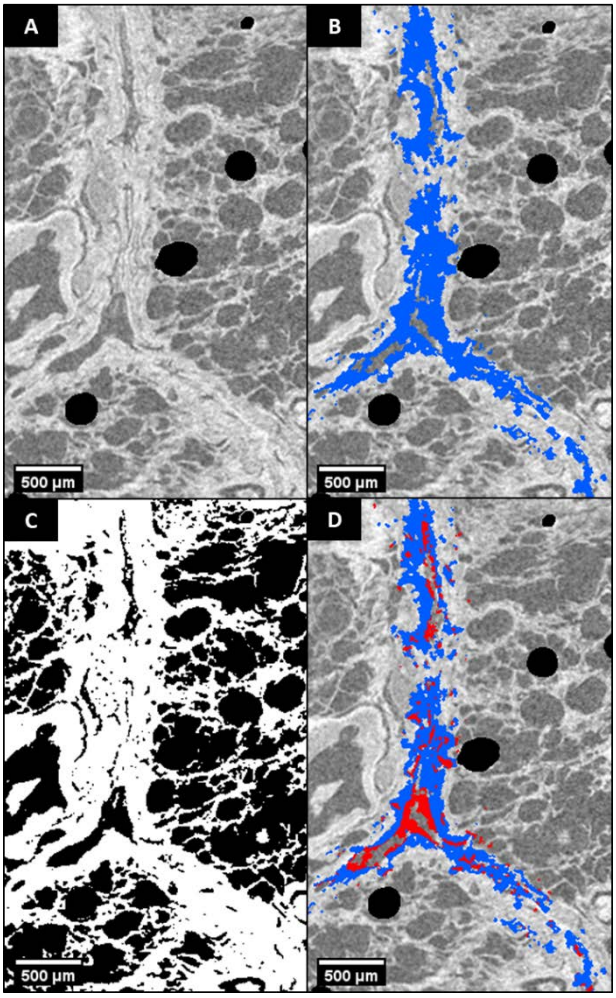

Figure 3.19: **Process of identifying and removing digital interpolation errors of the Ck18 localisation.**A: Magnified µCT slice located between two sections stained for Ck18. B: The initial interpolation of the Ck18 staining using ITK-SNAP, multiple interpolation errors are seen in the airway lumen (red areas). C: µCT after thresholding to generate a mask of the µCT slice to be used to correct the interpolation. D: The interpolation from panel b after being masked using panel C. The red areas show the interpolation errors which were removed from the interpolation data. This process was repeated on the full section volume containing inferred Ck18 localisation.

3.6.2 Comparison to manual segmentation

Like the blood vessels this more automated method of segmentation using directly registered IF images was compared to the previous manual segmentation on the cropped µCT volume. However the target of the segmentation was not the same in this instance, the manual segmentation targeted the airway lumen whereas the IF targeted the Ck18 positive airway epithelium. The epithelium is not clearly distinguishable in the µCT so direct comparison between the two was not possible. Proportion of direct overlap and Dice coefficients could not be used in this instance as unlike the blood vessels the segmentations were not overlapping. Therefore, levels of correspondence between the two sets of images were qualitatively assessed by observing whether the CK18 positive epithelium enveloped the airway lumen (as would be expected biologically). Figure 3.20 shows combined images of the manual (purple) and IF segmentation (blue) which illustrates the close association between segmentation methods. This also showed changes in the epithelial layer in different areas of the airways as there are areas of manual lumen segmentation, still part of the 3D network, which did not contain Ck18 positive staining. The manual lumen is mostly encapsulated by the epithelium, as would be expected. This also shows the masking of the interpolation was successful as the manual segmentation of the lumen is visible within the interpolated cytokeratin segmentation. The areas where the manual segmentation is more visible are either outside the section volume or where the airways transitions to alveoli, which does not contain Ck18.

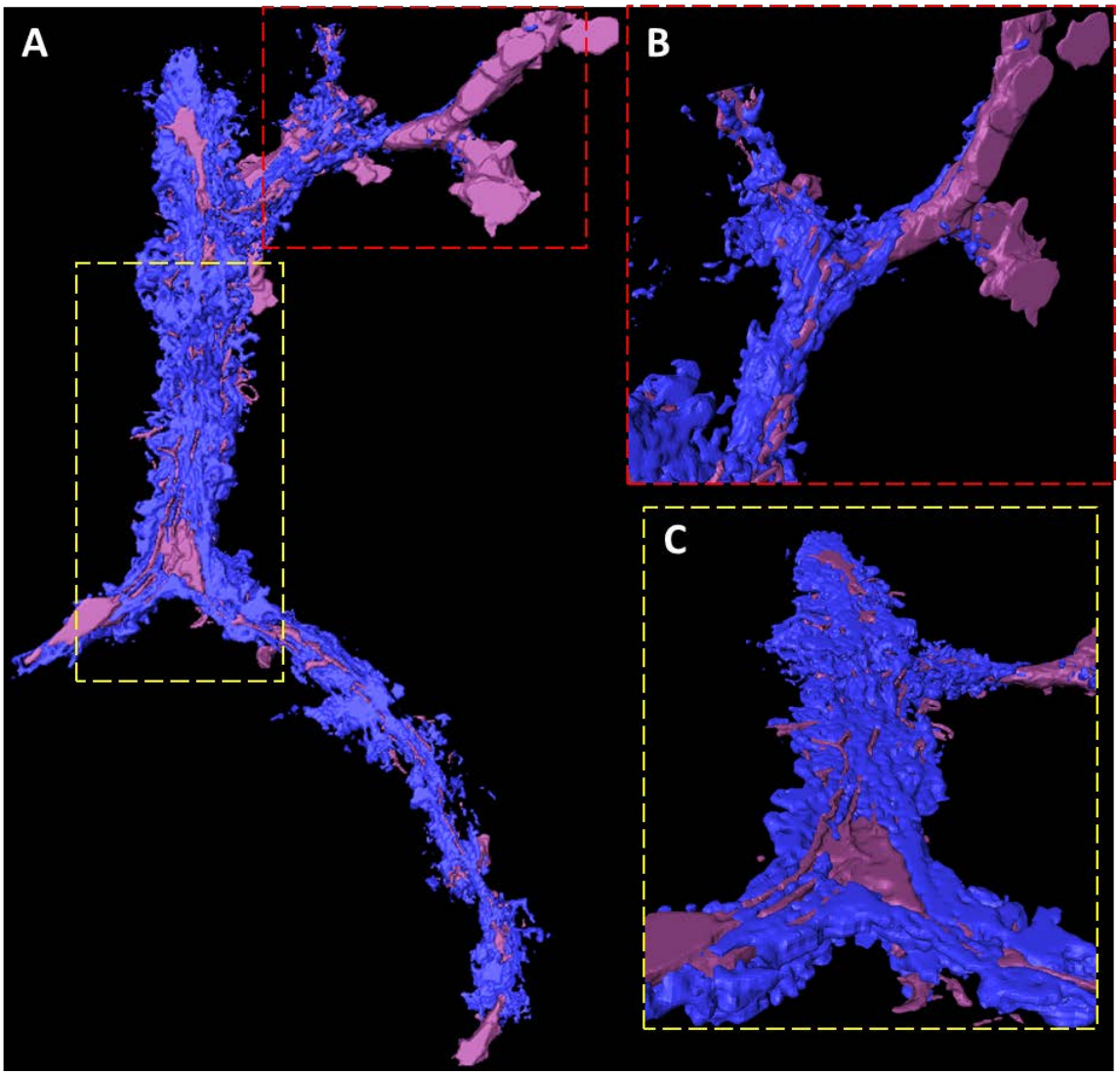

Figure 3.20: **Combined 3D visualisation of the manual airway lumen segmentation (purple) and the interpolated Ck18 localisation (blue) from IF-based segmentation.**A: The Ck18 localisation encapsulates the lumen segmentation showing that both are located in an airway. The coloured boxes show the areas which the magnified and tilted images (B & C) were taken from. The areas of lumen segmentation without CK18 show areas of the airway which do not contain Ck18 as it transitions towards the alveoli.

3.7 Utilising nuclei staining for analysis

Part of the method development for the results in chapter 5 used individual cellular markers and part of the analysis for this involved cell counts. Current methods for cell counting are very manual or rely on specialist equipment for automated cell counting using specific staining protocols (Cadena-Herrera *et al.*, 2015). Part of this development towards automation explored ways of counting the individual cells on a section automatically. As part of the IF staining methodology, as described in section 2.6, a DAPI nuclei counterstain was applied to the tissue.

This was imaged using the fluorescence slide scanner alongside the other two fluorescence channels. DAPI staining was potent enough that the signal expressed from the stained nuclei at 372 nm excitation was far greater than background autofluorescence. Figure 3.21 shows an example of DAPI staining on FFPE lung tissue section, here each individual stained spot represents a cell nucleus. This proved useful when combined with the immunofluorescence staining to confirm that cellular material was being bound to by the primary antibody. As this was imaged alongside the other channels the DAPI channel images were also warped alongside the FITC autofluorescence and the IF channel. Therefore each registered fluorescence image contained a registered DAPI nuclei stained image which correlated to the µCT. This proved useful for validation of individual cellular staining using the AA1 (mast cell) and CD68 (macrophage) primary antibodies.

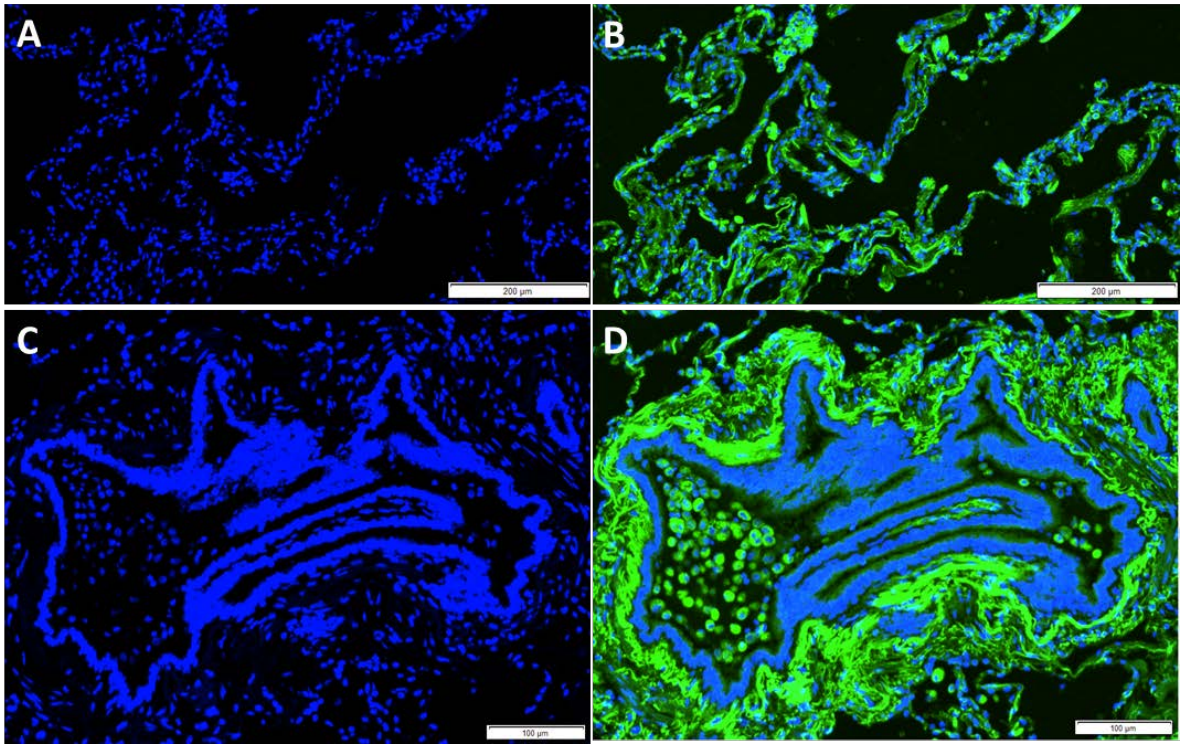

Figure 3.21: **Exemplar fluorescent DAPI staining of cell nuclei on fixed human lung tissue.**The left panels (A & C) show DAPI nuclei staining (blue) visualised using the DAPI channel (372 nm excitation). The right panels (B & D) show the DAPI staining overlaid onto tissue autofluorescence (green) captured using the FITC channel (490 nm excitation). Images A & B show the even distribution of cell nuclei in the lung parenchyma compared to images C & D which show dense nuclei localised in the airway epithelium, as well as infiltrating immune cells within the airway lumen.

3.7.1 Masking cellular staining for counts

DAPI was used to assist in generating consistent cell counts in each of the individual cell staining images as shown in chapter 5. The contrast of the DAPI channel enabled direct thresholding of the DAPI fluorescence image to generate binary images of the nuclei staining. This was used to mask the corresponding IF channel image (CD68 or AA1 staining) by multiplying the cellular stained image by the binary image. The result was that any overlap, this being the nucleus of the stained cell, would be multiplied by 1 and remain unchanged whereas the rest of the image would be multiplied by 0 and so removed from the resultant masked image. This was particularly useful in separating clusters of cells (particularly macrophages) into individual entities so that they could be counted as separate cells. Figure 3.22 shows the results of this masking process on a tight cluster of CD68 positively stained cells using DAPI to separate them. The binarised results of the cellular masking were automatically counted using the 'analyze particles' plugin in Fiji, this generated instantaneous counts of the cell nuclei on each section.

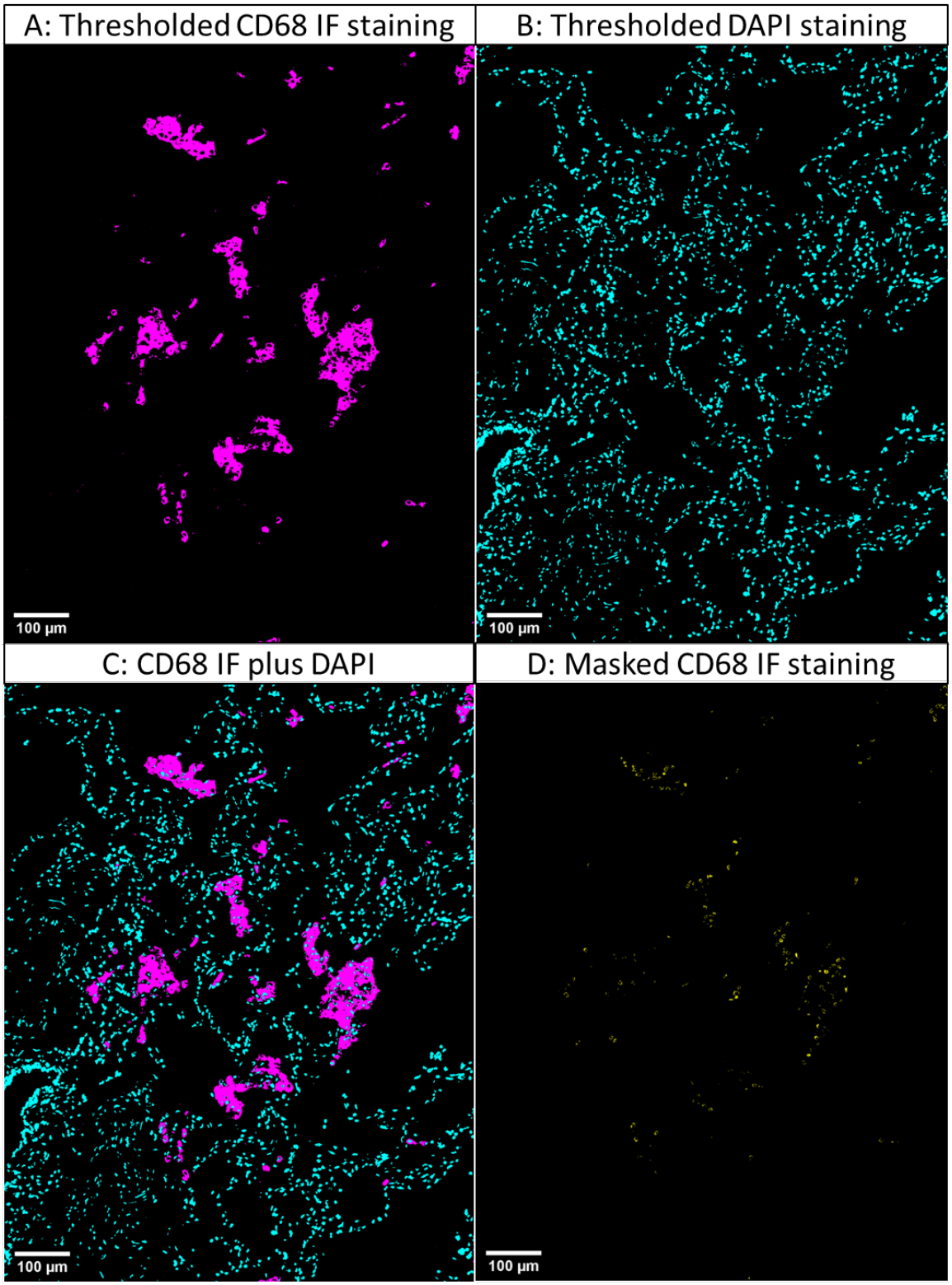

Figure 3.22: **Use of DAPI staining of cell nuclei to mask and separate CD68 positive cellular staining.** To separate the CD68 (macrophage) cell nuclei the thresholded CD68 (A) and DAPI (B) images were multiplied together (C). This removed all non-CD68 nuclei from the image. The resulting image (D) of CD68 positive cell nuclei could then be used for automated cell counts due to the separation of the clustered cells.

3.8 Visualisation of segmentation

The segmentation data was visualised in Avizo, an exemplar figure of the visualisation can be seen in Figure 3.23, the 3D µCT was shown using the volume rendering module in Avizo. The settings were tuned to remove the wax but keep the tissue structure as semi-transparent in the 3D visualisation. The large segmented features (blood vessels and Ck18) were visualised by generating a 3D surface from the segmentation data generated with minimal smoothing (setting at 1.5). The cellular segmentation masks were dilated by 3 points in a sphere shape to ease visualisation, these dilations were not used in analysis. Each surface could then be visualised independently or together with the µCT volume rendering. Videos were also generated using the animation maker in Avizo, as seen in the appendix A.7.2 and A.7.3 videos to illustrate how the 2D data was built together in 3D. Rotations of the volumes and networks assist in visualising the 3D nature of the data which is difficult to interpret on a 2D plane.

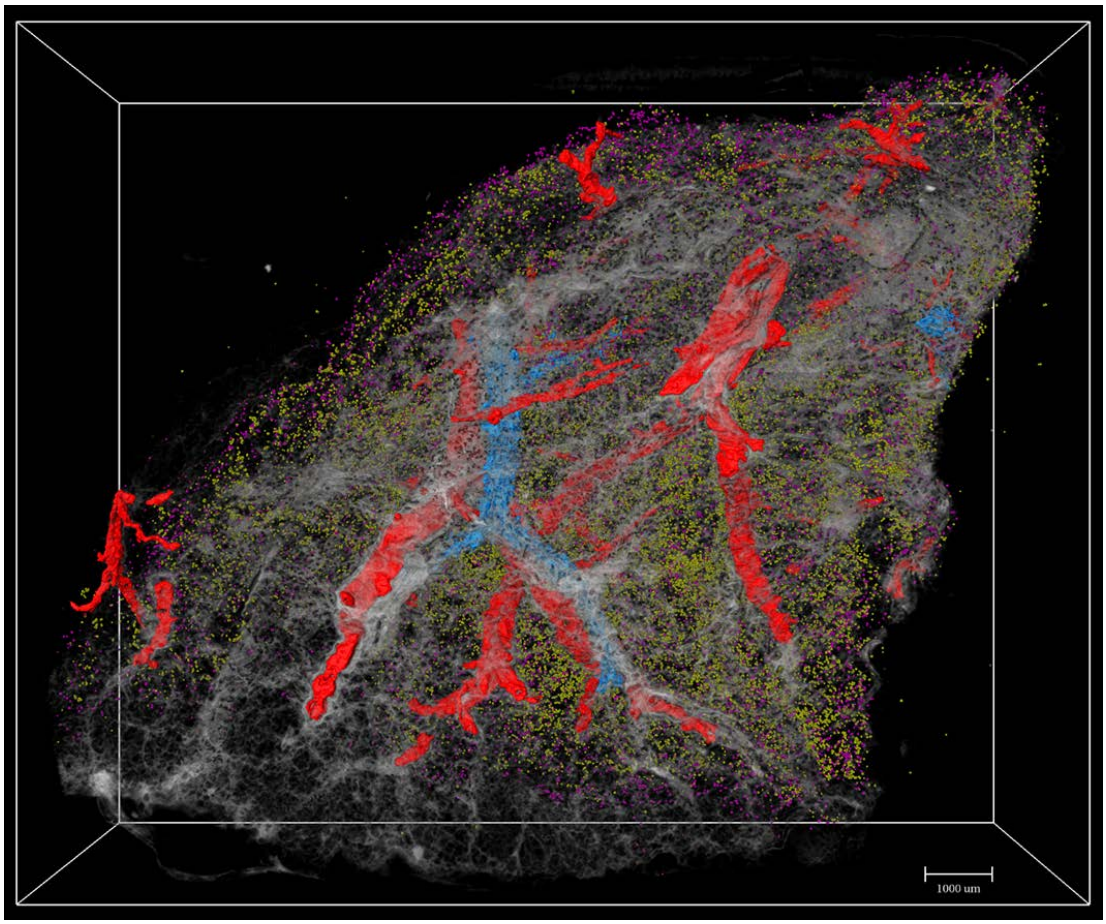

Figure 3.23: **Volume rendering of the 3D µCT data containing the segmentation results of the blood vessels and IF staining.** The µCT data is semi-transparent in order to visualise the segmentation contained within. Within the µCT are the segmented blood vessels (red), interpolated Ck18 (blue), the AA1 staining (3 planar sections, pink) and the CD68 staining (9 planar sections, yellow).

3.9 Calculating tissue volumes

The volume of soft tissue in each FFPE sample was calculated using the µCT datasets for each piece of tissue, the soft tissue volume was defined as the tissue volume excluding the airspaces (alveoli) and lumens of airways and blood vessels. The µCT volumes were thresholded to remove the paraffin wax, found both in the background and in the airspaces, from the tissue. A median filter (size: 2 voxel) was applied to remove outliers present in the background whilst maintaining the tissue structure, as seen in Figure 3.24. The tissue volume was calculated using the Voxel Counter plugin in Fiji. This counted the number of thresholded voxels in the stack and if calibrated also provided the volume in μm^3, which was converted to mm^3 for ease of reporting. The Voxel Counter plugin was also used to calculate the volume of the blood vessel segmentation in the same µCT datasets.

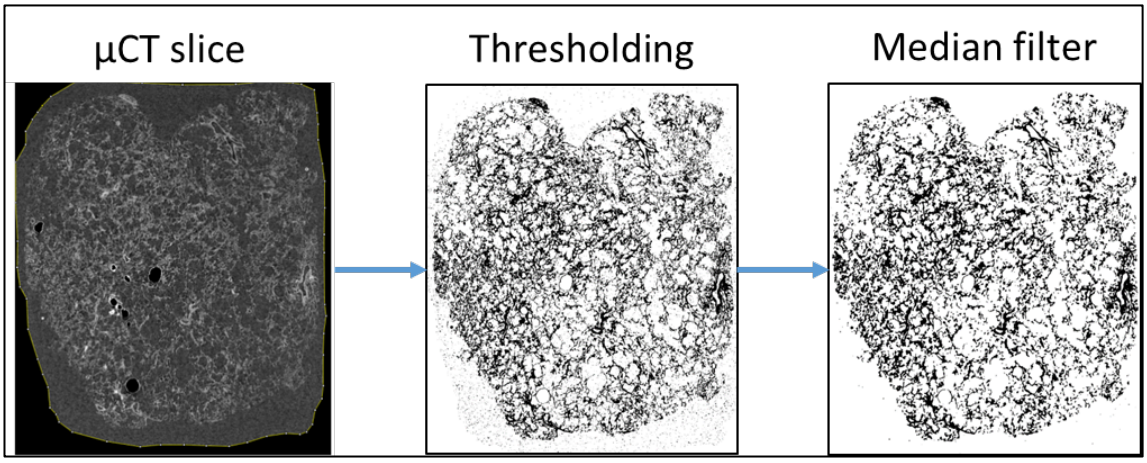

Figure 3.24: **Process of generating tissue volume estimation of µCT volumes.** The µCT slice is first thresholded selecting the tissue. This image contains background artefacts which were also thresholded, to rectify this a median filter (size: 2 voxel) was applied. The filtered image was used to estimate the tissue volume using the voxel counter plugin in Fiji. Figure adapted from Georgia May.

3.10 Distance maps

Distance maps, also known as distance transforms were used as a novel means, on µCT soft tissue images, of relating the distributions of the segmentations to other segmented features in the same µCT lung dataset. The results of these can be found in chapters 4 and 5. Distance maps were created from binary segmentation datasets (e.g. the segmented blood vessel network) in Avizo. The settings were set for outside distance maps using true Euclid distance metrics. The resulting distance map, as seen in Figure 3.25, provides a gradient of voxels with different values visualised with a rainbow colour map. These represent the smallest distance from the boundary of any segmented object in the image. The difference between 2D and 3D distance maps can be seen in Figure 3.25, with more area of light blue showing on the 3D distance map due to the close proximity of a blood vessel outside the visible 2D plane. The distance map dataset was used to calculate the relative 3D distance a segmented feature/cell was from the original segmentation (e.g. blood vessel). To perform this in Avizo a binary mask (segmented voxel value =1) from the same dataset is multiplied by the distance map. This changes the voxel value of the segmentation relative to the distance from another segmentation and was plotted as a distance in µm using the Histogram tool in Avizo.

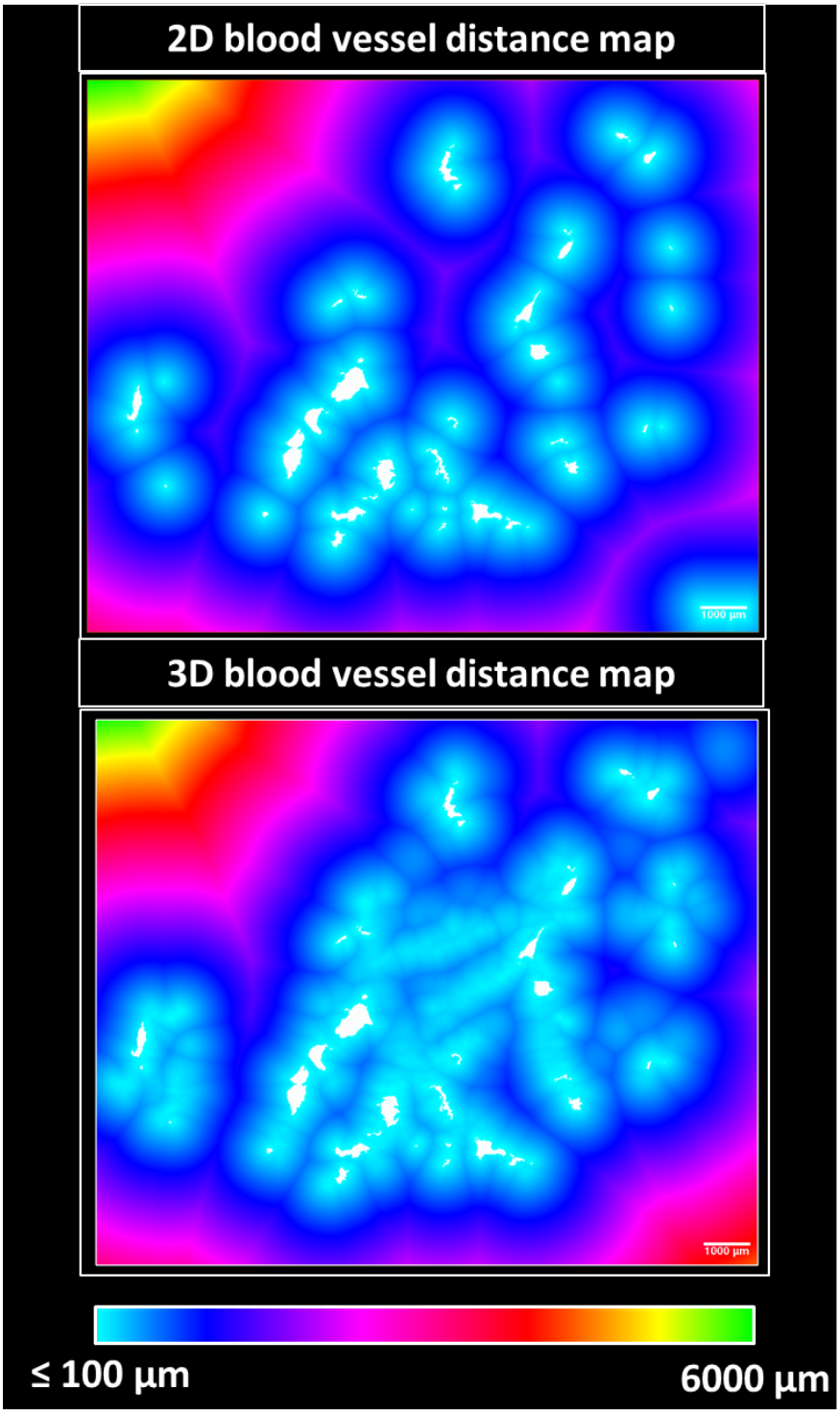

Figure 3.25: **Visualisation of the gradient of voxel values in a distance map from a segmented blood vessel.**Both images are from the same 2D slice of blood vessel segmentation (shown in white). The distance map from the segmentation was generated in 2D. The lower image distance map was generated from the 3D blood vessel segmentation. This resulted in more areas of the lower image showing closer to a blood vessel (cyan/blue) compared to the upper image. This highlights the difference between using 2D and 3D data for network analysis using distance maps.

3.11 Discussion

Using µCT images of soft tissue has the potential to transform what can be visualised in 3D at the micrometre resolution, just as patient CT provides substantially more 3D information over traditional X-rays at the millimetre resolution. Proof of concept was demonstrated by Scott and colleagues (Scott *et al.*, 2015), which was further developed by Katsamenis and colleagues (Katsamenis *et al.*, 2019); which included some preliminary work produced from this project. The optimised µCT scan setup (removing the plastic cassette), imaging parameters (low energy) and image processing (re-slicing and bubble removal) of FFPE soft tissue were all essential for use in correlative projects using µCT and immuno-histological imaging (Robinson *et al.*, 2019). The µCT was successfully resampled to the cut histology plane in previous works and in this project. This required near-perfect plane definition so that features could be matched in corresponding histology and µCT images. Without this step, which was completed manually by eye, registration of the two different imaging modalities would not be possible. This ensured that the µCT slices and cut histology sections could be matched on a slice for slice basis in the *xz* and *yz* planes. However, this did not account for differences in the *xy* plane caused by orientation of the tissue on the slide or tissue deformation from sectioning prior to being imaged. These previous studies did not directly address this instead, they used exceedingly time consuming and manual techniques to interpret and segment the data from the immuno-histological imaging into the 3D µCT. Other techniques of correlative plane alignment for registration have been used for other imaging types, such as those used in CLEM. Alignment in CLEM relies on additional fiducial markers such as fluorescence beads with metallic cores which can be seen in both the fluorescence and electron microscopy images (Kukulski *et al.*, 2012; Schellenberger *et al.*, 2014). These are used as reference points to semi-automatically align the planes for registration in specially tailored software for correlative imaging such as EC-CLEM (Paul-Gilloteaux *et al.*, 2017). Although this was not applicable for the FFPE tissue used in this project, it requires further investigation for use with µCT and other sample types or imaging modalities. This could prove useful for future 3D-3D correlative imaging studies utilising 3D fluorescence imaging (e.g. from light-sheet microscopy) with µCT to align the volumes for registration of 3D features in both datasets.

This chapter built upon previous work to demonstrate the enhanced utility of µCT imaging of FFPE lung samples facilitated by more automated co-registration of imaging modalities, thus leading to faster segmentation methods. The novel utilisation of tissue autofluorescence, often discarded or removed from fluorescence imaging (Baschong *et al.*, 2001; Pang *et al.*, 2013), provided comparable visualisation of tissue microstructure to µCT slices and was used as a base for automated co-registration with µCT datasets. The key structural features of human lung tissue

samples were revealed in both imaging modalities including blood vessels, airways and alveolar structures. However, µCT provided 3D information with isotropic voxel sizes ≤10 µm and since µCT image acquisition is non-destructive datasets are free of the sectioning artefacts and distortions often seen with traditional histology (McInnes, 2005).

µCT data correlated with immuno-histological images, as used in the majority of previous and current studies, have predominately used bright-field imaging of tinctorial or IHC stained sections as the secondary imaging modality (Tanabe *et al.*, 2020). Instead, in this study fluorescence imaging with immunostaining was chosen as a correlative imaging modality for tissue structure to complement µCT. The excellent image contrast between the IF signal and the background, facilitated automated localisation and segmentation of cellular staining, compared to bright-field techniques (Sood *et al.*, 2020). To achieve the best IF image contrast and signal to noise ratio the choice of the optimum fluorochrome label for the secondary antibody was informed by the results of a lambda scan of the tissue of interest. However, this selection was limited by the available wavelengths of the imaging equipment and also the peaks of autofluorescence which could not be quenched due to the need for strong autofluorescence signal for registration.

Sectioning artefacts present in the tissue section prevented direct co-registration of IF and µCT images and so elastic warping techniques were applied to overcome this. Manual methods of landmark based registration and warping exist already (Museyko *et al.*, 2015; Bogovic *et al.*, 2016). However, they are all extremely time consuming, often requiring hundreds of manually placed points per pair of images to perform sufficient image warping. Furthermore, this time is increased if multiple 2D tissue sections require registration to the 3D µCT data, as was the case for this project. These manual registrations can take anywhere between 20-60 minutes per pair of images for an expert to complete, depending on tissue section size and image quality (contrast, resolution etc.). Other 2D-3D registration techniques between µCT, histology or electron microscopy also involve extremely time consuming manual techniques (Museyko *et al.*, 2015; Morales *et al.*, 2016; López *et al.*, 2017), which in many cases did not result in the close to one to one registration reported in this chapter.

Previous registration methods and algorithms often require the two images to have the same pixel size and image dimensions or the presence of additional registration markers in the dataset (Paul-Gilloteaux *et al.*, 2017). The native voxel size of the µCT was between 5-10 µm whereas the IF images acquired using as 10x objective had a pixel size of 0.645 µm. To trial and develop these registration techniques one of the images needed to be scaled to match the size of the other. The decision to downscale the histology/IF to the µCT resolution was informed by the practicality of working on large file sizes which were easier to process and enabled the warping script to work

quickly with minimal chances of overloading the memory of the PC it is run on. Also to overcome sectioning artefacts in the IF or histology images, which were not present in the µCT (Katsamenis *et al.*, 2019), the µCT images would always be used as the fixed reference image. Although detailed cellular staining will be lost during the downscaling process, the localisation of staining could still be visualised at the µCT resolution. The results of the manual registration and warping of the IF images using BigWarp and subsequent segmentation showed that the labelled areas could still be clearly identified in the downscaled images. However, it is worth noting for future studies the size of the cell or sub-cellular structure being identified by IF as it could be lost in the downscaling step, if it is smaller than the resolution of the µCT scan.

To more rapidly co-register the images and overcome the issue of sectioning artefacts, SIFT feature correspondence (Lowe, 1999; Cheung and Hamarneh, 2009) was utilised to significantly speed up overall image processing time. This required input images to have high levels of contrast between the tissue and background in both the µCT and fluorescence images. As mentioned previously both of these imaging modalities were selected and/or optimised for image contrast and so proved ideal for feature extraction using SIFT correspondences. Identifying multiple tissue features of different sizes, created 'hierarchical SIFT correspondences'. This enabled warping which accounted for features of all different sizes present in the tissue, as is the case in heterogeneous tissue like the lung. This would also more closely match the results of a user who would manually identify features of different sizes in the tissue by eye. Also, this addressed another issue with manual registration which was consistency of the warping transformations. As a manual process each user or even the same user at different times would not be able to replicate the exact landmark positions on the images, similar to the inter-observer variabilities seen in digital pathology which can be addressed with machine learning (Fitzgerald *et al.*, 2019), resulting in different warping transformation being applied. Removing this 'user bias' by using SIFT should also ensure a more consistent approach. SIFT and other feature extraction algorithms have been successfully implemented in histopathological tissues in many studies (Mhala and Bhandari, 2016; Öztürk and Bayram, 2018). Including being used as the basis for neural networks for identifying features on clinical images and showing feature extraction usefulness on low resolution images such as clinical X-rays and mammograms (Cui *et al.*, 2017; Rao *et al.*, 2020).

Using the 'automated warping script', which implemented SIFT and BigWarp, each pair of images were registered and warped on average in less than 2 minutes while the accuracy of the automated registration matched or exceeded the existing manual techniques. Crucially, the registration process worked to remove the majority of sectioning artefacts despite some substantial mismatches due to tissue distortion in the paraffin wax sections (Zhou *et al.*, 2020). Visual inspection of the images showed that the majority of the inaccurate registration came from

the tissue periphery, especially along the cut edge of the tissue, where many complex distortions can occur. Future studies would need to be aware of this limitation if the area of interest in the tissue is within the tissue periphery or near the cut surface. However, if the area if interest is in the central area of the tissue the accuracy of the registration will be greater compared to the values of the whole tissue, used in this study, allowing for greater confidence in the resulting registration. Using a batch script also allowed whole stacks of fluorescence sections to be warped automatically without user intervention, further reducing the user effort required in co-registration.

Following direct registration using the 'automated warping script' blood vessels were identified from H&E and autofluorescence images, which assisted with identification of blood vessels in the corresponding µCT planes. Identification and segmentation of tissue vasculature has been achieved in many studies using µCT, particularly in high contrast samples such as bone (Zagorchev *et al.*, 2010). 'Active contour segmentation' has previously been used in studies to segment the vasculature of clinical images (CT, MRI etc.) in multiple tissue types (Shang *et al.*, 2010; Zeng *et al.*, 2018). To decrease segmentation times of the complex network of 3D blood vessels in µCT the 'active contour segmentation' tools in ITK-SNAP were utilised (Yushkevich *et al.*, 2006). Manually placed seed points determined from the localisation of blood vessel lumens from 2D histology images were used to initiate the segmentation. This confirmed the broad structural correspondence of features in the H&E images and µCT volumes as previously described (Museyko *et al.*, 2015; Yan *et al.*, 2017; Katsamenis *et al.*, 2019). Once a user was familiar with the µCT dataset it was possible to identify small blood vessels down to diameters of 25 µm allowing segmentation outside the section volume.

Previous identification and segmentation of specific 3D networks in µCT datasets have relied on observers identifying and outlining the network components (Robinson *et al.*, 2019) over the hundreds of individual µCT image planes in the dataset. Previous work which has used automatic network segmentation used samples with very high image contrast such as bone (Zhao *et al.*, 2015) or implemented complicated algorithms which are not widely applicable (Chicherova *et al.*, 2018). Using seed-point derived active contour segmentation allowed the full blood vessel network, down to approximately 25 µm diameter, to be segmented in a fraction of the time it would have taken manually. While manual identification of the blood vessels is still necessary to provide seed points and monitor the progress of segmentation, it is still significantly faster to complete than fully manual techniques. Further development of machine learning using this blood vessel segmentation for training purposes could be utilised to further reduce the segmentation times and manual inputs required in the future, as is currently being developed in other imaging modalities (Mookiah *et al.*, 2020).

However, the 'active contour segmentation' approach used for blood vessel lumen could not be used to segment the airway lumen. This was because the airways did not have the same image contrast (grey values often <15000 which is close to paraffin wax value) as the blood vessels between the wall and lumen and so could not be separated by thresholding as effectively (Wollatz *et al.*, 2017). The epithelium and basement membrane of the airways are visibly much thinner and contain less X-ray contrast to the surrounding airspaces than the blood vessel walls, which made thresholding for boundary definition difficult. Attempts to segment the incomplete thresholding of boundaries caused 'leaking' of segmentation out of the airway into the surrounding airspaces. Combined with the collapsed nature of the airways and the difficulty in identification without histology or IF a different method for localisation and segmentation was required.

Following co-registration, using the 'automated warping script', segmentation of IF-based cellular localisation was possible. Since the autofluorescence and IF channels were captured on the same section, they were consequently subject to the same deformations from sectioning. Therefore, registration and the warping transformation calculated using the autofluorescence image was applied to the IF image too. Ck18 positive IF staining could be easily thresholded to generate a segmentation mask, which could be directly overlaid onto the µCT plane to highlight the areas of Ck18 localisation without the need for manual segmentation.

As mentioned previously the resolution of the IF imaging was much higher than the µCT and therefore allows not only for registration, but for more detailed examination of the Ck18 positive staining, within the context of the 3D µCT volume. Using the structural context from co-aligned autofluorescence, the IF on tissue mapped accurately to the µCT volumes. Multiple stained sections at different levels in the section volume were registered to the µCT data to provide the foundations of a 3D dataset of immuno-localised features, which has been done previously using manual registration methods (Robinson *et al.*, 2019). Digital interpolation of the Ck18 localisation was used to build 3D segmentation with minimal user inputs. Interpolation of the Ck18 staining was constrained by the tissue information in the µCT to provide an accurate segmentation mask of the slices which did not have a matching IF section registered to them. Although not as accurate as registering every serial section, interpolation meant that less tissue sections needed to be stained with the Ck18 primary antibody. This enabled further work using the same tissue with different primary antibodies on the unstained sections to investigate different cell types. The ability to place specific immunoreactivity accurately within the µCT volume applies for any immuno-reactive marker as the registration used the tissue structures in the autofluorescence and not the IF channel. This was used to add to the understanding of the distributions of different cell types in 3D tissues. Future studies interested in a single feature or cell type could be used to further validate the interpolation by building a 3D distribution from serially stained tissue

sections. This could then also be registered to the µCT dataset for validation and compared to the work which has been done in 3D digital pathology previously (Tward *et al.*, 2020).

Building on this additional primary antibodies were used for IF staining of the same tissue volume, using the unstained sections between the Ck18 stained sections, but had the Ck18 localisation 'inferred' by the digital interpolation. Further details of the AA1 (mast cell) and CD68 (macrophage) staining can be found in chapter 5. However, methods for automating cell counts were successfully implemented at this development stage of the project. Previous studies have automated nuclei identification in images, however these often require extensive pre-processing of bright-field images (Lee and Kim, 2016; Xing and Yang, 2016) or more recently rely on neural networks (Naylor *et al.*, 2018). In this project the DAPI nuclei counterstain was used to identify cell nuclei on every imaged IF stained section. The 'automated warping script' was used to warp the DAPI channel, similarly to the IF channel the structural features from the autofluorescence were used to calculate the warping deformations applied to the DAPI image. This meant that the DAPI staining overlapped with the cellular IF staining in both the original images and the warped images. Due to the high image contrast in both the IF and the DAPI images it was easy to threshold both of them as binary masks separated from background fluorescence. The binary masks of the staining could be used for segmentation and analysis using the multiple analysis plugins in Fiji. The 'analyze particles' was successfully used to count the number of individual binary objects in the image and provide the size of each object. The main issue for counting individual cells, as was the case for AA1 and CD68, was that cells which were in direct contact or clustering were being counted as a single object (Blom *et al.*, 2017). DAPI on the other hand could count the individual cell nuclei of every nucleated cell in the tissue section visualised at the resolution of the 10x objective used. For greater accuracy in the separation of smaller cells and nuclei a higher magnification objective would be required. Using one image to filter the other by masking the cellular staining with the DAPI staining enabled better separation of cells whilst maintaining the specificity of the IF staining. These individual stained cell nuclei were automatically counted for the entire section image. This was far quicker than existing manual counting techniques, typically used on smaller cell cultures or small regions of interest on tissue sections, with less user variability and no arbitrary upper limit of counting (Piccinini *et al.*, 2017; Mohamed and Sayed, 2020). A potential issue with this technique is that some of the cells being counted would have a thickness greater than the section thickness of 4 µm and so would risk being counted twice on serially stained sections. By masking out cells without nuclei staining this worked to produce a more consistent counting measure over the tissue volume. No serial staining of neighbouring sections using the same antibody was completed with individual cellular stains being located approximately 40 µm apart. This removed the possibility of any double counting of

the cellular staining but remains a point for investigation in the future. This did mean that the measures reported could only be presented as cells per area (i.e. a relative 2D measure) and could not be used for cells per volume measurements as has been done in rigorous cellular studies (Weibel, 2015). This would require more IF images and potential modelling of the 2D patterns of the identified cells to build a 3D model of cell localisation within the tissue volume.

The 3D analysis of the µCT lung volume data was developed so that the soft tissue volumes of each FFPE block could be quickly approximated. The high contrast µCT imaging of soft tissue permitted binarisation of the data via thresholding, which was successful on the 2D µCT slices for validation of the warping and the refinement of the interpolation. This was expanded to the whole volume to generate a 3D binary mask of the soft tissue separated from the background paraffin wax. However it was sometimes necessary to make sub-volumes of the µCT stack due to differences in the grey values caused by edge artefacts in the µCT scan. This was a simple task as the sub-volumes could be combined afterwards, but could add additional processing time prior to analysis. The binarised volume was successfully used to produce and approximate the tissue volume in mm^3, this measure was used for comparing total tissue volumes of the samples and to normalise the data generated in chapters 4 and 5. Distance maps provided relative 3D distribution of segmented objects in the µCT volume. Distance maps in a biological setting have commonly been used as part of processed for cell counting and cell cluster separation, primarily investigating the distance relationship between the same cell types (Fatonah *et al.*, 2018; Kim *et al.*, 2020). In this project distance maps were used to compare the distribution of structures and cells in 3D. The 3D networks distance to the soft tissue volume and also the relative distribution of the cellular staining in relation to the 3D networks was investigated and results reported in chapters 4 and 5.

Overall the cumulative improvements in the time taken to generate the data for the localisation of blood vessels and immuno-histological features in the µCT lung volumes will enable larger studies involving large 3D datasets. By streamlining the whole process into a workflow with minimal user input it potentially opens up the work to a wider community of users who don't need to learn the process involved in the scripted registration of the images. As well as being utilised for clinically grouped samples (chapters 4 and 5 in this report), future work could build on this to evaluate larger populations of tissue samples. This would generate more statistically robust results to assess any potential changes between populations in relation to the microscopic 3D features and cells types.

3.12 Conclusions

In conclusion, this chapter presented the development of a methodology workflow, shown in Figure 3.26, for correlative imaging of FFPE human lung tissue samples using µCT and IF. This workflow was used to semi-automatically locate and identify blood vessels and immuno-labelled cell types without the need for manual segmentation. The cumulative time improvements from the workflow decreased the amount of time required to image, process the images and generate segmentation results from several months to less than 14 days per sample. This enabled a higher-throughput of data generation utilising more automated techniques for use in chapters 4 and 5 as well as potential future studies with even more samples. This combined with tissue volumes, cell counts and distance maps will provide an in depth analysis of features identified by IF within a 3D soft tissue volume provided by µCT.

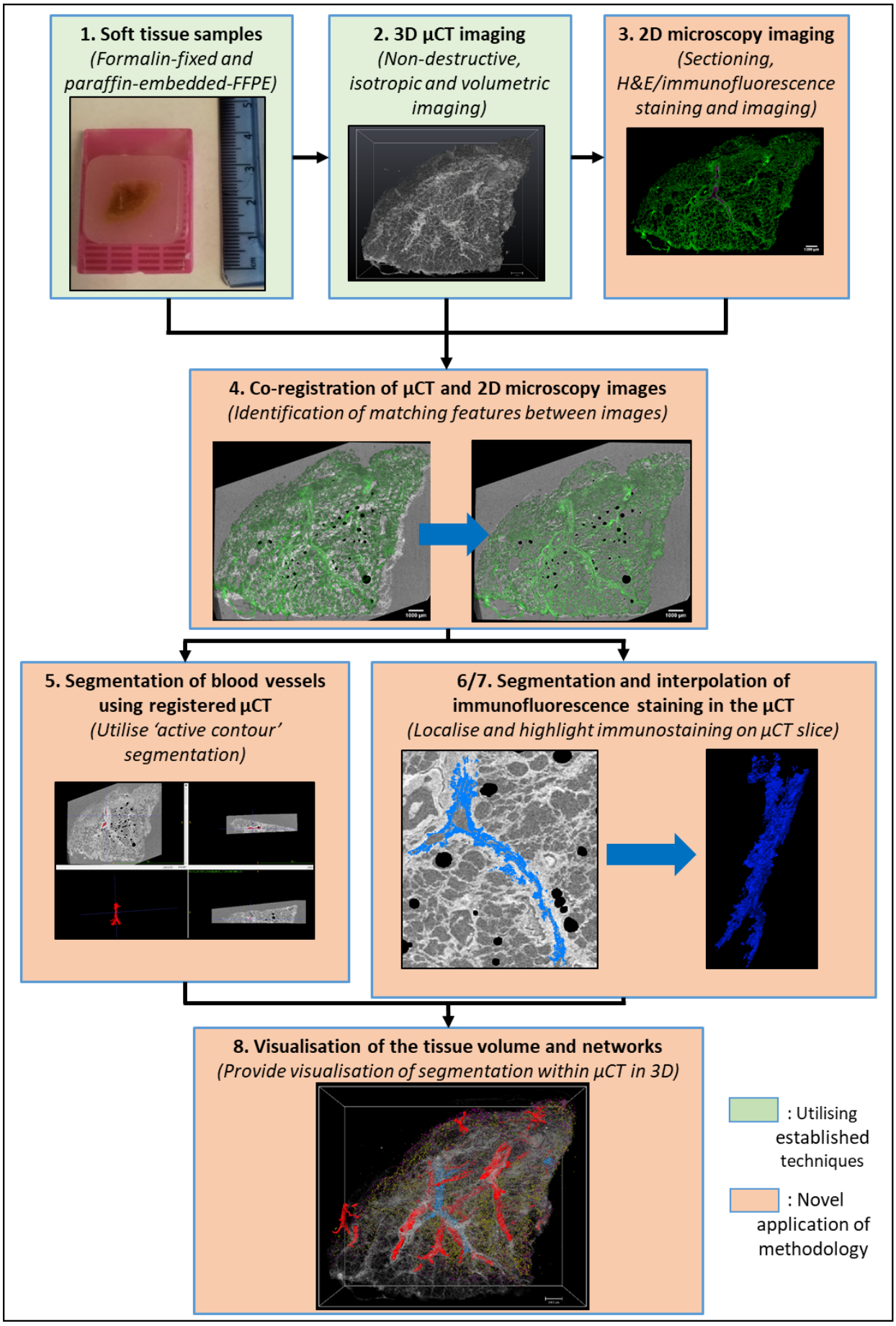
1. Soft tissue samples
(Formalin-fixed and paraffin-embedded-FFPE)
2. 3D µCT imaging
(Non-destructive, isotropic and volumetric imaging)
3. 2D microscopy imaging
(Sectioning, H&E/immunofluorescence staining and imaging)
4. Co-registration of µCT and 2D microscopy images
(Identification of matching features between images)
5. Segmentation of blood vessels using registered µCT
(Utilise 'active contour' segmentation)
6/7. Segmentation and interpolation of immunofluorescence staining in the µCT
(Localise and highlight immunostaining on µCT slice)
8. Visualisation of the tissue volume and networks
(Provide visualisation of segmentation within µCT in 3D)
: Utilising established techniques
: Novel application of methodology

Figure 3.26: **The main steps of the workflow presented in this chapter for automating registration and segmentation of biologically relevant features and cell types in 3D data provided by µCT.**(Previous page). Steps highlighted in green used previously published techniques. Steps highlighted in orange were developed in this project for greater automation, these involved novel techniques or utilising existing techniques on new types of data. 1: FFPE Soft tissue sample preparation. 2: Imaging of lung tissue at a high resolution (~10 µm) with sufficient contrast to visualise the tissue in 3D. 3: Section tissue and perform IF staining to identify specific cell types not visible in µCT. 4: Automated co-registration of the IF data with the µCT. 5: Identify and extract the blood vessel networks from the co-registered µCT using 'active contour segmentation'. 6: Localise specific immunoreactivity, provided by IF, within the µCT and use this data for automated segmentation. 7: Digital interpolation used to 'fill the gaps' to produce 3D segmentation of Ck18 8: Bring the µCT, blood vessels and registered IF segmentation together in order to localise specific networks and features within the 3D tissue volume.

Chapter 4 Blood vessel network analysis in COPD and non-COPD tissue

4.1 Introduction

The network of blood vessels form a crucial part of functional lung physiology contributing to gas exchange occurring in the alveoli and delivering oxygen to the rest of the body. The 3D network of blood vessels change as a direct or indirect effect of many lung pathologies. The larger blood vessels (>2mm diameter) detected using clinical CT are remodelled or lost in severe COPD (Wells *et al.*, 2015; Voelkel *et al.*, 2017). Less change had been observed in mild-moderate COPD with the loss of airways observed at earlier stages of disease compared to blood vessels. However these studies have either only looked at larger blood vessels in 3D (>2 mm diameter) or the smaller blood vessels (<2mm diameter) in 2D. The potential physiological changes occurring in mild-moderate COPD to the smallest blood vessels (down to 25 µm diameter) were investigated in this chapter. The 3D networks of blood vessels were segmented in lung µCT volumes using the methods detailed in chapter 3 (section 3.5.2) and analysed using physiologically relevant metrics. These included investigating changes in the volume, size and length of blood vessel networks. This would highlight any potential changes or loss in smaller vessels in mild-moderate COPD, which has not been observed at this scale in 3D before. The distribution of the network in relation to the tissue will provide insight into whether local areas of lung tissue have potentially lost blood vessels within the volume. Changes to the 3D network morphometrics, such as tortuosity and complexity of the networks (branching) in mild-moderate COPD has also not been explored at this scale in 3D before. Any change in the complexity of these small blood vessel networks could indicate early changes occurring in response to disease not observed previously. Combined these metrics were used to determine whether there was any significant difference to blood vessel networks in mild-moderate COPD compared to non-COPD tissue.

The methods for generating the segmentation of blood vessel networks using the methods from the previous chapter were tested on a larger scale to determine the feasibility of the method for larger studies. This was built upon to see if the segmentation data of the blood vessels was sufficient for providing in depth analysis of the blood vessel networks. As a binary segmentation mask of the µCT data network morphometrics such as volume and thickness could already be calculated using the data provided in chapter 3. Extra steps were required to investigate networks

characteristics, such as tortuosity, as detailed in this chapter. Performing the segmentation and analysis of these networks was important to validate the method of 'active contour segmentation' for blood vessel segmentation in µCT datasets. This was a proof of principle to show that data generation and physiologically relevant analysis was possible on multiple datasets. Further automation over manual segmentation shown here could lead to even larger studies with enough data to generate statistically significant results on larger cohorts of patient tissue samples.

4.2 Aims and objectives

The aim of this chapter was to identify and analyse the blood vessel networks present in the lung tissue volumes and assess if they change between non-COPD and mild-moderate COPD tissue.

The main objectives for achieving the aim of this chapter were as follows:

1. Segment the blood vessel networks in multiple non-COPD and COPD tissue blocks using methods detailed in chapter 3.
2. Normalise blood vessel measurements between different tissue samples of different sizes.
3. Analyse any potential changes to the physical network changes (thickness/length) and distribution of the networks in mild-moderate COPD tissue.
4. Assess the 3D characteristics (branching, tortuosity) of the blood vessel networks and how they change in 3D between non-COPD and mild-moderate COPD tissue.

4.3 Sample selection

As mentioned in section 2.4.3 multiple lung tissue blocks, chosen from archived tissue, which fit the criteria for non-COPD and mild-moderate COPD tissue had quick µCT scans performed on them. The main grouping difference was based on the GOLD status of the patient and their lung function score, a FEV_1/FVC of approximately 0.6 was used for mild-moderate COPD and a FEV_1/FVC of approximately 0.8 was used for the non-COPD tissue. The remaining clinical information was to match as much as possible including age, smoking history etc. A full summary of the clinical information of the selected tissue for chapters 4 and 5 can be found in appendix A.1

These quick scans identified 11 total tissue blocks which could appropriately be used in this study, six of these were non-COPD tissue and five were from mild-moderate COPD tissue. Figure 4.1 shows example images of quick scans which were accepted or rejected for use in this study. The

main reason for rejection was the presence of large homogenous areas of fibrosis or lack of substantial alveolar structure in the tissue block. The visible presence of blood vessels, alveoli and possible airways was used as another requirement for sample selection for grouping.

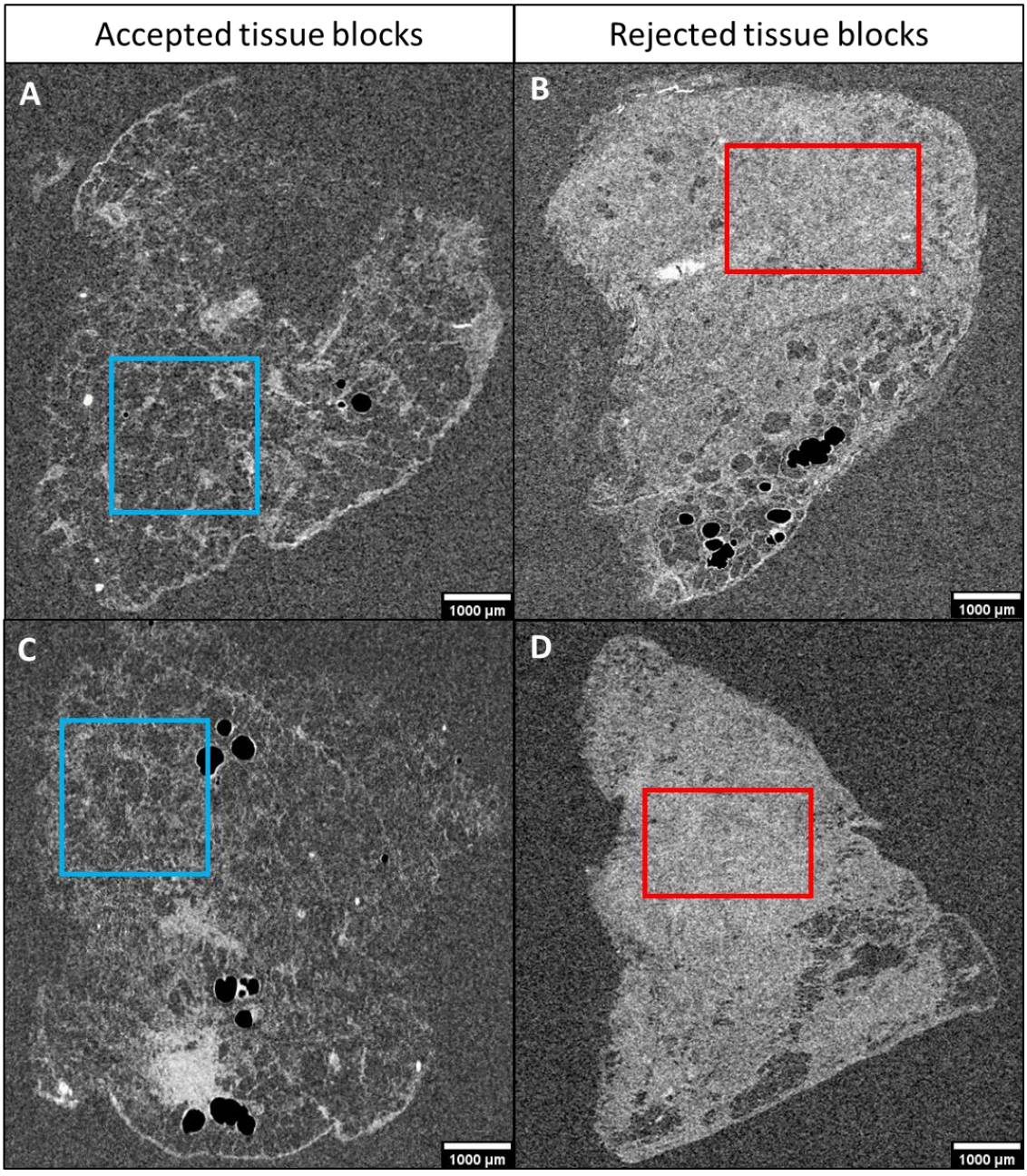

Figure 4.1: **Exemplar reconstructed 2D slices from the quick µCT scans (<20 min) used for sample selection.** A & C: Two µCT slices of tissue blocks which met the inclusion criteria, 'normal' lung structure (parenchyma) which was a key part of the inclusion criteria is highlighted by the blue box. B & D: Two reconstructed slices of tissue blocks which did not meet the inclusion criteria, the red boxes show homogenous areas of tissue lacking structural features which did not meet the inclusion criteria.

4.3.1 Tissue grouping and relevant clinical information

The 11 tissue blocks which were assessed and sorted into two clinical groups were all scanned at high resolution following the protocols reported in section 2.4.2. Table 4.1 below summarises the tissue groups with key pieces of clinical information and µCT scan information, for a full table of clinical information see appendix A.1. Each group was compared to ensure the only significant differences were in the disease status of the patients with the others (e.g. age) not being significantly different. The grouping of the samples was blinded from the investigator during imaging and analysis of the tissue to remove any potential bias. Only after all the imaging and analysis of the 11 tissue blocks was complete, used for chapters 4 and 5, were the groupings revealed to establish comparisons between the groups.

Table 4.1**: Summary of the 11 human lung tissue blocks and grouping used in chapters 4 and 5.** Data presented as median grouped values plus the interquartile range in parentheses, for full information see appendix A.1**.** P-values of numerical results show were calculated using the Mann-Whitney test between the grouped Non-COPD and COPD tissues. For Gender and smoking status P-values were calculated using Fisher's exact test.

Group	Non-COPD	COPD	P-value
Age	66.5 (2.5)	70 (6)	0.6948
Gender	3F 3M	3F 2M	>0.9999
FEV_1 %predicted	91 (14.25)	69 (6)	0.026
FEV_1/FVC	0.76 (0.035)	0.62 (0.05)	0.0022
GOLD status	0 (0)	2 (0)	n/a
Smoking status	3 current 3 ex	3 current 2 ex	>0.9999
µCT scan resolution (µm)	6 (0.5)	9.5 (0.5)	n/a

4.3.2 µCT results

The 11 µCT scans of the lung tissue, split into two groups, were used for data generation and analysis of all the results presented in this chapter and chapter 5. These groups were purposely chosen to be similar in the majority of criteria including age and indications. The only major difference was the lung function scores (FEV_1/FVC) with an average score of 0.8 used for the non-COPD group and an average score of 0.6 used for mild-moderate COPD. Representative high resolution (≤10 µm) µCT images of tissue from both groups can be seen in Figure 4.2.

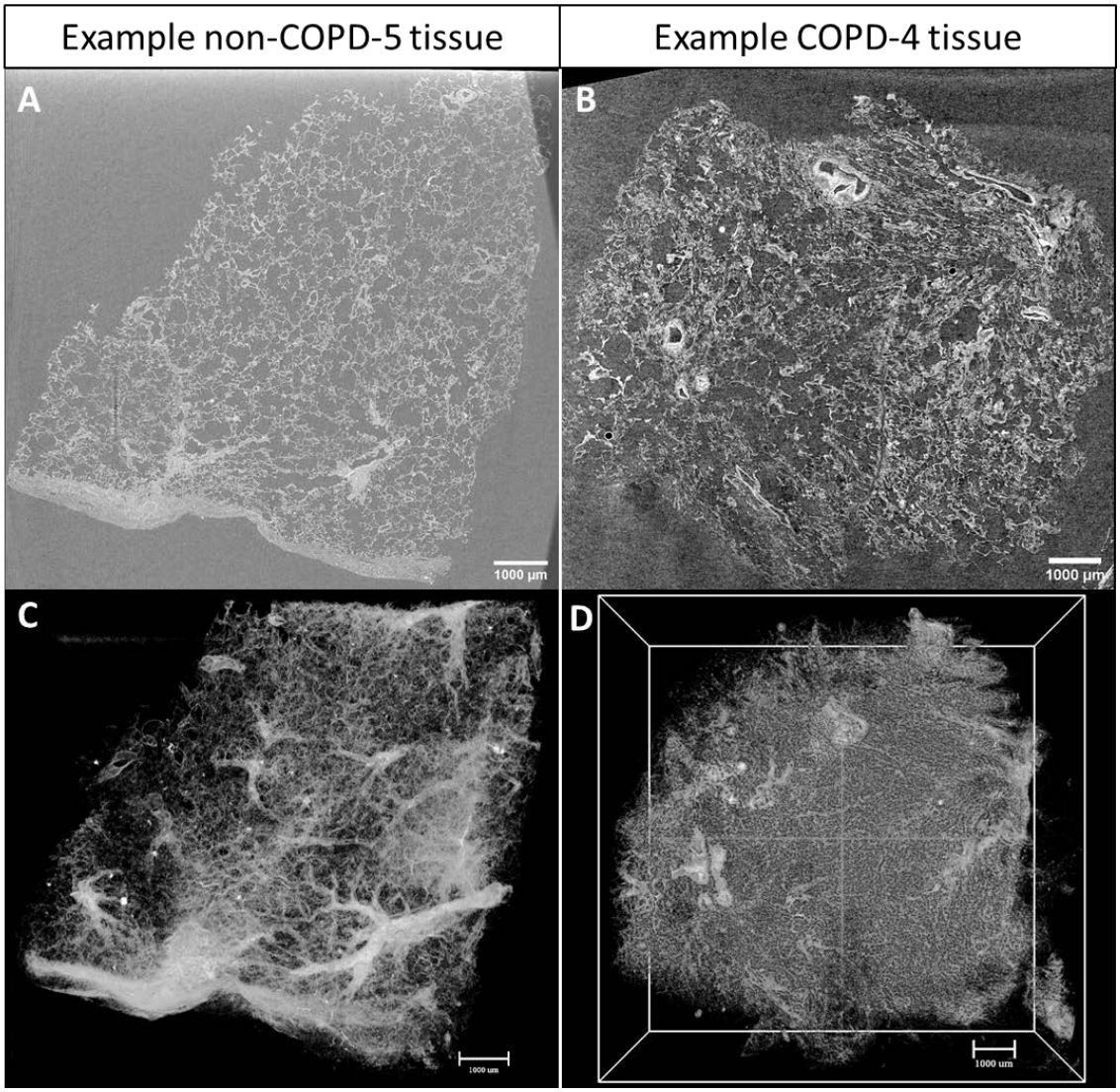

Figure 4.2: **Visualisation of the µCT results in 2D and 3D from both clinical groups.** A & B: Representative reconstructed µCT slices of non-COPD and mild-moderate COPD tissues from µCT scans at a less than 10 µm resolution (voxel size). C & D: Volume rendering of 3D tissue structure in the lower panels reveals the 3D parenchyma and networks within the tissue.

4.4 Results of blood vessel segmentation

Blood vessel lumens were successfully segmented in all 11 µCT tissue volumes using the 'active contour segmentation' implemented in ITK-SNAP (see methods described in section 3.5.2). The identification of blood vessels on the same 2D µCT slices seen in Figure 4.2 and representative 3D surfaces of the blood vessel network of the µCT in non-COPD and COPD tissue can be seen in Figure 4.3. Visually these blood vessels were complex comprising of several individual networks.

As expected the size of the tissue had a visible impact on the number of segmented blood vessels with larger tissue volumes visibly containing more segmentation.

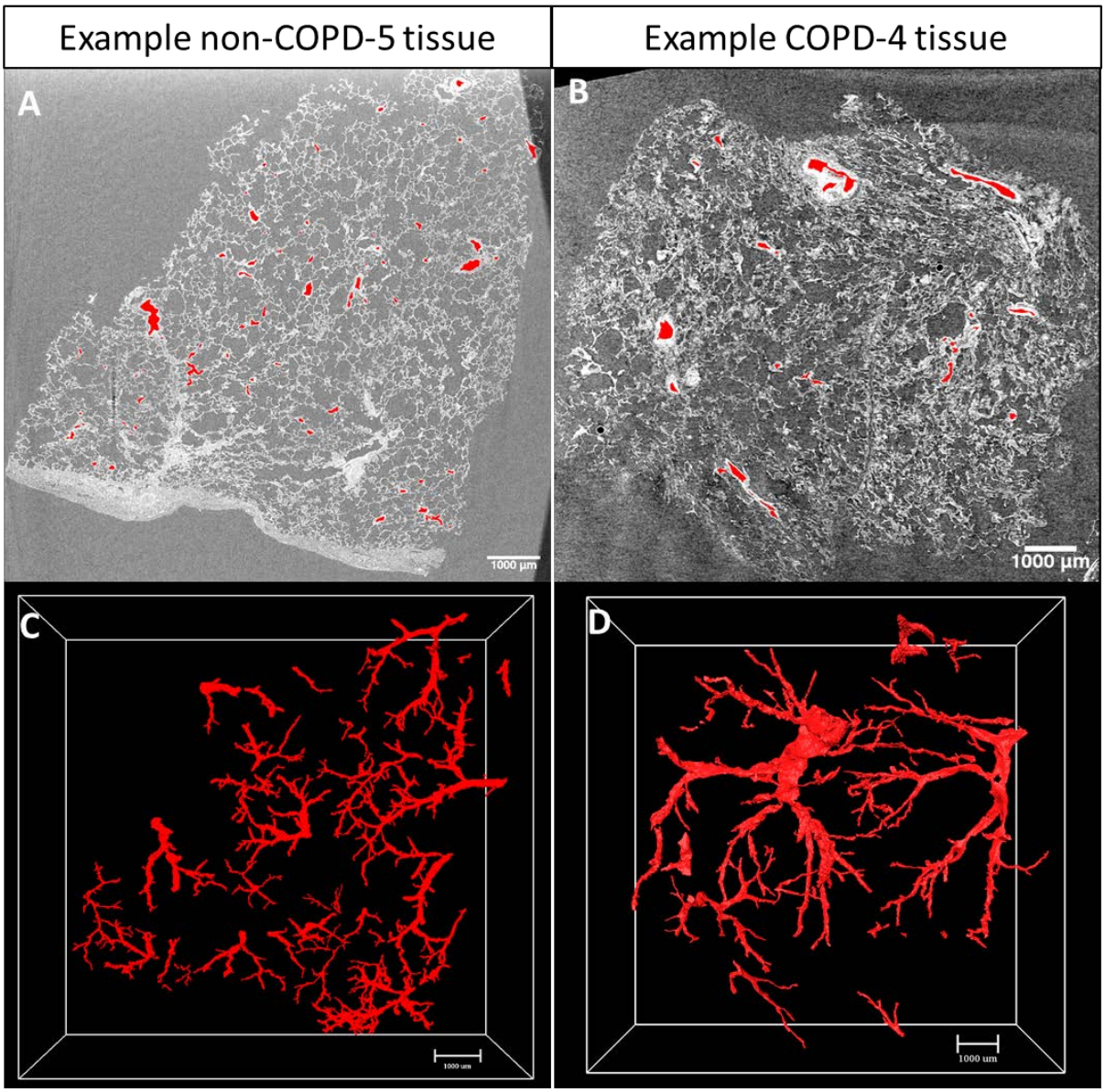

Figure 4.3: **Segmented blood vessel networks visualised in 2D and 3D from representative tissue from each clinical group.**The red labels on both the 2D µCT slices (A & B) highlight the localisation of the blood vessel lumen in the 2D plane. The 3D surfaces (C & D) show the complete blood vessel network (down to 25 µm thickness) segmented from the tissue volume.

Initial results of the segmentation parameters including the time taken are reported in Table 4.2. Each of the 11 µCT volumes were fully segmented on average in less than 10 hours, proving far quicker than if they were attempted manually. There was no observed significant difference between the grouped tissues of any of the segmentation parameters, except the number of seed points used to initiate the segmentations.

Table 4.2: **Summary of the blood vessel segmentation parameters for each lung tissue block.** Averaged data presented as median grouped values plus the interquartile range in parentheses. P-values were calculated using the Mann-Whitney test between the grouped Non-COPD and COPD tissues.

ID	Non-COPD-1	Non-COPD-2	Non-COPD-3	Non-COPD-4	Non-COPD-5	Non-COPD-6	Non-COPD-Median	COPD-1	COPD-2	COPD-3	COPD-4	COPD-5	COPD-Median	P-Value
µCT scan resolution (µm)	6	9	6	5	6	6	**6 (0.5)**	8.5	6	6	9	10	**9.5 (0.5)**	**0.2013**
Tissue volume [mm^3]	16	82.3	49	38	32	23	**35 (21)**	157	39	24	87	475	**87 (118)**	**0.1255**
Segmentation time (h)	6.5	6.25	12.5	6	6.5	7.5	**6.5 (0.94)**	14.5	13.75	11	9	16	**13.75 (3.5)**	**0.1623**
Number of seed points	97	71	87	64	73	78	**75.5 (13.25)**	179	111	103	95	120	**111 (17)**	**0.0087**
Segmented voxels	608,562	3,742,746	1,672,937	3,809,402	3,307,760	4,957,994	**3,809,402 (825,117)**	6,048,299	2,298,037	1,500,370	2,607,583	7,696,357	**6,048,299 (2,544,387)**	**0.7922**

4.4.1 Post-processing of blood vessel segmentation

Analysis of the blood vessel networks used the binary segmentation masks generated using ITK-SNAP. However, these required some post-processing steps in order to perform the analysis detailed below. As previously stated the presence of red blood cells prevented segmentation based on thresholds due to the relatively high X-ray absorbance (i.e. grey levels) of red blood cells in relation to the lumen. In the 2D segmentation these appeared as voids within the lumen segmentation and prevented accurate volume calculation, thickness measures and/or skeletonisation of the vessel lumen. The 'fill holes' function in Fiji was used to remove these voids in the segmentation. Prior to skeletonisation in Avizo several processes were required after filling the holes in the segmentation. Firstly a 2-point 3D median filter was applied to the segmentation, followed by the 'distance map for skeleton module' and the 'distance-ordered thinner module' (setting for 10 lens of ends). The result of this was run through the 'autoskeleton' module to produce the skeleton of the blood vessel segmentation.

4.5 Analysis of blood vessel networks

The total volume of soft tissue in each scanned FFPE block is reported in Figure 4.4, alongside this is the volume of segmented blood vessel lumens. From these two volumes the results were normalised as a vascular fraction, this was calculated as a proportion of blood vessels to the total

tissue volume. The results highlighted the need for this normalisation to vascular fraction as the raw blood vessel volumes were higher in some of the COPD tissues, but the fractions were not. This normalisation was also applied to the network characteristics to minimise the variable which was sample size. The cause for the apparent increase in volume was due to tissue size and not from other factors. The results reported in Figure 4.4 show that despite a large amount of variance in the volumes of tissue and blood vessels that the vascular fraction is similar in both Non-COPD and COPD tissue. The vascular fractions were compared using a Mann-Whitney test which showed, despite some variability, no significant difference between the non-COPD and COPD groups.

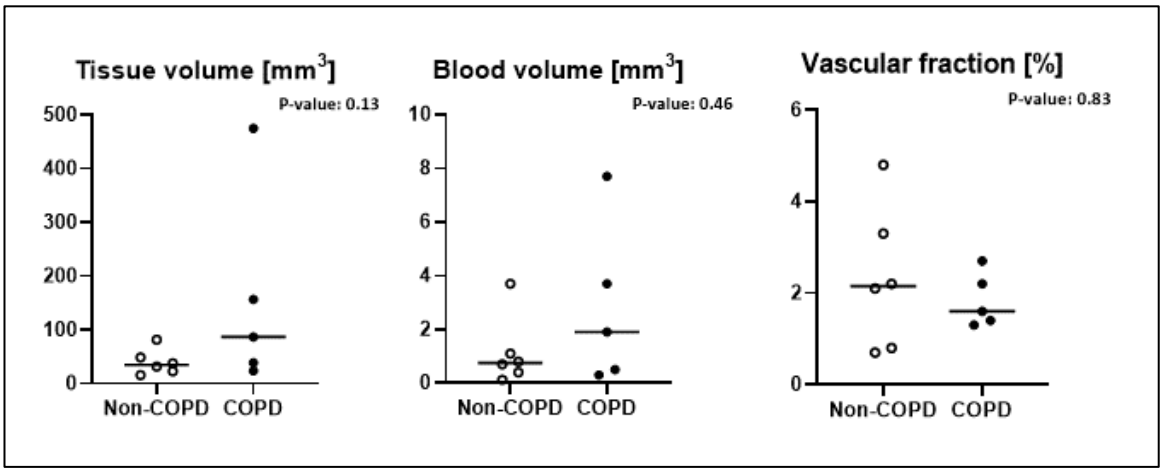

Figure 4.4: **Results and normalisation of tissue and blood vessel volumes in each of the grouped samples**.Each point on the graphs represents one measurement from each tissue block. The vascular fraction was calculated using the blood vessel volume result as a percentage of the total tissue volume. P-values were calculated using a Mann-Whitney test. Line denotes the median value of each group.

4.6 Analysing the thickness of the vessel lumen

Blood vessel luminal thickness was calculated via an internal distance map of the vessel correlated with the diameter of the largest sphere which fits inside the structure at a certain thickness. This was implemented using the BoneJ plugin (Doube *et al.*, 2010) which also automatically produces statistical analysis of the blood vessel luminal thickness.

4.6.1 Results of thickness maps

Thickness maps for each blood vessel lumen segmentation were successfully completed and representative datasets from each group are shown in Figure 4.5. These are images of 3D networks with a colour map indicating the thickness of the vessel lumen, as the key shows darker

vessels are thinner and brighter vessels are thicker. To truly visualise the 3D thickness of these vessels the networks need to be examined in 3D, see Appendix A.7.4 and A.7.5 videos which shows these networks rotating in a 3D space in the exemplar tissues. Initial qualitative inspection of the data showed no significant difference between the groups and the analysis confirmed no significant difference (P-value: 0.33) in the mean thickness of vessels (µm) between the groups (Non-COPD: 92 ± 29, COPD: 120 ± 40).

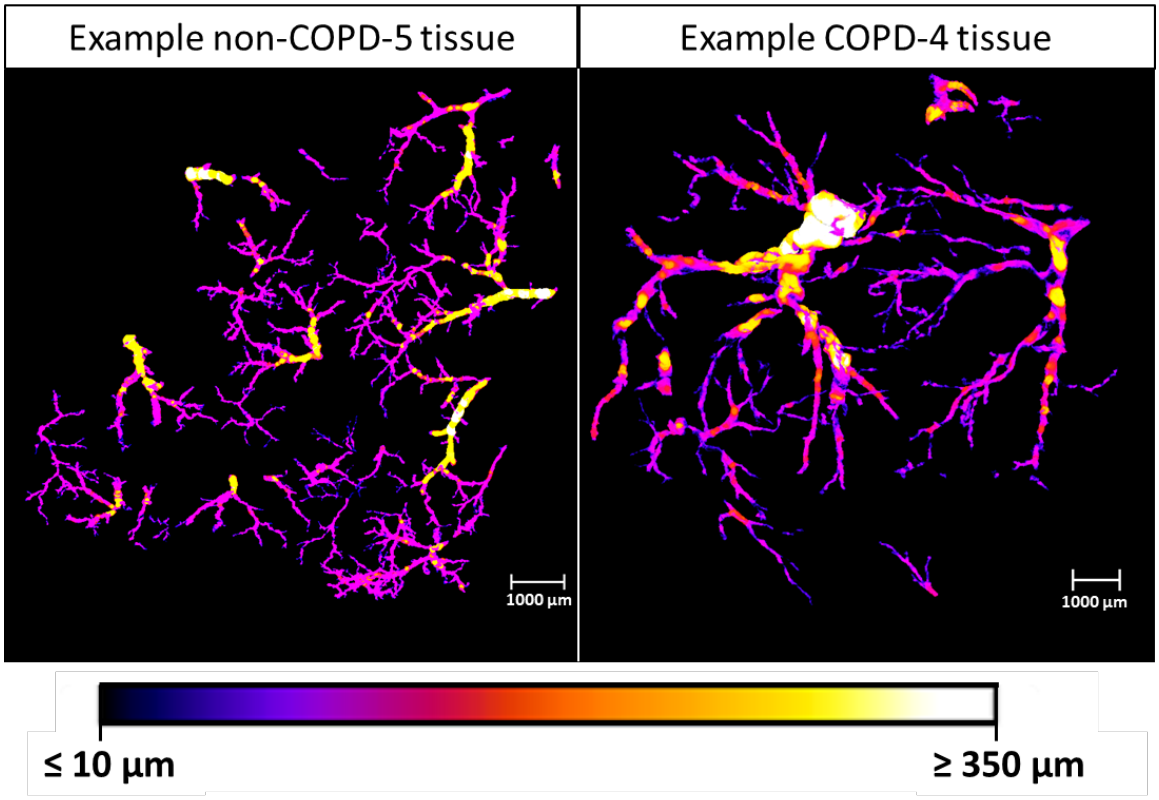

Figure 4.5: **Visualisations of the blood vessel lumen thickness in exemplar non-COPD and COPD tissue**.The colour map beneath the images shows the relative thickness of the segmented blood vessel lumens. In this example there is visibly a greater proportion of thinner vessels (<50 µm) in the non-COPD sample compared to the COPD sample. Thickness map and visualisation generated using the BoneJ plugin (Doube *et al.*, 2010) in Fiji.

To determine whether the distribution of vessel lumen thickness varied between the groups the vascular fractions of the thickness measures was calculated. This was important physiologically as a change in the proportion of the thinnest vessels could suggest changes occurring to the blood vessel network in response to disease (e.g. loss of the smallest blood vessels). The thickness results were divided into groups (bins) 10 µm apart up to 350 µm thickness. The number of voxels in each of these groups were used to calculate what percentage of the total tissue volume (from

section 4.5) consisted of blood vessels at each band of thickness. The results of this are plotted in Figure 4.6, here each plotted point is the mean vascular fraction of the non-COPD and COPD groups at different bins of blood vessel thickness (error bars= Std. Dev). The vessels up to a thickness of 100 µm are shown in the main graph with the insert in the top right showing the full range of thicknesses up to 350 µm.

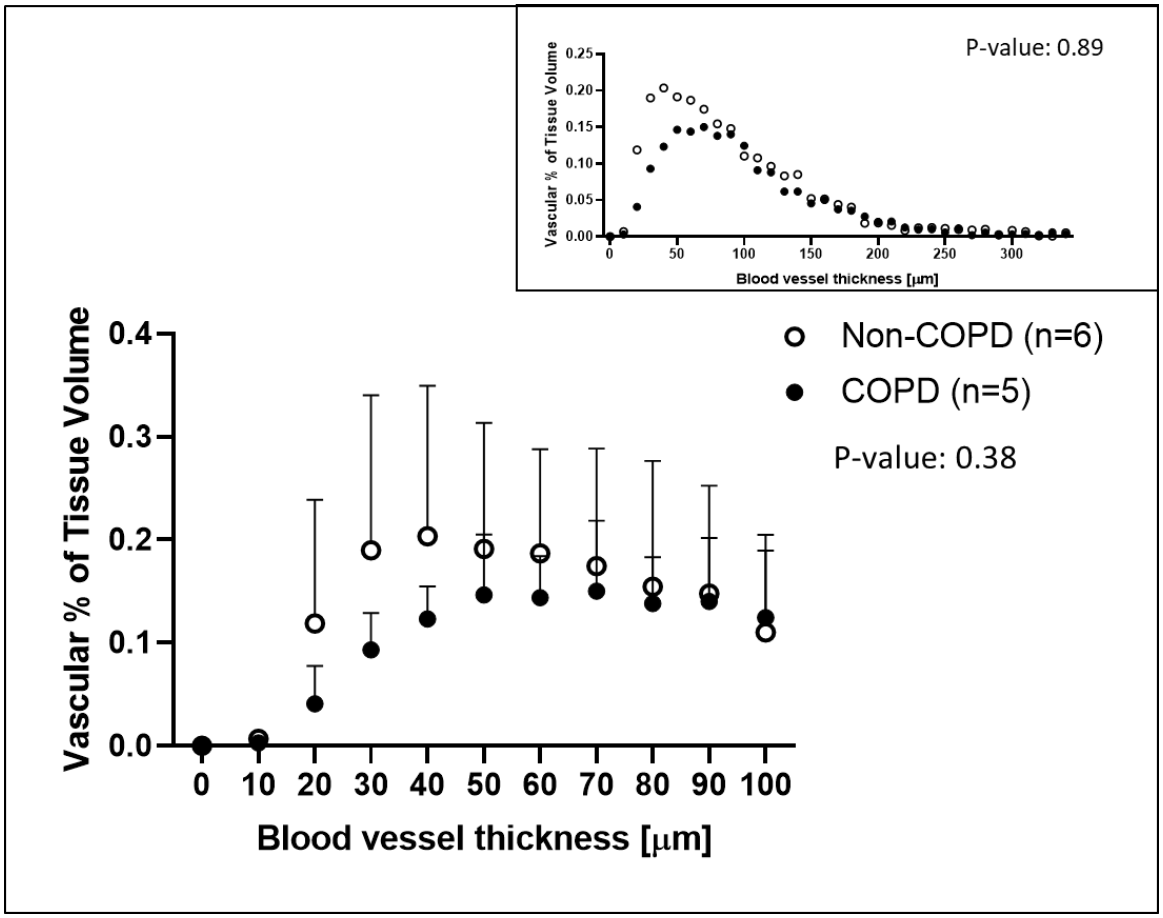

Figure 4.6: **Plotted mean group values of blood vessel lumen thickness separated by thickness bands 10 µm apart for non-COPD and COPD tissue**.The main graph focusses on blood vessel lumens at a thickness of ≤100 µm where the greatest difference in the results can be seen. The upper right graph shows the full range up to a thickness of 350 µm. Each measurement was calculated from individual thickness bins from each sample. Error bars show standard deviation. P-values calculated from two-way ANOVA. Area under the curve analysis was also performed on different ranges of data as reported in the section below.

Figure 4.6 shows a difference in the values between non-COPD and COPD tissue for distribution of the narrowest detected vessel at less than 100 µm thickness. Above this thickness threshold the differences in the proportion of vessels in thickness bands from 110 µm to 350 µm were even smaller. However, there was no significant difference in comparing the vascular fraction at any of

these individual thickness bins (lowest P-value: 0.2 at 30 µm thickness). Therefore, despite higher variance in the non-COPD values there was no significant change, when looking at this small number of samples in the thickness of the blood vessel networks between the non-COPD and COPD tissue groups. The results of the two-way ANOVA showed no significant differences in the variance of the data. Area under the curve analysis was also performed on the mean values for each thickness bin. On the full range (0-350 µm) the P-value was 0.47, which decreased to 0.089 when used to analyse the thickness of the smallest vessels (0-100 µm). To analyse the values where the most observed differences occurred in the individual Mann-Whitney tests further analysis of the range of thickness values between 20-100 µm was performed. The two-way ANOVA of values between 20-100 µm showed no significant differences (P-value: 0.29), whereas the area under the curve analysis showed an observed significant difference between the grouped blood vessel thickness in the range of 20-100 µm (P-value: 0.024).

4.7 Distribution of blood vessel networks-distance maps

To assess the distribution of the blood vessels within the tissue distance maps were used to calculate the distance any part of the soft tissue is from the nearest blood vessel in 3D. The binarised tissue fractions were multiplied by the blood vessel distance maps in Avizo. The voxel counts of tissue distances were different in each block due to differing tissue volumes, however this did not affect the trends seen in the distribution of tissue voxels. The results of each of the

tissue blocks from both groups are reported in Figure 4.7. In all of the tissue blocks except non-COPD-1 the majority (68-97%) of the tissue was within 1000 µm of the nearest blood vessel.

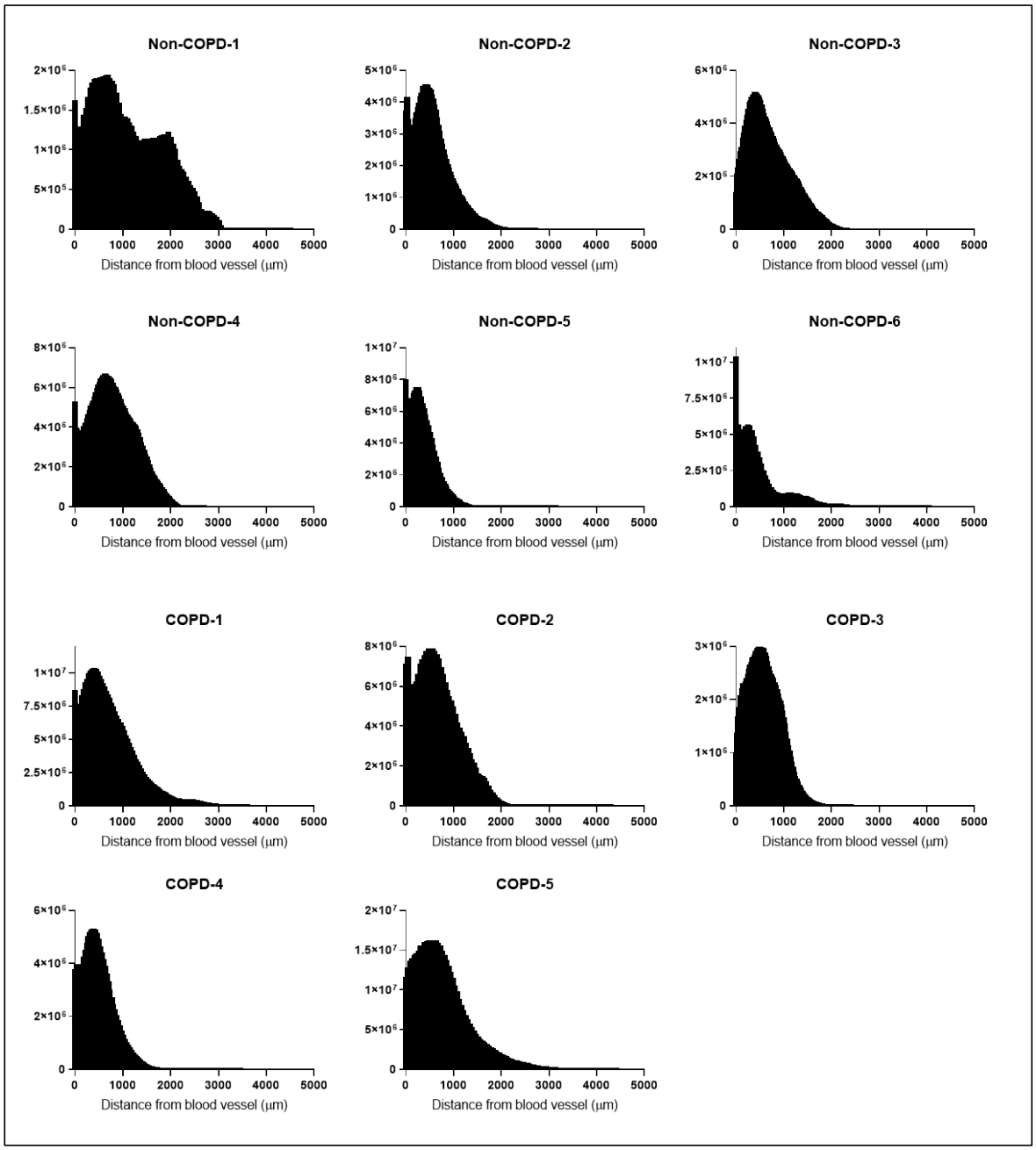

Figure 4.7: **Results of the individual distance maps of segmented tissue voxels from the nearest segmented blood vessel lumen**.Each peak shows the number of tissue voxels at the corresponding distance to the nearest blood vessel. The *y*-axis shows the number of voxels which varies between each sample depending on the total tissue volume.

Visualisation of the tissue distance from blood vessels was performed in Avizo using the depth rainbow colour map, as seen in Figure 4.8. The colour key shows that the blues and purples are tissue located close to blood vessels whereas the yellows and greens are tissue located further from blood vessels. The high levels of tissue coloured in shades of blue corresponds with the

graphs seen in Figure 4.7 showing that the majority of voxels were located less than 1000 µm to the nearest vessel. Visual inspection confirmed that the majority of the tissue located further from blood vessels was near to a pleural surface with the cut edges of the tissue maintaining close proximity to blood vessels. This is seen in the non-COPD-5 tissue, shown in Figure 4.8, at the top of the tissue is a large area of pleural surfaces which is coloured at a distance greater than 1000 µm from the nearest identified blood vessel (down to a 25 µm thickness). Overall there was no observed difference in the distribution of the blood vessels in relation to the lung tissue.

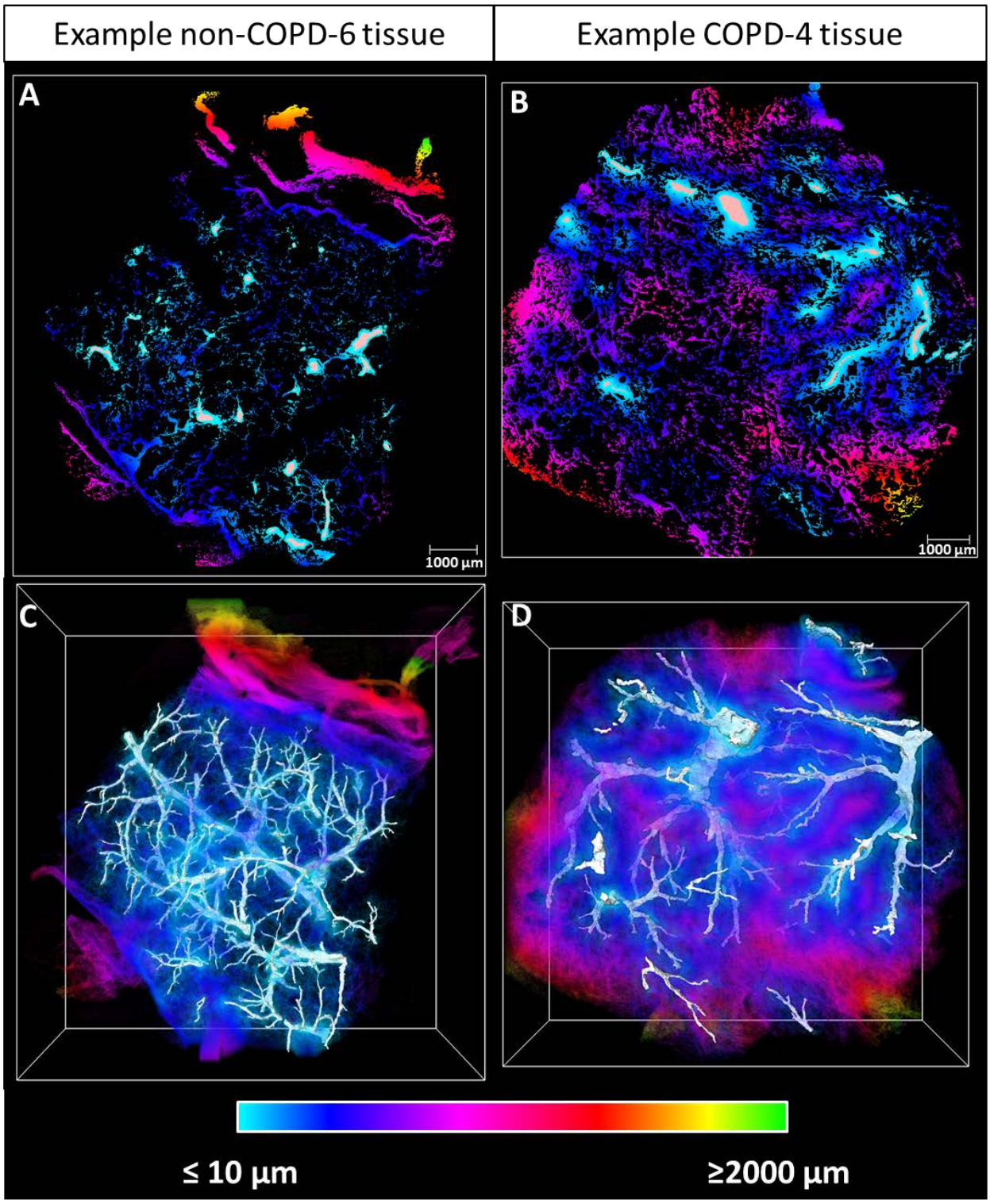

Figure 4.8: **Visualisations of lung tissue distance to the nearest segmented blood vessel in 2D and 3D**. Exemplar images from non-COPD and COPD tissue shown. The colours of the tissue correspond to the colour map which represents the increasing distance from blood vessels. A & B: 2D slices of the tissue distance from the blood vessels (off-white colour). C & D: 3D volume rendering of the distance colour map surrounding the 3D blood vessel lumen in white.

4.8 Changes in 3D network characteristics

4.8.1 Skeletonisation

Skeletonisation provided a simplified representation of the blood vessel segmentation, this skeleton of the network was used to measure several network characteristics in Avizo. The skeletonisation worked by finding a medial axis in the sequentially thinned segmentation to the point it is one voxel thick. The 'spatial graph view' and filament tab were used to analyse and visualise the skeletonised networks. As seen in Figure 4.9 the blood vessel network is converted into a series of nodes (spheres at branching and terminal points of the network) and segments which follow the network to join the nodes together. From the skeleton several measures of the network can be obtained as detailed in the next sections.

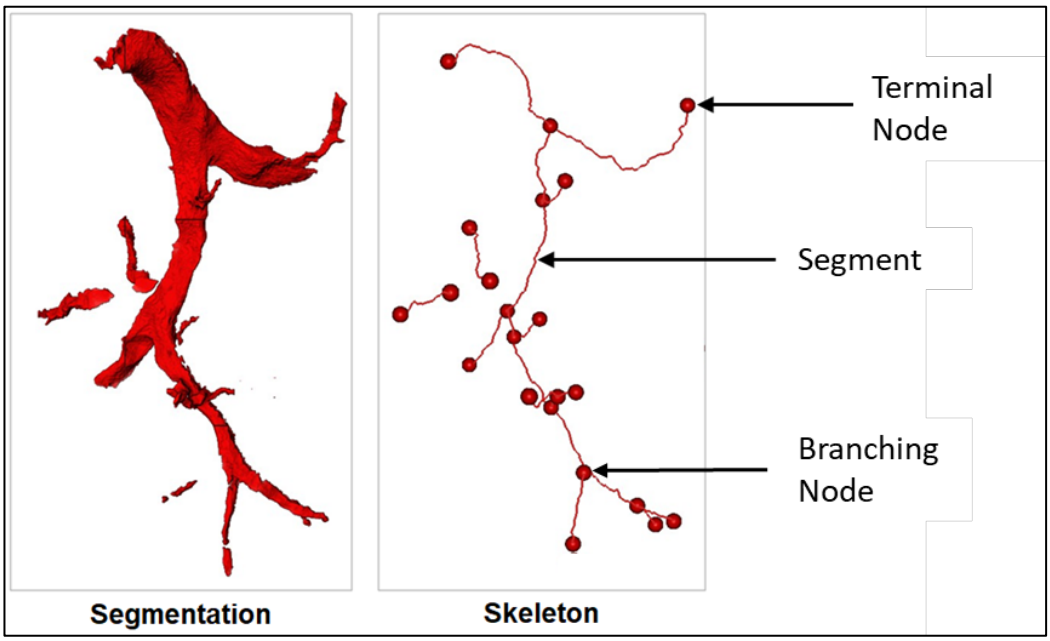

Figure 4.9: **Skeletonisation of the segmented blood vessel network.**The before and after images of an exemplar piece of blood vessel segmentation. The right hand image shows the three main components of the skeletonised network; terminal nodes were defined as nodes with one segment connected and branching nodes were defined as nodes with three of more connected segments.

4.8.2 Network characteristics

Network characteristics were calculated using the skeletons of the blood vessel networks from each tissue block, a representative image of the results of the skeletonisation in context with the full network can be seen in Figure 4.10.

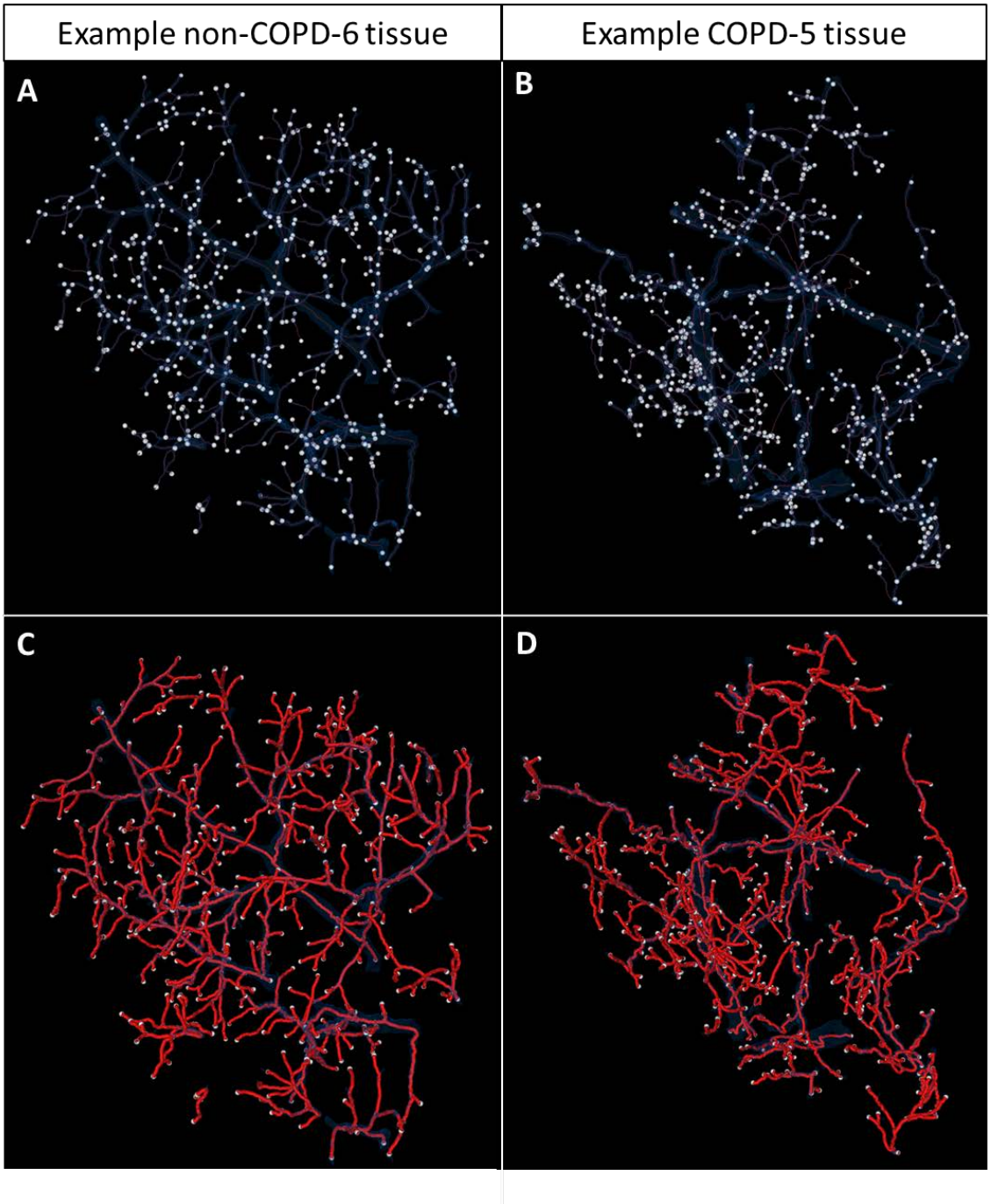

Figure 4.10: **Representative full blood vessel network skeletons of non-COPD and COPD tissue**.A & B: 3D representations of the skeletonised blood vessel network (red line), the terminal and branching nodes (white spheres) within the original segmentation (transparent blue). C & D: The same segmentation with the skeleton dilated by three voxels to ease visualisation.

Each of the measurements reported here including network length, number of components and branching were normalised by the total tissue volume of each sample. The results of the network length per tissue volume and number of components (individual networks) per tissue volume are reported in Figure 4.11. The two accompanying images in Figure 4.11 show examples of the skeletonised network of each separate component with different coloured nodes.

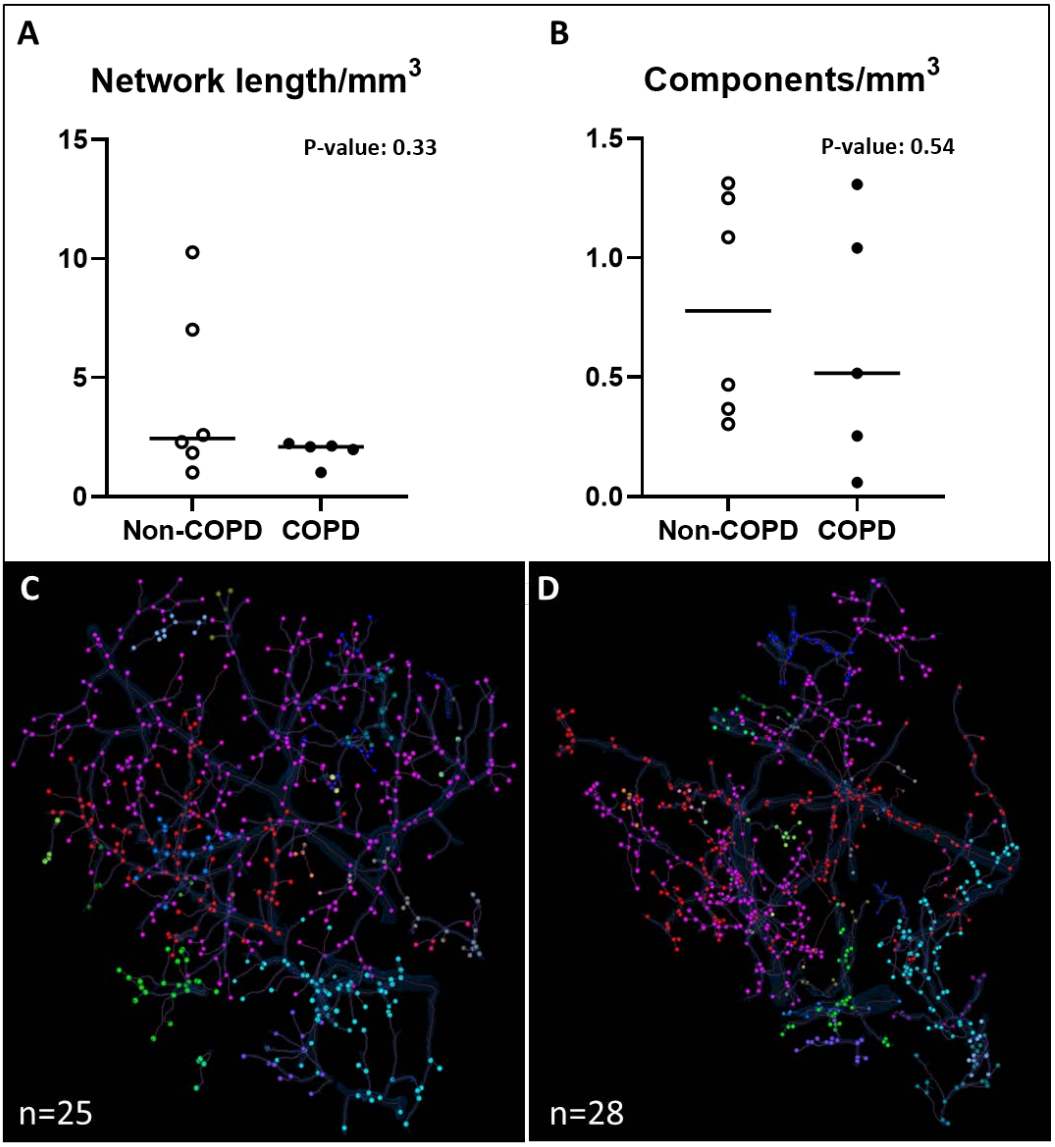

Figure 4.11: **Normalised total blood vessel network length and the number and visualisations of individual networks in exemplar tissue blocks**.Each value on the two graphs (A & B) was normalised by the tissue volume of each block. P-values were calculated using a Mann-Whitney test. Line denotes median values of each group. The lower images (C & D) show representative skeletonised networks from non-COPD-6 (left) and COPD-4 (right) tissue, highlighting individual networks with different coloured nodes (spheres). The *n*-number is the total number of individual blood vessel components in each tissue.

No significant difference in the total length of the blood vessel network was found between the non-COPD and COPD tissue with nearly identical median values (line on Figure 4.11). Interestingly, there was a large difference in the mean length of 4.2mm/mm^3 in non-COPD tissue compared to the COPD tissue with a mean length of 1.9 mm/mm^3. There was greater variability between the non-COPD results than the mean COPD tissue blocks. The main cause of this variability is that the smaller non-COPD tissue volumes contained a greater length of networks per volume compared to the smaller COPD tissue volumes. The larger tissue volumes in both groups presented similar values around 2mm/mm^3. The number of individual network components was similar in both the non-COPD and COPD tissue when standardised for tissue volume, with no significant difference calculated between them. The mean values for both groups were between 0.6 and 0.8 individual blood vessel networks per mm^3 of tissue.

4.8.3 Branching

The number of branching blood vessels was calculated from the branch nodes of the skeleton and the non-branching nodes were used to calculate the number of terminal nodes. The majority of these terminal nodes will either be located at the cut surface or where the blood vessels transition to vessels smaller than the resolution limit of the μCT scan. These results were normalised by the total tissue volume to give the number of branching and terminal nodes per mm^3 of tissue, as seen in Figure 4.12.

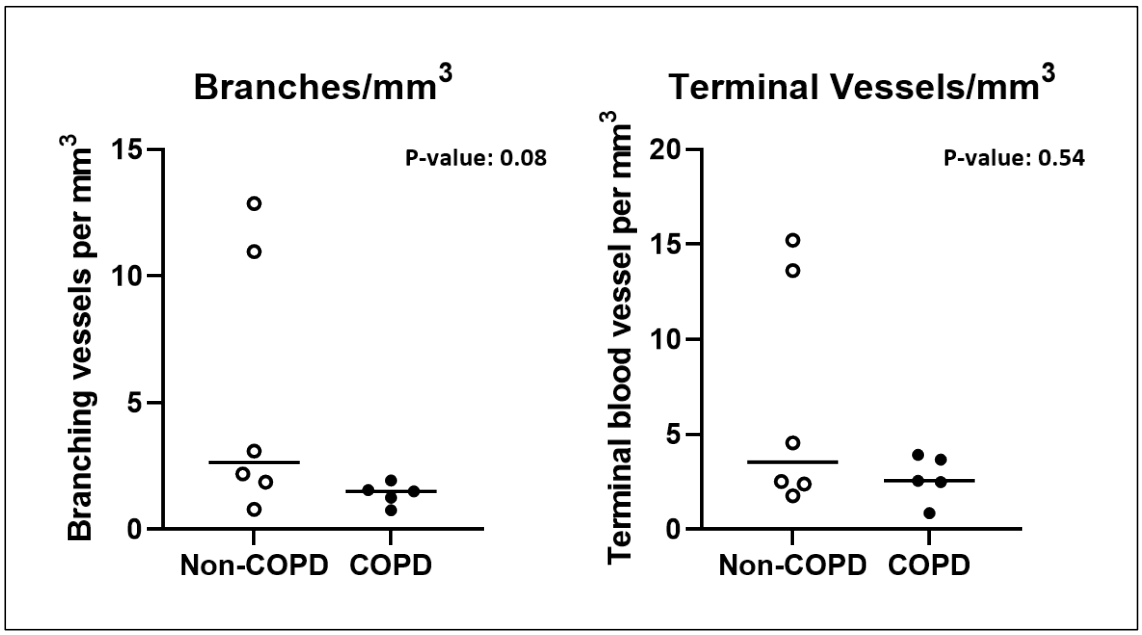

Figure 4.12: **Normalised results of blood vessel branching and the number of terminal vessels in each tissue block**.Each individual plot on the two graphs is normalised by the total tissue volume of each tissue block. P-values were calculated using a Mann-Whitney test. Line denotes the median value of each group.

The number of branching blood vessels in the network showed no significant difference between the non-COPD and COPD tissue, despite showing the lowest P-value (0.08) of any of the network characteristics. The mean number of branches decreased from 5.3 per mm^3 in non-COPD tissue to 1.4 per mm^3 in COPD tissue however the median values were similar. Two of the same non-COPD tissues contained significantly more branching vessels and terminal nodes than the other non-COPD and COPD tissues. These two tissues, from the same two patients, were the smallest tissue volumes in the non-COPD group and contained up to 10 more branching vessels per mm^3 of tissue compared to the two smallest COPD tissue volumes. Due to the size of the groups it is not possible to determine whether these were outliers or show a different sub-population in the non-COPD tissues.

4.8.4 Tortuosity

Tortuosity is defined as the ratio of the curved segment length to the shortest straight path between a pair of nodes in the network. Figure 4.13 provides a pictorial representation of this definition of tortuosity. Here tortuosity was used to determine differences in the morphology of the network i.e. were the blood vessels more straight or curved. A value of 1 would be given to a straight line and numbers greater than 1 indicate the vessel is curved to a higher degree with increasing tortuosity. As tortuosity is a metric of the network itself it was not normalised like the previous measures and the raw tortuosity value was recorded. The results of the tortuosity measures of the blood vessel networks are reported in in Figure 4.13. There was no significant difference between non-COPD and COPD tissue volumes with both groups having a mean tortuosity between 1.1 and 1.2. There was less variability in the tortuosity values compared to previous metrics with standard deviations of approximately 0.1 in both the non-COPD and COPD groups.

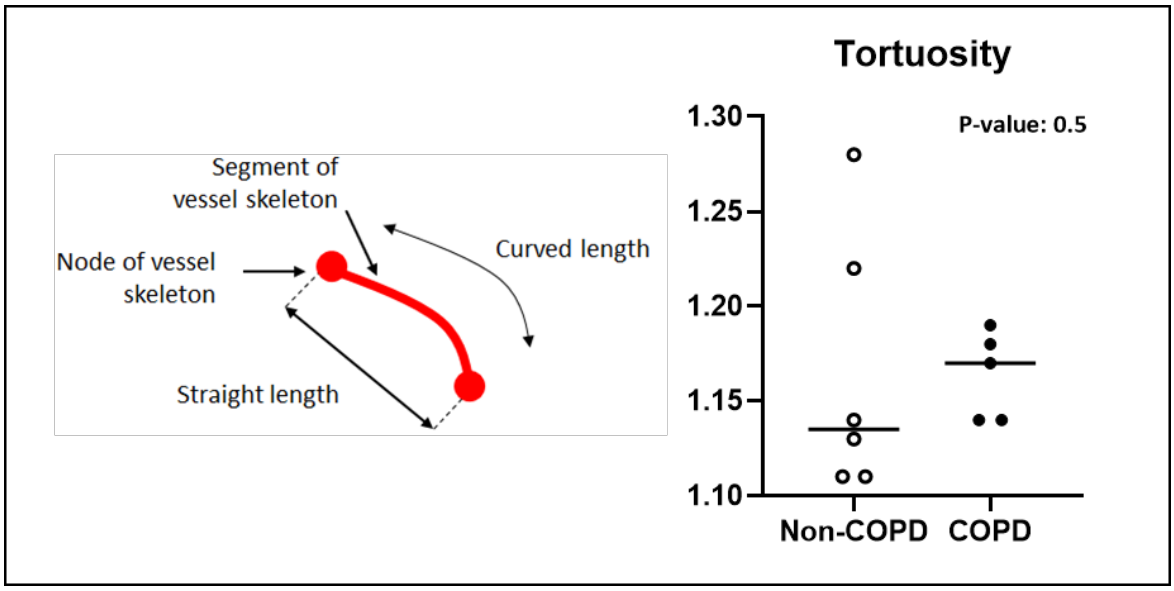

Figure 4.13: **Tortuosity representation and results for blood vessels in non-COPD and COPD tissue blocks**.The left image provides a visualisation of the tortuosity calculation using the skeletonised blood vessels actual segment length as a ration of the straight length. The graph shows the plots of the tortuosity value of each tissue block's blood vessel network. P-values were calculated using a Mann-Whitney test. Line denotes the median value of each group.

4.9 Discussion

This chapter and the work in the following chapter used FFPE human lung tissue samples which had been divided into non-COPD and mild-moderate COPD groups. Changes to the vasculature in severe COPD have been well-recorded using clinical CT (Estépar *et al.*, 2013; Saruya *et al.*, 2016) and 2D histological analysis of lung tissue (Santos *et al.*, 2002; Rahaghi *et al.*, 2019) but evidence of change in mild COPD is less prominent (Hueper *et al.*, 2015). These differences have not yet been reported in small blood vessels (<2 mm diameter) or the microvasculature in 3D, although it has been predicted that they are lost in mild-moderate COPD (Sakao *et al.*, 2014). To investigate this, blood vessels down to a 25 µm equivalent diameter were identified, segmented and analysed with several metrics. Due to the selection criteria, the tissue samples were relatively similar in terms of age and clinical indications with only the lung function scores/GOLD rating indicative of COPD (Calverley, 2004; Hsia *et al.*, 2010) being different. Therefore, any differences observed between the groups would likely be due to changes occurring in the tissue in response to mild disease. However variability caused by the accuracy of the GOLD classification for diagnosis, due to the complexity of the disease, has been previously reported and will apply to any study using these metrics for determining groups in COPD patients (ur Rehman *et al.*, 2019). As mild-moderate disease was being investigated it was also predicted that any changes to the

vasculature would be small and potentially heterogeneous. This would likely require larger clinical groups for significant inter-group differences to be recorded. This was indeed the case as no significant differences were recorded in any of the vasculature analysis metrics chosen to compare the non-COPD and COPD tissue samples used in this project. The small number of viable samples investigated and time constraints prevented further investigation to potentially find statistically robust differences between or within the groups. For future studies the use of composite scores could be used to condense the data for easier reading and analysis as well as potentially finding significant differences between the grouped composite scores. This could be applied to many of the metrics reported, for example a single value for the status of the 3D blood vessel network from combined network analysis in the non-COPD and COPD tissues. This would be calculated by taking an average of some or all of the individual network characteristics (branching, network length, individual networks, terminal branches, tortuosity, etc.) to provide an overall score for each tissue which could be analysed for any observed differences.

The segmentation results of the blood vessel lumen confirmed the vasculature results reported in chapter 3 by utilising 'active contour segmentation'. This saved a considerable amount of time over manual segmentation, with all 11 µCT volumes segmented in a total time of approximately 72 hours. Interestingly despite no significant difference between the grouped tissue in blood vessel volumes or segmentation times, the number of seed points used did differ significantly between the grouped tissues. Significantly more seed points were required to segment the COPD tissues compared to the non-COPD tissues. This is unlikely to be an effect of the disease as the volumes, thicknesses and network characteristics did not differ significantly between the groups. Most likely this difference in seed points is down to either the µCT scan quality, the abundance of vessels near the edge of the image where artefacts can occur or the performance of the computer/software/user on the day the segmentation was performed. However, despite no significant difference in the tissue volumes between groups the individual data does show some COPD tissues having a larger tissue volume than the non-COPD tissues. This could also potentially explain the difference in the number of seed points.

Previous studies investigating vasculature in other tissues, notably bone for µCT datasets have utilised active contour segmentation techniques to generate similar results (Tassani *et al.*, 2014; Korfiatis *et al.*, 2017). Different implementations of active contour/ region growing segmentation have also been used in µCT data of mouse lung tissue (Artaechevarria *et al.*, 2010). All of which have produced reliable analysis of 3D vasculature networks (Helmberger *et al.*, 2014). Many of

these analysis metrics were used here to investigate the potential effects of mild-moderate COPD on these small blood vessel networks.

The volume of blood vessels and the subsequent vascular fraction following normalisation using the tissue volume showed no significant difference between the clinical groups. This could be because the blood vessels are not lost at the same rate in COPD as the airways and so no detectable loss of the small blood vessels is observed in the mild-moderate forms of the disease here (Hueper *et al.*, 2015; Takayanagi *et al.*, 2017). The presence or absence of airways did not affect the vascular fraction of the tissue. The tissue with, by observation, the most abundant airway networks in both groups did not contain significantly more or less blood vessels than tissue which did not contain visible airways. There was some variation in the vascular fractions within the groups which indicates that larger number of samples need to be analysed to show what the average vascular fractions for each group are.

Blood vessel lumen thickness was used as a practical alternative to lumen diameter, which has been used for 2D analysis in previous studies investigating blood vessels (Rahaghi *et al.*, 2019). However in 3D, diameter is not a suitable measurement; the main reason for this was that the blood vessels, as seen in section 4.4, are not uniform round shapes with many flattened vessels present. This could be caused by processing artefacts of the FFPE tissue and/or the plane the µCT has been viewed in. These factors make it impossible to provide an accurate measure for lumen diameter and also prevented the lumen perimeter from being accurately measured to calculate an equivalent diameter. These measures do not take into account the 3D morphology of the vessel due to only measuring a single reconstructed 2D plane provided by a µCT slice which will most likely not be perpendicular to the centreline of the vessel. Lumen thickness was chosen as an alternative because it takes into account the 3D nature of the vessel, irrespective of uniformity of the shape, and was already incorporated in Fiji as local thickness. This used the 3D volumetric data provided by µCT to produce a more accurate measurement of lumen size by determining the thickness in 3D. The local thickness tool has also been used on µCT lung tissue volumes previously to investigate 3D tissue thickness changes occurring in IPF lung tissue (Katsamenis *et al.*, 2019).

Using pulmonary angiograms, blood vessels have been shown to narrow and eventually disappear in COPD (Sakao *et al.*, 2014). The total number of blood vessels with lumen diameters <500 µm has been reported to decrease in COPD, this was primarily measured in 2D studies using traditional histology and more recently the measures have been compared with 3D CT imaging (Rahaghi *et al.*, 2019). Blood vessel thickness has mostly been used in µCT studies to analyse changes in the vasculature of bone (Zhao *et al.*, 2015). Examples of this have found changes to the thickness of the blood vessels lumens in the bones of young and old rats (Núñez *et al.*, 2018). The

two-way ANOVA results of the blood vessel luminal thickness showed no significant difference in the variance between the groups but there was a higher proportion of thinner vessels (<50 μm) in the non-COPD samples. This was alluded to in the preliminary area under the curve analysis which did show a significant difference between the ranges of vessel thickness bins with the most observed difference (20-100 μm). More data of vessel thickness is required to expand on this and see if it contributes to an overall trend of less smaller vessels in COPD tissue compared to non-COPD tissue. Also the thickness of measured vessels was directly related to tissue volume as a greater volume of thinner microvasculature, outside the detection range, will be located closer to the pleural surface (Zhao *et al.*, 2019). Therefore, larger peripheral tissue containing more tissue further from the pleural surface will contain a greater proportion of larger (i.e. thicker) blood vessels greater than 25 μm; which could be identified in the μCT scans used in this project. This explained why greater variation of the results was seen in the non-COPD tissue which had a greater range of tissue volumes. A larger study is required to see if the lower proportion of thinner vessels in mild-moderate COPD continues, which could suggest a loss of the smallest (thinnest) blood vessels in mild-moderate COPD.

The thickness measures provided a potentially more accurate measure for the size of blood vessels in FFPE tissue than traditional 2D histology. Unless more complex and time consuming stereological approaches are used (Heidari *et al.*, 2015; Mühlfeld *et al.*, 2018), this cannot take into account the 3D nature of the blood vessel. Indeed, the thickness measures could be used for image based modelling of fluid flow in the small blood vessels; this would require higher resolution scans to detect the capillaries as well. Similar measures have been used on clinical images (MRI) to model the fluid flow of blood in microvasculature resulting in an observed reduction in fluid flow in mild COPD samples (Hueper *et al.*, 2015). Fluid flow has also been modelled from μCT data of lung lymphatics, a far more complicated 3D network of the lungs (Robinson *et al.*, 2019); which shows how this data could be used in the future.

Distance maps were used to investigate the distribution of the blood vessel networks, down to a 25 μm thickness, within the lung tissue samples. A change in the distribution of the blood vessels within the tissue could indicate blood vessel loss or remodelling in response to disease (Estépar *et al.*, 2013). The results showed that the vast majority of soft tissue was located within 1 mm of the nearest blood vessel. This illustrates the high level of vascularisation within the 3D lung samples and the relatively even distribution throughout the volume. There was no observed difference in distribution of vessels at the sizes being investigated. However it is possible that the smallest vessels, not detectable at the current resolution of the μCT scans, leading to the capillary beds

have a different distribution in disease. This would likely have more effect on the numerical measures of samples taken more towards the tissue periphery with large areas of pleura. The non-COPD-1 tissue for example, was the only sample with the majority of tissue located more than 1 mm away from the nearest blood vessel. Visual inspection of this tissue revealed a large pleural surface with few identifiable blood vessels nearby. The majority of identified blood vessels in this sample were located in the area of tissue further from the pleural surface. Future work to quantify this could be completed by segmenting the pleural surface and investigating the distance between the detected blood vessels and the pleura, as has been done previously for investigating lymphatics distribution in relation to the pleural surface (Robinson *et al.*, 2019).

Bullitt (Bullitt *et al.*, 2005) suggests that the 3D characteristics of blood vessels, as analysed in this chapter, are affected by and indicative of, the majority of diseases in all tissue types including the lung. In COPD the complexity of blood vessel networks has been predicted to decrease (Milne and King, 2014). In order to analyse the 3D characteristics of the blood vessels networks, as has been done in previous µCT imaging studies (Zagorchev *et al.*, 2010; Shields *et al.*, 2016), the networks were simplified into skeletons. Skeletonisation has been used to calculate network characteristics including branch number and tortuosity in segmented networks of blood vessels (Meiburger *et al.*, 2016) and lymphatics (Robinson *et al.*, 2019).

The total length of detected blood vessels per unit volume (mm^3 of tissue), down to 25 µm thickness, was very similar in the majority of tissue from both clinical groups with no significant difference between them. The normalised network length was greatest in the two smallest non-COPD samples, whereas the smallest COPD tissues did not contain higher network length per unit volume. This could indicate a loss of network length in the smallest (i.e. more peripheral) tissue samples, however this would require more tissue samples to investigate further. The number of individual networks in the tissue samples did not differ significantly between the two tissue groups. Qualitative assessment appears to show that each group can be sub-divided into two further groups; with one half of the non-COPD and COPD tissues containing less than 1.0 components per mm^3 of tissue and the other half containing between 1.0 and 1.5 components per mm^3. However, this measure is an approximation of components per volume and could miss network connections outside of the tissue volume (particularly near the cut surface) in the remaining lung tissue. If, as previously suggested, blood vessels are lost and remodelled then this could show a change in the number of individual blood vessel networks (Vitenberga *et al.*, 2019).

Changes to blood vessel morphology, particularly network branching, have been recorded in both COPD lung tissue and other tissue types using both clinical and lab-based imaging modalities (Estépar *et al.*, 2013). In COPD the remodelling of pulmonary vasculature, including the loss of

branching networks assessed by clinical CT, has been used to suggest a loss of the complexity of the blood vessel network in disease alongside the reported loss of airways (Santos *et al.*, 2002). This study investigated part of the microvasculature not detectable using clinical imaging technique (HRCT resolution limit ~0.8 mm) and so any loss of branching vessels could show this loss of complexity at a smaller scale in peripheral lung. The trend of the data suggests a potential decrease in the number of branching vessels down to 25 µm in COPD samples, compared with the non-COPD samples. This was the closest metric investigated to suggest a potential significant difference between the grouped tissues, with a P-value of 0.08. Larger group sizes are required to see if the level of branching decreases in the COPD samples as potentially suggested by the trends of these results. It would also be important to take account of the sampling site and size of the tissue samples, as more peripheral samples contained less detectable branches (vessels <25 µm) giving a lower values than samples further into the lung tissue.

The number of terminal nodes reflects the number of vessels that lead directly into or out of the tissue volume and the capillary beds. A decrease in the terminal vessels would suggest a loss of network complexity and available sites for gas exchange in mild-moderate COPD (Weibel, 2015; Hsia *et al.*, 2016). The number of terminal nodes was expected to be approximately twice the number of branches as these values are directly related. However this was not the case in some of the samples in both groups, most likely caused by blood vessel networks near the cut surface of the sampled tissue, these vessels may enter and leave the sampled tissue at the cut surface, and did not always contain branching vessels.

Tortuosity is a common metric used for measuring 3D networks. In lung it has been used to investigate the 'twistiness' of blood vessels and airways in numerous respiratory disease as evidence for damage and remodelling of these networks (Helmberger *et al.*, 2014). The blood vessel networks from all 11 samples showed near-identical values across both the non-COPD and COPD groups. This similarity suggests the blood vessels in these tissue volumes are not undergoing any significant remodelling in response to damage or disease. Other studies investigating tortuosity in COPD have shown an increase in the value if the patient suffers from increased pressures seen in pulmonary hypertension, a common co-morbidity of COPD (Helmberger *et al.*, 2014). However these have not been evidenced in mild-moderate COPD with no known hypertension as was the case in some of the tissues used here. The increased use of µCT imaging and faster image processing could be used on larger studies in future to see if the tortuosity of blood vessels is different in mild-moderate COPD.

4.10 Conclusions

Methodology presented in chapter 3 enabled segmentation of blood vessel networks in 11 tissue block in approximately four days. This demonstrated proof of concept for the methodology's viability for larger research studies with potential in the future to be included in clinical studies once the technology has sufficiently advanced. Numerous metrics can be used to analyse these blood vessel networks, which could also be applied to larger studies and also those looking at different diseases or tissue types. No significant difference in any of the blood vessel measurements was found between the non-COPD and mild-moderate COPD groups. Branching of vessels could potentially reveal a change in the networks but would require a larger study to test for significant changes. The proof of concept for lung vasculature analysis at a scale not seen with conventional clinical 3D imaging, provides a new perspective on vasculature changes in COPD lung tissue. Further work on more samples similar to those seen here could lead to a greater understanding of microscopic vasculature loss or changes, visualised and analysed with 3D data, in diseased and non-diseased tissue.

Chapter 5 Characterising specific cell types in 3D human lung tissue

5.1 Introduction

This chapter builds on the methods developed in chapter 3 using immunofluorescence (IF) imaging to characterise structural elements in the tissue that cannot be identified by μCT alone such as airway epithelium and specific infiltrating cell types. IF was chosen over other conventional bright-field staining due to high contrast in the produced images as well as the ability to utilise multiple fluorescent channels (wavelengths) for imaging. This enabled specific imaging of cell types using different primary antibodies with bound secondary antibodies which were excited at wavelengths of light containing the least autofluorescence (i.e. provided the best image contrast). This high contrast in the staining compared to background signal facilitated threshold based segmentation of cells highlighted by IF. The wavelength of light with the peak autofluorescence was used to identify the tissue structure and was a crucial part of the 'automated warping script' used for registration with the μCT (see section 3.4). A third fluorescence channel was used to image individual cell nuclei with DAPI staining. This counterstain was used to confirm that IF staining was identifying nucleated cells. DAPI staining was combined with IF cellular staining to automate counting of individual cells as described in section 3.7.

Cytokeratin-18 (Ck18), a structural protein present in airway epithelium, was chosen to identify specific cells that link to lung physiology as part of a structure (the airways) which is visible in both the IF and μCT images. As reported in chapter 3 this was used to confirm that the registration and segmentation of the IF staining in the μCT was accurate by comparing visible airway structures in both imaging modalities. Changes in the small airways are a well-documented feature of COPD and can occur early in pathogenesis (McDonough *et al.*, 2011). Ck18 was used as a marker for the possible physiological changes in small airways present in the same tissue from both mild-moderate COPD and non-COPD patients, as detailed in chapter 4 (section 4.3).

Mast cells and macrophages, two cell types with key roles in lung immunology, were used as exemplars for imaging individual infiltrating cells within the 3D context of the lung tissue volumes provided by μCT. AA1 (anti-mast cell tryptase marker) was chosen due to the known abundance of mast cells in the lungs in both healthy and diseased tissue. The availability of a potent primary antibody already used as a positive control in the Ck18 staining also played a pragmatic part in the

selection of the AA1 primary antibody. Mast cells play a major role in many lung pathologies, although it is not thought to play a major role in COPD (Soltani *et al.*, 2012), they are very important in other diseases such as asthma (Bradding and Arthur, 2016). CD68 (used as a macrophage marker (Byrne *et al.*, 2016)) was chosen as the known role of macrophages in COPD has been investigated previously (Yamasaki and Eeden, 2018). This 2D staining was correlated with µCT volumes to give context and provide analysis of the data from non-COPD and COPD tissue in 3D.

This chapter aims to use exemplar immunoreactivity of cell types linked to lung physiology (airway epithelium) and immunology (mast cells and macrophage) to investigate changes occurring between non-COPD and COPD tissue. While network analysis of the blood vessels described in the previous chapter failed to show any significant differences between the patient groups we might anticipate that structural and cellular changes are occurring in mild COPD. Unlike the blood vessels these would be expected to change in number and distribution in mild disease compared to healthy tissue. We are also expecting to see the changes in mild disease occurring in the smallest airways and immune cell population which can't be detected using clinical CT or µCT imaging alone.

5.2 Aims and objectives

The aim of this chapter was to localise and characterise the distribution of specific immunoreactivity in 3D using correlate µCT and immunofluorescence data between COPD and non-COPD human lung tissue

The main objectives for this chapter were as follows:

1. Perform and register IF staining of Ck18, AA1 and CD68 to µCT lung tissue scans
2. Assess the presence of Ck18 positive airway epithelial cells and use this to build a 3D map of Ck18 epithelial cells in non-COPD and mild-moderate COPD tissue
3. Image and quantify individual cellular populations of mast cells and macrophages within the lung volumes of non-COPD and mild-moderate COPD tissue
4. Combine IF localisation with chapter 4 results to analyse how the CK18 and immune cells are related to the 3D network of blood vessels
5. Analyse the distribution of specific cell types in their 3D environment by implementing the results of the correlative imaging workflow

5.3 Cytokeratin staining and imaging

5.3.1 CK18 immunofluorescence

Ck18, a structural protein present in the airway epithelium, was used as an exemplar for method development and this was expanded in this chapter to analyse potential physiological differences between non-COPD and mild-moderate COPD tissue. Ck18 localisation within the tissue was visualised using immunofluorescence (IF) (as detailed in section 2.6), the high contrast imaging of Ck18 facilitated the segmentation techniques developed in sections 3.4 and 3.5. This staining, registration and segmentation was carried out on several tissue sections from non-COPD and COPD tissue.

5.3.1.1 Presence of Ck18 epithelial staining

Ck18 positive staining of morphologically distinct epithelial cells was found in 8 of the 11 tissue blocks investigated in this study. The presence of Ck18 staining was not related to disease status and was most likely caused by the tissue sampling. As the tissue could only be identified as being macroscopically normal from surgery without being able to inspect whether the microstructure was intact. µCT scouting was used to try and rectify this in sample selection by looking for the presence of 3D networks, however this did not specify between blood vessel and airway networks. While all the tissue was identified as macroscopically normal, the lung is a heterogeneous organ therefore it is possible for the relatively small sampling site to lack intact airway structures. All the tissue blocks, including the three tissue blocks not containing Ck18, had 50-200 serial sections cut at a thickness of 4 µm to check for the presence of Ck18. Positive controls using the same antibody (Ck18) on different tissue and different antibodies on the same (non-Ck18) tissue were included in all the staining runs.

Four tissue blocks from each group contained at least one section with positive Ck18 staining of morphologically distinct epithelium. This was determined by comparison to the dense nuclei staining using DAPI or, if available, neighbouring H&E stained sections. Therefore the analysis of the staining was performed using four tissue blocks each from the non-COPD and COPD groups. A brief summary of patient characteristics is shown in Table 5.1, the columns greyed out show the tissue blocks excluded from Ck18 analysis.

Table 5.1: **Summary of the key clinical information and previous volume measurements of each of the tissue blocks used in this section.** The three tissues not containing Ck18 staining (Non-COPD-1, Non-COPD-3, COPD-3) have been excluded. Data presented as median grouped values plus the interquartile range in parentheses, for full information see appendix A.1**.** P-values of numerical results show were calculated using the Mann-Whitney test between the grouped Non-COPD and COPD tissues. For Gender and smoking status P-values were calculated using Fisher's exact test.

Group	Non-COPD	COPD	P-value
Age	66 (2.5)	70.5 (6)	0.6948
Gender	2F 2M	2F 2M	>0.9999
FEV_1 %predicted	91 (14.25)	71.5 (6)	0.026
FEV_1/FVC	0.75 (0.035)	0.605 (0.05)	0.0022
GOLD status	0 (0)	2 (0)	n/a
Smoking status	2 current 2 ex	2 current 2 ex	>0.9999
Tissue volume [mm^3]	35 (19.33)	122 (161.5)	0.1255
Blood vessel volume fraction [%]	2.75 (1.5)	1.9 (0.8)	0.829

5.3.1.2 Comparison to controls

As stated in section 2.6.1 each IF staining run contained negative and positive controls, shown in appendix A.8. It can be observed that there is no signal being generated by non-specific binding of the secondary or intrinsic background autofluorescence at the imaging wavelength from the negative controls. Positive staining was identified as fluorescence signal which was not present in the negative or positive controls using a different primary antibody.

5.3.2 Assessment of staining (2D)

Ck18 IF staining was used to identify structural proteins (intermediate filaments) present in the airway epithelium of the sectioned human lung tissue. This was used to localise airway epithelium over multiple 2D sections to begin the building of a 3D network of Ck18 positive staining. IF staining was successful on tissue sections, from the 8 tissue blocks detailed in section 5.3.1, specifically binding to morphologically distinct airway epithelium (of both collapsed and open airways). As seen in Figure 5.1 the Ck18 staining (pink) is clearly distinguishable from the background autofluorescence, which is low at the imaged wavelength of light. The staining is also clearly distinguishable from the autofluorescence captured using the FITC channel (green, Figure

5.1). This dual channel overlay image assisted in localising the Ck18 staining in relation to the lung parenchyma seen in the FITC channel image. The high-magnification images show the Ck18 staining on the inner edge of the collapsed airway lumen, indicating the location of the airway epithelium. Staining was consistent between the non-COPD and COPD tissues which contained positive Ck18 staining.

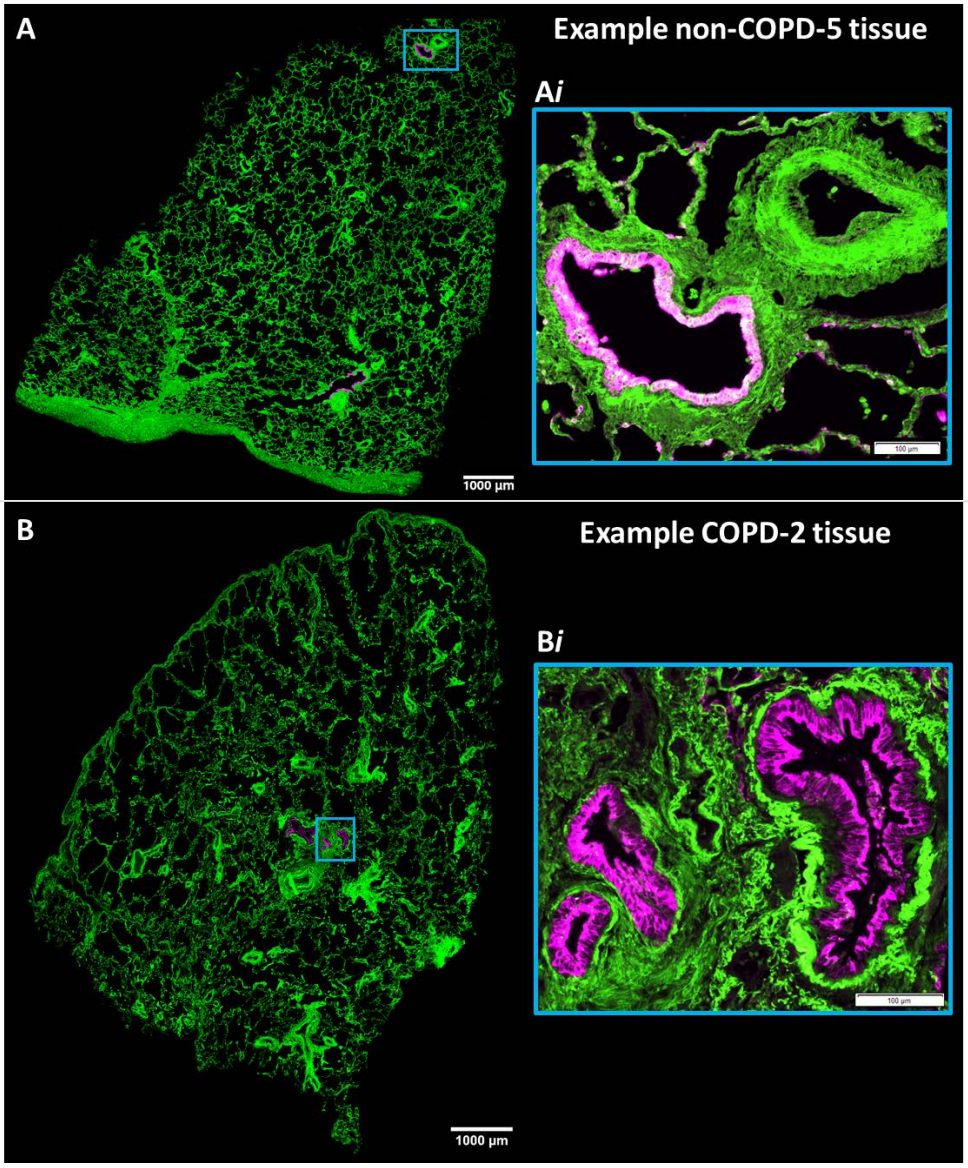

Figure 5.1: **Images representative of IF staining for positive Ck18 localisation (pink) overlaid on tissue autofluorescence (green)**.A & B: Wide-field IF images of tissue sections from non-COPD-5 and COPD-2 blocks are shown. The green tissue autofluorescence was captured at 490 nm excitation (FITC channel) and the Ck18 IF was captured at 629-669 nm excitation (CY5 channel). Overlay used to highlight location of Ck18 positive staining in relation to the lung parenchyma seen in the autofluorescence channel. Right hand images (A*i* & B*i*) captured using a 10x objective on the Olympus VS110 fluorescence slide scanning microscope.

5.3.3 Serial staining of Ck18

Each tissue block was stained for IF imaging of Ck18 localisation on sections approximately 40 µm apart to provide multiple levels of 2D staining throughout the sectioned tissue volume. This sectioned sub-volume of tissue was at a thickness between 200 and 800 µm, depending on the volume of tissue available for sectioning (50-200 serial sections from each block). All IF images were produced from the sectioned sub-volume and any analysis of the IF staining in 3D used this sub-volume of tissue dubbed the 'sectioned volume'. This applied to the µCT volume which was cropped in the z-direction to match the sectioned volume of tissue. Figure 5.2 shows a representative montage of images stained for Ck18, approximately 40 um apart, over part of the sectioned volume of tissue in representative non-COPD and COPD tissue blocks. The sections were also stained at different times for different imaging runs, the similarity of the staining highlights the robustness and repeatability of the IF staining using Ck18.

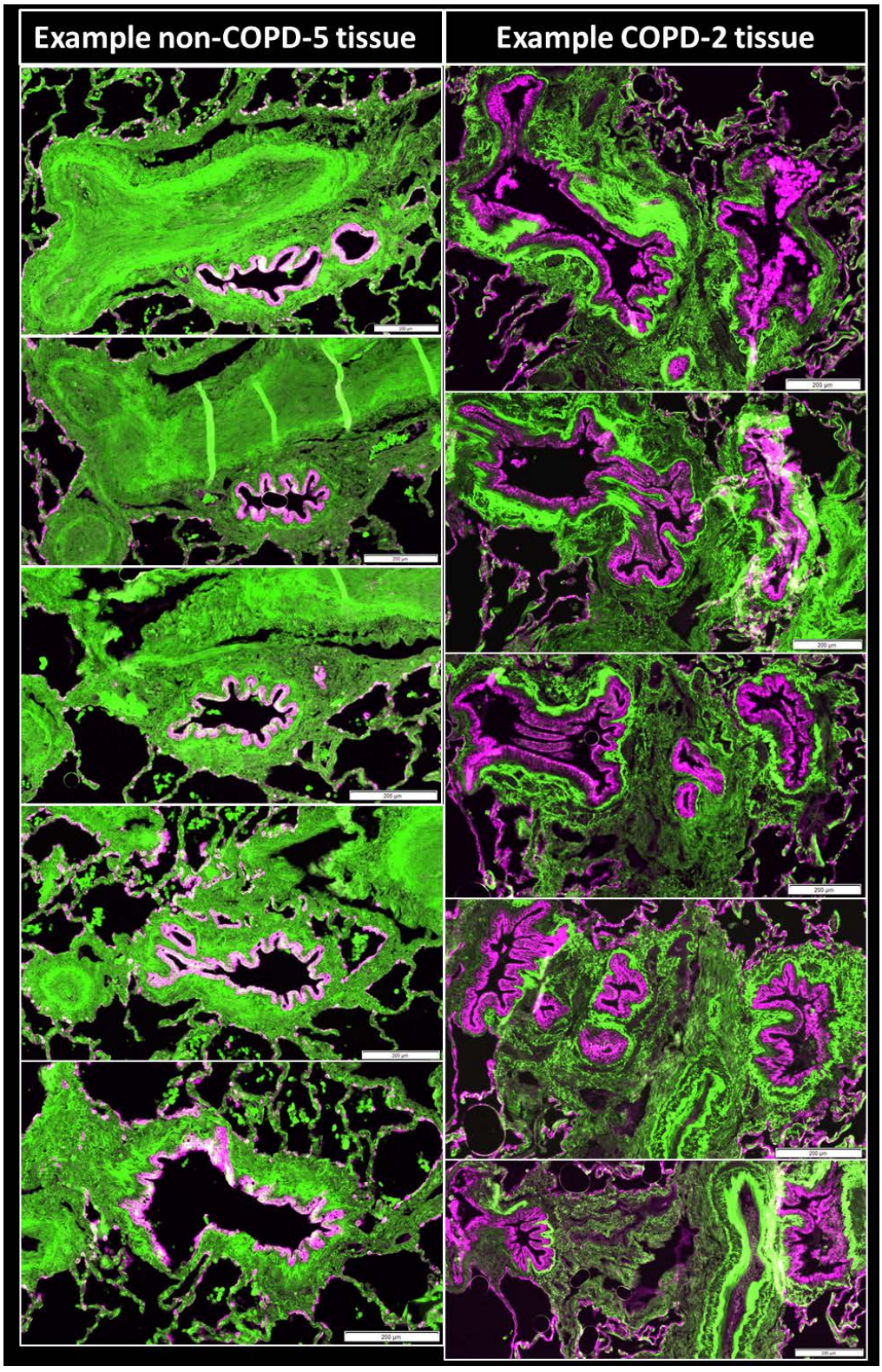

Figure 5.2: **Ck18 staining of representative non-COPD-5 and COPD-2 human lung tissue serial sections spaced 40 µm apart**.Magnified images of areas of tissue containing positive Ck18 staining are shown for both tissues. This staining follows airway epithelial staining over part of the section volume with a total depth of 200 µm being represented. Images captured using a 10x objective, scale bars =200 µm.

5.3.4 Segmentation of µCT

Using the 'automated warping script', detailed in section 3.4.5, the Ck18 stained IF images were successfully registered to the corresponding µCT slices and used to segment Ck18 localisation within the µCT volume. This script worked on batches of images following each IF staining run which successfully registered and segmented all of the IF stained images to the µCT volume. The script took approximately 2 minutes to register and warp the three IF images (autofluorescence, Ck18 and DAPI) to the µCT slice. The whole process was completed on 104 Ck18 stained sections (each containing the three channels mentioned above) from 8 different tissue blocks, in under 3.5 hours. Figure 5.3 shows the segmentation of Ck18 on µCT slices within the sectioned volume next to the original IF images to illustrate the direct transfer of the Ck18 localisation from the IF images to the µCT. Segmentation masks were generated by thresholding the IF images to remove signal from the non-epithelial staining, which produced weaker fluorescence signal than the Ck18 staining in the airway epithelium. These images match the first and last images seen in Figure 5.2 in the context of the 3D µCT.

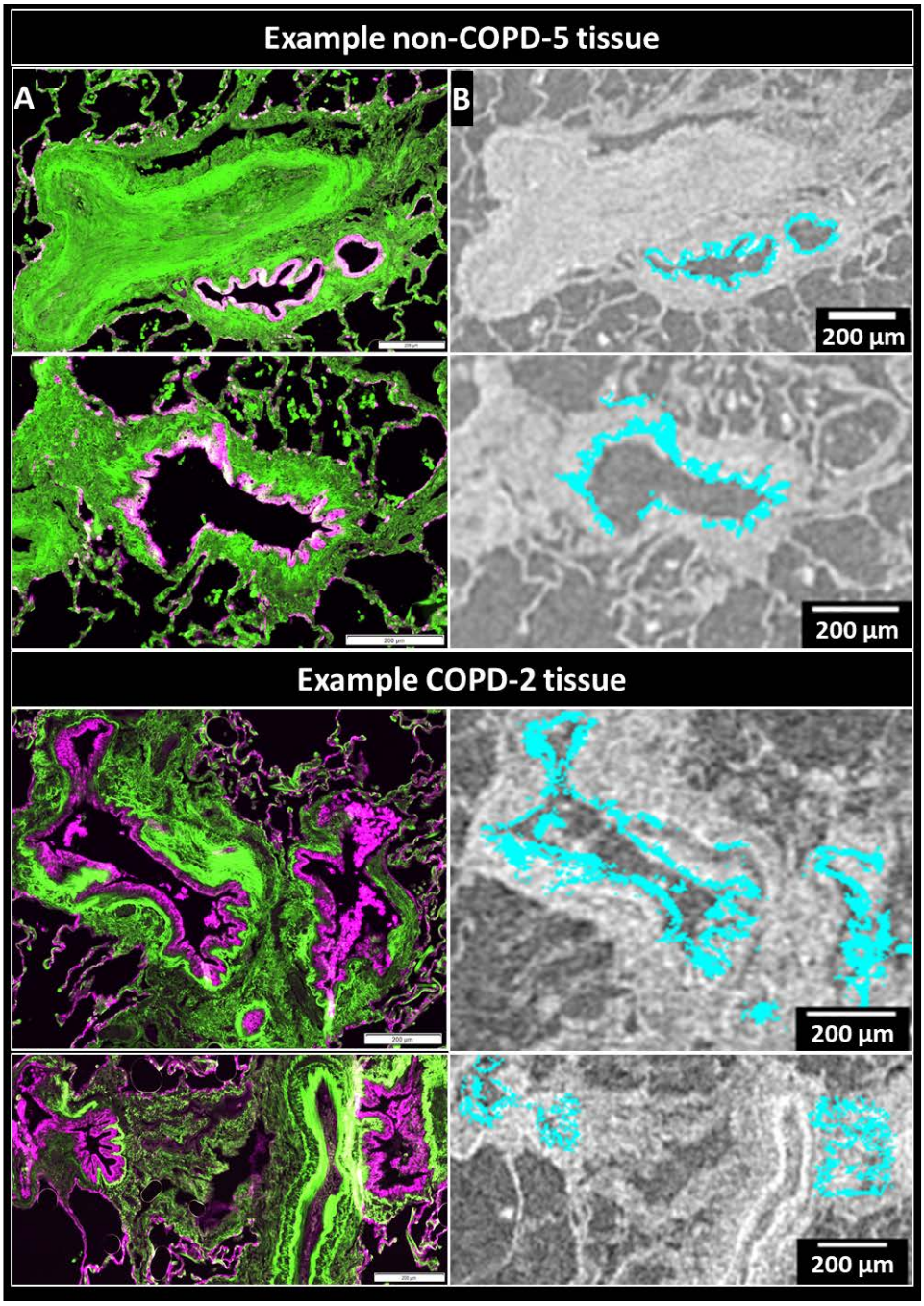

Figure 5.3: **Comparative localisation of Ck18 staining using IF and Ck18 segmentation on corresponding µCT images of representative non-COPD and COPD human lung tissue.** The left column (A) shows IF images previously seen in Figure 5.2 of Ck18 IF staining (pink) and the tissue autofluorescence (green). The right column (B) shows corresponding µCT images with segmented Ck18 localisation (cyan) directly inferred from the warped IF images. Only areas of positive epithelium staining were segmented via thresholding thus removing other areas of non-epithelial staining with weaker signal highlighted in the IF tissue. Images taken from non-COPD-5 and COPD-2 tissues captured using µCT and IF microscopy, scale bars = 200 µm.

5.3.5 Area fractions of Ck18 staining

Area fractions were calculated from the registered Ck18 staining, after thresholding for segmentation, as a percentage of the tissue area from the corresponding µCT slice. This was the same methodology used for vascular fraction (section 4.5) however, this was performed as a series of 2D analysis within the sectioned volume. Figure 5.4 provides a summary of the results from each individual tissue block from both groups. There was no significant difference (P-value: 0.68) between the non-COPD and COPD tissue groups. However the graph shows that in the majority of the tissue blocks the fractions vary as an airway is followed up or down the volume changing in size and shape as the airways branch or diminish throughout the sectioned volume. There are however a couple of exceptions to this; non-COPD-2 and COPD-5 showed little change in the Ck18 fraction across the section volume. Thus suggesting little change in the airway structure over this volume of tissue.

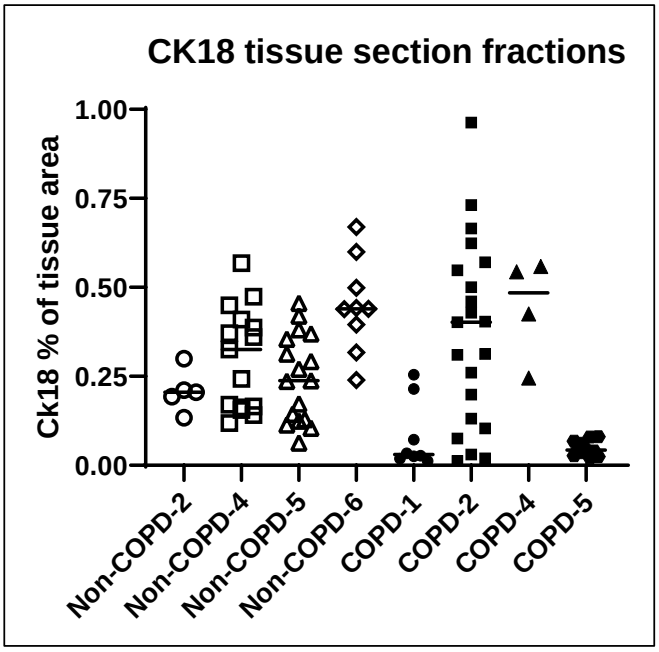

Figure 5.4: **Total percentage area of Ck18 localisation in the tissue sections of each of the tissue blocks.**Each individual plot equals a separate area measure normalised by the tissue area of the individual section, the line denotes the median value. Only sections with positive Ck18 epithelial staining were included in the measurements resulting in the variability in the n number of plots per tissue.

5.3.6 Interpolation and volume fractions

Following the generation of the segmentation masks within a single volume the Ck18 positive staining was interpolated (following the methods detailed in section 3.6) and representative images from each group can be found in Figure 5.5. The approximate volumes of these interpolated networks were measured and when compared with the 2D analysis showed no significant difference between the mean or median area tissue fractions (from the previous section) and the volume fractions. The volumes were consistent with the 2D analysis suggesting that the interpolation was not generating or losing Ck18 localisation information and could be used for 3D analysis and comparisons. The volume fractions of each group were calculated and analysed, using a Mann-Whitney test, to show no significant difference (P-value: 0.69) between the non-COPD and COPD groups.

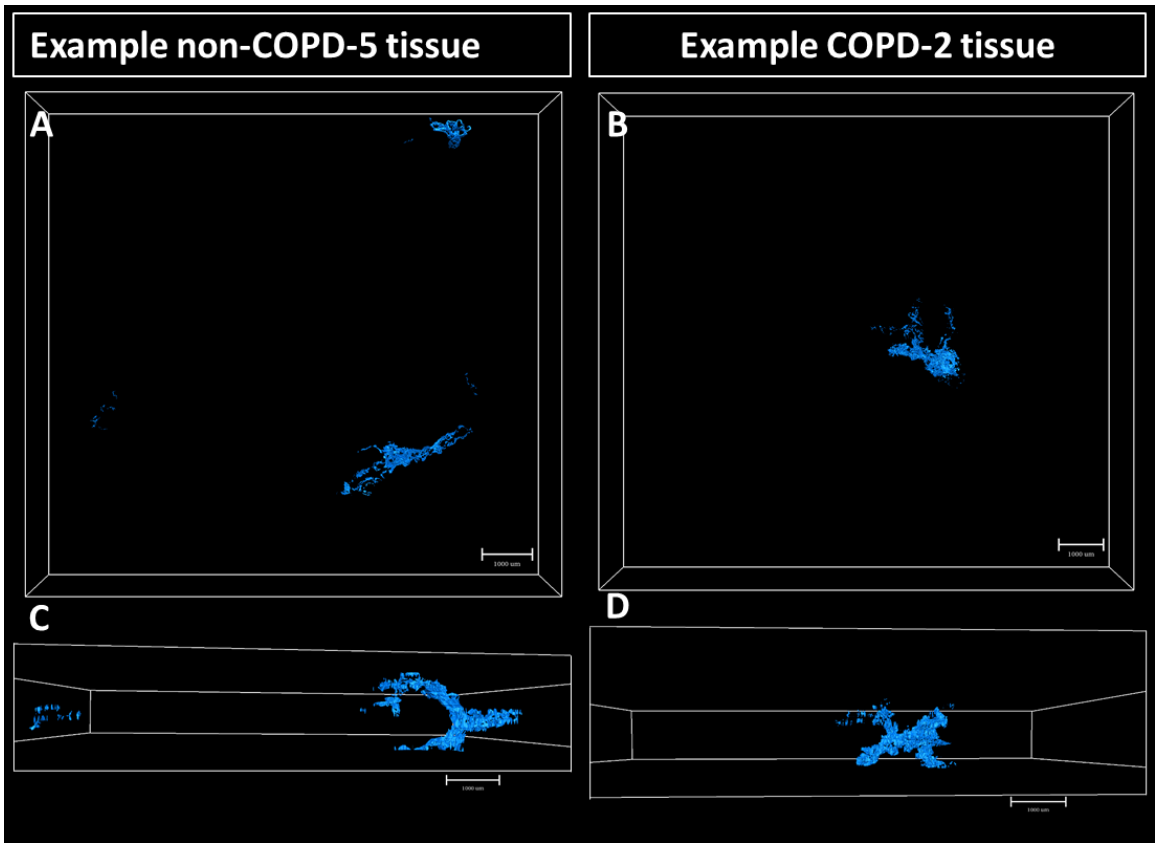

Figure 5.5: **Representative interpolation of Ck18 localisation from IF staining visualised in 3D in non-COPD-5 and COPD-2 tissue**.A & B: The interpolated Ck18 from the front (*xy*-plane) and the lower two panels (C & D) show the Ck18 from the bottom (*xz*-plane). Each segmented µCT slice was interpolated in ITK-SNAP (v 3.6) and exported to Avizo (v 9.3) where it was masked and visualised as a 3D surface.

5.3.7 Comparison to blood vessels

Combined visualisation of the interpolated Ck18 and blood vessel sectioned volumes can be seen in Figure 5.6, alongside the percentage of tissue volume measures calculated in sections 4.5 and 5.3.6. The tissue blocks shown in Figure 5.6 contain the smallest blood vessel volume fraction from each group but still illustrate the greater amount of identified blood vessels compared to Ck18 localisation. This is consistent across all tissue blocks when assessing the volume fractions. These differences can be quantified by comparing the volume fractions of the blood vessels and the interpolated Ck18 staining. This also confirmed that the presence of Ck18 had no direct impact on the blood vessel volumes, which showed more variation, in either the non-COPD or COPD tissue.

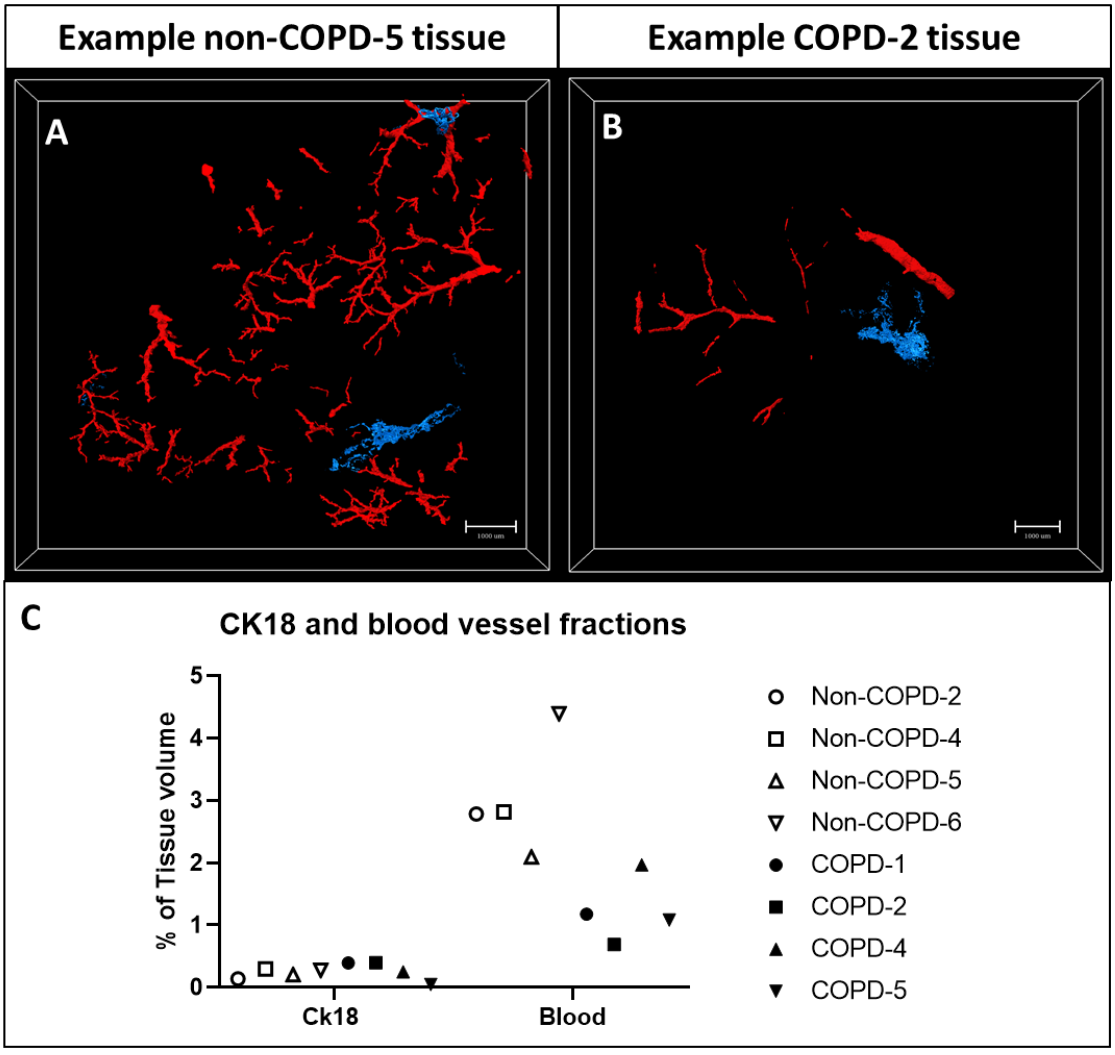

Figure 5.6: **Visual and measured comparison between the interpolated Ck18 and blood vessel volume fractions.**A & B: The visualised non-COPD-5 and COPD-2 tissues contain the least amount of blood vessels in the section volume. However, this is still a greater volume than the interpolated Ck18 localisation which is relatively constant in all the tissue blocks (as shown in C).

The Ck18 volume fraction appears to have no correlation to the blood vessel fraction with low Ck18 in all tissue blocks but more variance in the blood vessels. Although blood vessels appear lower in the COPD tissue here as reported in section 4.5 there was no significant difference in the total blood vessel volume of the tissue. There was no apparent direct relation between Ck18 and blood vessels in non-COPD or mild-moderate COPD tissue, however there is not enough data here to make any significant conclusions on this.

5.3.7.1 Blood vessel to Ck18 distance maps

The distance maps previously used to assess the distribution of blood vessels within the tissue (section 4.7) were used to calculate the distribution of Ck18 in relation to the blood vessel network. In lung physiology the relationship between blood vessels and airways is important for efficient gas exchange in the alveoli. Any potential change in the relative distribution of these networks could be indicative of diseases including COPD where small airways are lost (McDonough *et al.*, 2011). Using distance maps provides a novel look at the relationship of these networks in 3D at a much smaller scale than analysis provided by clinical CT.

Interpolation from stained sections (section 5.3.6) generated the predicted 3D distribution of all Ck18 immunostaining in the sectioned volume. The distance of each of the voxels predicted to contain CK18 immunoreactivity from any blood vessel was calculated using a distance map. The results of this are plotted and visualised in 3D in Figure 5.7 for the non-COPD tissue and Figure 5.8 for the COPD tissue. The majority of interpolated Ck18 staining was located within 500 µm of the nearest blood vessel with no significant difference between the non-COPD and COPD groups. The peak number of Ck18 positive voxels is located between 100 µm and 600 µm in the majority of the tissues. Despite the counts of Ck18 varying greatly (y-axis) the distribution suggested by the peaks of the data remain consistent in tissues with differing amounts of Ck18. An example of this is non-COPD-4 (Figure 5.7) and COPD-4 (Figure 5.8) which both have peaks in the number of Ck18 voxels at approximately a 250 µm distance but have counts (y-axis) differing by over 10,000. The differences can be seen in the visualisations with the Ck18 segmentation containing more purples and greens highlighting the Ck18 is located further from blood vessels than the segmentation which is blue. The majority of the tissues contained a single peak of Ck18 localisation in relation to blood vessels, those with two or more peaks contained multiple airways spaced throughout the tissue at differing distances to the nearest blood vessel.

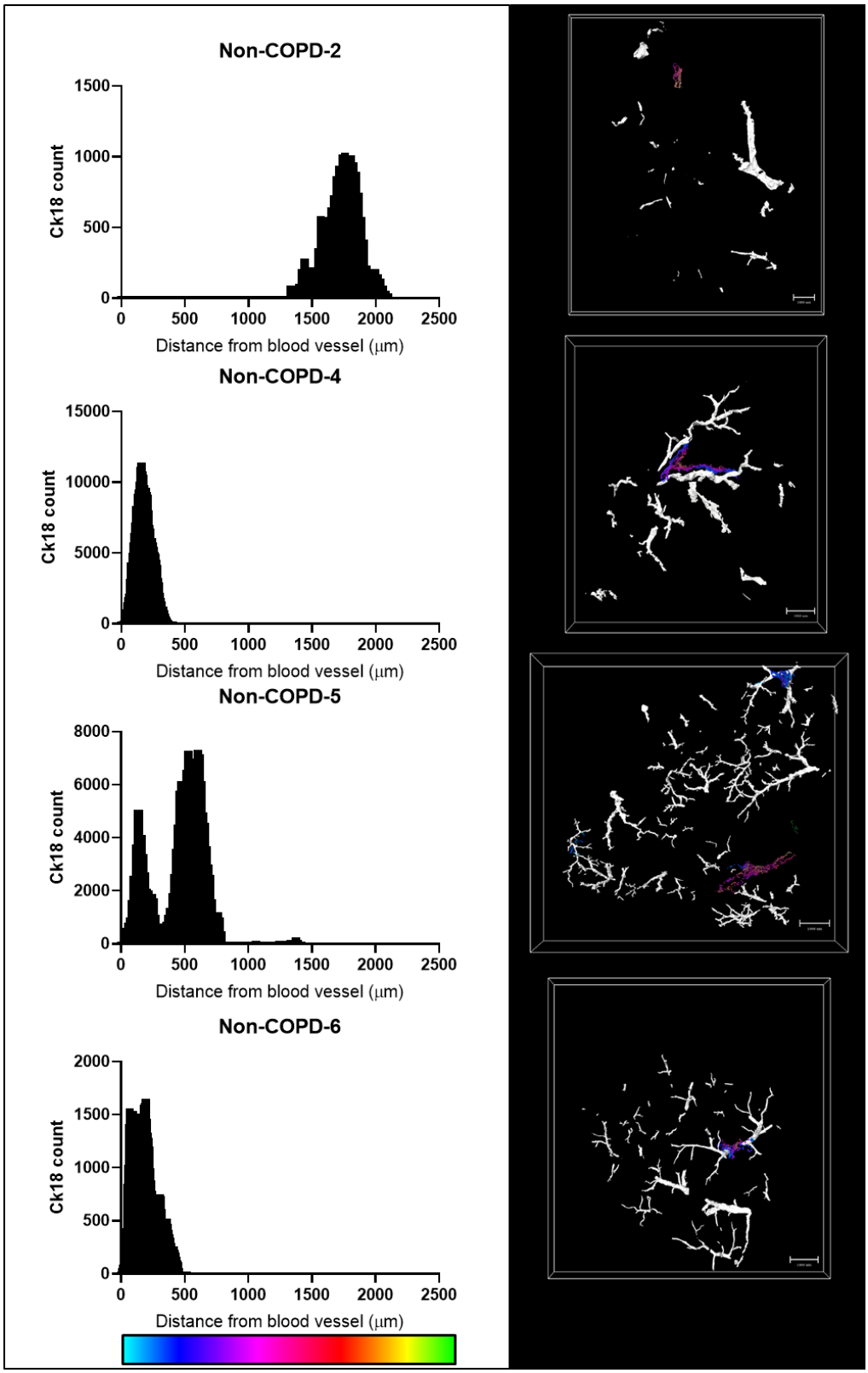

Figure 5.7: **Distribution of interpolated Ck18 in relation to blood vessels in the non-COPD tissues.** The graphs in the left column show the closest distance each voxel of interpolated Ck18 is to the nearest segmented blood vessel. The images in the right column show the segmented blood vessel network (white) and the interpolated Ck18. The colour of the Ck18 surface corresponds to the distance from the nearest blood vessel following the key seen at the bottom of the figure.

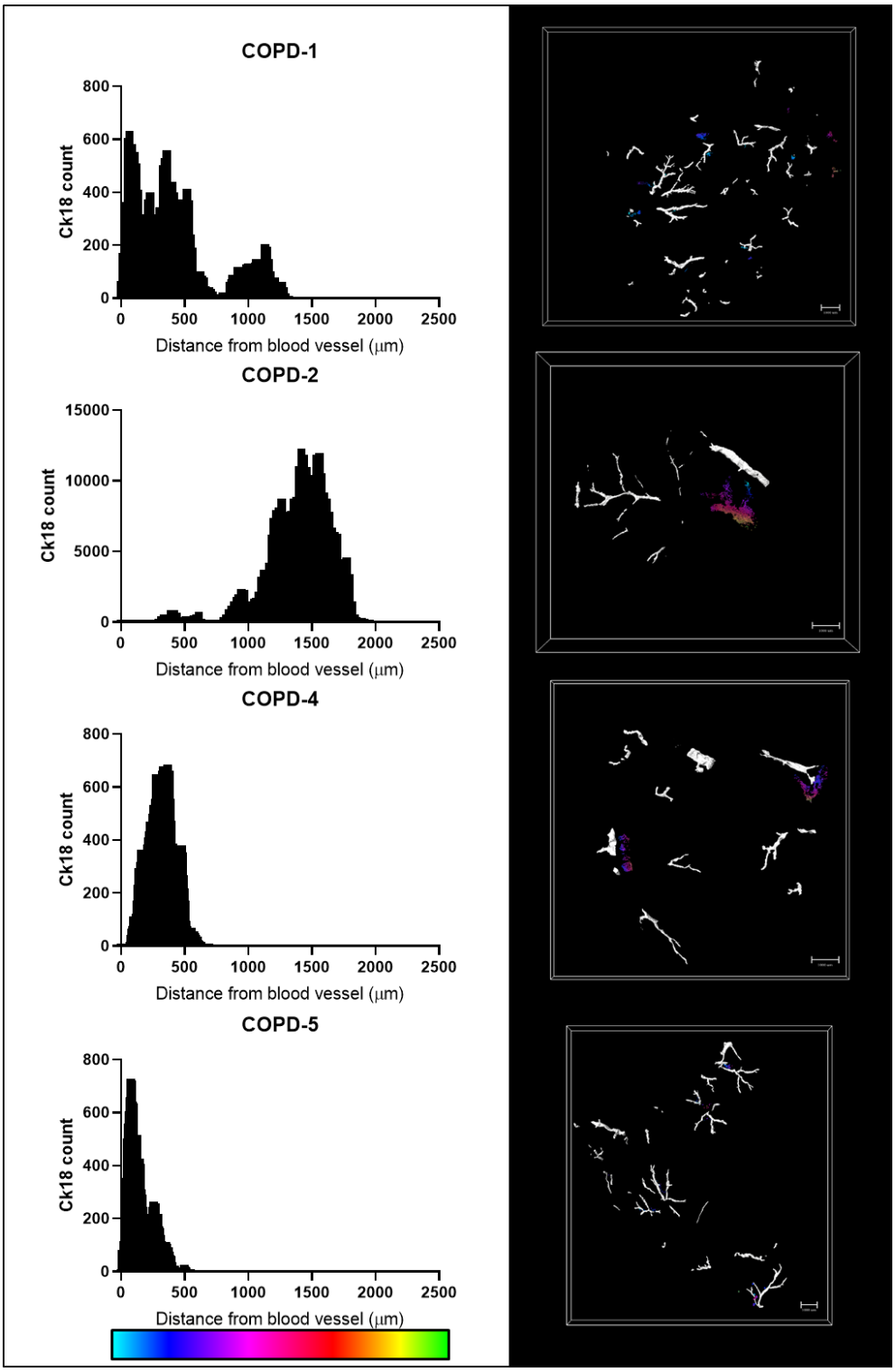

Figure 5.8: **Distribution of interpolated Ck18 in relation to blood vessels in the COPD tissue.** The graphs in the left column show the closest distance each voxel of interpolated Ck18 is to the nearest segmented blood vessel. The images in the right column show the segmented blood vessel network (white) and the interpolated Ck18. The colour of the Ck18 surface corresponds to the distance from the nearest blood vessel following the key seen at the bottom of the figure.

There were exceptional cases in the distributions with the non-COPD-2 and COPD-2 tissues both containing distance peaks between 1500 µm and 2000 µm from the nearest blood vessel. These are shown with the adjoining image to the relevant graph which visualises this increased distance from the blood vessels within the volume. This 3-4x difference in distance was not caused by any significant difference in the blood vessel or Ck18 fraction from the rest of the tissues in the groups. These measures are limited to the sectioned volume and the exceptions could be caused by blood vessels outside the section volume not being part of the distance map. Repeated measures using the full volume of blood vessels are required to investigate whether this is the cause of the differences seen in the data. Further work would be required by expanding the section volume with more staining also to provide a full map of the distribution of Ck18 positive epithelium in relation to blood vessels.

5.4 AA1 staining

Mast cell staining, using AA1 as a marker, was used to provide an immunological and pathological context to the methodology by identifying cells not visible in the µCT. As previously mentioned this was a pragmatic choice for an exemplar cell type which is abundant in both healthy and diseased lung tissue. Mast cells provided an interesting context in the lungs being involved in many respiratory diseases (e.g. asthma).

5.4.1 AA1 immunofluorescence

AA1 IF staining was completed on all the tissues from both the non-COPD and COPD groups of tissue. This used the same methodology for IF staining as the Ck18 by changing the primary antibody to AA1, and was similarly registered to the µCT using the 'automated warping script'. A brief summary of patient characteristics is shown in Table 5.2, unlike Ck18 staining no tissue blocks were excluded from analysis due to a lack of staining.

Table 5.2: **Summary of tissue blocks used in this section including the tissue and network volumes reported previously.** Data presented as median grouped values plus the interquartile range in parentheses, for full information see appendix A.1**.** P-values of numerical results show were calculated using the Mann-Whitney test between the grouped Non-COPD and COPD tissues. For Gender and smoking status P-values were calculated using Fisher's exact test.

Group	Non-COPD	COPD	P-value
Age	66.5 (2.5)	70 (6)	0.6948
Gender	2F 2M	2F 2M	>0.9999
FEV_1 %predicted	91 (14.25)	69 (6)	0.026
FEV_1/FVC	0.76 (0.035)	0.62 (0.05)	0.0022
GOLD status	0 (0)	2 (0)	n/a
Smoking status	2 current 2 ex	2 current 2 ex	>0.9999
Tissue volume [mm^3]	35 (21)	87 (118)	0.1255
Blood vessel volume fraction [%]	2.15 (1.9)	1.6 (0.8)	0.829
Ck18 volume fraction [%]	0.315 (0.16)	0.22 (0.35)	0.8

AA1 was initially used as a positive control due to the high efficacy and reliability of the primary antibody, as well as the knowledge that mast cells would always be present in the types of tissue we were investigating. However, after having some staining in most of the tissue it was decided to extend the staining to provide enough data for analysis. This also served as a proof of concept for the developed methodology on individual cellular staining. Exemplar images of AA1 staining, in relation to the lung parenchyma from tissue autofluorescence and in relation to other individual cells using DAPI nuclei staining, from both non-COPD and COPD tissue can be found in Figure 5.9.

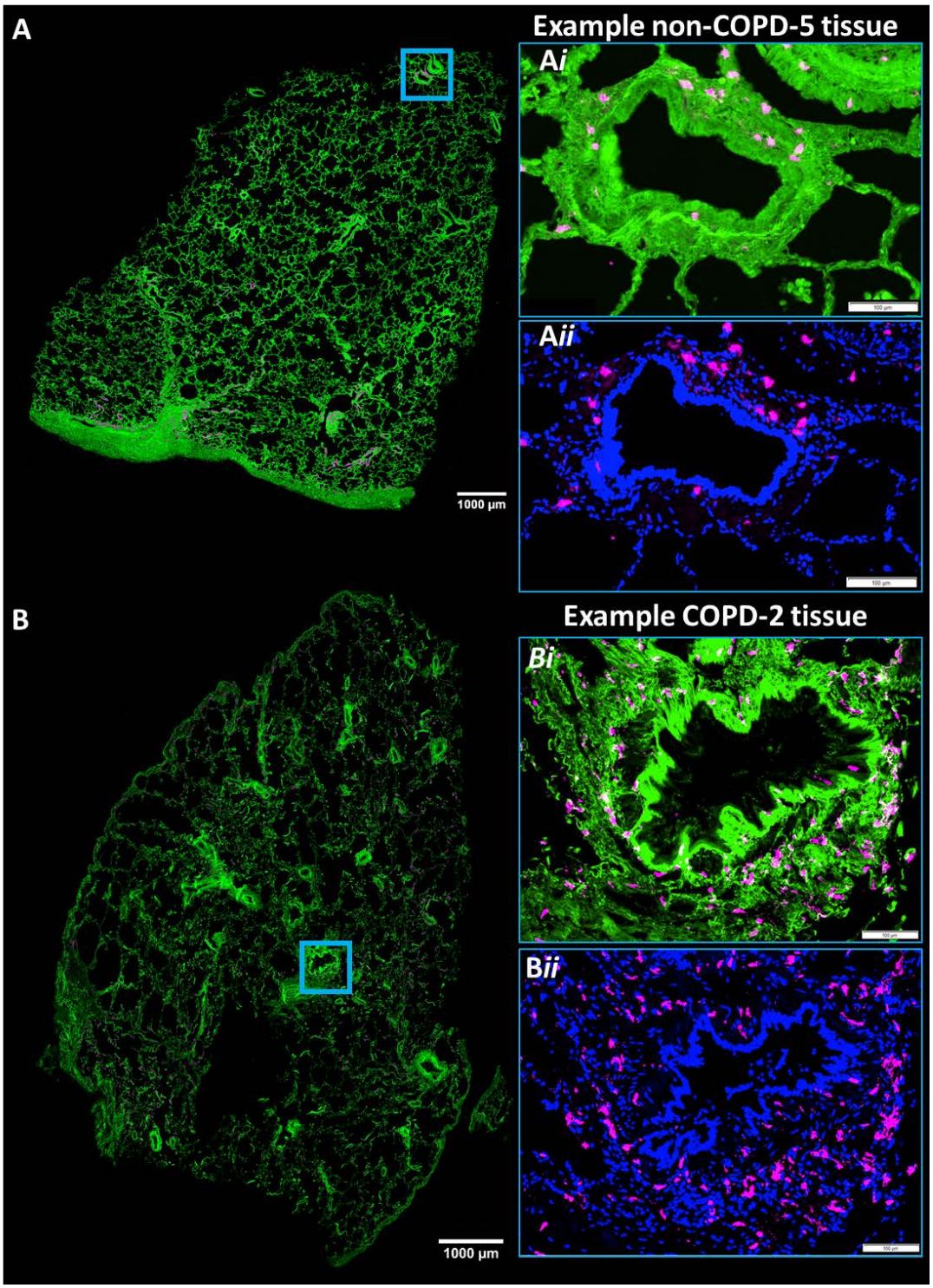

Figure 5.9: **Images representative of IF staining for positive AA1 localisation (pink) overlaid on tissue autofluorescence (green) and DAPI nuclei staining (blue).**A & B: Wide-field IF images of tissue sections from non-COPD-5 and COPD-2 blocks are shown. The green tissue autofluorescence was captured at 490 nm excitation (FITC channel), the AA1 IF was captured at 629-669 nm excitation (CY5 channel) and DAPI nuclei staining was captured at 372 nm excitation. Magnified right images used to highlight location of AA1 positive staining in relation to the lung parenchyma (autofluorescence, A*i* & B*i*) and other cell nuclei (DAPI, A*ii* & B*ii*).

5.4.2 Analysis of staining

After image acquisition, each AA1 stained section was masked using the DAPI staining as detailed in section 3.7.1 and AA1 positive cell nuclei were counted automatically. These counts were normalised by using the tissue area (mm^2) measured from the FITC channel image to calculate the number of cells per mm^2 of tissue. The results of the raw counts and normalised counts are shown in Figure 5.10. After normalisation there was no significant difference between the non-COPD and COPD groups with no observed differences between the values within the groups either. This was despite the much higher cell counts in the COPD-1 tissue with total counts at over 30,000 in half of the sections stained. Following normalisation the cells per mm^2 fit in with the other tissue measures, showing that these high counts were related to the higher amount of tissue in the sections compared to the other tissues.

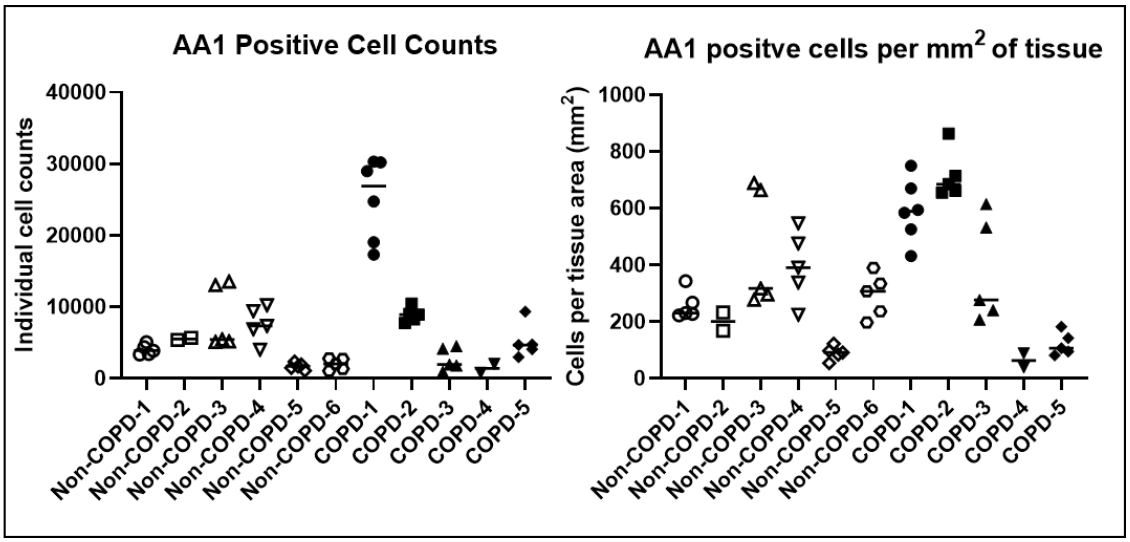

Figure 5.10: **Results of the AA1 positive mast cell counts and normalised values per tissue area for each section from all non-COPD and COPD tissue blocks**.The raw cell counts reported in the left graph were the measurements taken automatically using the analyze particles plugin in Fiji of the DAPI masked cellular staining. The FITC channel image of tissue autofluorescence was used to calculate the tissue area which was used to normalise the cell counts shown in the right graph. Line denotes the median value.

These results were based on thousands of cells being counted per section, something which would not be feasible in the standard cell counting workflow. In total 366,998 individual cells were counted across all of the sections stained for AA1 across both groups. This highlighted the strength of this technique for comprehensive counts of whole tissue sections, something not

really possible with manual counts. This was completed in approximately 5 minutes per section making it quicker than manual counts looking for much smaller numbers of positive cells per area of a section. Future work is required to compare this method with the current gold standard of manually counting cells in a specific region of interest in the tissue section. This is important to prove the accuracy of the method ensuring that no double counting or image artefacts (e.g. edge effects) are being included in the final counts.

Similar to the Ck18 staining the AA1 staining was completed on serially cut sections approximately 40 µm apart as a representation of cellular localisation within the section volume. However, unlike Ck18 there is no structure or feature directly associated with AA1 and so the change in the distribution of individual cells was visualised. With a distance of approximately 40 µm between sections in the z-direction there was no risk of double counting cells between sections. However, partial cells within the thickness of the tissue section (4 µm) were still counted, which would overestimate any calculations for the absolute number of cells per volume. Relative comparisons spaced throughout the volume were used to minimise the risk of double counting cells.

5.4.3 Segmentation of µCT

The AA1 staining was successfully segmented onto corresponding µCT planes using the same methodology as the Ck18 localisation. The only difference came in visualisation within the µCT volume as seen in Figure 5.11. For ease of visualisation the segmentation was dilated (as a sphere) in Avizo by 3 voxels, this was purely done for visualisation as the individual cells were too small to see clearly at a level of magnification which contained the whole µCT section volume of tissue. The 2D IF staining and subsequent localisation of AA1 staining in the µCT in 2D and 3D is visualised in Figure 5.11.

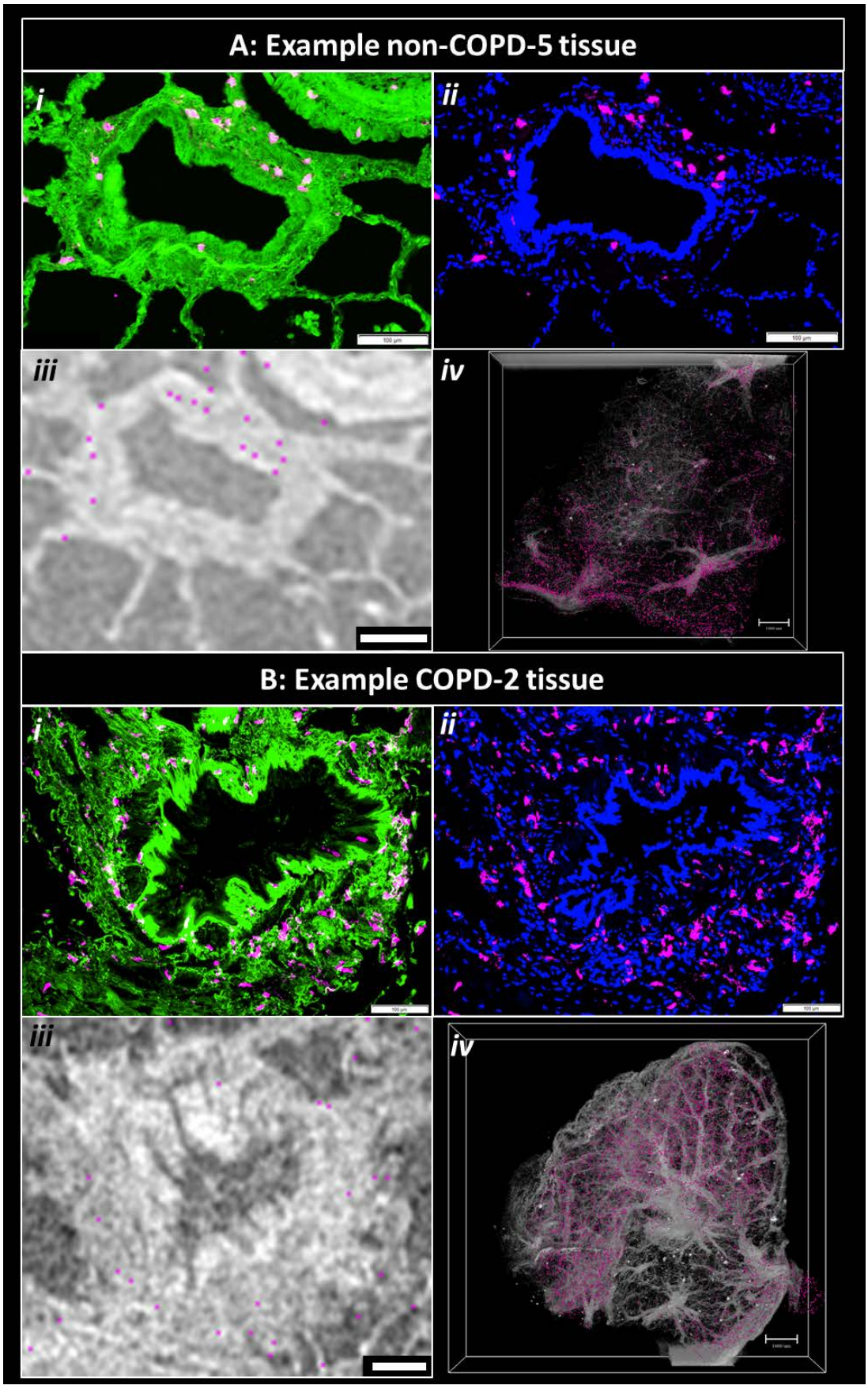
A: Example non-COPD-5 tissue
i
ii
iii
iv
B: Example COPD-2 tissue
i
ii
iii
iv

Figure 5.11: **Comparative 2D and 3D localisation of AA1 staining using IF and AA1 nuclei segmentation on corresponding µCT images of representative non-COPD-5 and COPD-2 human lung tissue**.(Previous page) A*i*, A*ii*, B*i* and B*ii* show IF images previously seen in Figure 5.9 of AA1 IF staining (pink), tissue autofluorescence (green, panels *i*) and DAPI staining (blue, panels *ii*). A*iii* & B*iii* show corresponding µCT images with segmented AA1 localisation (pink) after masking and eroding to a single voxel using the DAPI images. (Figure 5.11 continued): A*iv* & B*iv* show the AA1 localisation within the 3D sectioned volume. The visualised segmentation was dilated by 3 voxels to ease visualisation. Segmentation taken from 5 planes spaced evenly throughout the section volume, scale bars on high mag images = 200 µm.

5.4.4 Distance maps

Distance maps were used as a method to evaluate the distribution of mast cells in relation to the 3D networks of blood vessels and airways. These measures used the 'ultimate points' tool in Fiji to reduce the size of the cellular segmentation to a single central pixel, which provided a single distance measure for each AA1 cell nuclei. If mast cell mediators were more active in the lung it could relate to changes in the distance of mast cells to the blood vessels or airways. Here the distance of AA1 staining to the 3D networks of blood vessels and interpolated Ck18 within the sectioned volume were assessed. The results of the AA1 distances to blood vessels are reported in Figure 5.12. Here the pattern of distribution in all non-COPD and COPD tissues shows that the majority of AA1 staining is located within 2000 µm to the nearest blood vessel. The peak distance of the highest number of AA1 positive cells is approximately 500 µm from the nearest blood vessel. Non-COPD-5 is the only major exception of this where the highest peak of AA1 is located less than 100 µm from the nearest blood vessel.

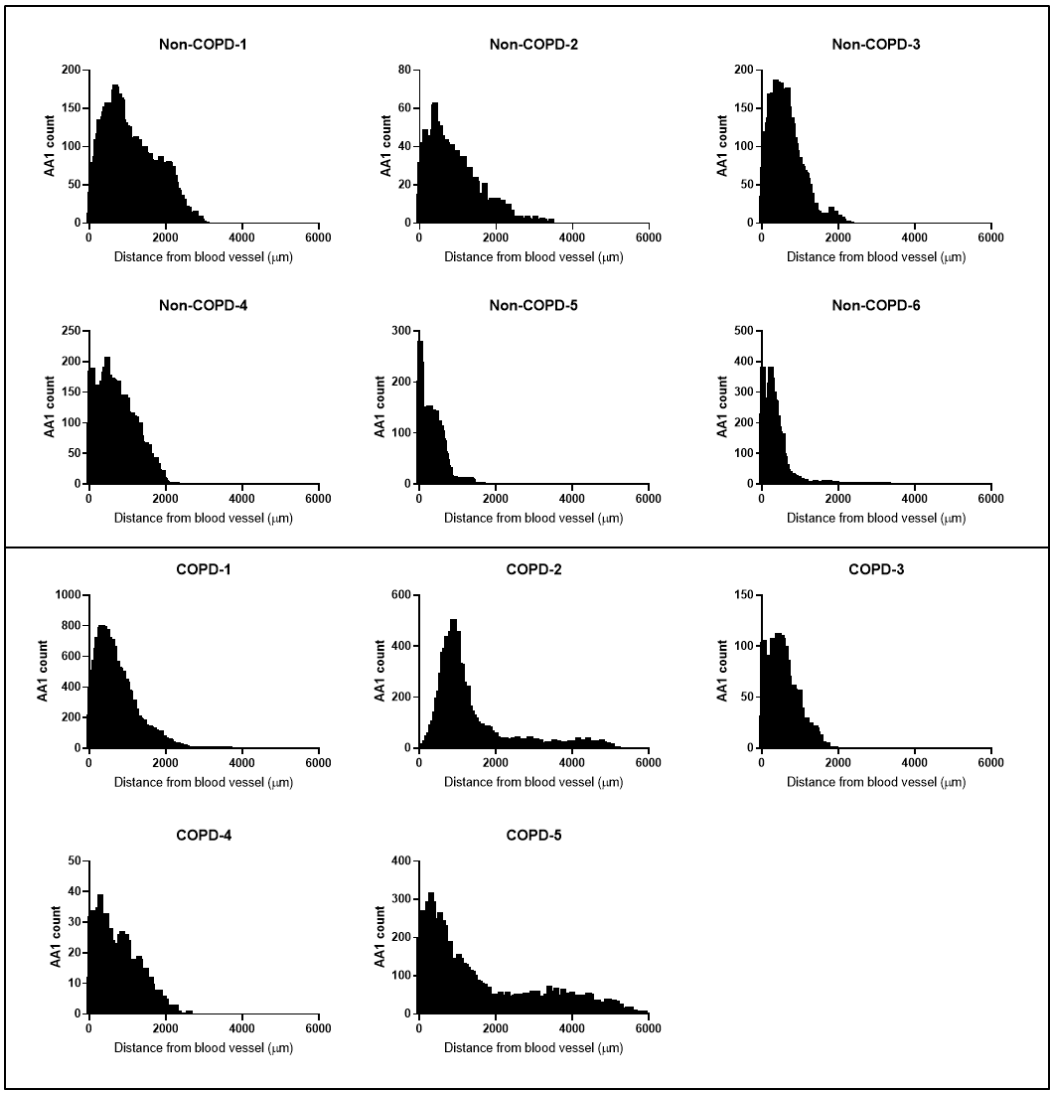

Figure 5.12: **Distribution of AA1 cellular staining in relation to blood vessels in each of the non-COPD and COPD tissues.**The graphs show the closest distance each segmented voxel of AA1, following erosion to a central point, is to the nearest segmented blood vessel.

The AA1 distributions in relation to blood vessels showed little differences between the two clinical groups and individual tissues within those groups. The distribution of the AA1 staining to the interpolated Ck18 was also completed and the results reported in Figure 5.13. This used the results of the Ck18 staining and segmentation and so only the eight tissues containing Ck18 could be analysed in this way. Here the distribution is different to the blood vessels with the majority of AA1 staining being located within 4000 µm of the nearest area of Ck18. The non-COPD tissue has peaks of AA1 at less than 100 µm from the nearest area of Ck18 whereas only COPD-4 has a similar peak from the COPD tissue. The other three COPD tissues have peaks in the number of AA1 cells of 1000-2000 µm. The main exception to this is Non-COPD-2 which had a relatively even distribution of cells up to 10,000 µm from the nearest area of Ck18.

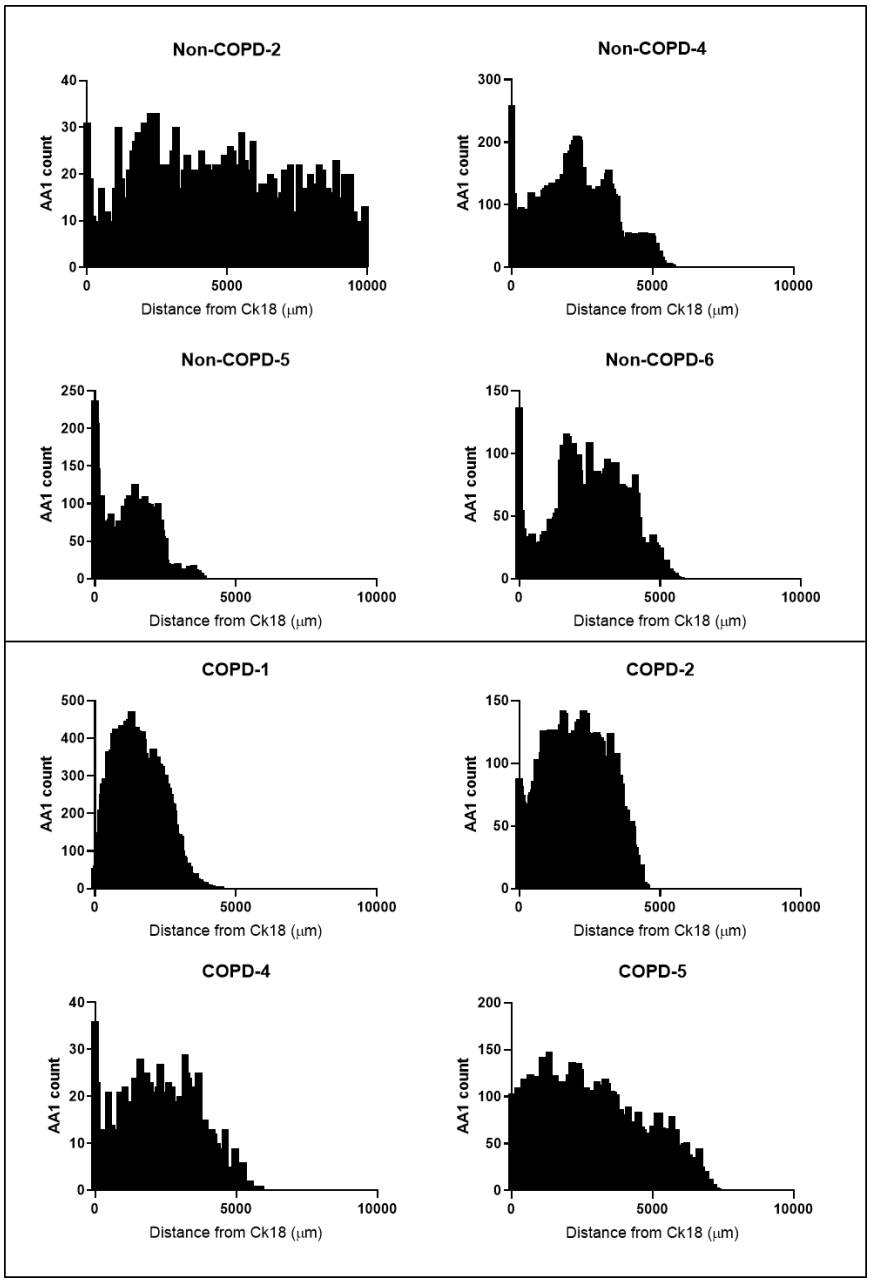

Figure 5.13: **Distribution of AA1 cellular staining in relation to interpolated Ck18 localisation in each of the non-COPD and COPD tissues containing Ck18 positive staining.**The graphs show the closest distance each segmented voxel of AA1, following erosion to a central point, is to the nearest segmented area of CK18.

The overall distribution of the AA1 positive cells to Ck18 is much more evenly spread out throughout the tissue compared to the distance from blood vessels. Representative cellular distances showing this difference are visualised in 3D in Figure 5.14. The main reason for the changes in this distribution were the greater blood vessel volume in all the tissues. This will naturally lead to the AA1, assuming an even distribution of cells, overall being located closer to the vessels. However, the location of the peaks was still similar in the non-COPD tissues with the highest number of AA1 being located in close proximity (<100 μm) to the nearest blood vessel or

area of Ck18. This was not the case for the COPD tissue which had peaks of AA1 further away from Ck18 compared to blood vessels.

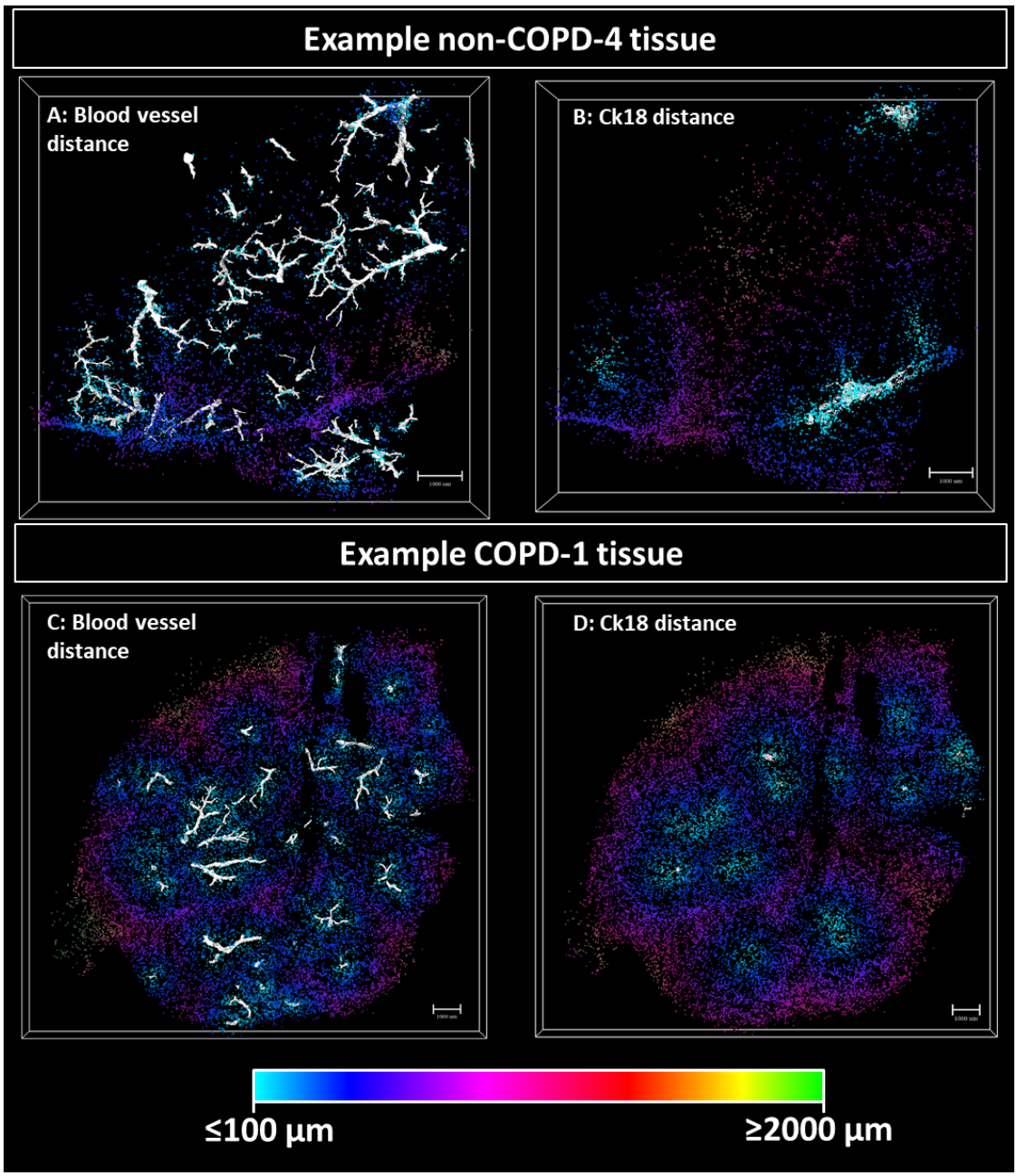

Figure 5.14: **Representation of visualised AA1 cell distances to the nearest blood vessels and Ck18 localisation in the non-COPD-4 and COPD-1 tissue.** The white networks in each image represent the blood vessel (A & C) and interpolated Ck18 (B & D). The AA1 segmentation was dilated by 3 voxels to ease visualisation and is taken from 5 planes within the section volume. The colour of the AA1 segmentation corresponds to the distance key at the bottom of the figure.

5.5 CD68 imaging

Macrophages have a well-defined role in COPD and so were chosen as a secondary application of IF staining of individual cell types localised in the 3D μCT. One of the tissues was selected for an exemplar analysis of CD68, as a marker for macrophages, in COPD tissue. This tissue block (COPD-4) was successfully stained on available tissue sections with CD68 and imaged, the results of this primary data are reported below.

5.5.1 Analysis of staining

The COPD-4 tissue block was successfully stained using CD68 (see Table 5.2 for tissue information). The staining was masked with DAPI, counted and normalised using the same methodology as the AA1 staining. Importantly here the masking helped to separate clusters of cells into individual objects which were counted separately, an issue which was unique to the CD68 over the AA1 staining. The results of the raw cell counts of CD68 and AA1 are reported in Figure 5.15 alongside the normalised values per tissue area (mm^2).

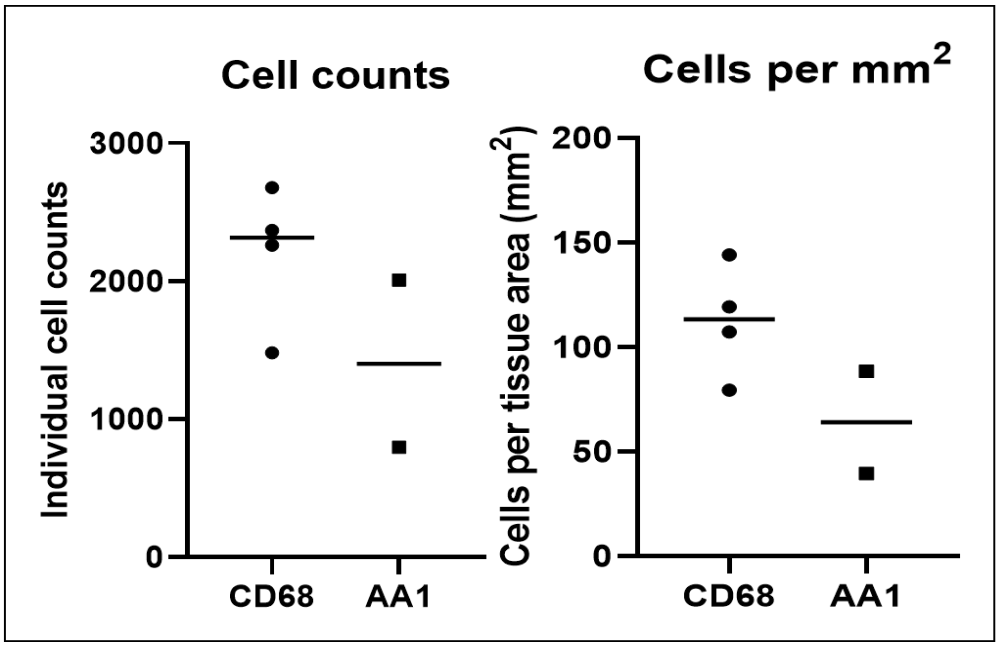

Figure 5.15: **Preliminary results of the CD68 and AA1 positive cell counts alongside the normalised values from COPD-4 tissue sections.** Preliminary results of the CD68 and AA1 positive cell counts alongside the normalised values from COPD-4 tissue sections. The raw cell counts reported in the left graph were the measurements taken automatically using the analyze particles plugin in Fiji of the DAPI masked cellular staining. The FITC channel image of tissue autofluorescence was used to calculate the tissue area which was used to normalise the cell counts shown in the right graph. Line denotes the median value.

5.5.2 CD68 staining and comparison to AA1

Figure 5.16 shows the combined IF visualisation of CD68 and AA1 staining, on neighbouring sections in the COPD-4 sectioned volume, the results of the cell counts were reported above in Figure 5.15. Here there was a higher number of CD68 positive cells compared to the number of AA1 positive cells with the mean number of CD68 cells per mm^2 being almost double that of AA1 cells. Visible inspection of the stained sections shows the CD68 staining is found throughout the lung parenchyma and is also present in the airspaces whereas the AA1 staining is only found within the lung tissue. The CD68 staining visibly 'clumps' together in the raw staining images shown, however for the cell counts these were separated using the DAPI masks. This demonstrates the feasibility in the analysis of these two cell types within the same volume. However, more staining is required in the other non-COPD and COPD tissues to provide sufficient statistics on significance on the differences between these cell types in COPD.

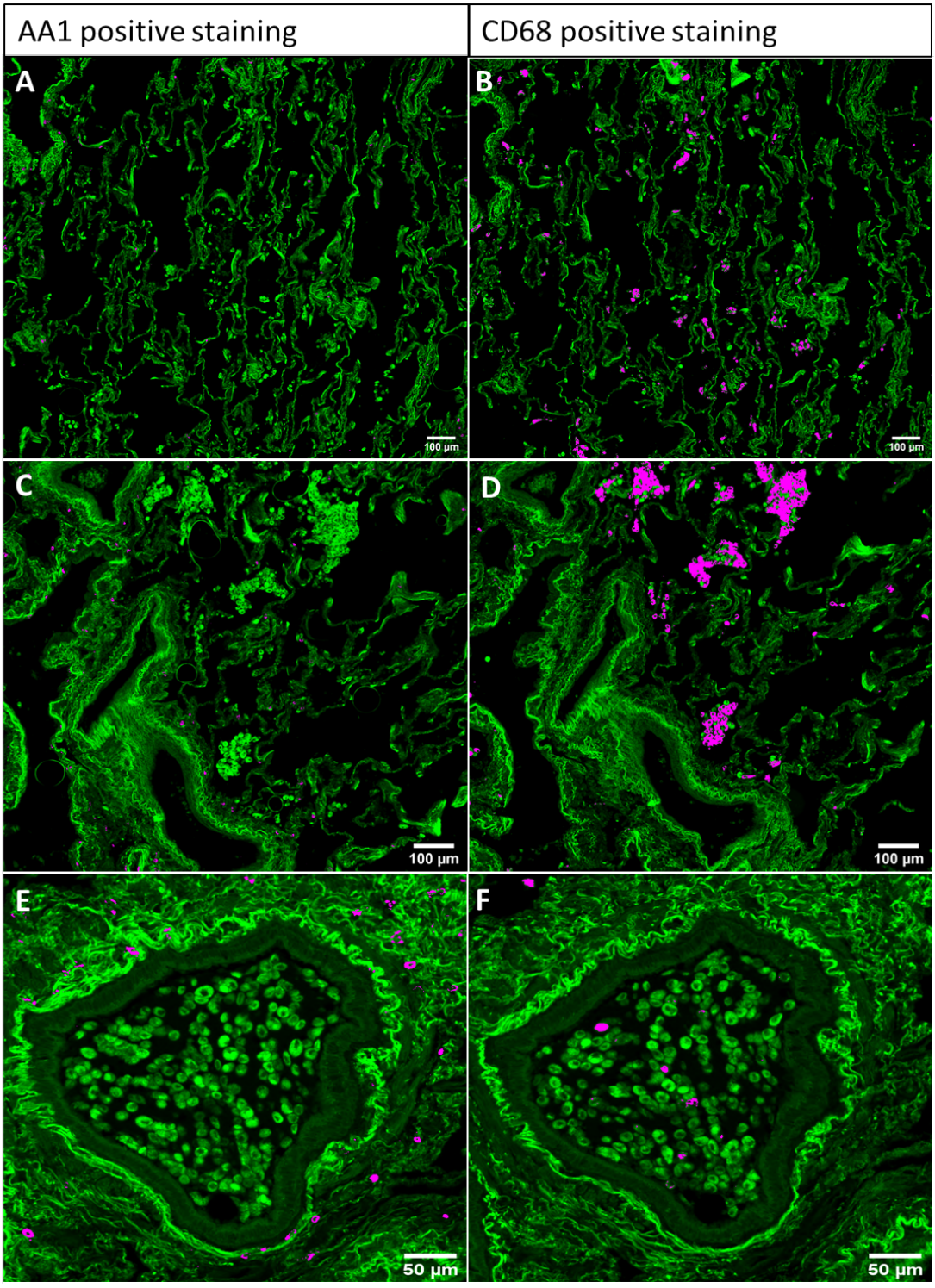

Figure 5.16: **Results of preliminary visualisation of AA1 and CD68 positive staining on neighbouring sections in the COPD-4 tissue.** Each image shows fluorescence microscopy images of tissue autofluorescence from the FITC channel (green) and cellular IF staining (pink). The left column shows the results of AA1 staining whereas the right column shows CD68 staining. A & B: A stained area of lung parenchyma. C & D: A stained area containing blood vessels. E & F: A stained area of airway at high magnification. Images captured on neighbouring tissue sections using a 10x objective.

5.5.3 Distance maps

The blood vessel and Ck18 distance maps produced for AA1 distances were used to calculate the distance of the CD68 staining from the blood vessels and interpolated Ck18 staining. The results of these distance maps and those for AA1 in the same tissue are reported in Figure 5.17. The distribution of the AA1 and CD68 was similar in both distance from blood vessels and Ck18. This was despite there being more CD68 positive cells in the volume, explaining the higher number of cells in each peak.

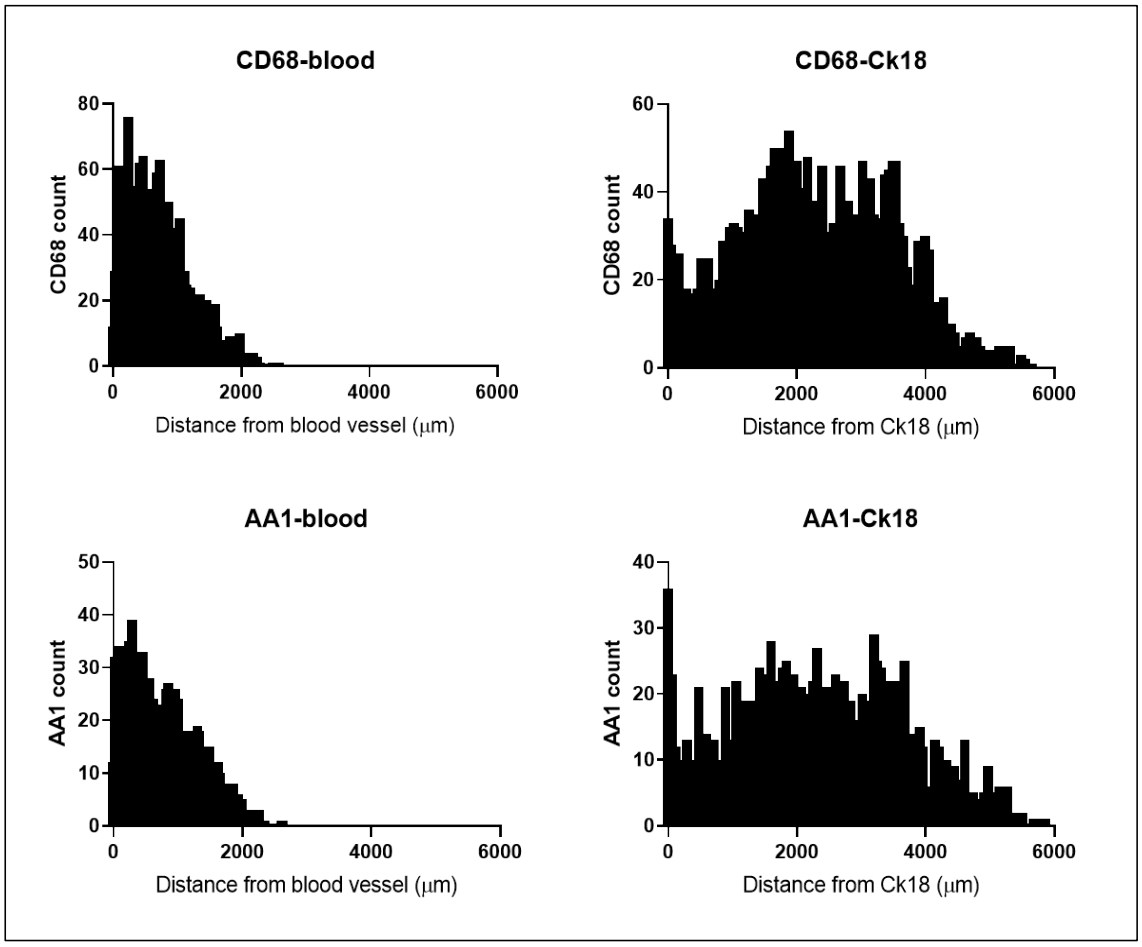

Figure 5.17: **Preliminary results of the distribution of CD68 and AA1 cellular staining in relation to blood vessels and Ck18 localisation in COPD-4 tissue.** The upper graphs show the closest distance each segmented voxel of CD68, following erosion to a central point, is to the nearest segmented blood vessel and interpolated segmentation of Ck18. The lower graphs show the closest distance each segmented voxel of AA1, following erosion to a central point, is to the nearest segmented blood vessel and interpolated segmentation of Ck18.

5.6 Discussion

This chapter built upon the registration and segmentation methods developed in chapter 3 to provide localisation of features and cells in the context of the 3D tissue volume. This was driven by the use of correlative imaging of 3D tissue microstructure using µCT and specific cellular localisation using 2D IF imaging. The same clinically grouped tissue used in chapter 4 was used as an example for the potential use of these techniques to compare immunoreactivity of features and cells in 3D. Something which is not possible with either imaging technique individually. The non-COPD (n=6) and COPD (n=5) FFPE tissues were all successfully sectioned, stained for IF and analysed for any differences between the groups. Rapid registration and segmentation of IF was used to further validate results in chapter 3 and demonstrate the potential for future use in larger studies, which are needed to start drawing biologically significant inferences from differences between the groups.

A main part of sample selection after finding FFPE tissue with relevant clinical information was using quick µCT scans to scout for appropriate tissue, as reported in section 4.3. Scouting with µCT has been used in multiple correlative studies to not only assess the large volume but to identify specific features for further imaging and analysis. This has been used in bone imaging with low resolution X-ray based imaging to find the area of interest which was then imaged using much higher resolution electron microscopy (Akhter *et al.*, 2017; Norman *et al.*, 2018). The quick µCT scans were successful for finding appropriate tissues with intact microstructures and networks of interest as evidenced in chapter 4. However, this did not confirm the presence of airways in all of the tissues volume with only eight out of eleven volumes containing any Ck18 positive staining. The heterogeneous nature of the lungs mean that there were airways in the tissue, but they were further into the lung tissue or outside the sectioned volume used for IF staining. More sectioning and IF staining for Ck18 would be required in the future to assess whether airways containing Ck18 were present in the tissue blocks. This heterogeneity was qualitatively observed in the small number of samples despite similar clinical information within the grouped tissue. A quantitative measure of lung tissue heterogeneity would provide useful context to the variations seen in the analysed data from each tissue block in this and future studies. Assessing randomised sub-volumes of interest within the tissue, as has been done previously (Robinson *et al.*, 2019), could be used to quantify the variability of the tissue throughout a sampled tissue volume.

Directly utilising the methods developed in chapter 3, the Ck18 primary antibody was used to identify airway epithelial cells in the grouped tissues. This was not used as a direct marker for all the airways or the alveoli, which do not contain Ck18. There was signal produced from some of these structures but the signal was significantly weaker and could be thresholded out for

segmentation. Future work using different primary antibodies, for example elastin could be used to investigate alveoli changes directly (Merrilees *et al.*, 2008). However, most of the Ck18 staining for airway epithelium formed an incomplete layer surrounding the airway lumen, with gaps in the staining suggesting minor epithelial/airway damage or a lack of Ck18 antigenicity. Examples of more prolific epithelial damage and detachment from the basement membrane were seen in both the non-COPD and COPD tissues indicating this was not the result of disease pathogenesis. Visual 'clumps' of Ck18 staining within the airway lumen or sometimes in the parenchyma provided evidence of airway damage or loss.

The airway epithelium is known to be damaged as a result of the chronic inflammation in COPD (Hadzic *et al.*, 2020) and so it was expected to see less Ck18 staining in the COPD tissues. However, the area and volume fractions of the Ck18 staining were all less than 1% of the tissue in all eight of the examined tissues. COPD is a heterogeneous disease which affects parts of the lung differently with complete airway obstruction in some areas whilst other parts of the lung will have intact airways, regardless of symptoms of disease (Agusti *et al.*, 2010). However determining the cause of this damage is not possible in a small descriptive study such as this. Most of the tissue was from archival biobanks of FFPE blocks collected over a period of several years. Although the protocol was the same for each tissue, high amounts of variability in the levels of damage caused by extraction, fixation, embedding and sectioning were observed. This is a well-known and accepted issue in studies working on FFPE tissues (Rastogi *et al.*, 2013). This is however, something to be aware of when investigating damaged tissue microstructures, particularly more fragile structures like airway epithelium.

Distance maps provided novel insight into the distribution of localised features and cell types, provided by IF staining, in relation to 3D networks within the tissue volume. This was used to investigate the relationship between the blood vessels (identified in chapter 4) with the interpolated Ck18 networks within the sectioned volume. More information was also obtained about the networks themselves by assessing what features and cell types were in close proximity to them. The 3D distance map data was generated from blood vessels down to a 25 µm thickness, reporting the relative distribution of the airway epithelium containing Ck18. The majority of the Ck18 localisation was within 500 µm of the nearest blood vessel. This makes sense biologically as both the airways and blood vessels are closely associated in the lungs leading towards the alveoli and capillaries for gas exchange (Hsia *et al.*, 2016; Mühlfeld *et al.*, 2018). One tissue sample from each group had a different distribution with a peak Ck18 distance from the blood vessels being 1.5-2 mm, this demonstrates the heterogeneity of the networks in their distribution throughout

the tissue. This is likely different throughout the lung, future studies using multiple tissue samples from the same patient, and a larger pool of patient samples, could be used to assess the levels of heterogeneity in the 3D network distributions. This could be used to compare any potential differences occurring in COPD, or other respiratory diseases, in the context of the relative distributions of the blood vessels and Ck18 positive airway epithelium.

Single infiltrating cells (e.g. mast cells and macrophages) are not visible at the resolution of the µCT. The confidence in the localisation of the individual cellular staining in the µCT was validated by autofluorescence registration which is maintained with the IF registration, as was seen with the Ck18 localisation. AA1 cellular IF imaging was originally used as a positive control for the Ck18 staining due to the high reliability and efficacy of AA1 IF staining. Mast cells, which AA1 staining localises, are also relevant infiltrating cells involved in respiratory diseases like asthma (Bradding and Arthur, 2016). However, there has been no conclusive evidence of mast cell activity influencing the progression or treatment of COPD (Soltani *et al.*, 2012). The AA1 staining in this study was a pragmatic exemplar of individual cellular staining, unlike Ck18, which could be used for individual cell counts and distribution measures in the context of 3D lung tissue microstructure.

In order to take advantage of the full 3D tissue microstructure information provided by the µCT it was decided that all cells in the tissue section should be counted. However the act of individually counting thousands of cells per tissue section was deemed impractical and a more automated alternative was developed using DAPI staining, as reported in section 3.7. This again utilised the high image contrast provided by IF to easily threshold the AA1 and DAPI staining from the images. However, to fully verify this method it will need to be compared to manual cell counts as this is the current standard for cellular analysis of tissue sections. Cell counts were normalised in this study by the surface area of the tissue in the section, unlike the blood vessels and Ck18 the cellular staining could not be reported as a number of cells per volume. This was because the sections were spaced approximately 40 µm apart in the z-direction. These normalised cell counts could not be averaged into a volume measurement because it was not known how many cells were present across multiple neighbouring tissue sections. However, there is the potential for modelling to be employed to determine the 3D distribution as part of the tissue volume, which has been done previously in 3D cell culture models and material studies (Jarockyte *et al.*, 2018; Mehboob *et al.*, 2018). A future study is required to stain neighbouring serial sections and use a combination of wide-field and confocal fluorescence imaging to assess how many cells are double counted over neighbouring sections which could be used to produce a more accurate measure of cells per tissue volume.

Mast cell mediators are known to act on blood vessels and airways in the lung (Komi and Bjermer, 2019), and using distance maps provided a novel measure for distribution of mast cells within tissue in relation to these 3D structures. Mast cells in all of the tissue blocks had a much more consistent distribution in relation to blood vessels, with almost all identified mast cells being within 2 mm of a blood vessel. This is most likely linked to part of the function of mast cells to act as vasodilators via the release of multi-potent molecules. Most notably histamine as well as proteases, heparin and numerous cytokines which contribute to vascular homeostasis and requires mast cells to be located in close proximity to blood vessels (Krystel-Whittemore *et al.*, 2016). The distributions were not different between the non-COPD and COPD samples which was expected in mild disease; although studies have previously shown some changes in mast cell distributions, this is most notable in severe COPD (Andersson *et al.*, 2010). The blood vessels and mast cells were relatively evenly distributed throughout the tissue, which also explained why the peak of mast cells was located close to the blood vessels morphologically. As stated in chapter 4 the segmented blood vessels only go down to a thickness of 25 µm and so it is probable that the mast cells distances are even closer to the smallest vessels not reported here. Initial work using the different thickness bins reported in section 4.6 was used to produce individual distance maps of each subset of blood vessels in increments of a 20 µm thickness. The results of this in one dataset from each group are reported in appendix A.9, this showed that the majority of mast cells in this sample are located in close proximity to the narrowest blood vessels (<80 µm thickness) with the distribution widening as the vessel bins get thicker. Future work is required to investigate the relation of mast cells to the size of the blood vessels and whether the distribution of mast cells in relation to 3D blood vessels changes if blood vessels are lost or remodelled as a result of disease.

Distance maps were also generated from the interpolated Ck18 localisation to assess the mast cell distances from the airway epithelium. There was significantly less Ck18 segmentation compared to the blood vessel segmentation which does affect the width of the peaks in the distributions as the mast cells, in most tissues are within 5 mm of the nearest area of Ck18. However, despite this the non-COPD tissues all have peaks in close proximity (<20 µm), this is expected as mast cells reside in the tissue surrounding the airways (Komi and Bjermer, 2019). Mast cells act directly upon airways to cause constriction and increase mucous production as part of their immune response, which requires a large number to be in very close contact with the airways (Krystel-Whittemore *et al.*, 2016), as was observed here. This peak in all the tissues is most likely explained by the clinical status of each patient. None of the tissue samples were from healthy or young individuals, all of which had lung cancer as well as numerous other conditions, which could cause

increased levels of mast cells in the lungs and surrounding airways in response (Campillo-Navarro *et al.*, 2014). Mast cells are not found in the airspaces which explains why the peaks are wider due to the mast cells being spread across the lung parenchyma. Only one of the COPD tissues has the similar peak distance at <20 µm, the remaining three COPD tissues have peaks further away at a 1-2 mm distance. Although more data is required to draw any biologically significant conclusions this could indicate a shift in the location of mast cells in mild-moderate COPD, possibly in response to airway inflammation or loss.

Macrophages have a well-defined role in the pathogenesis of COPD (Yamasaki and Eeden, 2018). Unfortunately due to time constraints, equipment failure and antibody reliability the CD68 staining for the more pathologically relevant cell type in COPD was only completed in one of the grouped tissues. The first step of any future work would be to address this by finding a reliable antibody and performing the same level of staining as was seen for the AA1 staining, as mast cells are ubiquitous in the lung. Visually comparing the CD68 staining to neighbouring AA1 staining showed many more cells across the tissue section and unlike AA1 the CD68 was located in both the lung parenchyma and the airspaces. This could be the result of this sample being from a COPD lung where increased activity of macrophages have been reported previously (Yamasaki and Eeden, 2018). Further staining and analysis of non-COPD tissue is required to show any differences between the clinically grouped tissues. The CD68 staining was also found to cluster in the tissue section, this is a reported feature of lung macrophages, which has previously been investigated in COPD (Vasudevan *et al.*, 2020). The clustering could be analysed in future work using existing techniques in relation to the 3D tissue microstructures. The DAPI masking of cells was originally developed to address the issue of these ‘clumped’ cells to ensure each clustered macrophage was counted separately. Future use of serial staining and registration could be combined with existing clustering analysis tools to investigate the clustering of macrophages in relation to 3D tissue microstructure in respiratory diseases.

The distribution of macrophages in relation to blood vessels is similar to the AA1 distribution in the one sample compared. This was interesting because macrophages were found in the lung parenchyma and the airspaces whereas mast cells were only in the parenchyma so it was expected that the distributions would be different. There was a difference in the distribution of CD68 and AA1 in relation to the interpolated Ck18 localisation. The distance to the macrophages peaked around 2 mm from the nearest area of Ck18, whereas the distance to mast cells peaked at <20 µm. This illustrated a high concentration of mast cells in direct relation to the airways, as described previously (Komi and Bjermer, 2019), compared to the macrophages which did not peak in such close proximity. Further staining and analysis of relative distributions of CD68 staining is required to fully assess how the macrophages are distributed in relation to the 3D

networks within the tissue volume. This could provide a novel insight into macrophage localisation in the context of 3D tissue structures in COPD or other respiratory diseases.

5.7 Conclusions

Methodology developed in chapter 3 enabled automated registration and segmentation of IF staining to the μCT sectioned volumes free of sectioning artefacts. The time consuming part of this methodology workflow is now the image acquisition, with the registration of each set of images completed in approximately 2 minutes. In this chapter 151 stained tissue sections were registered in approximately 8 hours (including pre-processing time). This demonstrated proof of concept for the methodology's viability for larger studies. Area and volume counts of the Ck18 were used to assess the level of airway epithelium present in the tissue as an exemplar of IF identifying tissue microstructures. Automated cell counts of mast cells and macrophages using DAPI staining to define nuclei were exemplars used to count thousands of cells per tissue section, which could be related to the full tissue volume. The methods developed here could be applied to any cell type of interest, with a working primary antibody, whether structural or individual immune cell for investigating disease in context of 3D microstructures. 2D data from IF staining was easily transferred into the 3D domain provided by μCT, a visual summary of the COPD tissue block containing all the different IF staining and segmentation is shown in Figure 5.18. A video of the COPD-4 tissue containing all the segmentation in the sectioned volume can be found in Appendix A.7.6. This resulted in novel methods of quantifying the 3D distribution of cells (from 2D staining) in relation to segmented 3D networks. Which could be used in numerous applications for investigating cellular information, identified by conventional IF in relation to 3D tissue microstructures provided by μCT. Further work on more samples similar to those used in this study and completion of CD68 staining could lead to a greater understanding of the numbers, and distributions, of these immune cells in relation to the 3D networks, in diseased and non-diseased tissue.

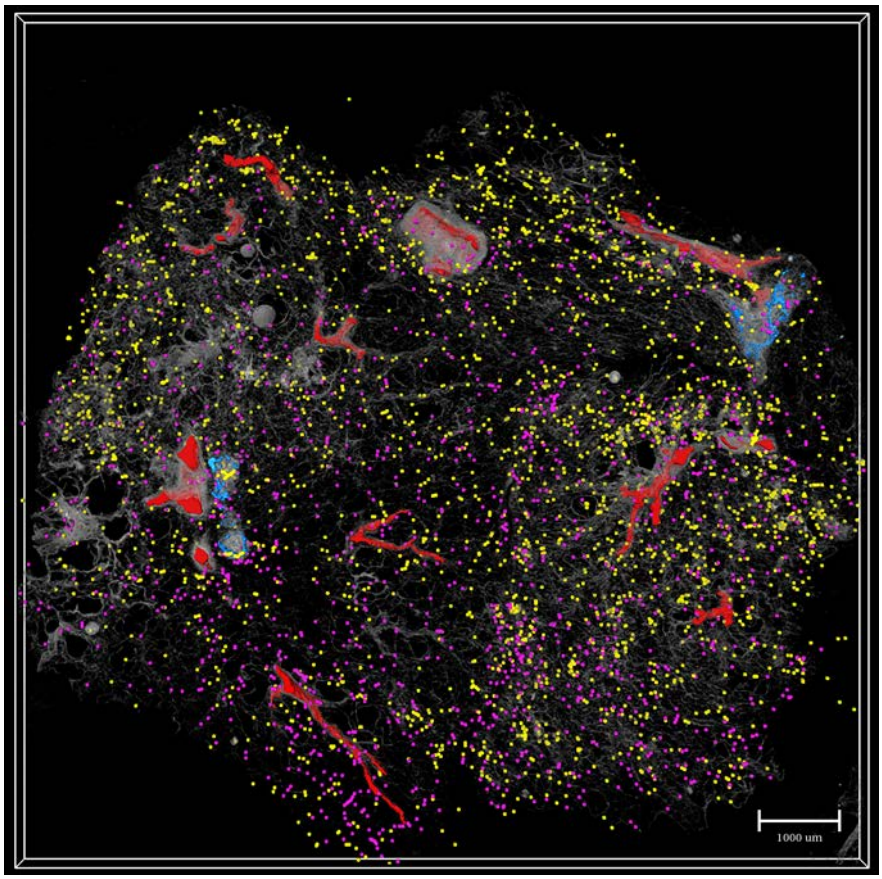

Figure 5.18: **Visualised summary of the combined µCT imaging, network segmentation and IF localised cell types used in chapter 5.**The semi-transparent grey volume rendering represents the µCT data. In red is the segmented blood vessel network and in blue is the interpolated Ck18 localisation. The spheres represent individual cellular localisation (dilated to ease visualisation). In pink are the localised AA1 staining for mast cells and in yellow is the localised CD68 staining for macrophages. Representative image taken from the COPD-4 tissue which contained complete staining and segmentation as a proof of concept for future work and studies.

Chapter 6 General Discussion

Lung tissue microstructure is key to the complex function of the lungs, and changes to these structures are associated with the pathology of many respiratory diseases including COPD. Imaging techniques most commonly used to image the lungs are not capable of capturing the 3D lung volume at a microscopic scale to detect the associated networks and cell distributions at this resolution. Traditional 2D imaging provides a thin cross-section of part of the lung tissue and, as lung tissue structure is heterogeneous, may not be representative of the whole lung tissue volume. Clinical X-ray based imaging lacks sufficient resolution and contrast to image lung tissue structures less than 0.8 mm in size, lab-based µCT systems have been developed in recent years to provide the resolution and contrast needed to image lung tissue microstructures in 3D (Scott *et al.*, 2015; Katsamenis *et al.*, 2019). However, these do not provide the resolution or specificity needed to identify specific features and cell types which can be visualised and analysed in 2D with traditional histology. Combining µCT and IF imaging techniques provided specificity to µCT and 3D context to IF imaging, offering a unique perspective into tissue structure and function.

The first hypothesis of this study stated that developing and utilising techniques for further automation of correlative imaging data would significantly decrease the time taken to process the images in order to produce usable data. As shown in chapter 3 the correlative imaging workflow using the developed 'automated warping script' (appendix A.6) significantly decreased the time taken to process the µCT and IF data into a form that correlative imaging data can be extracted. This difference from several weeks or months down to a matter of days proved this hypothesis to be true. However the development of further automation will continue beyond this project (see future work), which would further develop and prove this hypothesis. The second hypothesis required the 3D blood vessel network to be identified and analysed in the lung tissue volumes. This was achieved, as reported in chapter 3, via semi-automated segmentation of the vessel lumens which could be used for volumetric and network analysis, as reported in chapter 4. This lead to analysis of the 3D vessel networks for biologically relevant comparisons between clinical groups of non-COPD and COPD human lung tissue. Following method development for the first hypothesis, 'active contour segmentation' was utilised to decrease the time taken to generate the blood vessel network data for analysis. This 3D network data was also be combined with the cellular data as part of the next hypothesis. The third hypothesis required immune cells, identified using 2D IF staining and imaging, to be registered into the 3D tissue volume of the µCT; as reported in chapter 5. This was used for 2D analysis of cell counts which were expanded into the

3D domain following combination with the blood vessel network data from chapter 4. This did provide a novel way of analysing the cellular data, however it did not provide a true 3D distribution of the immune cells within the tissue. Future work, with ideas discussed in the next section, would be required to prove this hypothesis with additional data or potential modelling. As it stands the data provided in this thesis could not fully prove this hypothesis for 3D distribution of cells, although it did provided a novel means of analysing 2D cellular imaging data in 3D via correlating with μCT.

The main issue addressed in this study was the time consuming methodologies required to bring together (co-register) the information from these different imaging modalities. This bottle-neck in image processing, registration and segmentation has prevented the wide-spread use of large scale studies of soft tissues using correlative μCT and histological imaging. Combined with a lack of standardisation between users in both the imaging and the registration has prevented the wider use of these correlative techniques in larger studies. The work presented in this thesis shows the development of a novel correlative imaging workflow with greater amounts of automation for use in larger studies. Compared to previous studies, which took several days to register and segment small samples manually (Robinson, 2020), this methodology could reduce the total time of correlative projects by several weeks or months depending on the samples type and size. The accuracy of the automated alignment of IF and μCT images was comparable with existing manual techniques for feature matching between images. The current values of ~70% alignment could potentially be higher if the outer 100 μm of the image, where most of the inaccurate registration occurred, was omitted from analysis. Future work determining the accuracy of the non-peripheral areas of the tissue could further validate its use and development in more correlative imaging studies. The methodology workflow developed and applied in this project highlights the progress made in correlative 2D-3D imaging of FFPE soft tissue using μCT and histological imaging. The majority of previously published works using these imaging techniques have used manual techniques of registration and/or segmentation to correlate the information from 2D histological imaging into the 3D μCT (Jones *et al.*, 2016; Robinson *et al.*, 2019). Previous studies using more automated methods of segmentation have used the μCT data alone, only using histology images for reference or qualitative confirmation (Wollatz *et al.*, 2017; Koo *et al.*, 2018). These studies were not able to segment features or cell types which are only revealed by correlating μCT data with images from other techniques.

Prior to this study the correlative μCT imaging studies either used bright-field 2D microscopy visualised with tinctorial stains or IHC (Schaad *et al.*, 2017; Katsamenis *et al.*, 2019; Tanabe *et al.*, 2020) or 2D/3D electron microscopy (Morales *et al.*, 2016; Parlanti *et al.*, 2017; Parlanti *et al.*, 2019). Previous studies also combined μCT, 2D histology and electron microscopy on the same

sample for true multidimensional imaging at different scales (Handschuh *et al.*, 2013; Siqueira Jr *et al.*, 2018). Here, IF imaging was used as a complimentary imaging modality to provide the same level of information shown in previous studies using IHC with greatly improved image contrast. This enabled thresholding to be used for automated segmentation of immunocytochemistry based staining. The novel utilisation of autofluorescence, captured alongside IF, for automated registration of the wide-field fluorescence microscopy images to the µCT whilst taking into account sectioning artefacts has the ability to progress the field in future projects. The application of this registration for automated segmentation of IF staining in the µCT, demonstrated in this thesis, provided comparative results to previous studies in a fraction of the time. The increased levels of automation provided by using IF imaging for registration and segmentation of µCT images opens up the use for larger studies investigating diseases at the 3D microstructural and cellular level in FFPE soft tissues. However there are limitations with using fluorescence imaging over bright-field, firstly the IF staining is not permanent. This can be addressed by ensuring the stained slides are imaged as soon as possible after staining and that the slides are stored properly. Another limitation is that IF staining and imaging takes a greater amount of time than tinctorial or IHC stains. The staining protocol used in this study required overnight incubation, although this could be further optimised so that staining can be completed in one day instead of two. Also image acquisition takes a magnitude of time longer than bright-field due to the use of multiple fluorescent channels. In this study three fluorescent channels were used to image the IF stained tissue, which would take approximately three times longer to capture than bright-field images using one channel. This is of course dependent on exposure times of each channel, which could be further optimised to reduce the total time taken for image acquisition. Part of the reason the images were captured using a 10x objective was that using a 20x objective would have taken approximately four times longer to image each tissue section. Fortunately the added detail from higher magnification imaging was not required for this study but it is something to factor into future studies for total data acquisition times.

Similar techniques for the semi-automated blood vessel segmentation using region growing tools, like ‘active contour segmentation’ used here, have previously been used in clinical CT scans (van Rikxoort and Ginneken, 2013). These have also been used on lung µCT images to identify vessels much smaller than the resolution of clinical 3D imaging (Scott *et al.*, 2015), and was used to segment blood vessel lumens in this report. The segmentation results were generated 3-4x quicker than manual segmentation whilst providing comparative results. Without the benefit of µCT this identification of 3D blood vessel networks would require time-consuming serial sectioning with individual alignment of images from each tissue section. Only recently has digital

wide-field microscopy made this feasible for the size of tissue samples studied here (1-2 mm diameter) (Jones *et al.*, 2016). The segmented blood vessel networks could also be used with fluid modelling to map potential changes in blood flow rates in the lung (Robinson *et al.*, 2019), on blood vessels not detectable with clinical imaging techniques. However, inconsistencies in the paraffin wax section thickness can cause difficulty for accurate measurements of tissue sections (Libard *et al.*, 2019), these are overcome by using non-destructive isotropic µCT. Another potential issue with the measurement of FFPE lung tissue is that the removal and processing of the tissue will affect the size of histological based measurements by potentially up to 50% compared to *in vivo* measures*,* depending on the tissue type (Schneider and Ochs, 2014). However, previous well-established measures from histopathological samples have been made despite this consistent artefact differing from *in vivo* measures. The absolute numbers were not truly reflecting measures like tissue volume or vessel thickness *in vivo*, however the relative results and changes would still be indicative of changes in disease. Recently a potential method has been proposed to scan tissues by µCT before and after sample preparation to address what changes are occurring in the tissue due to shrinkage (Robinson *et al.*, 2019). This could potentially be used on fresh lung tissue prior to fixation alongside the development of rapid µCT scans optimised for fresh tissue which is currently underway at the University of Southampton.

Following development, the correlative imaging workflow was applied to a small exemplar study of COPD and non-COPD tissues to demonstrate the amount of biologically relevant information that can be generated in a relatively short amount of time. Despite several metrics for analysing the blood vessels, Ck18 and infiltrating cells no significant differences was observed between the groups. This may reflect the samples used which came from lung cancer patients undergoing surgical resection. The tissue was judged to be macroscopically normal with patients assigned to different groups based on their lung function scores. These scores were calculated from spirometry tests which, although widely used can present wide levels of variability regardless of the disease state of the patient (Vogelmeier *et al.*, 2017). The tests were also completed at several different hospitals with differing diagnostic and research standards. Secondly, from the initially identified tissue from the archived tissue bank, matching the clinical criteria, the choice of samples included was based on the quick µCT scans of the tissue reported in section 4.3. Upon visual inspection of the µCT scans specific exclusion criteria were applied to ensure that it would be possible to analyse the blood vessels and airways of the tissue, resulting in the 11 tissue samples selected having similar tissue microstructure. The similarities of the tissues were reflected in the analysis, despite variation in tissue size and presence of airways, which did not lead to any observable differences. However, the analysed data forms a good basis for future studies with a larger number of samples which can be used to draw biologically significant

conclusions. Something which was not possible with the small exemplar study size presented in this thesis. Other limitations not related to the samples used in the study include the time taken to generate the datasets. Although this has been significantly decreased from several weeks or months to approximately 2 weeks of constant work, which is a big step forward, it is still too long for larger studies. This time scale is also dependent on access to specific pieces of lab equipment, namely the soft tissue optimised µCT system, the fluorescent slide scanning microscope and high specification computer workstations. Without these the amount of time to generate and segment the data will increase significantly. To mitigate these limitations a greater uptake of the technology and equipment is needed for larger studies or multiple different studies to run simultaneously. This would require a great deal of funding and physical lab space to accommodate the acquisition and placement of the equipment.

Overall this work has shown the potential for correlative studies in FFPE lung tissue samples investigating the 3D networks and infiltrating cell populations in non-COPD and mild-moderate COPD tissue. Correlative imaging techniques have been widely used on mineralised tissue, most notably bone, this is due to the high contrast µCT images which can be more easily correlated to traditional histology (Lundin *et al.*, 2017). Previous studies have also shown the use of similar techniques in soft tissue imaging of the lung to investigate other respiratory diseases, such as IPF (Tanabe *et al.*, 2020). However correlative µCT projects of soft tissue are not limited to the lung, following the methods developed and presented in this thesis, other tissues have been examined following the exemplar studies using lung tissue. Work by the writer during the period of this project has already contributed to work in other tissues by using correlative µCT and H&E imaging of kidney to validate novel imaging techniques using phase tomography (Zdora *et al.*, 2020). This shows how the research field is branching out to image different soft tissues as well as lung. The future of µCT imaging forming a new branch of X-ray histology to help inform research by adding 3D imaging to traditional studies (Katsamenis *et al.*, 2019) is seen as the future of the field over the next several years. The work in this project has developed this principle and will allow larger studies using more automation to be able to draw biologically significant conclusions of diseases which affect tissue microstructures and the cellular population associated with them.

6.1 Future work

The workflow reported in chapter 3 which was used for the data generation in chapters 4 and 5 illustrated the value of correlating 2D IF images with 3D µCT data. Currently, this workflow has dramatically decreased the time taken to image and process the µCT data from several months to

less than 2 weeks per paraffin wax block. Data acquisition of the µCT imaging, tissue sectioning, staining and IF imaging are now the main bottlenecks in the workflow. However, both sectioning and immunostaining can be automated and has been done in a diagnostic setting for many years (Mawhinney *et al.*, 1990), providing potential options to further automate the workflow. µCT imaging hardware and methodology are being improved to decrease total scan times with the hope of producing similar imaging results in less than an hour compared to the 8 or more hours using current methods. This is still likely to take several years at the current pace of µCT development, increased uptake of the technology could drive this development sooner, but this is reliant on more studies like this one advocating its wider use in soft tissue imaging. The work in this report showed that localisation of IF staining could be accurately registered as confirmed by tissue morphology overlaps. This confirmed its potential for further use to investigate the localisation of antigens identified by any working primary antibody within a 3D tissue volume, even if they are not necessarily associated with specific structural features. There remain other areas in the registration steps which could be more efficient to make the workflow more automated and facilitate a higher sample throughput in the future. The initial resampling of the µCT to the plane of histology sectioning is a manual and time consuming process. Although it only needs to be done once per sample, implementing methods of automating this step (Chicherova *et al.*, 2018) would be valuable. The blood vessel segmentation, which currently relies on manual seed point placement could also be further automated. This could be achieved by implementing existing methods using machine learning to segment blood vessels (Wollatz *et al.*, 2017), combined with automated training from registered immunostaining of blood vessels to automatically locate seed points for segmenting the blood vessel lumen.

Using the developed techniques for the exemplar study of mild-moderate COPD tissue showed no biologically significant differences between the clinically similar groups. Some areas however showed the potential for differences, most notably the blood vessel branching, which with an increased number of samples would be interesting to see if any biologically significant differences are observed. This could also be expanded to compare the differences with more severe COPD samples with a GOLD rating of 3 or tissues with severe emphysema, which have not been studied in the 3D scale provided by the correlative workflow used here. Assuming access to clinically relevant FFPE tissue with intact microstructures an expanded study of the microvasculature in COPD could be completed in 4-6 months. Again assuming tissue availability different respiratory diseases could also be investigated using the same methodology as has been done previously with IPF tissue (Jones *et al.*, 2016). Different soft tissue types have been less-well studied by these approaches in comparison to lung, the application and further development of the automated registration for use with different tissue types would be interesting for broadening its use in

numerous research fields. The main issue to be addressed is that many soft tissues are not as heterogeneous as lung and it remains to be seen if the automated feature extraction tools work on more homogenous tissues. This is already being explored by a PhD student who is working on further development of the X-ray histology workflow for use in multiple tissue types. Developments in image acquisition technologies, such as phase contrast enhanced imaging, could also provide contrast to more homogenous tissues such as kidney or liver for use in correlative imaging studies (Zdora *et al.*, 2020).

The use of IF staining in the developed correlative imaging workflow for localisation of cell types within the 3D volume based on antigenicity facilitates future studies of any cell type, so long as they can be identified by a specific primary antibody in FFPE tissue sections. Future work for this project would be the completion of the CD68 staining in the remaining 10 tissues to at least the same level as the AA1 staining, which would take 3-6 months using the developed workflow. Macrophages have a much more well-defined role in COPD so it will be particularly interesting to see if there are any changes to the CD68 analysis between groups. There are numerous other pathologically relevant cell types which could be investigated in COPD, as well as a multitude of other respiratory diseases. Future work using the methodologies presented here are already being used in PhD projects investigating different cell types in COPD. The novel use of distance maps from segmented 3D networks presented here could be used as a new metric for measuring cellular distribution in wide-field imaging within the context of the 3D tissue. However, the measures presented here cannot give the cellular analysis in context of the tissue volume due to the staining being done on thin (4 μm) sections of tissue. To provide true 3D cellular data there are potential methods which could be used. The first would be to use newly developed nuclei counter stains for μCT imaging which do not affect antibody based staining (Metscher, 2020). This would provide the 3D localisation of cell nuclei which could be registered to the 2D IF staining to identify individual labelled cells per unit volume. This could potentially be further investigated to assess the relationship between the individual cells and the 3D tissue microstructures. Another option would be to perform 3D fluorescence imaging using a light sheet microscope, this uses thin planes of fluorescent light through a volume of tissue to build 3D IF data which could then potentially be registered to the 3D μCT volume (Power and Huisken, 2017). However, there are numerous issues including sample preparation and size which currently limit the use of light sheet microscopy for correlative studies.

With a longer time scale and a larger budget the work reported in this thesis could be used to investigate much larger cohorts of patient tissue samples, in a fraction of the time currently taken

for similar studies. This could be applied to a multitude of tissue types as µCT developments enable faster image acquisition with greater contrast and higher resolution. This could be achieved by hardware developments such as better optics, detectors or different acquisition techniques like phase contrast (Zdora *et al.*, 2020). However, this would require extensive hardware development outside the scope of this project. The data that could potentially be acquired following these developments would allow image registration to immuno-histological images with a greater degree of accuracy. Closer registration and observed similarities between histology and non-destructive µCT could then be used for true 3D X-ray histology from µCT tissue volumes (Katsamenis *et al.*, 2019). These images could potentially be used to characterise the 3D distribution of cellular information far more accurately than the methodology used in this study. This information could then be used in numerous studies of disease investigating the changing numbers and distributions of individual immune cells or structural proteins within clinically relevant 3D soft tissue volumes. Further into the future this registered information could be used for machine learning and the use of artificial intelligence for image analysis. This is a relatively new area of study being looked at in both research and clinical areas (Holzinger *et al.*, 2017; Adams *et al.*, 2020). The registered data of different cell types and features identified by IF and correlated with µCT, using the developed techniques reported in this thesis, could be used as training datasets for automated segmentation and subsequent analysis of more µCT datasets. This could eventually lead to the point where cells and features can be identified in µCT (or equivalent) data without the need for additional destructive imaging techniques. However it is important to note that correlative imaging workflows, like those reported here, will be required for a long time before that point is potentially reached for both research and clinical imaging.

Over the next few years it is hoped that the methodology workflow and results presented here will be used to drive larger studies of soft tissues using correlative X-ray histology. Over the course of the last year of this project the world has been facing the COVID-19 pandemic which has opened up a new field of respiratory research. The techniques presented here could be used to further study the effects the virus is having on lung tissue microstructure and how the distribution of cell types of interest are changing between patients. Interest in this work has already been expressed by COVID-19 research groups who are currently trying to find new methods for investigating the effects of the virus. The use of the developed methodology and results to provide new context and insight into well-studied conditions like COPD and the potential use in new respiratory studies demonstrates the utility and usefulness of the work reported here to be used in many differing future studies.

Appendix A

A.1 Full Table of patient characteristics used in this project

	Tissue ID	HL093	HL098	HL079	HL066B	HL086	EV118I	HL384	TL1127	HL094	HL382	EV027	EV020	EV104	HL119	HL085	HL116	HL126	HL156	HL162
Patient characteristics	Secondary ID	Lung1	Lung2	Lung3	COPD-1	COPD-2	COPD-3	COPD-4	COPD-5	Non-COPD-1	Non-COPD-2	Non-COPD-3	Non-COPD-4	Non-COPD-5	Non-COPD-6	-	-	-	-	-
	Procedure	Lobectomy	Bullectomy	Bullectomy	Lobectomy	Lobectomy	Lobectomy	Lobectomy	Lobectomy	Lobectomy	Lobectomy	Lobectomy	Lobectomy	Lobectomy	Lobectomy	Lobectomy	Lobectomy	Lobectomy	Lobectomy	Lobectomy
	Indication	Bronchiectasis	Pneumothorax	Pneumothorax	Cancer	Cancer	Cancer	Cancer	Cancer	Cancer	Cancer	Cancer	Cancer	Cancer	Cancer	Cancer	Cancer	Cancer	Cancer	Cancer
	Age	31	21	21	71	76	64	70	65	67	66	69	70	66	66	67	70	73	74	67
	Sex	F	M	M	F	M	F	F	M	F	F	M	F	M	M	M	F	M	M	M
Spirometry	FEV1	2.67	N/A	N/A	1.42	1.97	1.15	1.61	2.1	2.36	1.9	1.77	1.99	2.65	3.34	N/A	1.37	2.04	3.32	1.85
	% predicted	77	N/A	N/A	74	69	68	83	65	100	97	63	126	85	85	N/A	80.5	100	106	51
	FVC	3.35	N/A	N/A	2.58	3.17	2.33	2.44	3.5	3.08	2.52	2.18	2.67	3.36	4.44	N/A	2.15	2.68	4.19	2.99
	% predicted	82	N/A	N/A	100	82	88	105	86	100	107	59	138	84	N/A	N/A	82.7	90	98	67
	FEV1/FVC	0.79	N/A	N/A	0.56	0.62	0.64	0.66	0.59	0.77	0.75	0.81	0.75	0.79	0.75	0.77	0.64	0.76	0.79	0.62
Medical History	GOLD status	0	N/A	N/A	2	2	2	1	2	0	0	0	0	0	0	0	1	0	0	2
	Smoking status	None	None	None	Current	Current	Current	Ex	Ex	Current	Ex	Ex	Ex	Current	Current	None	Ex	Current	Ex	Ex
	Pack years	-	-	-	50	-	35	50	60	78	25	72	26	10	72	-	40	31	15	45
	Years ex	-	-	-	-	-	-	-	4	-	-	28	1	-	-	-	-	-	34	6
	Recent infections	N	N	N	N	N	-	N/A	N/A	N	-	N	N	N/A	N	N	N	N	N	N
	History of allergy	N	N	N	N	N	-	N/A	N/A	Y	-	N	Y	N/A	N	Y	Y	Y	N	N
	History of asthma	N	N	N	N	N	-	N/A	NN/A	N	-	Y	N	N/A	N	N	N	N	Y	N
	Co-morbidities	Lupus, thyrotoxicosis	None	None	Hypertension, COPD	IHD, angina, hypertension	-	hypertension, hypercholestraemia	hypertension		Rheumatoid arthritis	Asthma, Hip and knee replacement	Nil	Coeliac disease, meneres disease, prostate hypertrophy	Hypertension, Barrett's esophagus, anaemia, poss COPD	Angina, hypertension, reflux	Hypertension	Angina, MI, Hypertension, Lupus	Hypertension	Emphysema, Hypertension, Diabetes (type II), Osteoarthritis, Hypercholesterolaemia
	Medications	warfarin, carbimazole, plaquenil	None	None	Simvastatin, Anolodipine	Atenolol, Aspirin GTN, simvastatin, ranitidine, amilodipine, bendroflumethazide	peptac, mebeverine	Simvastatin, ramipril	amlodipine, losartan, spiriva	None	Hydroxychloroquine, meloxicam, thyroxine, lansoprazole, co-dydramol	Lansoprazole, Symbicort, Spiriva, Ventolin	Nicorette, Glucosamine	combodart	Lansoprazole, Ramipril, Quetiapine fumarate	Aspirin, amlodipine, valsartan, simvastatin	Angitel, Omeprazole, Metopropol, Innovace	Aspirin, Plzotifen, cocodamol, Lansoprazole, GTN, Elantan, Perindopril, Fusemide, Arovastatin	Ipratropium, Lisinopril, Aspirin, Mirtrazapine, Salmeterol	Salmeterol, Gliclazide, Bendroflumethizide, Spiriva, Dihydrocodeine, Simvastatin, Ramipril, Salbutamol, Omeprazole, Metformin, Rosiglitazone, Amitryptyline
	Steroids	N	N	N	N	N	N	N	N/A	N	N	Y	N	N	N	N	N	N	N	N

A.2 Table of laboratory equipment used in this PhD project

Equipment name	Main uses in project	Company
HistoStar paraffin wax embedder	Used for embedding formalin-fixed tissue in paraffin wax	Thermo Scientific
Med-X	Prototype µCT scanner used for image acquisition of all µCT datasets	Nikon X-Tek Systems Ltd.
Leica RM2135 wax microtome	Used for sectioning FFPE lung tissue	Leica Biosystems
Olympus VS110	Fluorescence slide scanning microscope used for image acquisition of H&E and IF stained sections	Olympus
IRIDIS-5 visualisation cluster	HPC used for image processing and segmentation	University of Southampton

A.3 Table of software used in this PhD project

Software (version no.)	Main uses in project	Company	Links/references
Inspect-X	Proprietary software for driving the Med-X µCT scanner and image acquisition	Nikon X-Tek Systems Ltd.	https://www.nikonmetrology.com/en-gb/product/inspect-x
CTPro (v 5.1.6054.18526)	Reconstruction of µCT projections into 3D datasets	Nikon X-Tek Systems Ltd.	
Avizo (v 9.3)	µCT plane correspondence to histology 3D visualisation Segmentation Network analysis and skeletonisation Distance maps	Thermo Fisher Scientific	-
VS110 / VS Desktop	Proprietary software for image acquisition using the VS110 slide scanning microscope Visualisation and conversion of raw wide-field microscopy images	Olympus	-
ITK-Snap (v 3.6)	Blood vessel segmentation Interpolation of Ck18 staining		http://www.itksnap.org
NICE EnginFrame (v 2020.0-r58)	User interface for access to the IRIDIS-5 HPC computer cluster at the University of Southampton	Amazon web company	https://www.ni-sp.com/nice-enginframe/
GraphPad Prism (v 8.4.3)	Statistical analysis and plotting graphs used in chapters 4 and 5	GraphPad Software	https://www.graphpad.com/
Fiji (ImageJ)	Basic image processing of µCT and histology images (e.g. rotation, background subtraction, filtering) Scripting 2D visualisation Plugins (detailed below) used for image processing and analysis	-	https://imagej.net
Fiji plugin-BigWarp	Main component of ;automated warping script'	-	https://imagej.net/BigWarp
Fiji plugin-Feature extraction	Main component of ;automated warping script'	-	https://imagej.net/Feature_Extraction
Fiji plugin- BoneJ	Calculating thickness maps	-	https://imagej.net/BoneJ

A.4 The 'Rotate_Reslice_Blockface' script as plain text for use in Fiji

```
/*Copyright 2018, 2019 University of Southampton
 Mr Matthew Lawson
  Clinical and experimental sciences
  Faculty of Medicine
  Licensed under the Apache License, Version 2.0 (the "License");
  you may not use this file except in compliance with the License.
  You may obtain a copy of the License at
     http://www.apache.org/licenses/LICENSE-2.0
  Unless required by applicable law or agreed to in writing, software
  distributed under the License is distributed on an "AS IS" BASIS,
  WITHOUT WARRANTIES OR CONDITIONS OF ANY KIND, either express or implied.
  See the License for the specific language governing permissions and
  limitations under the License.
*/
//script for rotating and reslicing micro CT stacks into the same orientation as the cutting face of the block
//user asked to draw line to calculate 1st angle of rotation
setTool("line");
 ID = getImageID();
waitForUser("Draw Line on Front Edge of Block!"); run("Measure");
            Angle1 =getResult("Angle");
            run("Select None");
                        title = getTitle(); //print(stackName);
dotIndex = indexOf(title, ".");
basename = substring(title, 0, dotIndex); //removes .tif from title
run("Rotate... ", "grid=1 interpolation=Bicubic stack enlarge stack angle="+ Angle1);
run("Reslice [/]...", "output=1 start=Left rotate avoid");
selectWindow(title);
close();
selectWindow("Reslice of "+basename);
//user asked to draw line to calculate 2nd angle of rotation
setTool("line");
 ID = getImageID();
title = "User Action Required:";
 msg = "draw a line to measure the angle at the front of the tissue\nthen click \"OK\".";
waitForUser("Draw Line on Front Edge of Block!"); run("Measure");
            Angle2 =getResult("Angle");
            run("Select None");
run("Rotate... ", " grid=1 interpolation=Bicubic stack enlarge stack angle="+Angle2);
//user will be asked to draw a rectangle around the roi to crop down the final resliced image
setTool("rectangle");
 ID = getImageID();
 title = "User Action Required:";
 msg = "draw a rectangle around the roi\n move the slider to ensure all tissue is in the rectangle\nthen click \"OK\".";
 waitForUser(title, msg);
run("Reslice [/]...", "output=1.000 start=Top avoid");
selectWindow("Reslice of "+basename);
close();
selectWindow("Reslice of Reslice");
//save resliced file with appropriate name
```

A.5 Fiji script used with Weka for large images

```
// @File(label="Input directory", description="Select the directory with input images", style="directory") inputDir
// @File(label="Output directory", description="Select the output directory", style="directory") outputDir
// @File(label="Weka model", description="Select the Weka model to apply") modelPath
// @String(label="Result mode",choices={"Labels","Probabilities"}) resultMode
// @Integer(label="Number of tiles in X:", description="Number of image subdivisions in the X direction", value=3) xTiles
```

```
// @Integer(label="Number of tiles in Y:", description="Number of image subdivisions in the Y direction", value=3) yTiles
// @Integer(label="Number of tiles in Z (set to 0 for 2D processing):", description="Number of image subdivisions in the Z direction
(ignored when using 2D images)", value=3) zTiles
import trainableSegmentation.WekaSegmentation;
import trainableSegmentation.utils.Utils;
import ij.io.FileSaver;
import ij.IJ;
import ij.ImagePlus;
// starting time
startTime = System.currentTimeMillis();
// caculate probabilities?
getProbs = resultMode.equals( "Probabilities" );
// create segmentator
segmentator = new WekaSegmentation( zTiles > 0 );
// load classifier
segmentator.loadClassifier( modelPath.getCanonicalPath() );
// get list of input images
listOfFiles = inputDir.listFiles();
for ( i = 0; i < listOfFiles.length; i++ )
{
  // process only files (do not go into sub-folders)
  if( listOfFiles[ i ].isFile() )
  {
    // try to read file as image
    image = IJ.openImage( listOfFiles[i].getCanonicalPath() );
    if( image != null )
    {
      tilesPerDim = new int[ 2 ];
      if( image.getNSlices() > 1 )
      {
        tilesPerDim = new int[ 3 ];
        tilesPerDim[ 2 ] = zTiles;
      }
      tilesPerDim[ 0 ] = xTiles;
      tilesPerDim[ 1 ] = yTiles;
      // apply classifier and get results (0 indicates number of threads is auto-detected)
      result = segmentator.applyClassifier( image, tilesPerDim, 0, getProbs );
      if( !getProbs )
        // assign same LUT as in GUI
        result.setLut( Utils.getGoldenAngleLUT() );
      // save result as TIFF in output folder
      outputFileName = listOfFiles[ i ].getName().replaceFirst("[.][^.]+$", "") + ".tif";
      new FileSaver( result ).saveAsTiff( outputDir.getPath() + File.separator + outputFileName );
      // force garbage collection (important for large images)
      result = null;
      image = null;
      System.gc();
    }
  }
}
// print elapsed time
estimatedTime = System.currentTimeMillis() - startTime;
IJ.log( "** Finished processing folder in " + estimatedTime + " ms **" );
System.gc();
```

A.6 The developed ‘automated warping script’ as plain text for use in Fiji

```
/*Copyright 2019, 2020 University of Southampton
 Mr Matthew Lawson
  Clinical and experimental sciences
  Faculty of Medicine
```

```
Script for assigning SIFT landmarks to CT and FITC fluorescence images
Instructions for use:
1. create an input and output directory folders
2. Within the input directory place all the CT and fluorescence images to be transformed by the bigWarp plugin
3. Ensure consistent file naming- for this script ensure that matching CT and fluorescence slices have the same number at the start e.g.
'tissue no'_Sectionxx_...
4. Ensure file names end consistently for each image type e.g. "_CT.tif" for the CT image and "_FITC.tif" for the fluorescence image
used for warping e.g. autofluorescence,
5. up to 5 immunofluorescent markers (channels) can be implemented with this macro. If the number of markers > 5, the macro will
have to be modified accordingly.
6. Example file names: "HL093_Section31_Ck18_CT.tif", "HL093_Section31_Ck18_FITC.tif", "HL093_Section31_Ck18_CY5.tif",
"HL093_Section31_Ck18_DAPI.tif"
- the above example names would cover one CT slice to section pair for warping in an image separated into 3 fluorescence channels
7. saved files in the output folder will end with .bigwarped for each image
*/

//*******************************************************************************************
//Select file locations and output save locations

dirIN = getDirectory("Choose the image source folder");
dirOUT = getDirectory("Choose the output folder");

win = 32;  //filter for searching for duplicate landmarks, higher number will result in more deleted landmarks, if result is a black image
consider increasing this number

//*******************************************************************************************
//dialog box asking for nbr of immunofluorescence channels, and the images' suffix (CT, DAPI, CY5,...)

channelNbr = getNumber("How many channels (images to be registered) in addition to CT and autofluorescence?", 0);
channelList = newArray(channelNbr);

title1 = "Untitled";
title2 = "Untitled";

for(i=0; i<channelNbr; i++){
        channelList[i] = "Untitled";
}

Dialog.create("Enter file name endings for each image type here (e.g. CT, FITC,...)");
Dialog.addString("CT:", title1);
Dialog.addString("Autofluorescence:", title2);
for(i=0; i<channelNbr; i++){
        Dialog.addString("Immunofluorescence (IFI) "+i+":", channelList[i]);
}

Dialog.show();
title1 = Dialog.getString();
title2 = Dialog.getString();
for(i=0; i<channelNbr; i++){
        channelList[i] = Dialog.getString();
```

```
}
Array.sort(channelList);

list = getFileList(dirIN);

//*******************************************************************************************
// Sort the images by slice number and image type (CT, Autofluorescence (ex: FITC), up to 5 Immunofluorescence (ex:DAPI, CY5, ...)
// Creates lists for each image type

listCT = newArray(0);
for (i=0; i<list.length; i++){
	if(endsWith(list[i], title1+".tif")){
		listCT = Array.concat(listCT, list[i]);
	}
}
Array.sort(listCT);

listAutoFl = newArray(0);
for (i=0; i<list.length; i++){
	if(endsWith(list[i], title2+".tif")){
		listAutoFl = Array.concat(listAutoFl, list[i]);
	}
}
Array.sort(listAutoFl);

if(channelNbr == 1){
	listIFl1 = newArray(0);
	for(i=0; i<lengthOf(list); i++){
		if(endsWith(list[i], channelList[0]+".tif")){
			listIFl1 = Array.concat(listIFl1, list[i]);
		}
	}
}
if(channelNbr == 2){
	listIFl1 = newArray(0);
	listIFl2 = newArray(0);
	for(i=0; i<lengthOf(list); i++){
		if(endsWith(list[i], channelList[0]+".tif")){
			listIFl1 = Array.concat(listIFl1, list[i]);
		}
		if(endsWith(list[i], channelList[1]+".tif")){
			listIFl2 = Array.concat(listIFl2, list[i]);
		}
	}
}
if(channelNbr == 3){
	listIFl1 = newArray(0);
	listIFl2 = newArray(0);
	listIFl3 = newArray(0);
	for(i=0; i<lengthOf(list); i++){
		if(endsWith(list[i], channelList[0]+".tif")){
			listIFl1 = Array.concat(listIFl1, list[i]);
		}
		if(endsWith(list[i], channelList[1]+".tif")){
			listIFl2 = Array.concat(listIFl2, list[i]);
		}
		if(endsWith(list[i], channelList[2]+".tif")){
			listIFl3 = Array.concat(listIFl3, list[i]);
		}
	}
}
if(channelNbr == 4){
	listIFl1 = newArray(0);
	listIFl2 = newArray(0);
```

```
		listIFl3 = newArray(0);
		listIFl4 = newArray(0);
		for(i=0; i<lengthOf(list); i++){
			if(endsWith(list[i], channelList[0]+".tif")){
				listIFl1 = Array.concat(listIFl1, list[i]);
			}
			if(endsWith(list[i], channelList[1]+".tif")){
				listIFl2 = Array.concat(listIFl2, list[i]);
			}
			if(endsWith(list[i], channelList[2]+".tif")){
				listIFl3 = Array.concat(listIFl3, list[i]);
			}
			if(endsWith(list[i], channelList[3]+".tif")){
				listIFl4 = Array.concat(listIFl4, list[i]);
			}
		}
}
if(channelNbr == 5){
		listIFl1 = newArray(0);
		listIFl2 = newArray(0);
		listIFl3 = newArray(0);
		listIFl4 = newArray(0);
		listIFl5 = newArray(0);
		for(i=0; i<lengthOf(list); i++){
			if(endsWith(list[i], channelList[0]+".tif")){
				listIFl1 = Array.concat(listIFl1, list[i]);
			}
			if(endsWith(list[i], channelList[1]+".tif")){
				listIFl2 = Array.concat(listIFl2, list[i]);
			}
			if(endsWith(list[i], channelList[2]+".tif")){
				listIFl3 = Array.concat(listIFl3, list[i]);
			}
			if(endsWith(list[i], channelList[3]+".tif")){
				listIFl4 = Array.concat(listIFl4, list[i]);
			}
			if(endsWith(list[i], channelList[4]+".tif")){
				listIFl5 = Array.concat(listIFl5, list[i]);
			}
		}
}

setBatchMode(true);

// ********************************************************************************
// loop through each list of images to match each CT image to its corresponding fluorescent images

for(f=0; f<listCT.length; f++){
		open(dirIN + listCT[f]);
		targetPath = dirIN + listCT[f];
		CTtitle = getTitle();
		CTname = File.nameWithoutExtension;

		open(dirIN + listAutoFl[f]);
		AutoFlPath = dirIN + listAutoFl[f];
		AutoFlTitle = getTitle();
		AutoFlname = File.nameWithoutExtension;

		if(channelNbr == 1){
			IFl1Path = dirIN + listIFl1[f];
		}
		if(channelNbr == 2){
```

```
		IFl1Path = dirIN + listIFl1[f];
		IFl2Path = dirIN + listIFl2[f];
	}
	if(channelNbr == 3){
		IFl1Path = dirIN + listIFl1[f];
		IFl2Path = dirIN + listIFl2[f];
		IFl3Path = dirIN + listIFl3[f];
	}
	if(channelNbr == 4){
		IFl1Path = dirIN + listIFl1[f];
		IFl2Path = dirIN + listIFl2[f];
		IFl3Path = dirIN + listIFl3[f];
		IFl4Path = dirIN + listIFl4[f];
	}
	if(channelNbr == 5){
		IFl1Path = dirIN + listIFl1[f];
		IFl2Path = dirIN + listIFl2[f];
		IFl3Path = dirIN + listIFl3[f];
		IFl4Path = dirIN + listIFl4[f];
		IFl5Path = dirIN + listIFl5[f];
	}

	//*****************************************************************
	// SIFT
	//repeated SIFT and coordinate saving of matching features with different size filters

	for (size=4; size<=28; size=size+4) {
		print("\nRunning SIFT with feature descriptor size: "+size);
		run("Extract SIFT Correspondences", "source_image=[CTtitle] target_image=[AutoFlTitle] initial_gaussian_blur=1.5
steps_per_scale_octave=3 minimum_image_size=64 maximum_image_size=1024 feature_descriptor_size="+size+"
feature_descriptor_orientation_bins=8 closest/next_closest_ratio=0.92 filter maximal_alignment_error=25 minimal_inlier_ratio=0.05
minimal_number_of_inliers=7 expected_transformation=Affine");
		selectWindow(CTtitle);
		asd = selectionType();
		if( asd == -1 )	{
		print ("=== NO MATCH at size: " + size + " ===");
		run("Select None");
		}
		else {
		print("=== MATCHES FOUND at size: " + size + " ===");
		selectWindow(CTtitle);
		roiManager("Add");
		selectWindow(AutoFlTitle);
		roiManager("Add");
		}
	}

	selectWindow("Log");
	saveAs("text", dirOUT+CTname+"_SIFT_log.txt");
	run("Close");

	print("SIFT computation finished. Searching for duplicates...");
	print("");

	// ********************************************************************
	// search for duplicate landmarks by creating new array and not adding duplicate results to it

	n = roiManager("count");
	run("Set Measurements...", "display redirect=None decimal=3");
	for(i=0; i<n; i=i+2){
		roiManager("Select", i);
		roiManager("Measure");
	}
```

```
        nRes = nResults();
        if (nResults==0) {
    print("skipping image "+f);
    run ("Close All");
    continue;
  }

        for(i=1; i<n; i=i+2){
                roiManager("Select", i);
                roiManager("Measure");
        }

        CTx = newArray(nRes);
        CTy = newArray(nRes);
        Histox = newArray(nRes);
        Histoy = newArray(nRes);
        total = 0;
        discarded = 0;

        for (a=0; a<nRes; a=a+1) {
                aCT = a;
                aHist = a+nRes;

                xCT = getResult("X", aCT);
                yCT = getResult("Y", aCT);
                xCTRight = xCT + win;
                xCTLeft = xCT - win;
                yCTup = yCT + win;
                yCTDown = yCT - win;

                xHist = getResult("X", aHist);
                yHist = getResult("Y", aHist);
                xHistRight = xHist + win;
                xHistLeft = xHist - win;
                yHistUp = yHist + win;
                yHistDown = yHist - win;

                exists = false;
                for (l = 0; l < total; l=l+1) {
                        if (CTx[l]<xCTRight && CTx[l]>xCTLeft && CTy[l]<yCTup && CTy[l]>yCTDown && Histox[l]<xHistRight &&
Histox[l]>xHistLeft && Histoy[l]<yHistUp && Histoy[l]>yHistDown){
                                exists = true;
                        }
                }

                if (exists==false){
                        CTx[total] = xCT;
                        CTy[total] = yCT;
                        Histox[total] = xHist;
                Histoy[total] = yHist;
                total += 1;
                } else{
                        print("Discarded duplicate CT - Hist: ("+xCT+", "+yCT+") - ("+xHist+","+yHist+")");
                        discarded += 1;
                }
        }

        selectWindow("Results");
        run("Close");

        print("");
        print("SIFT output with size filter 4 to 28 = "+n+" landmarks");
```

```
	print("Duplicates with 32x32 pixels exclusion window = "+discarded);
	print("Number of landmarks left for Bigwarp = "+total);
	selectWindow("Log");
	saveAs("text", dirOUT+CTname+"_SIFT_UniqueLandmarks_log.txt");
	run("Close");

	run("Input/Output...", "jpeg=85 gif=-1 file=.csv use_file");

	// ********************************************************************
	// create a table with co-ordinates in the 'bigwarp format' and save as a .csv

	for(i=0; i<total; i=i+1){
		setResult("Pt", i, "Pt-"+i);
		setResult("TRUE", i, "TRUE");
		setResult("Histox", i, Histox[i]);
		setResult("Histoy", i, Histoy[i]);
		setResult("CTx", i, CTx[i]);
		setResult("CTy", i, CTy[i]);
	}
	updateResults;
	saveAs("Results", dirOUT+CTname +"_sift landmarks.csv");
	landmarksPath = dirOUT+CTname +"_sift landmarks.csv";

	selectWindow("Results");
	run("Clear Results");
	run("Close");

	roiManager("save", dirOUT+CTname+"_ROI.zip");
	run("Close");

	//*********************************************************************
	// Bigwarp
	// use unique landmark coordinates from SIFT to transform fluorescent images to match the CT

	AutoFlPath=replace(AutoFlPath,"\\","/");
	targetPath=replace(targetPath,"\\","/");
	landmarksPath=replace(landmarksPath,"\\","/");

	// matching autofluorescence image(s) to CT
	run("Big Warp Apply", "landmarks_image_file=["+landmarksPath+"] moving_image_file=["+AutoFlPath+"]
target_space_file=["+targetPath+"] resolution=Target field=Target point=[] x=0.1000 y=0.1000 z=0.1000 x_0=18.0000 y_0=23.0000
z_0=5.0000 x_1=20 y_1=31 z_1=7 interpolation=[Nearest Neighbor] threads=4");
	run("Enhance Contrast", "saturated=0.35");
	saveAs("Tiff", dirOUT+AutoFlname+"_bigwarped.tif");
	close();

	// matching immunofluorescence image(s) to CT
	if(channelNbr == 1){
		open(IFl1Path);
		IFl1name = File.nameWithoutExtension;
		IFl1Path=replace(IFl1Path,"\\","/");
		run("Big Warp Apply", "landmarks_image_file=["+landmarksPath+"] moving_image_file=["+IFl1Path+"]
target_space_file=["+targetPath+"] resolution=Target field=Target point=[] x=0.1000 y=0.1000 z=0.1000 x_0=18.0000 y_0=23.0000
z_0=5.0000 x_1=20 y_1=31 z_1=7 interpolation=[Nearest Neighbor] threads=4");
		run("Enhance Contrast", "saturated=0.35");
		saveAs("Tiff", dirOUT+IFl1name+"_bigwarped.tif");
		close();
	}

	if(channelNbr == 2){
		open(IFl1Path);
		IFl1name = File.nameWithoutExtension;
		IFl1Path=replace(IFl1Path,"\\","/");
```

```
		run("Big Warp Apply", "landmarks_image_file=["+landmarksPath+"] moving_image_file=["+IFl1Path+"]
target_space_file=["+targetPath+"] resolution=Target field=Target point=[] x=0.1000 y=0.1000 z=0.1000 x_0=18.0000 y_0=23.0000
z_0=5.0000 x_1=20 y_1=31 z_1=7 interpolation=[Nearest Neighbor] threads=4");
		run("Enhance Contrast", "saturated=0.35");
		saveAs("Tiff", dirOUT+IFl1name+"_bigwarped.tif");
		close();

		open(IFl2Path);
		IFl2name = File.nameWithoutExtension;
		IFl2Path=replace(IFl2Path,"\\","/");
		run("Big Warp Apply", "landmarks_image_file=["+landmarksPath+"] moving_image_file=["+IFl2Path+"]
target_space_file=["+targetPath+"] resolution=Target field=Target point=[] x=0.1000 y=0.1000 z=0.1000 x_0=18.0000 y_0=23.0000
z_0=5.0000 x_1=20 y_1=31 z_1=7 interpolation=[Nearest Neighbor] threads=4");
		run("Enhance Contrast", "saturated=0.35");
		saveAs("Tiff", dirOUT+IFl2name+"_bigwarped.tif");
		close();
	}

	if(channelNbr == 3){
		open(IFl1Path);
		IFl1name = File.nameWithoutExtension;
		IFl1Path=replace(IFl1Path,"\\","/");
		run("Big Warp Apply", "landmarks_image_file=["+landmarksPath+"] moving_image_file=["+IFl1Path+"]
target_space_file=["+targetPath+"] resolution=Target field=Target point=[] x=0.1000 y=0.1000 z=0.1000 x_0=18.0000 y_0=23.0000
z_0=5.0000 x_1=20 y_1=31 z_1=7 interpolation=[Nearest Neighbor] threads=4");
		run("Enhance Contrast", "saturated=0.35");
		saveAs("Tiff", dirOUT+IFl1name+"_bigwarped.tif");
		close();

		open(IFl2Path);
		IFl2name = File.nameWithoutExtension;
		IFl2Path=replace(IFl2Path,"\\","/");
		run("Big Warp Apply", "landmarks_image_file=["+landmarksPath+"] moving_image_file=["+IFl2Path+"]
target_space_file=["+targetPath+"] resolution=Target field=Target point=[] x=0.1000 y=0.1000 z=0.1000 x_0=18.0000 y_0=23.0000
z_0=5.0000 x_1=20 y_1=31 z_1=7 interpolation=[Nearest Neighbor] threads=4");
		run("Enhance Contrast", "saturated=0.35");
		saveAs("Tiff", dirOUT+IFl2name+"_bigwarped.tif");
		close();

		open(IFl3Path);
		IFl3name = File.nameWithoutExtension;
		IFl3Path=replace(IFl3Path,"\\","/");
		run("Big Warp Apply", "landmarks_image_file=["+landmarksPath+"] moving_image_file=["+IFl3Path+"]
target_space_file=["+targetPath+"] resolution=Target field=Target point=[] x=0.1000 y=0.1000 z=0.1000 x_0=18.0000 y_0=23.0000
z_0=5.0000 x_1=20 y_1=31 z_1=7 interpolation=[Nearest Neighbor] threads=4");
		run("Enhance Contrast", "saturated=0.35");
		saveAs("Tiff", dirOUT+IFl3name+"_bigwarped.tif");
		close();
	}

	if(channelNbr == 4){
		open(IFl1Path);
		IFl1name = File.nameWithoutExtension;
		IFl1Path=replace(IFl1Path,"\\","/");
		run("Big Warp Apply", "landmarks_image_file=["+landmarksPath+"] moving_image_file=["+IFl1Path+"]
target_space_file=["+targetPath+"] resolution=Target field=Target point=[] x=0.1000 y=0.1000 z=0.1000 x_0=18.0000 y_0=23.0000
z_0=5.0000 x_1=20 y_1=31 z_1=7 interpolation=[Nearest Neighbor] threads=4");
		run("Enhance Contrast", "saturated=0.35");
		saveAs("Tiff", dirOUT+IFl1name+"_bigwarped.tif");
		close();

		open(IFl2Path);
```

```
		IFl2name = File.nameWithoutExtension;
		IFl2Path=replace(IFl2Path,"\\","/");
		run("Big Warp Apply", "landmarks_image_file=["+landmarksPath+"] moving_image_file=["+IFl2Path+"]
target_space_file=["+targetPath+"] resolution=Target field=Target point=[] x=0.1000 y=0.1000 z=0.1000 x_0=18.0000 y_0=23.0000
z_0=5.0000 x_1=20 y_1=31 z_1=7 interpolation=[Nearest Neighbor] threads=4");
		run("Enhance Contrast", "saturated=0.35");
		saveAs("Tiff", dirOUT+IFl2name+"_bigwarped.tif");
		close();

		open(IFl3Path);
		IFl3name = File.nameWithoutExtension;
		IFl3Path=replace(IFl3Path,"\\","/");
		run("Big Warp Apply", "landmarks_image_file=["+landmarksPath+"] moving_image_file=["+IFl3Path+"]
target_space_file=["+targetPath+"] resolution=Target field=Target point=[] x=0.1000 y=0.1000 z=0.1000 x_0=18.0000 y_0=23.0000
z_0=5.0000 x_1=20 y_1=31 z_1=7 interpolation=[Nearest Neighbor] threads=4");
		run("Enhance Contrast", "saturated=0.35");
		saveAs("Tiff", dirOUT+IFl3name+"_bigwarped.tif");
		close();

		open(IFl4Path);
		IFl4name = File.nameWithoutExtension;
		IFl4Path=replace(IFl4Path,"\\","/");
		run("Big Warp Apply", "landmarks_image_file=["+landmarksPath+"] moving_image_file=["+IFl4Path+"]
target_space_file=["+targetPath+"] resolution=Target field=Target point=[] x=0.1000 y=0.1000 z=0.1000 x_0=18.0000 y_0=23.0000
z_0=5.0000 x_1=20 y_1=31 z_1=7 interpolation=[Nearest Neighbor] threads=4");
		run("Enhance Contrast", "saturated=0.35");
		saveAs("Tiff", dirOUT+IFl4name+"_bigwarped.tif");
		close();
	}

	if(channelNbr == 5){
		open(IFl1Path);
		IFl1name = File.nameWithoutExtension;
		IFl1Path=replace(IFl1Path,"\\","/");
		run("Big Warp Apply", "landmarks_image_file=["+landmarksPath+"] moving_image_file=["+IFl1Path+"]
target_space_file=["+targetPath+"] resolution=Target field=Target point=[] x=0.1000 y=0.1000 z=0.1000 x_0=18.0000 y_0=23.0000
z_0=5.0000 x_1=20 y_1=31 z_1=7 interpolation=[Nearest Neighbor] threads=4");
		run("Enhance Contrast", "saturated=0.35");
		saveAs("Tiff", dirOUT+IFl1name+"_bigwarped.tif");
		close();

		open(IFl2Path);
		IFl2name = File.nameWithoutExtension;
		IFl2Path=replace(IFl2Path,"\\","/");
		run("Big Warp Apply", "landmarks_image_file=["+landmarksPath+"] moving_image_file=["+IFl2Path+"]
target_space_file=["+targetPath+"] resolution=Target field=Target point=[] x=0.1000 y=0.1000 z=0.1000 x_0=18.0000 y_0=23.0000
z_0=5.0000 x_1=20 y_1=31 z_1=7 interpolation=[Nearest Neighbor] threads=4");
		run("Enhance Contrast", "saturated=0.35");
		saveAs("Tiff", dirOUT+IFl2name+"_bigwarped.tif");
		close();

		open(IFl3Path);
		IFl3name = File.nameWithoutExtension;
		IFl3Path=replace(IFl3Path,"\\","/");
		run("Big Warp Apply", "landmarks_image_file=["+landmarksPath+"] moving_image_file=["+IFl3Path+"]
target_space_file=["+targetPath+"] resolution=Target field=Target point=[] x=0.1000 y=0.1000 z=0.1000 x_0=18.0000 y_0=23.0000
z_0=5.0000 x_1=20 y_1=31 z_1=7 interpolation=[Nearest Neighbor] threads=4");
		run("Enhance Contrast", "saturated=0.35");
		saveAs("Tiff", dirOUT+IFl3name+"_bigwarped.tif");
		close();

		open(IFl4Path);
		IFl4name = File.nameWithoutExtension;
		IFl4Path=replace(IFl4Path,"\\","/");
```

```
                run("Big Warp Apply", "landmarks_image_file=["+landmarksPath+"] moving_image_file=["+IFl4Path+"]
target_space_file=["+targetPath+"] resolution=Target field=Target point=[] x=0.1000 y=0.1000 z=0.1000 x_0=18.0000 y_0=23.0000
z_0=5.0000 x_1=20 y_1=31 z_1=7 interpolation=[Nearest Neighbor] threads=4");
                run("Enhance Contrast", "saturated=0.35");
                saveAs("Tiff", dirOUT+IFl4name+"_bigwarped.tif");
                close();

                open(IFl5Path);
                IFl5name = File.nameWithoutExtension;
                IFl5Path=replace(IFl5Path,"\\","/");
                run("Big Warp Apply", "landmarks_image_file=["+landmarksPath+"] moving_image_file=["+IFl5Path+"]
target_space_file=["+targetPath+"] resolution=Target field=Target point=[] x=0.1000 y=0.1000 z=0.1000 x_0=18.0000 y_0=23.0000
z_0=5.0000 x_1=20 y_1=31 z_1=7 interpolation=[Nearest Neighbor] threads=4");
                run("Enhance Contrast", "saturated=0.35");
                saveAs("Tiff", dirOUT+IFl5name+"_bigwarped.tif");
                close();
        }

        roiManager("reset");
        run("Close All");

}
setBatchMode(false);
run("Close All");
exit("END OF MACRO");
```

A.7 Link to repository of supplementary videos

All videos generated for visualisation of the data in this project can be found at the following

http://doi.org/10.5281/zenodo.4309950

A.7.1 Blood vessel segmentation with ITK-SNAP

Video showing the real time process of segmenting a blood vessel from µCT lung data using ITK-SNAP.

A.7.2 Lung 1 summary video

Video summary of the µCT data from method development tissue HL093 (Lung1) showing the 2D slices through the sectioned volume building into the 3D volume rendering. The segmentation of blood vessels (red) and Ck18 can also be seen in 2D and 3D.

A.7.3 Lung 2 summary video

Video summary of the µCT data from method development tissue HL098 (Lung2) showing the 2D slices through the sectioned volume building into the 3D volume rendering. The segmentation of blood vessels (red) and Ck18 can also be seen in 2D and 3D.

A.7.4 Non-COPD-5 Blood vessel thickness-3D

A 360° rotation of the 3D blood vessel thickness map of the Non-COPD-5 tissue seen in Figure 4.5.

A.7.5 COPD-4 Blood vessel thickness-3D

A 360° rotation of the 3D blood vessel thickness map of the COPD-4 tissue seen in Figure 4.5.

A.7.6 COPD-4 Full segmentation of sectioned volume

A 360° rotation of the full segmentation seen in Figure 5.18. The µCT volume has been made semi-transparent to visualise the segmentation of blood vessels (red), Ck18 (blue), dilated AA1-mast cells (pink) and dilated CD68-macrophages (yellow).

A.8 Images of exemplar negative controls used in IF imaging

The upper image shows a section of FFPE lung tissue stained only with an Alexa Fluor® 647 secondary antibody imaged with the Cy5 channel. The lower image shows a neighbouring tissue section stained for Ck18 using the same secondary antibody.

Secondary antibody only control example

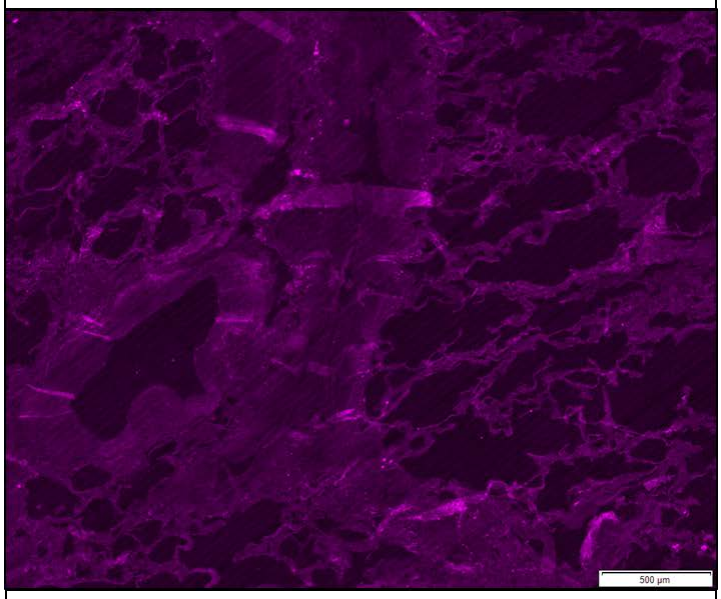

Example Ck18 positive staining on neighbouring section

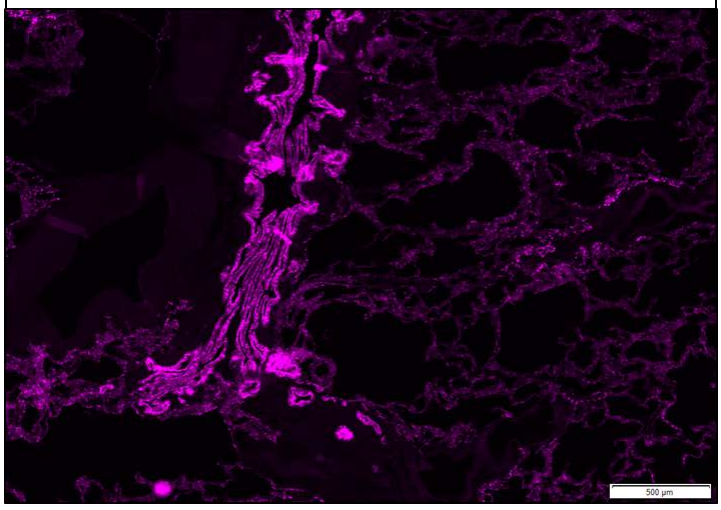

A.9 Preliminary results of AA1 distances from thick and thin blood vessels.

The top graph shows the non-COPD-5 tissue distance plots as line graphs from the thinnest and thickest blood vessels identified in the volume (µm). The lower graph shows the COPD-4 tissue distance plots as line graphs from the thinnest and thickest blood vessels in the volume.

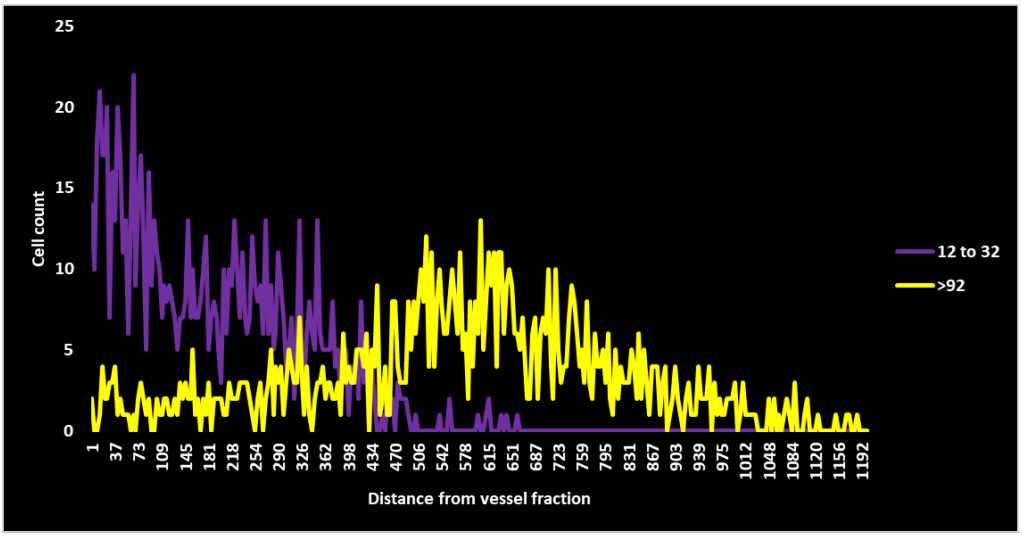

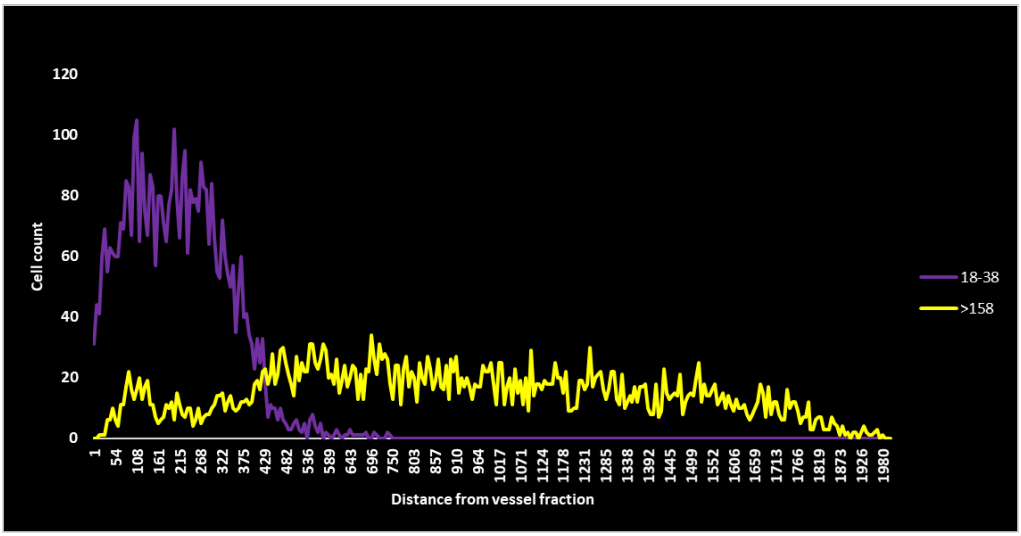

List of References

Adams, J., Qiu, Y., Xu, Y. and Schnable, J.C. (2020) Plant segmentation by supervised machine learning methods. *The Plant Phenome Journal,* 3 (1), e20001.

Agusti, A., Calverley, P.M.A., Celli, B., Coxson, H.O., Edwards, L.D., Lomas, D.A., Macnee, W., Miller, B.E., Rennard, S., Silverman, E.K., Tal-Singer, R., Wouters, E., Yates, J.C., Vestbo, J. and The Evaluation Of, C.L.T.I.P.S.E.I. (2010) Characterisation of COPD heterogeneity in the ECLIPSE cohort. *Respiratory Research,* 11 (1), 122.

Akhter, M.P., Kimmel, D., Lappe, J.M. and Recker, R.R. (2017) Effect of macroanatomic bone type and estrogen loss on osteocyte lacunar properties in healthy adult women. *Calcified Tissue International,* 100 (6), 619-630.

Alilou, M., Orooji, M., Beig, N., Prasanna, P., Rajiah, P., Donatelli, C., Velcheti, V., Rakshit, S., Yang, M. and Jacono, F. (2018) Quantitative vessel tortuosity: A potential ct imaging biomarker for distinguishing lung granulomas from adenocarcinomas. *Scientific Reports,* 8 (1), 1-16.

Andersson, C.K., Mori, M., Bjermer, L., Lofdahl, C.-G. and Erjefalt, J.S. (2010) Alterations in lung mast cell populations in patients with chronic obstructive pulmonary disease. *American Journal of Respiratory and Critical Care Medicine,* 181 (3), 206-217.

Ando, T., Bhamidimarri, S.P., Brending, N., Colin-York, H., Collinson, L., De Jonge, N., De Pablo, P.J., Debroye, E., Eggeling, C., Franck, C., Fritzsche, M., Gerritsen, H., Giepmans, B.N.G., Grunewald, K., Hofkens, J., Hoogenboom, J.P., Janssen, K.P.F., Kaufmann, R., Klumperman, J., Kurniawan, N., Kusch, J., Liv, N., Parekh, V., Peckys, D.B., Rehfeldt, F., Reutens, D.C., Roeffaers, M.B.J., Salditt, T., Schaap, I.a.T., Schwarz, U.S., Verkade, P., Vogel, M.W., Wagner, R., Winterhalter, M., Yuan, H. and Zifarelli, G. (2018) The 2018 correlative microscopy techniques roadmap. *Journal of Physics D: Applied Physics,* 51 (44), 443001.

Arganda-Carreras, I., Kaynig, V., Rueden, C., Eliceiri, K.W., Schindelin, J., Cardona, A. and Sebastian Seung, H. (2017) Trainable Weka segmentation: A machine learning tool for microscopy pixel classification. *Bioinformatics,* 33 (15), 2424-2426.

Arifin, A.Z. and Asano, A. (2006) Image segmentation by histogram thresholding using hierarchical cluster analysis. *Pattern Recognition Letters,* 27 (13), 1515-1521.

Artaechevarria, X., Pérez-Martín, D., Reinhardt, J.M., Munoz-Barrutia, A. and Ortiz-De-Solórzano, C. (2010) Automated quantitative analysis of a mouse model of chronic pulmonary inflammation using micro X-ray computed tomography *Medical Image Computing and Computer Assisted Intervention Society (Pulmonary Imaging Workshop)*. Citeseer.

Aung, H., Sivakumar, A., Gholami, S., Venkateswaran, S. and Gorain, B. (2019) An Overview of the Anatomy and Physiology of the Lung *Nanotechnology-Based Targeted Drug Delivery Systems for Lung Cancer*. Elsevier, 1-20.

Ballarin, A., Bazzan, E., Zenteno, R.H., Turato, G., Baraldo, S., Zanovello, D., Mutti, E., Hogg, J.C., Saetta, M. and Cosio, M.G. (2012) Mast cell infiltration discriminates between histopathological phenotypes of chronic obstructive pulmonary disease. *American Journal of Respiratory and Critical Care Medicine,* 186 (3), 233-239.

Barker, A.F. (2002) Bronchiectasis. *New England Journal of Medicine,* 346 (18), 1383-1393.

Barnes, P.J. (2017) Cellular and molecular mechanisms of asthma and COPD. *Clinical Science,* 131 (13), 1541-1558.

Barnes, P.J. (2020) COPD 2020: new directions needed. *American Journal of Physiology-Lung Cellular and Molecular Physiology,* 319 (5), L884-L886.

Baschong, W., Suetterlin, R. and Laeng, R.H. (2001) Control of autofluorescence of archival formaldehyde-fixed, paraffin-embedded tissue in confocal laser scanning microscopy (CLSM). *Journal of Histochemistry & Cytochemistry,* 49 (12), 1565-1571.

Bayguinov, P.O., Fisher, M.R. and Fitzpatrick, J.A. (2020) Assaying three-dimensional cellular architecture using X-ray tomographic and correlated imaging approaches. *Journal of Biological Chemistry,* 295 (46), 15782-15793.

Bérubé, K., Prytherch, Z., Job, C. and Hughes, T. (2010) Human primary bronchial lung cell constructs: the new respiratory models. *Toxicology,* 278 (3), 311-318.

Bhatt, S.P., Soler, X., Wang, X., Murray, S., Anzueto, A.R., Beaty, T.H., Boriek, A.M., Casaburi, R., Criner, G.J. and Diaz, A.A. (2016) Association between functional small airway disease and FEV1 decline in chronic obstructive pulmonary disease. *American Journal of Respiratory and Critical Care Medicine,* 194 (2), 178-184.

Biga, L.M., Dawson, S., Harwell, A., Hopkins, R., Kaufmann, J., Lemaster, M., Matern, P., Morrison-Graham, K., Quick, D. and Runyeon, J. (2020) *Anatomy & Physiology*. OpenStax & Oregon State University.

Blanco, I., Piccari, L. and Barberà, J.A. (2016) Pulmonary vasculature in COPD: The silent component. *Respirology,* 21 (6), 984-994.

Blazquez-Llorca, L., Hummel, E., Zimmerman, H., Zou, C., Burgold, S., Rietdorf, J. and Herms, J. (2015) Correlation of two-photon in vivo imaging and FIB/SEM microscopy. *Journal of Microscopy,* 259 (2), 129-136.

Blom, S., Paavolainen, L., Bychkov, D., Turkki, R., Mäki-Teeri, P., Hemmes, A., Välimäki, K., Lundin, J., Kallioniemi, O. and Pellinen, T. (2017) Systems pathology by multiplexed immunohistochemistry and whole-slide digital image analysis. *Scientific Reports,* 7 (1), 1-13.

Bodduluri, S., Puliyakote, A.S.K., Gerard, S.E., Reinhardt, J.M., Hoffman, E.A., Newell, J.D., Nath, H.P., Han, M.K., Washko, G.R. and Estépar, R.S.J. (2018) Airway fractal dimension predicts respiratory morbidity and mortality in COPD. *The Journal of Clinical Investigation,* 128 (12), 5374-5382.

Bogovic, J.A., Hanslovsky, P., Wong, A. and Saalfeld, S. (2016) Robust registration of calcium images by learned contrast synthesis *2016 IEEE 13th International Symposium on Biomedical Imaging (ISBI)*, 13-16 April 2016. 1123-1126.

Borst, J.W. and Visser, A.J.W.G. (2010) Fluorescence lifetime imaging microscopy in life sciences. *Measurement Science and Technology,* 21 (10).

Bouxsein, M.L., Boyd, S.K., Christiansen, B.A., Guldberg, R.E., Jepsen, K.J. and Müller, R. (2010) Guidelines for assessment of bone microstructure in rodents using micro–computed tomography. *Journal of Bone and Mineral Research,* 25 (7), 1468-1486.

Bracke, K.R. and Brusselle, G.G. (2015) Chronic Obstructive Pulmonary Disease IN: Mestecky, J., Strober, W., Russell, M.W., Kelsall, B.L., Cheroutre, H. and Lambrecht, B.N. (eds.) *Mucosal Immunology (Fourth Edition)*. Boston: Academic Press, 1857-1866.

Bradding, P. and Arthur, G. (2016) Mast cells in asthma–state of the art. *Clinical & Experimental Allergy,* 46 (2), 194-263.

Bullitt, E., Muller, K.E., Jung, I., Lin, W. and Aylward, S. (2005) Analyzing attributes of vessel populations. *Medical Image Analysis,* 9 (1), 39-49.

Bushby, A.J., Mariggi, G., Armer, H.E. and Collinson, L.M. (2012) Correlative light and volume electron microscopy: using focused ion beam scanning electron microscopy to image transient events in model organisms. *Methods in Cell Biology,* 111, 357-382.

Byrne, A.J., Maher, T.M. and Lloyd, C.M. (2016) Pulmonary macrophages: A new therapeutic pathway in fibrosing lung disease? *Trends in Molecular Medicine,* 22 (4), 303-316.

Cadena-Herrera, D., Esparza-De Lara, J.E., Ramírez-Ibañez, N.D., López-Morales, C.A., Pérez, N.O., Flores-Ortiz, L.F. and Medina-Rivero, E. (2015) Validation of three viable-cell counting methods: Manual, semi-automated, and automated. *Biotechnology Reports,* 7, 9-16.

Calverley, P.M. (2004) The GOLD classification has advanced understanding of COPD. *American Journal of Respiratory and Critical Care Medicine,* 170 (3), 211-212.

Campillo-Navarro, M., Chávez-Blanco, A.D., Wong-Baeza, I., Serafín-López, J., Flores-Mejía, R., Estrada-Parra, S., Estrada-García, I. and Chacón-Salinas, R. (2014) Mast Cells in Lung Homeostasis: Beyond Type I Hypersensitivity. *Current Respiratory Medicine Reviews,* 10 (2), 115-123.

Chandel, R. and Gupta, G. (2013) Image filtering algorithms and techniques: A review. *International Journal of Advanced Research in Computer Science and Software Engineering,* 3 (10).

Cheung, W. and Hamarneh, G. (2009) nSIFT: n-Dimensional Scale Invariant Feature Transform. *IEEE Transactions on Image Processing,* 18 (9), 2012-2021.

Chicherova, N., Hieber, S.E., Khimchenko, A., Bikis, C., Muller, B. and Cattin, P. (2018) Automatic deformable registration of histological slides to muCT volume data. *Journal of Microscopy,* 271 (1), 49-61.

Cosio, M.G., Bazzan, E., Rigobello, C., Tinè, M., Turato, G., Baraldo, S. and Saetta, M. (2016) Alpha-1 antitrypsin deficiency: beyond the protease/antiprotease paradigm. *Annals of the American Thoracic Society,* 13 (Supplement 4), S305-S310.

Crisford, H., Sapey, E. and Stockley, R.A. (2018) Proteinase 3; a potential target in chronic obstructive pulmonary disease and other chronic inflammatory diseases. *Respiratory Research,* 19 (1), 180.

Crosby, K., Simendinger, J., Grange, C., Ferrante, M., Bernier, T. and Stanen, C. (2014) Immunohistochemistry protocol for paraffin-embedded tissue section-advertisement. *Journal of Visualized Experiments*.

Crowley, G., Kwon, S., Caraher, E.J., Haider, S.H., Lam, R., Batra, P., Melles, D., Liu, M. and Nolan, A. (2019) Quantitative lung morphology: semi-automated measurement of mean linear intercept. *BMC Pulmonary Medicine,* 19 (1), 206.

Cui, S., Jiang, H., Wang, Z. and Shen, C. (2017) Application of neural network based on sift local feature extraction in medical image classification *2017 2nd International Conference on Image, Vision and Computing (ICIVC)*. IEEE, 92-97.

De Bournonville, S., Vangrunderbeeck, S. and Kerckhofs, G. (2019) Contrast-Enhanced MicroCT for Virtual 3D Anatomical Pathology of Biological Tissues: A Literature Review. *Contrast Media & Molecular Imaging,* 2019, 8617406.

Dewhurst, J.A., Lea, S., Hardaker, E., Dungwa, J.V., Ravi, A.K. and Singh, D. (2017) Characterisation of lung macrophage subpopulations in COPD patients and controls. *Scientific Reports,* 7 (1), 1-12.

Dharmage, S.C., Perret, J. and Custovic, A. (2019) Epidemiology of asthma in children and adults. *Frontiers in Pediatrics,* 7, 246.

Doube, M., Kłosowski, M.M., Arganda-Carreras, I., Cordelières, F.P., Dougherty, R.P., Jackson, J.S., Schmid, B., Hutchinson, J.R. and Shefelbine, S.J. (2010) BoneJ: free and extensible bone image analysis in ImageJ. *Bone,* 47 (6), 1076-1079.

Dunning, C. and Bazalova-Carter, M. (2020) Design of a combined X-ray fluorescence Computed Tomography (CT) and photon-counting CT table-top imaging system. *Journal of Instrumentation,* 15 (06), P06031.

Estépar, R.S.J., Kinney, G.L., Black-Shinn, J.L., Bowler, R.P., Kindlmann, G.L., Ross, J.C., Kikinis, R., Han, M.K., Come, C.E. and Diaz, A.A. (2013) Computed tomographic measures of pulmonary vascular morphology in smokers and their clinical implications. *American Journal of Respiratory and Critical Care Medicine,* 188 (2), 231-239.

Fatonah, N.S., Tjandrasa, H. and Fatichah, C. (2018) Automatic Leukemia Cell Counting using Iterative Distance Transform for Convex Sets. *International Journal of Electrical and Computer Engineering,* 8 (3), 1731.

Fischer, A.H., Jacobson, K.A., Rose, J. and Zeller, R. (2008) Hematoxylin and eosin staining of tissue and cell sections. *Cold Spring Harbor Protocols,* 2008 (5), pdb. prot4986.

Fitzgerald, S., Wang, S., Dai, D., Murphree Jr, D.H., Pandit, A., Douglas, A., Rizvi, A., Kadirvel, R., Gilvarry, M. and Mccarthy, R. (2019) Orbit image analysis machine learning software can be used for the histological quantification of acute ischemic stroke blood clots. *PloS One,* 14 (12), e0225841.

Glenny, R.W. (2011) Emergence of matched airway and vascular trees from fractal rules. *Journal of Applied Physiology,* 110 (4), 1119-1129.

Goldman, L.W. (2007) Principles of CT: radiation dose and image quality. *Journal of Nuclear Medicine Technology,* 35 (4), 213-225.

Group, N.E.T.T.R. (2003) A randomized trial comparing lung-volume–reduction surgery with medical therapy for severe emphysema. *New England Journal of Medicine,* 348 (21), 2059-2073.

Hadzic, S., Wu, C.-Y., Avdeev, S., Weissmann, N., Schermuly, R.T. and Kosanovic, D. (2020) Lung epithelium damage in COPD–An unstoppable pathological event? *Cellular Signalling,* 68, 109540.

Handschuh, S., Baeumler, N., Schwaha, T. and Ruthensteiner, B. (2013) A correlative approach for combining microCT, light and transmission electron microscopy in a single 3D scenario. *Frontiers in Zoology,* 10 (1), 1-16.

Hartl, D., Tirouvanziam, R., Laval, J., Greene, C.M., Habiel, D., Sharma, L., Yildirim, A.Ö., Dela cruz, C.S. and Hogaboam, C.M. (2018) Innate Immunity of the Lung: From Basic Mechanisms to Translational Medicine. *Journal of Innate Immunity,* 10 (5-6), 487-501.

Heidari, Z., Sakhavar, N., Mahmoudzadeh-Sagheb, H. and Ezazi-Bojnourdi, T. (2015) Stereological analysis of human placenta in cases of placenta previa in comparison with normally implanted controls. *Journal of Reproduction & Infertility,* 16 (2), 90.

Helmberger, M., Pienn, M., Urschler, M., Kullnig, P., Stollberger, R., Kovacs, G., Olschewski, A., Olschewski, H. and Balint, Z. (2014) Quantification of tortuosity and fractal dimension of the lung vessels in pulmonary hypertension patients. *PLOS One,* 9 (1), e87515.

Hogan, B.L., Barkauskas, C.E., Chapman, H.A., Epstein, J.A., Jain, R., Hsia, C.C., Niklason, L., Calle, E., Le, A., Randell, S.H., Rock, J., Snitow, M., Krummel, M., Stripp, B.R., Vu, T., White, E.S., Whitsett, J.A. and Morrisey, E.E. (2014) Repair and regeneration of the respiratory system: complexity, plasticity, and mechanisms of lung stem cell function. *Cell Stem Cell,* 15 (2), 123-138.

Holzinger, A., Malle, B., Kieseberg, P., Roth, P.M., Müller, H., Reihs, R. and Zatloukal, K. (2017) Machine learning and knowledge extraction in digital pathology needs an integrative approach *Towards Integrative Machine Learning and Knowledge Extraction*. Springer, 13-50.

Hsia, C.C., Hyde, D.M., Ochs, M. and Weibel, E.R. (2010) An official research policy statement of the American Thoracic Society/European Respiratory Society: standards for quantitative assessment of lung structure. *American Journal of Respiratory and Critical Care Medicine,* 181 (4), 394-418.

Hsia, C.C., Hyde, D.M. and Weibel, E.R. (2016) Lung structure and the intrinsic challenges of gas exchange. *Comprehensive Physiology*.

Hsieh, J. (2003) *Computed tomography: principles, design, artifacts, and recent advances*. SPIE press.

Hueper, K., Vogel-Claussen, J., Parikh, M.A., Austin, J.H., Bluemke, D.A., Carr, J., Choi, J., Goldstein, T.A., Gomes, A.S. and Hoffman, E.A. (2015) Pulmonary microvascular blood flow in mild chronic obstructive pulmonary disease and emphysema. The MESA COPD Study. *American Journal of Respiratory and Critical Care Medicine,* 192 (5), 570-580.

Jablonski, A. (1933) Efficiency of anti-Stokes fluorescence in dyes. *Nature,* 131 (839-840), 21.

Jambusaria, A., Hong, Z., Zhang, L., Srivastava, S., Jana, A., Toth, P.T., Dai, Y., Malik, A.B. and Rehman, J. (2020) Endothelial heterogeneity across distinct vascular beds during homeostasis and inflammation. *Elife,* 9, e51413.

Jan, S. and Andrei, P. (2004) Reduction of ring artefacts in high resolution micro-CT reconstructions. *Physics in Medicine and Biology,* 49 (14), N247.

Jarockyte, G., Dapkute, D., Karabanovas, V., Daugmaudis, J.V., Ivanauskas, F. and Rotomskis, R. (2018) 3D cellular spheroids as tools for understanding carboxylated quantum dot behavior in tumors. *Biochimica et Biophysica Acta (BBA) - General Subjects,* 1862 (4), 914-923.

Johnson Jr, R.L., Heigenhauser, G.J., Hsia, C.C., Jones, N.L. and Wagner, P.D. (2010) Determinants of gas exchange and acid–base balance during exercise. *Comprehensive Physiology*, 515-584.

Jones, M.G., Fabre, A., Schneider, P., Cinetto, F., Sgalla, G., Mavrogordato, M., Jogai, S., Alzetani, A., Marshall, B.G., O'reilly, K.M.A., Warner, J.A., Lackie, P.M., Davies, D.E., Hansell, D.M.,

Nicholson, A.G., Sinclair, I., Brown, K.K. and Richeldi, L. (2016) Three-dimensional characterization of fibroblast foci in idiopathic pulmonary fibrosis. *JCI Insight,* 1 (5), e86375.

Kahnert, K., Alter, P., Young, D., Lucke, T., Heinrich, J., Huber, R.M., Behr, J., Wacker, M., Biertz, F., Watz, H., Bals, R., Welte, T., Wirtz, H., Herth, F., Vestbo, J., Wouters, E.F., Vogelmeier, C.F. and Jörres, R.A. (2018) The revised GOLD 2017 COPD categorization in relation to comorbidities. *Respiratory Medicine,* 134, 79-85.

Kampschulte, M., Schneider, C., Litzlbauer, H., Tscholl, D., Schneider, C., Zeiner, C., Krombach, G., Ritman, E., Bohle, R. and Langheinrich, A. (2013) Quantitative 3D micro-CT imaging of human lung tissue *RöFo-Fortschritte auf dem Gebiet der Röntgenstrahlen und der bildgebenden Verfahren*. © Georg Thieme Verlag KG, 869-876.

Katsamenis, O.L., Olding, M., Warner, J.A., Chatelet, D.S., Jones, M.G., Sgalla, G., Smit, B., Larkin, O.J., Haig, I., Richeldi, L., Sinclair, I., Lackie, P.M. and Schneider, P. (2019) X-ray micro-computed tomography for non-destructive 3D X-ray histology. *The American Journal of Pathology,* 189 (8), 1608-1620.

Kerckhofs, G., Stegen, S., Van Gastel, N., Sap, A., Falgayrac, G., Penel, G., Durand, M., Luyten, F.P., Geris, L., Vandamme, K., Parac-Vogt, T. and Carmeliet, G. (2018) Simultaneous three-dimensional visualization of mineralized and soft skeletal tissues by a novel microCT contrast agent with polyoxometalate structure. *Biomaterials,* 159, 1-12.

Khosroshahi, M.E. and Rahmani, M. (2012) Detection and evaluation of normal and malignant cells using laser-induced fluorescence spectroscopy. *Journal of Fluorescence,* 22 (1), 281-288.

Kim, T., Kim, D. and Lee, S. (2020) Cell counting algorithm using radius variation, watershed and distance transform. *Journal of Information Processing Systems,* 16 (1), 113-119.

Kirkham, P.A. and Barnes, P.J. (2013) Oxidative stress in COPD. *Chest,* 144 (1), 266-273.

Komi, D.E.A. and Bjermer, L. (2019) Mast cell-mediated orchestration of the immune responses in human allergic asthma: current insights. *Clinical Reviews in Allergy & Immunology,* 56 (2), 234-247.

Koo, H.-K., Vasilescu, D.M., Booth, S., Hsieh, A., Katsamenis, O.L., Fishbane, N., Elliott, W.M., Kirby, M., Lackie, P., Sinclair, I., Warner, J.A., Cooper , J.D., Coxson , H.O., Paré, P.D., Hogg , J.C. and Hackett, T.-L. (2018) Small airways disease in mild and moderate chronic obstructive pulmonary disease: a cross-sectional study. *The Lancet Respiratory Medicine,* 6 (8), 591-602.

Koo, H.-K., Vasilescu, D.M., Booth, S., Scott, A.E., Katsamenis, O., Warner, J., Sinclair, I., Hogg, J.C. and Hackett, T.-L. (2016) Investigating the nature of small airways disease in mild/moderate COPD: micro-CT analysis Of paraffin embedded lung tissue *C69. Here's Looking At You: Imaging Studies in COPD*. American Thoracic Society, A5815-A5815.

Korfiatis, V.C., Tassani, S. and Matsopoulos, G.K. (2017) An independent active contours segmentation framework for bone micro-CT images. *Computers in Biology and Medicine,* 87, 358-370.

Krystel-Whittemore, M., Dileepan, K.N. and Wood, J.G. (2016) Mast Cell: A Multi-Functional Master Cell. *Frontiers in Immunology,* 6 (620).

Kukulski, W., Schorb, M., Welsch, S., Picco, A., Kaksonen, M. and Briggs, J.a.G. (2012) Chapter 13 - Precise, Correlated Fluorescence Microscopy and Electron Tomography of Lowicryl

Sections Using Fluorescent Fiducial Markers IN: Müller-Reichert, T. and Verkade, P. (eds.) *Methods in Cell Biology*. Academic Press, 235-257.

Lauerová, L., Kovařik, J., Bártek, J., Rejthar, A. and Vojtěšek, B. (1988) Novel monoclonal antibodies defining epitope of human cytokeratin 18 molecule. *Hybridoma,* 7 (5), 495-504.

Leblond, F., Davis, S.C., Valdés, P.A. and Pogue, B.W. (2010) Pre-clinical whole-body fluorescence imaging: Review of instruments, methods and applications. *Journal of Photochemistry and Photobiology B: Biology,* 98 (1), 77-94.

Lee, H. and Kim, J. (2016) Segmentation of overlapping cervical cells in microscopic images with superpixel partitioning and cell-wise contour refinement *Proceedings of the IEEE Conference on Computer Vision and Pattern Recognition Workshops*. 63-69.

Lee, S.C., Kim, H.K., Chun, I.K., Cho, M.H., Lee, S.Y. and Cho, M.H. (2003) A flat-panel detector based micro-CT system: performance evaluation for small-animal imaging. *Physics in Medicine and Biology,* 48 (24), 4173-4185.

Libard, S., Cerjan, D. and Alafuzoff, I. (2019) Characteristics of the tissue section that influence the staining outcome in immunohistochemistry. *Histochemistry and Cell Biology,* 151 (1), 91-96.

López, C.S., Bouchet-Marquis, C., Arthur, C.P., Riesterer, J.L., Heiss, G., Thibault, G., Pullan, L., Kwon, S. and Gray, J.W. (2017) A fully integrated, three-dimensional fluorescence to electron microscopy correlative workflow. *Methods in Cell Biology,* 140, 149-164.

Lowe, D.G. (1999) Object recognition from local scale-invariant features *International Conference on Computer Vision*. Ieee, 1150.

Lowe, D.G. (2004) Distinctive image features from scale-invariant keypoints. *International Journal of Computer Vision,* 60 (2), 91-110.

Lundin, E.L., Stauber, M., Papageorgiou, P., Ehrbar, M., Ghayor, C., Weber, F.E., Tanner, C. and Goksel, O. (2017) Automatic registration of 2D histological sections to 3D microCT volumes: Trabecular bone. *Bone,* 105, 173-183.

Maillard, J., Klehs, K., Rumble, C., Vauthey, E., Heilemann, M. and Fürstenberg, A. (2021) Universal quenching of common fluorescent probes by water and alcohols. *Chemical Science,* 12 (4), 1352-1362.

Malik, S.T., Birch, B.R., Voegeli, D., Fader, M., Foria, V., Cooper, A.J., Walls, A.F. and Lwaleed, B.A. (2018) Distribution of mast cell subtypes in interstitial cystitis: implications for novel diagnostic and therapeutic strategies? *Journal of Clinical Pathology,* 71 (9), 840-844.

Martin, C., Frija, J. and Burgel, P.-R. (2013) Dysfunctional lung anatomy and small airways degeneration in COPD. *International Journal of Chronic Obstructive Pulmonary Disease,* 8, 7.

Mawhinney, W., Warford, A., Rae, M. and Lauder, I. (1990) Automated immunochemistry. *Journal of Clinical Pathology,* 43 (7), 591-596.

Mcdade, T.W., Georgiev, A.V. and Kuzawa, C.W. (2016) Trade-offs between acquired and innate immune defenses in humans. *Evolution, Medicine, and Public Health,* 2016 (1), 1-16.

Mcdonough , J.E., Yuan , R., Suzuki , M., Seyednejad , N., Elliott , W.M., Sanchez , P.G., Wright , A.C., Gefter , W.B., Litzky , L., Coxson , H.O., Paré , P.D., Sin , D.D., Pierce , R.A., Woods , J.C., Mcwilliams , A.M., Mayo , J.R., Lam , S.C., Cooper , J.D. and Hogg , J.C. (2011) Small-airway obstruction and emphysema in chronic obstructive pulmonary disease. *New England Journal of Medicine,* 365 (17), 1567-1575.

Mcdonough, J.E., Yuan, R., Suzuki, M., Seyednejad, N., Elliott, W.M., Sanchez, P.G., Wright, A.C., Gefter, W.B., Litzky, L., Coxson, H.O., Paré, P.D., Sin, D.D., Pierce, R.A., Woods, J.C., Mcwilliams, A.M., Mayo, J.R., Lam, S.C., Cooper, J.D. and Hogg, J.C. (2011) Small-Airway Obstruction and Emphysema in Chronic Obstructive Pulmonary Disease. *New England Journal of Medicine,* 365 (17), 1567-1575.

Mcinnes, E. (2005) Artefacts in histopathology. *Comparative Clinical Pathology,* 13 (3), 100-108.

Mehboob, H., Tarlochan, F., Mehboob, A. and Chang, S.-H. (2018) Finite element modelling and characterization of 3D cellular microstructures for the design of a cementless biomimetic porous hip stem. *Materials & Design,* 149, 101-112.

Meiburger, K., Nam, S., Chung, E., Suggs, L., Emelianov, S. and Molinari, F. (2016) Skeletonization algorithm-based blood vessel quantification using in vivo 3D photoacoustic imaging. *Physics in Medicine & Biology,* 61 (22), 7994.

Merrilees, M.J., Ching, P.S., Beaumont, B., Hinek, A., Wight, T.N. and Black, P.N. (2008) Changes in elastin, elastin binding protein and versican in alveoli in chronic obstructive pulmonary disease. *Respiratory Research,* 9 (1), 41.

Metscher, B. (2020) A Simple Nuclear Contrast Staining Method for MicroCT-Based 3D Histology Using Lead(II) Acetate. *BioRxiv*, 2020.2009.2018.303024.

Metscher, B.D. (2009) MicroCT for developmental biology: A versatile tool for high-contrast 3D imaging at histological resolutions. *Developmental Dynamics,* 238 (3), 632-640.

Mhala, N.C. and Bhandari, S.H. (2016) Improved approach towards classification of histopathology images using bag-of-features *2016 International Conference on Signal and Information Processing (IConSIP)*. IEEE, 1-5.

Miller, A.J. and Spence, J.R. (2017) In vitro models to study human lung development, disease and homeostasis. *Physiology*.

Milne, S. and King, G.G. (2014) Advanced imaging in COPD: insights into pulmonary pathophysiology. *Journal of Thoracic Disease,* 6 (11), 1570.

Mohamed, E.A. and Sayed, W.M. (2020) Implication of JAK1/STAT3/SOCS3 pathway in Aging of cerebellum of Male Rat: Histological and Molecular study. *Scientific Reports,* 10 (1), 1-13.

Moiseenko, A., Kheirollahi, V., Chao, C.M., Ahmadvand, N., Quantius, J., Wilhelm, J., Herold, S., Ahlbrecht, K., Morty, R.E. and Rizvanov, A.A. (2017) Origin and characterization of alpha smooth muscle actin-positive cells during murine lung development. *Stem Cells,* 35 (6), 1566-1578.

Monici, M. (2005) Cell and tissue autofluorescence research and diagnostic applications. *Biotechnology Annual Review,* 11, 227-256.

Mookiah, M.R.K., Hogg, S., Macgillivray, T.J., Prathiba, V., Pradeepa, R., Mohan, V., Anjana, R.M., Doney, A.S., Palmer, C.N. and Trucco, E. (2020) A Review of Machine Learning Methods for Retinal Blood Vessel Segmentation and Artery/Vein Classification. *Medical Image Analysis*, 101905.

Morales, A.G., Stempinski, E.S., Xiao, X., Patel, A., Panna, A., Olivier, K.N., Mcshane, P.J., Robinson, C., George, A.J., Donahue, D.R., Chen, P. and Wen, H. (2016) Micro-CT scouting for transmission electron microscopy of human tissue specimens. *Journal of Microscopy,* 263 (1), 113-117.

Mühlfeld, C., Wrede, C., Knudsen, L., Buchacker, T., Ochs, M. and Grothausmann, R. (2018) Recent developments in 3-D reconstruction and stereology to study the pulmonary vasculature. *American Journal of Physiology-Lung Cellular and Molecular Physiology,* 315 (2), L173-L183.

Museyko, O., Marshall, R.P., Lu, J., Hess, A., Schett, G., Amling, M., Kalender, W.A. and Engelke, K. (2015) Registration of 2D histological sections with 3D micro-CT datasets from small animal vertebrae and tibiae. *Computer Methods in Biomechanics and Biomedical Engineering,* 18 (15), 1658-1673.

Naylor, P., Laé, M., Reyal, F. and Walter, T. (2018) Segmentation of nuclei in histopathology images by deep regression of the distance map. *IEEE Transactions on Medical Imaging,* 38 (2), 448-459.

Norman, D., Watson, D., Burnett, B., Fenne, P. and Williams, M. (2018) The cutting edge—micro-CT for quantitative toolmark analysis of sharp force trauma to bone. *Forensic Science International,* 283, 156-172.

Núñez, J., Goring, A., Javaheri, B., Razi, H., Gomez-Nicola, D., Hesse, E., Pitsillides, A., Thurner, P., Schneider, P. and Clarkin, C. (2018) Regional diversity in the murine cortical vascular network is revealed by synchrotron X-ray tomography and is amplified with age. *European Cells & Materials,* 35, 281-299.

O'koren, E.G., Hogan, B.L. and Gunn, M.D. (2013) Loss of basal cells precedes bronchiolitis obliterans–like pathological changes in a murine model of chlorine gas inhalation. *American Journal of Respiratory and Critical Care Medicine,* 49 (5), 788-797.

Öztürk, Ş. and Bayram, A. (2018) Comparison of HOG, MSER, SIFT, FAST, LBP and CANNY features for cell detection in histopathological images. *HELIX,* 8 (3), 3321-3325.

Pahlevaninezhad, H., Lee, A.M.D., Lam, S., Macaulay, C. and Lane, P.M. (2014) Coregistered autofluorescence-optical coherence tomography imaging of human lung sections. *Journal of Biomedical Optics,* 19 (3), 036022.

Pakkasela, J., Ilmarinen, P., Honkamäki, J., Tuomisto, L.E., Andersén, H., Piirilä, P., Hisinger-Mölkänen, H., Sovijärvi, A., Backman, H. and Lundbäck, B. (2020) Age-specific incidence of allergic and non-allergic asthma. *BMC Pulmonary Medicine,* 20 (1), 1-9.

Pang, Z., Barash, E., Santamaria-Pang, A., Sevinsky, C., Li, Q. and Ginty, F. (2013) Autofluorescence removal using a customized filter set. *Microscopy Research and Technique,* 76 (10), 1007-1015.

Parlanti, P., Cappello, V., Brun, F., Tromba, G., Rigolio, R., Tonazzini, I., Cecchini, M., Piazza, V. and Gemmi, M. (2017) Size and specimen-dependent strategy for x-ray micro-ct and tem correlative analysis of nervous system samples. *Scientific Reports,* 7 (1), 1-12.

Parlanti, P., Rigolio, R., Tromba, G., Manzini, C., Popratiloff, A. and Cappello, V. (2019) Correlative Synchrotron Micro-CT and FIB-SEM Imaging for the Analysis of Multifocal Pathologies. *Microscopy and Microanalysis,* 25 (S2), 1052-1053.

Paul-Gilloteaux, P., Heiligenstein, X., Belle, M., Domart, M.-C., Larijani, B., Collinson, L., Raposo, G. and Salamero, J. (2017) eC-CLEM: flexible multidimensional registration software for correlative microscopies. *Nature Methods,* 14 (2), 102-103.

Piccinini, F., Tesei, A., Arienti, C. and Bevilacqua, A. (2017) Cell counting and viability assessment of 2d and 3d cell cultures: expected reliability of the trypan blue assay. *Biological Procedures Online,* 19 (1), 1-12.

Pietzsch, T., Saalfeld, S., Preibisch, S. and Tomancak, P. (2015) BigDataViewer: visualization and processing for large image data sets. *Nature Methods,* 12 (6), 481-483.

Polan, D.F., Brady, S.L. and Kaufman, R.A. (2016) Tissue segmentation of computed tomography images using a Random Forest algorithm: a feasibility study. *Physics in Medicine & Biology,* 61 (17), 6553.

Poobalasingam, T., Salman, D., Li, H., Alcada, J. and Dean, C.H. (2016) Imaging the lung: the old ways and the new. *Histology & Histopathology*, 11827.

Power, R.M. and Huisken, J. (2017) A guide to light-sheet fluorescence microscopy for multiscale imaging. *Nature Methods,* 14 (4), 360-373.

Rahaghi, F.N., Argemí, G., Nardelli, P., Domínguez-Fandos, D., Arguis, P., Peinado, V.I., Ross, J.C., Ash, S.Y., De La Bruere, I. and Come, C.E. (2019) Pulmonary vascular density: comparison of findings on computed tomography imaging with histology. *European Respiratory Journal,* 54 (2), 1900370.

Ramos-Vara, J. (2005) Technical aspects of immunohistochemistry. *Veterinary Pathology,* 42 (4), 405-426.

Rao, L.J., Neelakanteswar, P., Ramkumar, M., Krishna, A. and Basha, C.Z. (2020) An Effective Bone Fracture Detection using Bag-of-Visual-Words with the Features Extracted from SIFT *2020 International Conference on Electronics and Sustainable Communication Systems (ICESC)*. IEEE, 6-10.

Rastogi, V., Puri, N., Arora, S., Kaur, G., Yadav, L. and Sharma, R. (2013) Artefacts: a diagnostic dilemma–a review. *Journal of Clinical and Diagnostic Research: JCDR,* 7 (10), 2408.

Robertson, D. and Isacke, C.M. (2011) Multiple Immunofluorescence Labeling of Formalin-Fixed Paraffin-Embedded Tissue. *BMC Cell Biology,* 724, 69-77.

Robertson, D., Savage, K., Reis-Filho, J.S. and Isacke, C.M. (2008) Multiple immunofluorescence labelling of formalin-fixed paraffin-embedded (FFPE) tissue. *BMC Cell Biology,* 9 (1), 13.

Robinson, P. and Morgan, L. (2018) Bronchiectasis in PCD looks different to CF on CT scan. *Multidisciplinary Respiratory Medicine,* 13 (1), 24.

Robinson, S.K. (2020) to Lawson, M.J.,

Robinson, S.K., Ramsden, J.J., Warner, J., Lackie, P.M. and Roose, T. (2019) Correlative 3D imaging and microfluidic modelling of human pulmonary lymphatics using immunohistochemistry and high-resolution µCT. *Scientific Reports,* 9 (1), 6415.

Rohr, K., Stiehl, H.S., Sprengel, R., Buzug, T.M., Weese, J. and Kuhn, M. (2001) Landmark-based elastic registration using approximating thin-plate splines. *IEEE Transactions on Medical Imaging,* 20 (6), 526-534.

Russell, M.R.G., Lerner, T.R., Burden, J.J., Nkwe, D.O., Pelchen-Matthews, A., Domart, M.-C., Durgan, J., Weston, A., Jones, M.L., Peddie, C.J., Carzaniga, R., Florey, O., Marsh, M.,

Gutierrez, M.G. and Collinson, L.M. (2017) 3D correlative light and electron microscopy of cultured cells using serial blockface scanning electron microscopy. *Journal of Cell Science,* 130 (1), 278-291.

Ryu, J.H., Moua, T., Daniels, C.E., Hartman, T.E., Eunhee, S.Y., Utz, J.P. and Limper, A.H. (2014) Idiopathic pulmonary fibrosis: evolving concepts *Mayo Clinic Proceedings*. Elsevier, 1130-1142.

Sakao, S., Voelkel, N.F. and Tatsumi, K. (2014) The vascular bed in COPD: pulmonary hypertension and pulmonary vascular alterations. *European Respiratory Review,* 23 (133), 350-355.

Santos, S., Peinado, V.I., Ramirez, J., Melgosa, T., Roca, J., Rodriguez-Roisin, R. and Barbera, J. (2002) Characterization of pulmonary vascular remodelling in smokers and patients with mild COPD. *European Respiratory Journal,* 19 (4), 632-638.

Saruya, S., Matsuoka, S., Yamashiro, T., Matsushita, S., Fujikawa, A., Yagihashi, K., Kurihara, Y. and Nakajima, Y. (2016) Quantitative CT measurements of small pulmonary vessels in chronic obstructive pulmonary disease: do they change on follow-up scans? *Clinical Physiology and Functional Imaging,* 36 (3), 211-217.

Schaad, L., Hlushchuk, R., Barré, S., Gianni-Barrera, R., Haberthür, D., Banfi, A. and Djonov, V. (2017) Correlative imaging of the murine hind limb vasculature and muscle tissue by MicroCT and light microscopy. *Scientific Reports,* 7 (1), 1-12.

Schellenberger, P., Kaufmann, R., Siebert, C.A., Hagen, C., Wodrich, H. and Grünewald, K. (2014) High-precision correlative fluorescence and electron cryo microscopy using two independent alignment markers. *Ultramicroscopy,* 143, 41-51.

Schiller, H.B., Montoro, D.T., Simon, L.M., Rawlins, E.L., Meyer, K.B., Strunz, M., Vieira Braga, F.A., Timens, W., Koppelman, G.H. and Budinger, G.S. (2019) The Human Lung Cell Atlas: a high-resolution reference map of the human lung in health and disease. *American Journal of Respiratory Cell and Molecular Biology,* 61 (1), 31-41.

Schindelin, J., Arganda-Carreras, I., Frise, E., Kaynig, V., Longair, M., Pietzsch, T., Preibisch, S., Rueden, C., Saalfeld, S. and Schmid, B. (2012) Fiji: an open-source platform for biological-image analysis. *Nature Methods,* 9 (7), 676.

Schneider, J.P. and Ochs, M. (2014) Alterations of mouse lung tissue dimensions during processing for morphometry: a comparison of methods. *American Journal of Physiology-Lung Cellular and Molecular Physiology,* 306 (4), L341-L350.

Schulman, E., Kagey-Sobotka, A., Macglashan, D., Adkinson, N., Peters, S., Schleimer, R. and Lichtenstein, L. (1983) Heterogeneity of human mast cells. *The Journal of Immunology,* 131 (4), 1936-1941.

Scott, A.E., Vasilescu, D.M., Seal, K.a.D., Keyes, S.D., Mavrogordato, M.N., Hogg, J.C., Sinclair, I., Warner, J.A., Hackett, T.-L. and Lackie, P.M. (2015) Three Dimensional Imaging of Paraffin Embedded Human Lung Tissue Samples by Micro-Computed Tomography. *PLOS One,* 10 (6), e0126230.

Seibold, M.A., Smith, R.W., Urbanek, C., Groshong, S.D., Cosgrove, G.P., Brown, K.K., Schwarz, M.I., Schwartz, D.A. and Reynolds, S.D. (2013) The idiopathic pulmonary fibrosis honeycomb cyst contains a mucocilary pseudostratified epithelium. *PLOS One,* 8 (3), e58658.

Shang, Y., Deklerck, R., Nyssen, E., Markova, A., De Mey, J., Yang, X. and Sun, K. (2010) Vascular active contour for vessel tree segmentation. *IEEE Transactions on Biomedical Engineering,* 58 (4), 1023-1032.

Sharma, R.K., Mathur, Y., Chhabra, G., Luhadia, A., Luhadia, S.K. and Dhandoria, G. (2018) A study of skin sensitivity to various allergens by skin prick test in patients of bronchial asthma and allergic rhinitis. *Indian Journal of Allergy, Asthma and Immunology,* 32 (2), 47.

Shi, S.-R., Shi, Y. and Taylor, C.R. (2011) Antigen retrieval immunohistochemistry: review and future prospects in research and diagnosis over two decades. *Journal of Histochemistry and Cytochemistry,* 59 (1), 13-32.

Shields, K.J., Verdelis, K., Passineau, M.J., Faight, E.M., Zourelias, L., Wu, C., Chong, R. and Benza, R.L. (2016) Three-dimensional micro computed tomography analysis of the lung vasculature and differential adipose proteomics in the Sugen/hypoxia rat model of pulmonary arterial hypertension. *Pulmonary Circulation,* 6 (4), 586-596.

Siqueira Jr, J., Pérez, A., Marceliano-Alves, M., Provenzano, J., Silva, S., Pires, F., Vieira, G., Rôças, I. and Alves, F. (2018) What happens to unprepared root canal walls: a correlative analysis using micro-computed tomography and histology/scanning electron microscopy. *International Endodontic Journal,* 51 (5), 501-508.

Smith, B.M., Austin, J.H., Newell Jr, J.D., D'souza, B.M., Rozenshtein, A., Hoffman, E.A., Ahmed, F. and Barr, R.G. (2014) Pulmonary emphysema subtypes on computed tomography: the MESA COPD study. *The American Journal of Medicine,* 127 (1), 94. e97-94. e23.

Soltani, A., Ewe, Y.P., Lim, Z.S., Sohal, S.S., Reid, D., Weston, S., Wood-Baker, R. and Walters, E.H. (2012) Mast cells in COPD airways: relationship to bronchodilator responsiveness and angiogenesis. *European Respiratory Journal,* 39 (6), 1361.

Sood, A., Sui, Y., Mcdonough, E., Santamaría-Pang, A., Al-Kofahi, Y., Pang, Z., Jahrling, P.B., Kuhn, J.H. and Ginty, F. (2020) Comparison of Multiplexed Immunofluorescence Imaging to Chromogenic Immunohistochemistry of Skin Biomarkers in Response to Monkeypox Virus Infection. *Viruses,* 12 (8), 787.

Sorzano, C.O.S., Thévenaz, P. and Unser, M. (2005) Elastic registration of biological images using vector-spline regularization. *IEEE Transactions on Biomedical Engineering,* 52 (4), 652-663.

Stämpfli, M.R. and Anderson, G.P. (2009) How cigarette smoke skews immune responses to promote infection, lung disease and cancer. *Nature Reviews Immunology,* 9 (5), 377.

Stanke, F. (2015) The contribution of the airway epithelial cell to host defense. *Mediators of inflammation,* 2015.

Suarez, C.J., Dintzis, S.M. and Frevert, C.W. (2012) Respiratory IN: Treuting, P.M. and Dintzis, S.M. (eds.) *Comparative Anatomy and Histology*. San Diego: Academic Press, 121-134.

Takayanagi, S., Kawata, N., Tada, Y., Ikari, J., Matsuura, Y., Matsuoka, S., Matsushita, S., Yanagawa, N., Kasahara, Y. and Tatsumi, K. (2017) Longitudinal changes in structural abnormalities using MDCT in COPD: do the CT measurements of airway wall thickness and small pulmonary vessels change in parallel with emphysematous progression? *International Journal of Chronic Obstructive Pulmonary Disease,* 12, 551.

Tanabe, N., Mcdonough, J.E., Vasilescu, D.M., Ikezoe, K., Verleden, S.E., Xu, F., Wuyts, W.A., Vanaudenaerde, B.M., Colby, T.V. and Hogg, J.C. (2020) Pathology of Idiopathic Pulmonary Fibrosis Assessed by a Combination of Microcomputed Tomography, Histology, and Immunohistochemistry. *The American Journal of Pathology*.

Tassani, S., Korfiatis, V. and Matsopoulos, G. (2014) Influence of segmentation on micro-CT images of trabecular bone. *Journal of Microscopy,* 256 (2), 75-81.

Timmermans, F.J. and Otto, C. (2015) Contributed review: Review of integrated correlative light and electron microscopy. *Review of scientific instruments,* 86 (1), 011501.

Townsley, M.I. (2011) Structure and composition of pulmonary arteries, capillaries, and veins. *Comprehensive Physiology,* 2 (1), 675-709.

Tward, D., Brown, T., Kageyama, Y., Patel, J., Hou, Z., Mori, S., Albert, M., Troncoso, J. and Miller, M. (2020) Diffeomorphic registration with intensity transformation and missing data: Application to 3D digital pathology of Alzheimer's disease. *Frontiers in Neuroscience,* 14, 52.

Ur Rehman, A., Hassali, M.a.A., Abbas, S., Ali, I.a.B.H., Harun, S.N., Muneswarao, J. and Hussain, R. (2019) Pharmacological and non-pharmacological management of COPD; limitations and future prospects: a review of current literature. *Journal of Public Health*, 1-10.

Vaes, A.W., Spruit, M.A., Van Keer, K., Barbosa-Breda, J., Wouters, E.F., Franssen, F.M., Theunis, J. and De Boever, P. (2020) Structural analysis of retinal blood vessels in patients with COPD during a pulmonary rehabilitation program. *Scientific Reports,* 10.

Van Rikxoort, E. and Ginneken, B. (2013) Automated segmentation of pulmonary structures in thoracic computed tomography scans: A review. *Physics in Medicine and Biology,* 58, R187-R220.

Vareille, M., Kieninger, E., Edwards, M.R. and Regamey, N. (2011) The airway epithelium: soldier in the fight against respiratory viruses. *Clinical Microbiology Reviews,* 24 (1), 210-229.

Vasilescu, D.M., Knudsen, L., Ochs, M., Weibel, E.R. and Hoffman, E.A. (2012) Optimized murine lung preparation for detailed structural evaluation via micro-computed tomography. *Journal of Applied Physiology (1985),* 112 (1), 159-166.

Vasudevan, S., Vásquez, J.J., Chen, W., Aguilar-Rodriguez, B., Niemi, E.C., Zeng, S., Tamaki, W., Nakamura, M.C. and Arjomandi, M. (2020) Lower PDL1/2 and AXL Expression on Lung Myeloid Cells Suggests Inflammatory Bias in Smoking and COPD. *American Journal of Respiratory Cell and Molecular Biology,* (ja).

Vestbo, J., Hurd, S.S., Agustí, A.G., Jones, P.W., Vogelmeier, C., Anzueto, A., Barnes, P.J., Fabbri, L.M., Martinez, F.J. and Nishimura, M. (2013) Global strategy for the diagnosis, management, and prevention of chronic obstructive pulmonary disease: GOLD executive summary. *American Journal of Respiratory and Critical Care Medicine,* 187 (4), 347-365.

Virk, H., Arthur, G. and Bradding, P. (2016) Mast cells and their activation in lung disease. *Translational Research,* 174, 60-76.

Vitenberga, Z., Pilmane, M. and Babjoniševa, A. (2019) An Insight into COPD Morphopathogenesis: Chronic Inflammation, Remodeling, and Antimicrobial Defense. *Medicina,* 55 (8), 496.

Voelkel, N.F., Mizuno, S. and Cool, C.D. (2017) The Spectrum of Pulmonary Disease in COPD *COPD*. Springer, 195-207.

Vogelmeier, C.F., Criner, G.J., Martinez, F.J., Anzueto, A., Barnes, P.J., Bourbeau, J., Celli, B.R., Chen, R., Decramer, M. and Fabbri, L.M. (2017) Global strategy for the diagnosis, management, and prevention of chronic obstructive lung disease 2017 report. GOLD

executive summary. *American Journal of Respiratory and Critical Care Medicine,* 195 (5), 557-582.

Wang, M.Y., Long, F., Tang, F., Jing, Y.Y., Wang, X.Y., Yao, L.F., Ma, J., Fei, Y.Y., Chen, L., Wang, G.F. and Mi, L. (2017) Autofluorescence imaging and spectroscopy of human lung cancer. *Applied Sciences-Basel,* 7 (1).

Wang, Y., Bai, C., Li, K., Adler, K.B. and Wang, X. (2008) Role of airway epithelial cells in development of asthma and allergic rhinitis. *Respiratory Medicine,* 102 (7), 949-955.

Weber, E., Sozio, F., Borghini, A., Sestini, P. and Renzoni, E. (2018) Pulmonary lymphatic vessel morphology: a review. *Annals of Anatomy-Anatomischer Anzeiger*.

Weibel, E.R. (2009) What makes a good lung? *Swiss medical weekly,* 139 (2728).

Weibel, E.R. (2015) On the tricks alveolar epithelial cells play to make a good lung. *American Journal of Respiratory and Critical Care Medicine,* 191 (5), 504-513.

Wells, J.M., Iyer, A.S., Rahaghi, F.N., Bhatt, S.P., Gupta, H., Denney, T.S., Lloyd, S.G., Dell'italia, L.J., Nath, H. and Estepar, R.S.J. (2015) Pulmonary artery enlargement is associated with right ventricular dysfunction and loss of blood volume in small pulmonary vessels in chronic obstructive pulmonary disease. *Circulation: Cardiovascular Imaging,* 8 (4), e002546.

Wilson, M.S. and Wynn, T.A. (2009) Pulmonary fibrosis: pathogenesis, etiology and regulation. *Mucosal Immunology,* 2 (2), 103-121.

Woelfle, U., Sauter, G., Santjer, S., Brakenhoff, R. and Pantel, K. (2004) Down-regulated expression of cytokeratin 18 promotes progression of human breast cancer. *Clinical cancer research,* 10 (8), 2670-2674.

Wollatz, L., Johnston, S.J., Lackie, P.M. and Cox, S.J. (2017) 3D Histopathology—a Lung Tissue Segmentation Workflow for Microfocus X-ray-Computed Tomography Scans. *Journal of Digital Imaging,* 30, 772-781.

Xing, F. and Yang, L. (2016) Robust nucleus/cell detection and segmentation in digital pathology and microscopy images: a comprehensive review. *IEEE Reviews in Biomedical Engineering,* 9, 234-263.

Yamasaki, K. and Eeden, S.F.V. (2018) Lung macrophage phenotypes and functional responses: role in the pathogenesis of COPD. *International Journal of Molecular Sciences,* 19 (2), 582.

Yan, L., Qi, J., Zhu, S., Lin, T., Zhou, X. and Liu, X. (2017) 3D micro CT imaging of the human peripheral nerve fascicle. *International Journal of Clinical and Experimental Medicine,* 10 (7), 10315-10323.

Yushkevich, P.A., Piven, J., Hazlett, H.C., Smith, R.G., Ho, S., Gee, J.C. and Gerig, G. (2006) User-guided 3D active contour segmentation of anatomical structures: Significantly improved efficiency and reliability. *NeuroImage,* 31 (3), 1116-1128.

Zagorchev, L., Oses, P., Zhuang, Z.W., Moodie, K., Mulligan-Kehoe, M.J., Simons, M. and Couffinhal, T. (2010) Micro computed tomography for vascular exploration. *Journal of Angiogenesis Research,* 2 (1), 7.

Zdora, M.-C., Thibault, P., Kuo, W., Fernandez, V., Deyhle, H., Vila-Comamala, J., Olbinado, M.P., Rack, A., Lackie, P.M., Katsamenis, O.L., Lawson, M.J., Kurtcuoglu, V., Rau, C., Pfeiffer, F. and Zanette, I. (2020) X-ray phase tomography with near-field speckles for three-dimensional virtual histology. *Optica,* 7 (9), 1221-1227.

Zeng, Y.-Z., Liao, S.-H., Tang, P., Zhao, Y.-Q., Liao, M., Chen, Y. and Liang, Y.-X. (2018) Automatic liver vessel segmentation using 3D region growing and hybrid active contour model. *Computers in biology and medicine,* 97, 63-73.

Zhang, B., Niu, W., Dong, H.Y., Liu, M.L., Luo, Y. and Li, Z.C. (2018) Hypoxia induces endothelial-mesenchymal transition in pulmonary vascular remodeling. *International Journal of Molecular Medicine,* 42 (1), 270-278.

Zhang, B., Wang, J., Liu, W., Yin, Y., Qian, D., Zhang, H., Shi, B., Li, C., Zhu, J. and Zhang, L. (2016) Cytokeratin 18 knockdown decreases cell migration and increases chemosensitivity in non-small cell lung cancer. *Journal of Cancer Research and Clinical Oncology,* 142 (12), 2479-2487.

Zhao, F., Liang, J., Chen, D., Wang, C., Yang, X., Chen, X. and Cao, F. (2015) Automatic segmentation method for bone and blood vessel in murine hindlimb. *Medical Physics,* 42 (7), 4043-4054.

Zhao, W., Liu, H., Leader, J.K., Wilson, D., Meng, X., Wang, L., Chen, L.-A. and Pu, J. (2019) Computerized identification of the vasculature surrounding a pulmonary nodule. *Computerized Medical Imaging and Graphics,* 74, 1-9.

Zhou, C., Zheng, T., Luo, T., Yan, C., Sun, Q., Ren, M., Zhao, P., Chen, W., Ji, B. and Wang, Z. (2020) Continuous imaging of large-volume tissues with a machinable optical clearing method at subcellular resolution. *Biomedical Optics Express,* 11 (12), 7132-7149.

Zukic, D., Vicory, J., Mccormick, M., Wisse, L.E., Gerig, G., Yushkevich, P. and Aylward, S. (2016) ND morphological contour interpolation. *Insight Journal,* (2016 January-December).